UNIVERSITY OF CALIFORNIA

Los Angeles

Emittance preservation in a plasma wakefield accelerator

A dissertation submitted in partial satisfaction

of the requirements for the degree

Doctor of Philosophy in Physics

by

Yujian Zhao

2023

ABSTRACT OF THE DISSERTATION

Emittance preservation in a plasma wakefield accelerator

by

Yujian Zhao
Doctor of Philosophy in Physics
University of California, Los Angeles, 2023
Professor Warren B. Mori, Chair

Plasma-based acceleration (PBA) is being considered as the basis for a future linear collider, where electrons and positron bunches must collide with extremely small spot sizes. In order to be focused to such spot sizes the beams must have extremely small emittances. Thus one challenge to a PBA collider is preserving the emittance of the accelerated beams.

In this dissertation, the evolution and preservation of the witness beam emittance in a plasma-based accelerator in the nonlinear blowout regime is investigated using theory and particle-in-cell simulations. It it found that the use of plasma density ramps as matching sections are beneficial for emittance emittance growth mitigation and preservation even when the witness beam is focused so tightly within the plasma that its space charge force pulls ions inwards within the beam.

In order to study the evolution of a beam in the wakefield, details of the motion of a single beam particle in the accelerating and focusing fields of a nonlinear wakefield are presented. The exact solution to the transverse equation of motion of a single beam particle under the assumption of adiabatic acceleration is derived. Approximate and thus simpler solutions are provided under the assumptions that plasma density also changes adiabatically.

Some important concepts, including the beam's envelope equation, geometric emittance, normalized emittance, single and beam C-S parameters, transport matrices, and matching are reviewed and elaborated upon. Emittance evolution and the importance of matching are discussed in the context of a uniform plasma.

Using the approximate solution (WKB solution) of a single particle's motion, analytical expressions for the evolution of the beam emittance and the C-S parameters in an arbitrary adiabatic plasma profile are provided neglecting the acceleration of the beam inside the plasma. It is shown that the beam emittance can be preserved when the beams C-S parameters are matched to the entrance of the density profile even when the beam has an initial energy spread. It is also shown that the emittance growth for an unmatched beam is minimized when it is focused to the same vacuum plane as for a matched beam. The emittance evolution without ion motion is studied using 3D particle-in-cell QuickPIC simulation and the results agree well with the theoretical predictions.

In some of the proposed experiments for the recently commissioned FACET II facility, the matching condition may not be perfectly satisfied and the wake may not be perfectly symmetric. It is shown that for a given set of beam parameters that are consistent with FACET II capabilities, the emittance growth can still be minimized by choosing the optimal focal plane even when the assumptions of the theory are not satisfied. Additional considerations for FACET II experiments were investigated. The plasma source is a lithium plasma confined by a helium buffer gas. The plasma is formed from field ionization which can lead to a nonlinear focusing force inside the helium buffer gas due to its high ionization potential leading to a nonuniform transverse profile for the plasma. It is found in simulations that for an initial beam emittance of 20 μm, the helium ionization is found to be small and the witness beam's emittance can still be preserved.

Emittance evolution for beam and plasma parameters relevant to a single stage of a multi-staged plasma-based linear collider (LC) is investigated. In some plasma-based LC designs the transverse space charge forces for extreme accelerating beam parameters are

expected to pull background ions into the beam which can lead to longitudinally varying nonlinear focusing forces and result in emittance growth of the beam. To mitigate this, the use of an adiabatic plasma density ramp as a matching section is proposed and examined using theory and PIC simulations. The witness beam is matched to the low density plasma entrance, where the beam initially has a large matched spot size so the ion motion effects are relatively small. As the beam propagates in the plasma density upramp (downramp), it is adiabatically focused (defocused) and its phase space distribution evolves slowly towards an equilibrium distribution including the effects of the adiabatically changing ion motion. Simulation results from QPAD, a new quasi-3D, quasi-static PIC code, show that within a single acceleration stage, this concept can limit the projected emittance growth to only $\sim$2% for a 25 GeV, 100 nm emittance witness beam and $\sim$20% for a 100 GeV, 100 nm emittance witness beam. The trade-off between the adiabaticity of the plasma density ramp and the initial ion motion at the entrance for a given length of the plasma density ramp is also discussed.

Additional issues for building a plasma based linear collider are discussed. Preliminary particle-in-cell simulation results which examine and illustrate problems like staging, shaped witness beam (for improved beam loading), emittance growth and hosing of a witness beam with an initial offset, ion motion triggered by the driver, and asymmetric witness beams are presented. The implications of these issues on a plasma based linear collider are discussed. Simulation results for witness beams with initial energy of 500 GeV such as would exist in a final stage of a PBA linear collider or an afterburner are presented.

The dissertation of Yujian Zhao is approved.

Troy A. Carter

Chandra J. Joshi

George J. Morales

Warren B. Mori, Committee Chair

University of California, Los Angeles

2023

TABLE OF CONTENTS

LIST OF FIGURES

ACKNOWLEDGMENTS

First of all, I would like to thank my advisor, Warren Mori. He is a great physicist as well as a great mentor. When we discussed physics, I was always inspired by his insightful thoughts and physical intuition. I admire his strong ability to understand complicated concepts, which makes our communication very easy. Throughout these years, he constantly praised me for my progress and hard work, thanked me for giving him updates, and never ever criticized me (or any other student, as far as I know). He never pushed me to do anything, which gives me so much freedom, but he always provided me with insightful thoughts and great suggestions when I was stuck and asked him for help. He is also supportive about my life choice and showed a lot of empathy. From the bottom of my heart, I am greatly thankful for his respect, trust, and support. He is not only my role model academically, but also in real life. He really made my PhD life enjoyable. Thank you so much Warren.

I also want to thank Dr. Weiming An. Weiming gave me so much help during my PhD life. When I just started my research, there were so many times that I went upstairs and knocked at the door of his office, and asked him a bunch of questions. He was always extremely patient, would sit next to me and showed me the commands entered in my laptop, derived equations line by line on the whiteboard, etc. Our work together led to my first publication. He was basically my mentor in my first 2 years of research. When I implemented the ionization module in QuickPIC, Weiming still helped me understand the structure of the code and provided guidance through zoom calls, even though he was back in China as a professor at that time. I sincerely appreciate all the help and kindness from Weiming and hope his academic future keeps getting brighter.

I would also like to express my great appreciation to Dr. Xinlu Xu. Xinlu is the first person I talked to in Warren's group due to a coincidence: I attended a party ('Chinese people at Physics and Astronomy Building') where I sat next to Xinlu's wife, who later arranged a meeting for me and Xinlu after knowing I had some interests in joining Warren's

group. Xinlu introduced me to Warren, which initiated my entire PhD life. Xinlu has had such an important influence to my research. He generously shared his notes and scripts with me, and when I asked him about his notes and papers, he was always helpful, and gave me valuable advice. The continuation of his previous work leads to my first publication, and of course he gave me a lot of support and guidance in this process. I learned a lot from his intelligence and expertise.

I also want to greatly thank Dr. Fei Li. After Weiming left the group, Fei basically replaced his role. Fei is very intelligent, hard-working, productive and helpful. He helped me understand the structure and logic of QuickPIC when I was developing the ionization model. He patiently answered all my questions about QPAD, which is the code I heavily rely on and he wrote. Since the pandemic started, he was the most important person to me besides Warren, although most of our communication was through Slack. He was always very approachable and respond to my Slack messages not only quickly but also in great detail. His work and effort facilitated my research very much.

I also want to thank Lance Hildebrand. When I just started my research, everything was new to me. Lance was one year above me, his cubical was next to mine, and he was also my mentor in the physics graduate mentorship program. So naturally I felt we were closer. I could remember there were many times that I went to his cubical and asked if he had a few minutes for a few questions, he always paused his work immediately and helped me out. Later on it turned out that our research had a lot of overlap. We had a lot of conversations, did math on the whiteboard together, and inspired each other. We were roommates for AAC in 2018, 2022 and APS in 2019, and had a lot of fun during those academic trips. During the pandemic, we still had frequent Slack chats and zoom calls to learn about each other's progress, difficulty and new ideas. He is a great colleague and friend, as well as an essential component of my life at UCLA.

I want to thank all the members and previous members in the simulation of plasmas group. Everyone in the group has either helped me or brought joy and happiness to my

life. I thank Frank Tsung for all aspects of help. I thank Viktor Decyk for helping me with the code development. I thank Ben Winjum for helping me with Jupyter notebooks and Python. I thank Thamine Dalichaouch for his help with ionization module and beam loading optimization. I thank Roman Lee for helping me with Fortran. I miss the time when we both sneaked into the office during the pandemic and had some interesting conversations. I thank Kyle Miller, Qianqian Su, Jacob Pierce, Sarah Chase for your help and friendship.

I want to thank all my committee members. Thank Chan Joshi for giving me opportunity to work on FACET II related research, helping me edit my papers, and giving me valuable advice and feedback. Thanks George Morales for his 222 series classes. They set a foundation for my graduate research. Thanks Troy Carter for his E & M classes. I enjoyed them a lot in my first year.

I want to thank all my fellow graduate students and friends Ji Zou, Kevin Chen, Ziqi Pi, Hongda Jiang, Andy Chan. I can never forget the time when we studied together for the comp exam. The friendship established from that time continued until today. We had so much fun hanging out, having dinner, playing poker, etc. They made my life at UCLA colorful.

I also want to sincerely thank my family. I would like to thank my parents, who always give me unconditional love and support. Thank my lovely wife Yutong Guo, who has been supporting me, encouraging me. My second half of PhD life was in the Covid pandemic, and I am extremely grateful for her company and love during those tough days.

In the end, I would like to say that I know it's impossible to squeeze the names of all the people who helped me / impacted me here. I just want to say thank you to all of you. Without any of you, my life at UCLA wouldn't be complete. Because of each of you, I am who I am today.

VITA

2012–2016 B.S. (Applied Physics)
University of Science and Technology of China, Hefei, P.R. China

2016–2017 M.S. (Physics)
University of California, Los Angeles, California, U.S.A.

2017–present Ph.D. candidate, Department of Physics, University of California, Los Angeles, California, U.S.A.

PUBLICATIONS

Yujian Zhao, Lance Hildebrand, Weiming An, Xinlu Xu, Fei Li, Thamine N. Dalichaouch, Qianqian Su, Chan Joshi, and Warren B. Mori, "Emittance preservation in the presence of ion motion in a single stage of a plasma based acceleration linear collider", to be submitted to PRL.

Yujian Zhao, Weiming An, Xinlu Xu, Fei Li, Lance Hildebrand, Mark J. Hogan, Vitaly Yakimenko, Chan Joshi, and Warren B. Mori, "Emittance preservation through density ramp matching sections in a plasma wakefield accelerator", Physics Review Accelerators and Beams **23**, 011302 (2020)

Lance Hildebrand, Weiming An, Xinlu Xu, Fang Li, Yujian Zhao, Mark J. Hogan, Vitaly Yakimenko, S S. Nagaitsev, E Adli, Chan Joshi, and Warren B. Mori, "Mitigation techniques for witness beam hosing in plasma - based acceleration", 2018 IEEE Advanced Accelerator Concepts Workshop (AAC)

Q. Su, J. Larson, T. N. Dalichaouch, F. Li, W. An, L. Hildebrand, Y. Zhao, V. Decyk, P. Alves, S. M. Wild, and W. B. Mori, "Optimization of transformer ratio and beam loading in a plasma wakefield accelerator with a structure-exploiting algorithm", arXiv:2301.09697

CHAPTER 1

Introduction

1.1 Background

Particle colliders are crucial in unveiling the detailed physics of the standard model of elementary particles and fields, leading to a better understanding of the universe and the laws that govern it. The energy frontier of particle physics is several trillion electron volts (TeV) in the center of mass of the collision, but colliders capable of reaching this regime are incredibly large and complex, and therefore are costly and time-consuming to build. The largest particle collider in the world, the Large Hadron Collider (LHC), is 27 kilometers in circumference and cost more than $10 billion to construct. Due to its size and complexity, the operating costs can exceed $1 billion per year. Building this gigantic machine involved 10,000 scientists and engineers from over 100 countries, as well as hundreds of universities and laboratories. As a result, there has been an active research effort to find new accelerator paradigms to be used in next-generation colliders. The goal for advanced acceleration methods is to reduce the footprint and cost by increasing the accelerating gradient by two or more orders of magnitude and increasing its wall plug efficiency.

Plasma-based accelerators (PBA) are particularly attractive because they are capable of producing accelerating fields that are orders of magnitude larger than those used in conventional colliders. The acceleration field in a conventional accelerator is limited by breakdown of the walls of the accelerating structure to $20 \sim 100$ MeV/m. A plasma is already broken down so the accelerating field it can sustain can be much higher, and is limited by the plasma

density.

The accelerating field of in a plasma wave moving near the speed of light can be estimated by the scaling law [3][4]

$$E[\mathrm{GV/m}] \sim m_e c\omega_p/e \approx 100\sqrt{n_p[10^{18}\mathrm{cm}^{-3}]} \tag{1.1}$$

where n_p is the plasma density. This means if the plasma density is $10^{18}\mathrm{cm}^{-3}$, an accelerating field of ∼100 GV/m can be achieved in a "relativistic" plasma wave. This is more than a thousand times higher than the breakdown limit of RF-accelerators. As a result, the size and cost of a high energy collider could be reduced substantially if plasma wave structures could replace conventional accelerating structures.

In PBAs, a drive beam (either laser or particle) produces a plasma wave (wakefield) that moves near the speed of light, c, and thus it can accelerate charged particles to very high energies. In 1979, T. Tajima and J. Dawson [3] proposed a method for accelerating electrons by exciting a plasma wave using a high power and short pulse length laser [5]. This idea is now commonly referred to as Laser Wakefield Acceleration (LWFA) [6]. In LWFA, the laser ponderomotive force pushes the plasma electrons forward and outward, leaving behind background ions. Due to the resulting space-charge separation, the electrons are then attracted back to the axis by the ions causing them to oscillate, thereby forming the plasma wave wake. A few years later, in 1985, P. Chen et al. proposed the idea of using a relativistic electron beam to drive a plasma wakefield instead of a laser [7]. This concept is referred to as Plasma Wakefield Acceleration (PWFA). In PWFA, the space charge field (electric field) from the drive electron beam plays the role of the ponderomotive force from the laser in LWFA. In both LWFA and PWFA, a separate beam (sometimes referred to as the trailing or witness beam) propagates behind the driver (laser / particle beam). If this beam is sitting at the correct phase inside the plasma wave wake, it can be accelerated to very high energy until the driver runs out of energy (pump depletion length) or the accelerated beam outruns the wakefield (dephasing length). In order that the accelerator is efficient, pump depletion should occur before dephasing. LWFA and PWFA have been actively investigated

during the past four decades by an ever growing plasma based acceleration (PBA) community [8].

Experiments on plasma-based acceleration, both LWFA and PWFA, have made tremendous progress in the past several decades. In 2004 and 2005, high acceleration gradients and acceleration in plasma wave wakefields generated by electron beams and lasers were demonstrated [9, 10, 11, 12, 13]. In the LWFA experiments, the self-injected beams had $1\% \sim 10\%$ energy spread and $1 \sim 10\mu m$ normalized emittances. Soon thereafter, in 2007, it was shown experimentally at the Stanford Linear Accelerator Center (SLAC) that energy doubling of 42 GeV electrons can be achieved in a meter-scale plasma wakefield accelerator [14]. Thus, stable acceleration over pump depletion distances was demonstrated. The experiment used a single 42-giga electronvolt drive bunch, propagating in a Lithium plasma. While most of the beam electrons lost energy as they created the wakefield, some electrons at the back of the same beam were accelerated with an acceleration gradient of 52 $\mathrm{GV/m^{-1}}$. This was an important milestone that demonstrated the viability of plasma accelerators for high-energy physics applications. In 2014, Litos et al. reported high-efficiency acceleration of a discrete trailing bunch of electrons that contained sufficient charge to extract a substantial amount of energy from the high-gradient, nonlinear plasma wakefield accelerator. The experiment showed the acceleration of about 74 picocoulombs of charge contained in the core of the trailing bunch with an accelerating gradient of about 4.4 GeV/m [15]. In 2015, a new regime of PWFAs where particles in the front of a single positron bunch transfer their energy to a substantial number of those in the rear of the same bunch by exciting a wakefield in the plasma was demonstrated experimentally [16]. About a billion positrons gained 5 GeV of energy with a narrow energy spread over a distance of just 1.3 metres. In 2014, a multi-GeV LWFA electron stage was demonstrated driven by a petawatt class laser propagating in a capillary-discharge plasma [17]. In 2016, staging between two LWFA stages where the electron beam from one was refocused into another with an active plasma lens was demonstrated [18]. More details on the status of theory, simulation, and experiment can be found in [8].

The ultimate long term goal for PBA is to reduce the size and cost (construction and operation) for a next generation linear collider at the energy frontier. Shorter term goals include developing compact XFELs where the electron beam is generated by either LWFA or PWFA [8]. After experiments confirmed that the theoretical predictions that plasma wave wakes have very large accelerating fields and that these wakefields could be produced over meaningful distances, thought was given to the conceptual design of a PBA based linear collider (PBA-LC) [19] [1][20]. These concepts rely on a series of stages where a new driver (laser or particle beam) creates a wake and a single witness beam (electrons or positrons) gains 10s of GeV in each stage. For example, in Ref.[19], a PWFA-LC design was proposed that uses a conventional accelerator to produce trains of 25 GeV drive bunches. They are distributed into 20 one meter long PWFA cells which each give 25 GeV (same as the drive beam) of energy to the witness bunch in each stage. There are arms for both the electron and the positron witness beams where the final energy of each beam is 500+ GeV, so there is a 1 TeV+ center of mass energy. Each cell provides 25 GeV of energy to the main beam in about a meter of plasma. Another design was proposed in Ref. [1] with the same basic concept but some changes in the drive beam and plasma parameters. A layout of a PWFA-LC is shown in Fig.1.1 (taken from Ref.[1]). There have also been conceptual designs for a LWFA-LC [20].

A related concept is the idea of an afterburner [2], where a single PWFA stage is added at the end of an existing collider to double the energy of the output beam (both electrons and positrons). This concept assumes that a linear collider already exists. When it became clear that the construction of the International Linear Collider (ILC) – a 1 TeV center of mass machine [21] based on conventional accelerators was put on hold, the community began contemplating about designing a collider fully based on PBA. An afterburner could be placed at the end of a PBA-LC as well, to double its energy in a single, longer, stage.

In order to understand the importance of the results in this dissertation it is useful to discuss design issues for any future collider. Metrics to consider when designing any collider

are the center of mass energy, luminosity, wall-plug efficiency, and size and construction cost. The luminosity, L, is given by $L(\mathrm{cm}^{-2}\mathrm{s}^{-1}) = f_{rep}N^2/(4\pi\sigma_x\sigma_y)$, where f_{rep} is the repetition rate of the collisions, N is the number of particles in each bunch, and σ_x and σ_y are the r.m.s. beam sizes at the collision point in the two transverse directions, respectively. The desired L for a 1 TeV center of mass electron-positron (e^-e^+) linear collider is $10^{34}\mathrm{cm}^{-2}\mathrm{s}^{-1}$ within 1% of the center of mass (CM) energy [1, 19]. For such a luminosity, the beams have an average power of $\sim$ 20 MW, e.g., there are $N \approx 10^{10}$ particles in the 500 GeV electron and positron bunches and a repetition rate of 10 kHz . For a total efficiency of 10%, the collider would require 200 MW/TeV of average power. It is important therefore that there be a high energy transfer efficiency from the driver to the wakefield and from the wakefield to the witness beam. The cost, which is assumed to be tied to the size of the accelerator, must be significantly smaller than one built using existing technology. Thus, the average acceleration gradient (energy/total length) must be large, which is why PBA is attractive.

The nonlinear blowout regime of PBA [22, 23, 24, 25] can simultaneously provide high efficiency, high gradient, and beam characteristics for the electron arm that could lead to high luminosity [8]. Recently, the blowout regime has also begun to show promise for the positron arm [26, 27, 28]. A more detailed description of this regime is discussed below.

In the PBA-LC designs, the goal is to have beams with normalized emittances of $\sqrt{\epsilon_{Nx}\epsilon_{Ny}} \approx$ 100 nm in order to achieve the small $\sqrt{\sigma_x\sigma_y}$ at the interaction point. The geometric emittance of a beam is important as it is a measure of the tendency of a particle beam to diffract. It is defined as $\epsilon \equiv \sqrt{\langle x^2\rangle \langle x'^2\rangle - \langle xx'\rangle^2}$, ($'$ means $\frac{1}{c}\frac{d}{dt}$) where the beam's rms spot size is $\sigma_x \equiv \sqrt{\langle x^2\rangle}$. The diffraction length of a laser in a vacuum is the Rayleigh length $z_R = \pi w_0^2/\lambda$ while for a particle beam it is, $\beta^* \equiv \sigma_0^2/\epsilon$, where w_0 is the $\sqrt{2}$ of the rms of the laser amplitude and σ_0 is the beam's spot size at the vacuum focus.

The need for such small emittances places constraints on the how much emittance growth can occur within and between stages. As shown in Chapter 2 it is the normalized emittance that is the figure of merit for a beam as it is accelerated. The normalized emittance is

roughly defined as $\epsilon_N \equiv \bar{\gamma}\epsilon$ where $\bar{\gamma}$ is the average relativistic Lorentz factor of the beam.

This dissertation is focused on understanding how emittance grows and how to mitigate this growth for realistic electron beams being accelerated in single and multiple nonlinear PWFA stages. The results can also apply to LWFA stages that operated in the blowout regime.

In the remainder of this chapter, we provide a quick introduction to some basic concepts for PBA, challenges for a PBA-LC, and simulation tools used in PBA research; and then provide an outline for the dissertation.

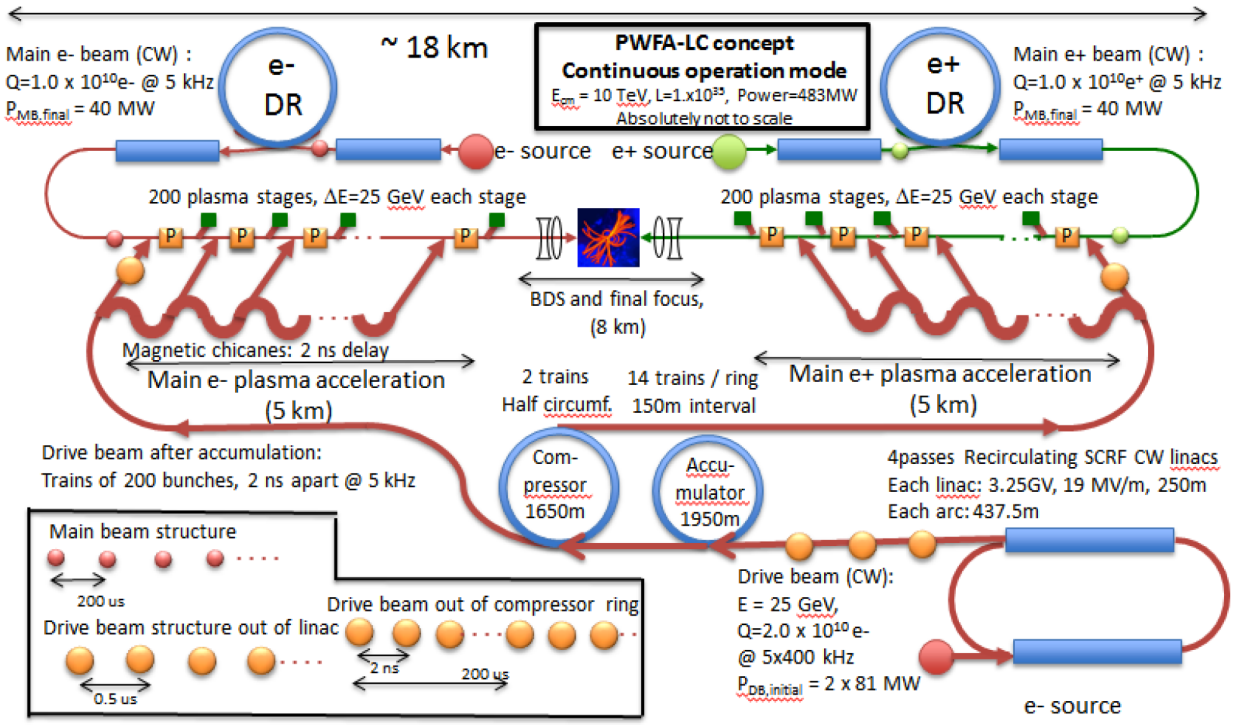

Figure 1.1: Layout of a PWFA-based 10 TeV Linear Collider [1]

1.2 Basic concepts

Next, some basic concepts for PBA are presented. These include introducing the co-moving coordinates, the quasi-static approximation, linear and nonlinear wakefields regimes, and

beam loading.

1.2.1 Maxwell's equations in co-moving coordinates

A key physics assumption used in PBA research is the quasi-static approximation (QSA) [29]. Before we describe QSA, we first introduce the co-moving coordinates $(x, y, \xi = (ct - z); s = z)$ where the laser or particle beam is moving predominantly in the $\hat{z}$ direction. We then rewrite Maxwell's equations in terms of the co-moving coordinates.

We start from Maxwell's equations in MKS units written in terms of the $(x, y, z; t)$ coordinates and the scalar (ϕ) and vector ($\mathbf{A}$) potentials in the Lorenz Gauge:

$$-\left(\nabla^2 - \frac{1}{c^2}\frac{\partial^2}{\partial t^2}\right)\begin{pmatrix}\phi\\ \mathbf{A}\end{pmatrix} = \begin{pmatrix}\rho/\epsilon_0\\ \mu_0\mathbf{J}\end{pmatrix} \tag{1.2}$$

where the Lorenz gauge condition is:

$$\nabla\cdot\mathbf{A} + \frac{1}{c^2}\frac{\partial\phi}{\partial t} = 0 \tag{1.3}$$

The fields can be calculated from the potentials as

$$\mathbf{B} = \nabla\times\mathbf{A},\ \mathbf{E} = -\nabla\phi - \frac{\partial\mathbf{A}}{\partial t} \tag{1.4}$$

and the continuity equation is,

$$\nabla\cdot\mathbf{J} + \frac{\partial\rho}{\partial t} = 0 \tag{1.5}$$

In a typical PBA scenario, the drive beam is moving at near the speed of light c, and, thus, so is the phase velocity of the wakefield generated by the driver. If we assume the driver is not evolving, the wakefield generated by the driver only depends on the relative position to the driver. Imagine you are standing at the tail of a boat traveling with a constant velocity. You are looking at the beautiful wake behind the boat. Your eyes are always staring at a white foam of a tall wave that is located behind the tail of the boat. When your friend asks you what you are looking at, you might say "I am looking at the wave that is behind the

tail of the boat", rather than reporting the exact location on the earth (e.g. GPS location), since this exact location is moving along with the boat, which is less convenient to use.

This exact same concept applies to PBA. Let's say the driver is propagating in the $\hat{z}$ direction. It is thus preferable to describe the quantities (like charge density, electric field, current density, etc) in the wakefield in terms of the position relative to the driver (more precisely, relative to a fixed point of the driver, like the head of the driver). If the driver is moving at v_d then the relevant variable is $v_d t - z$, instead of z, the coordinate in the lab frame (the use of $z - v_d t$ is essentially equivalent, however we choose $v_d t - z$ to follow the common convention of the community in the recent years). For a beam driver for which γ_d is very large, then it is common to use $ct - z$ instead.

As we discussed above, much of the physics is dominated by its dependence on the variable $ct - z$, rather than on t or z alone. This motivates us to perform a coordinate transformation, from our 'lab' coordinates $(x, y, z; t)$, to the 'co-moving' coordinates $(x, y, \xi = ct - z; s = z)$ where ξ is a measure of the distance (actually a negative of the distance) behind the driver (more precisely, the distance behind a fixed point on the driver). Note a transformation based purely on a coordinate transformation is for mathematical convenience. It is not the same as making a Lorentz transformation where the fields themselves need to also be transformed.

According to this coordinate transformation, the derivatives transform as

$$\frac{\partial}{\partial t} = \frac{\partial}{\partial \xi}\frac{\partial \xi}{\partial t} + \frac{\partial}{\partial s}\frac{\partial s}{\partial t} = c\frac{\partial}{\partial \xi} \tag{1.6}$$

$$\frac{\partial}{\partial z} = \frac{\partial}{\partial s}\frac{\partial s}{\partial z} + \frac{\partial}{\partial \xi}\frac{\partial \xi}{\partial z} = \frac{\partial}{\partial s} - \frac{\partial}{\partial \xi} \tag{1.7}$$

Thus the equations for the potentials and the continuity equation are now,

$$\left(-\nabla^2 + 2\frac{\partial^2}{\partial \xi \partial s} - \frac{\partial^2}{\partial s^2}\right)\begin{pmatrix}\phi \\ \mathbf{A}\end{pmatrix} = \begin{pmatrix}\rho/\epsilon_0 \\ \mu_0 \mathbf{J}\end{pmatrix} \tag{1.8}$$

and

$$\nabla_\perp \cdot \mathbf{J}_\perp + \frac{\partial(c\rho - J_z)}{\partial \xi} + \frac{\partial J_z}{\partial s} = 0 \tag{1.9}$$

where $\nabla_\perp \equiv \hat{x}\frac{\partial}{\partial x} + \hat{y}\frac{\partial}{\partial y}$

1.2.2 Quasi-static approximation

In plasma based acceleration, typically the drive beam evolves on a much longer time (or distance) scale ($\sim \sqrt{2\gamma}k_p^{-1}$ for a particle beam drive and z_R for a laser driver) compared with the plasma wakefield wavelength (k_p^{-1}). Since the wakefield depends on the driver's profile (or the wakefield only changes if the driver evolves), the wakefield at a given point (a given distance behind the driver) evolves very slowly as the driver propagates (it does not change if the drivers shape does not change). Mathematically, this can be stated as,

$$\frac{\partial}{\partial s} \ll \frac{\partial}{\partial \xi} \tag{1.10}$$

which is called quasi-static approximation (QSA) [29]. Note that in the original work on the QSA, the variables were $(x, y, \xi; \tau = t)$. It was recognized early on that it is better to use $s = z$ and not $\tau = t$ [30, 31].

A more intuitive way to understand the meaning of Eq. (1.8) is by considering the following scenario: Again you are standing at the tail of a boat, staring at the beautiful wake behind it. Your eyes are always staring at a point that is 10 meters behind the tail of the boat. While you are staring at that point, the boat has propagated for 100 meters. You may not even notice a difference because the change of the wake at that point can be small. On the contrary, at a given moment, if you take look at what is going on at 9 meters behind the boat, the wake there should look very different from the wake at 10 meters behind the boat. The change due to a different distance behind the boat ($\xi = ct - z$) is much more significant than the change due to the propagation of the boat ($s = z$).

After applying QSA, the derivatives transform as

$$\frac{\partial}{\partial t} = c\frac{\partial}{\partial \xi},\ \frac{\partial}{\partial z} = -\frac{\partial}{\partial \xi} \tag{1.11}$$

which upon substituting into Eqs. (1.2),(1.3) and (1.9) leads to

$$-\nabla_\perp^2 \begin{pmatrix} \phi \\ \mathbf{A} \end{pmatrix} = \begin{pmatrix} \rho/\epsilon_0 \\ \mu_0 \mathbf{J} \end{pmatrix} \tag{1.12}$$

$$\nabla_\perp \cdot \mathbf{A}_\perp + \frac{1}{c}\frac{\partial \psi}{\partial \xi} = 0 \tag{1.13}$$

$$\nabla_\perp \cdot \mathbf{J}_\perp + \frac{\partial}{\partial \xi}(c\rho - J_z) = 0 \tag{1.14}$$

where we define pseudo-potential ψ to be:

$$\psi = \phi - cA_z \tag{1.15}$$

Note that Eqs (1.12) and (1.13) could also have been obtained by dropping all $\frac{\partial}{\partial s}$ terms in Eqs (1.8) and (1.9). From Eq. (1.4), the longitudinal electric field (accelerating field) can be written as,

$$\begin{aligned} E_z &= -\frac{\partial \phi}{\partial z} - \frac{\partial A_z}{\partial t} \\ &= \frac{\partial \phi}{\partial \xi} - c\frac{\partial A_z}{\partial \xi} \\ &= \frac{\partial \psi}{\partial \xi} \end{aligned} \tag{1.16}$$

so that the accelerating force on an electron is

$$F_z = -e\frac{\partial \psi}{\partial \xi} \tag{1.17}$$

The transverse electric field can be rewritten as,

$$\begin{aligned} \mathbf{E}_\perp &= -\nabla_\perp \phi - \frac{\partial \mathbf{A}_\perp}{\partial t} \\ &= -\nabla_\perp \phi - c\frac{\partial \mathbf{A}_\perp}{\partial \xi} \end{aligned} \tag{1.18}$$

This is the electric field components of the Lorentz force. To calculate the magnetic field components, we need to calculate:

$$\begin{aligned}\hat{z}\times\mathbf{B} &= \hat{z}\times(\nabla\times\mathbf{A})\\ &= \nabla\mathbf{A}\cdot\hat{z}-(\hat{z}\cdot\nabla)\cdot\mathbf{A}\\ &= \nabla A_z-\frac{\partial\mathbf{A}}{\partial z}\\ &= \nabla_\perp A_z-\frac{\partial\mathbf{A}_\perp}{\partial z}\\ &= \nabla_\perp A_z+\frac{\partial\mathbf{A}_\perp}{\partial\xi}\end{aligned} \tag{1.19}$$

For an electron in a high energy beam, $\mathbf{v_z}\approx c\hat{z}$. So the transverse ('focusing') field is,

$$\begin{aligned}\mathbf{K}_\perp &= \mathbf{E}_\perp+c\hat{z}\times\mathbf{B}\\ &= -\nabla_\perp\phi+c\nabla_\perp A_z\\ &= -\nabla_\perp\psi\end{aligned} \tag{1.20}$$

And the focusing force on an electron is

$$\mathbf{F}_\perp=-e\mathbf{K}_\perp=e\nabla_\perp\psi \tag{1.21}$$

Now we can see the importance of the pseudo-potential ψ. Once we solve for it, the longitudinal and transverse forces on a relativistic particle are simply the longitudinal and transverse derivatives of ψ. Note that if $\mathbf{F}_\perp=e\nabla_\perp\psi$ and $F_z=-e\dfrac{\partial\psi}{\partial\xi}$ then it follows that $-\nabla_\perp F_z=\dfrac{\partial}{\partial\xi}\mathbf{F}_\perp$, which is the Panofsky-Wenzel theorem for plasma wave wakefields [32, 33].

From Eq. (1.12), we can get the differential equation for ψ:

$$-\nabla_\perp^2\psi=(\rho-J_z/c)/\epsilon_0 \tag{1.22}$$

Therefore, if Eq. (1.22) can be solved then the full forces on the witness beam are known. This equation is useful because based on Eq. (1.14), we can get

$$\int d\mathbf{x}_\perp(\rho-\frac{J_z}{c})=0 \tag{1.23}$$

for each ξ slice. Solving for ψ requires using Eq. (1.22). However, the source term depends on the motion of the plasma particles and ψ also contributes to the force on the plasma particles. Note that the source term from the beam essentially vanishes. Shortly, in sections 1.2.4 and 1.2.5 we analyze how the wakefield can be determined self-consistently for a beam driver in both linear and nonlinear regimes. These derivations are simpler to follow when using normalized units which are introduced next.

1.2.3 Normalized units

In this section, we introduce normalized units. In the study of plasma based acceleration, it is convenient to normalize all the quantities by their corresponding 'natural scale'. There are several advantages of doing so. First, it allows us to understand the relative strength of a parameter. Second, it makes the equations look cleaner and more compact. They also look the same regardless of which system of units one starts from, e.g. cgs or MKS. Last but not least, since all the quantities are dimensionless, it is easier to implement in a computer program. Normalized units are used extensively in the description of plasma based accelerators.

In the following, we list some commonly used quantities and their corresponding normalization factors, for MKS units:

Quantity	Normalized by
Time	$1/\omega_p$
Length	c/ω_p
Velocity	c
Mass	m_e
Charge	e
Electric field ($\mathbf{E}$)	$m_e c\omega_p/e$
Magnetic field ($\mathbf{B}$)	$m_e\omega_p/e$
Force	$m_e c\omega_p$
Scalar potential (ϕ)	$m_e c^2/e$
Vector potential ($\mathbf{A}$)	$m_e c/e$
Vacuum permittivity (ϵ_0)	1
Vacuum permeability (μ_0)	1
density	n_p

Table 1.1: Normalized units

We next rewrite some the quantities and equations in the previous section in terms of the normalized units. The pseudo-potential 1.15 becomes:

$$\psi = \phi - A_z \tag{1.24}$$

Eq. (1.22) becomes,

$$-\nabla_\perp^2 \psi = \rho - J_z \tag{1.25}$$

and Eqs. 1.16 and (1.21) remain in the same form,

$$E_z = \frac{\partial \psi}{\partial \xi} \tag{1.26}$$

$$\mathbf{F}_\perp = \nabla_\perp \psi \tag{1.27}$$

1.2.4 Linear regime

In this section, we review the linear theory of PWFA. As we have seen, the forces from the wakefield on a particle moving near the speed of light can be obtained from the pseudo-potential $\psi \equiv \phi - A_z$. The accelerating field and the focusing force in the wakefield are the longitudinal and transverse gradient of ψ, respectively. So the problem reduces to calculating ψ, for a given beam's density profile.

We start from Eq. (1.25). This is a 2D Poisson equation. In order to calculate ϕ, we need to figure out the source term on the right hand side: $\rho - J_z$. First, we need to realize that the beam's contribution to this source term vanishes because the beam moves at (nearly) speed of light. So the contribution to this source term only comes from the plasma particles.

Next, we need to linearize the equations. We assume a neutral plasma that starts at rest, so ρ_0 and $\mathbf{J_0}$ vanish. To lowest order the ion perturbations are m/M (mass ratio between electrons and ions) times smaller than those of the electron, and can thus be neglected. Therefore, the linearized version of 1.25 is,

$$\nabla_\perp{}^2 \psi = -\rho_1 - v_{z1} \tag{1.28}$$

We next use an important conservation law based on the QSA, $\gamma - p_z = 1 + \psi$ [34] where it is assumed that a plasma electron starts at rest (more details are given in Apppendix A). In linear regime, we also assume the plasma electron velocity is much less than c, then this equation can be linearized to $1 - v_{z1} = 1 + \psi$, from which it follows that, $v_{z1} = -\psi$. Substituting this into Eq. (1.28) leads to,

$$\left(\nabla_\perp{}^2 - 1\right) \psi = -\rho_1 \tag{1.29}$$

We still need to figure out ρ_1. To do that, we start from the continuity equation for plasma electrons,

$$\frac{\partial \rho}{\partial t} + \nabla \cdot (\rho v) = 0 \tag{1.30}$$

Upon linearizing it, we have,

$$\frac{\partial \rho_1}{\partial t} - \nabla \cdot \mathbf{v}_1 = 0 \tag{1.31}$$

Applying $\frac{\partial}{\partial t}$ to both sides gives,

$$\frac{\partial^2 \rho_1}{\partial t^2} - \nabla \cdot \frac{\partial \mathbf{v}_1}{\partial t} = 0 \tag{1.32}$$

The linearized Euler's equation is

$$\frac{\partial \mathbf{v}_1}{\partial t} = -\mathbf{E}_1 \tag{1.33}$$

and upon substituting this into Eq. (1.32) leads to

$$\frac{\partial^2 \rho_1}{\partial t^2} + \nabla \cdot \mathbf{E}_1 = 0 \tag{1.34}$$

From the linearized Gauss's law, it follows that

$$\nabla \cdot \mathbf{E}_1 = \rho_1 + \rho_b \tag{1.35}$$

Substituting this into the Eq. (1.34) gives

$$\frac{\partial^2 \rho_1}{\partial t^2} + \rho_1 = -\rho_b \tag{1.36}$$

which can be rewritten as,

$$\frac{\partial^2 \rho_1}{\partial \xi^2} + \rho_1 = -\rho_b \tag{1.37}$$

where ρ_b is the source term and $\xi \equiv ct - z$.

Therefore, the excitation of a wake, ψ, by a drive beam, ρ_b, is described by two coupled equations:

$$\begin{cases} \left(\nabla_\perp{}^2 - 1\right)\psi = -\rho_1 \\ \left(\dfrac{\partial^2}{\partial \xi^2} + 1\right)\rho_1 = -\rho_b \end{cases} \tag{1.38}$$

Eliminating ρ_1 leads to a single equation for ψ [35]

$$\left(\frac{\partial^2}{\partial\xi^2}+1\right)\left(\nabla_\perp{}^2-1\right)\psi=\rho_b \tag{1.39}$$

We look for a separable Greens function to this equation, i.e., we assume $G=G_\perp(\mathbf{r})G_\parallel(\xi)$, which leads to

$$\left(\frac{\partial^2}{\partial\xi^2}+1\right)G_\parallel(\xi)=\delta(\xi) \tag{1.40}$$

and

$$\left(\nabla_\perp{}^2-1\right)G_\perp(\mathbf{r})=\delta(\mathbf{r}) \tag{1.41}$$

Therefore, the final solution for ψ can be written as,

$$\psi=(G_\parallel(\xi)G_\perp(\mathbf{r}))*\rho(\xi,\mathbf{r}) \tag{1.42}$$

where $*$ is the convolution. The relevant Greens functions for these operators are,

$$G_\parallel(\xi)=\Theta(\xi)\sin(\xi) \tag{1.43}$$

and

$$G_\perp(\mathbf{r})=-\frac{K_0(\mathbf{r})}{2\pi} \tag{1.44}$$

where $\Theta(\xi)$ is the Heaviside step function and $K_0(\mathbf{r})$ is modified Bessel function of the second kind. We can therefore write the full expression for ψ as an integral of ρ_b over the Green's functions,

$$\psi(\xi,\mathbf{r})=\frac{1}{2\pi}\int_\xi^\infty d\xi'\int_0^{2\pi}d\theta'\int_0^\infty dr'r'\rho_b\left(\mathbf{r}',\xi'\right)\sin\left(\xi-\xi'\right)K_0\left(|\mathbf{r}-\mathbf{r}'|\right) \tag{1.45}$$

Once we have ψ, we can calculate E_z and $\mathbf{F}_\perp$ by taking a longitudinal and transverse gradient with respect to ψ. The linear problem is thus solved in principle. However, the form for ψ obtained in the blowout regime has ideal properties for accelerating electrons. Next, we discuss how to obtain ψ in this nonlinear regime and later discuss why the wakefields are ideal in this regime.

1.2.5 Nonlinear blowout regime

When the drive beam's peak density is much larger than the plasma density, the plasma electrons are completely expelled away by the space-charge force of the electron beam [22, 23]. The plasma ions are much more massive, so they essentially stay immobile during the time when the drive beam passes by (unless the driver's density is extremely high, $n_b/n_0 \gg M/m$, and ion motion is triggered, but that's a different topic, which is discussed below and whose consequences are studied in Chapter 4). The electrons, which are initially blown outwards (forwards and sideways) form a thin plasma electron sheath. The sheath electrons are then pulled back to the axis at the rear of the wake. The sheath thus forms a roughly spherical bubble that surrounds an 'ion column'. This regime is called blowout or bubble regime [22, 23, 25]. Typically the witness beam is loaded at the back of the bubble to be simultaneously accelerated and focused. The goal of this section is to study the accelerating and focusing fields on the witness (trailing) beam in PWFA. Note that a predictive nonlinear theory for the blowout regime was proposed in 2006 [23]. Here we will only do some simple analysis to derive the focusing force and show some properties of the accelerating field (first recognized by Rosenzweig et al. [22]).

We start from Eq. (1.25). We are only interested in ψ inside the ion channel, since that is where the witness beam is loaded. In order to solve for ψ, we need to know the source term $\rho - J_z$. In the previous section, we have already shown that relativistically moving drive or witness beams do not contribute to this source term because the forces from the radial electric and azimuthal magnetic self-fields essentially cancel each other. Also, in the blowout regime, the plasma electrons are completely blown out, so they make no contribution either to the source term inside the ion column. Only the uniform ion background contributions to $\rho - J_z$ inside the bubble. The immobile ions have no J_z, and their density is $\rho = en_0$, where n_0 is the plasma density. In normalized units, this is just 1. So Eq. (1.25) becomes

$$-\nabla_\perp^2 \psi = 1 \tag{1.46}$$

inside the ion column. This is a 2D Poisson equation. If we assume azimuthal symmetry, then we can solve for ψ:

$$\psi(r,\xi) = \psi_0(\xi) - \frac{r^2}{4} \tag{1.47}$$

where we used the boundary condition that ψ is finite at $r = 0$. So the focusing force is,

$$\mathbf{F}_\perp = \nabla_\perp \psi = -\frac{r}{2}\hat{r} = -\frac{x\hat{x} + y\hat{y}}{2} \tag{1.48}$$

The equation of motion for an electron in the absence of energy gain is therefore

$$\frac{d^2x}{dt^2} + \frac{x}{2\gamma} = 0 \text{ and } \frac{d^2y}{dt^2} + \frac{y}{2\gamma} = 0 \tag{1.49}$$

which are decoupled. The particle oscillates in the x and y planes with a frequency $1/\sqrt{2\gamma}$ which is referred to as the betatron frequency. More detail will be given in chapter 2. Substituting Eq. (1.47) into Eq. (1.26), gives the accelerating field,

$$E_z = \frac{d\psi_0(\xi)}{d\xi} \tag{1.50}$$

From Eq. (1.48) and Eq. (1.50) we can see two nice properties of wakefields in the blowout regime:

1. The transverse focusing force $\mathbf{F}_\perp$ is linear (proportional to r), points radially inward, and does not depend on the longitudinal position $\xi = ct - z$ inside the bubble.

2. The accelerating field E_z does not depend on the transverse position r.

The first property ensures that the beam particles at different longitudinal positions will oscillate at the same betatron frequency, if they have the same energy. The second property ensures that the beam particles will not gain additional slice energy spread. If either of these properties is satisfied, then the Panofsky Wenzel theorem [32, 33] guarantees that the other is as well, if either $\nabla_\perp F_z$ or $-\frac{\partial}{\partial\xi}\mathbf{F}_\perp$ vanishes then so does the other.

1.2.6 Beam loading

In this section, we are going to review the beam loading theory in the nonlinear blowout regime [36]. The beam loading theory in linear regime was derived by Katsouleas et, al in 1987 [37]. However, as described in the previous section, the nonlinear blowout regime has nice properties for accelerating and focusing, and is also the main focus in this dissertation, therefore we will only review the nonlinear beam loading theory.

The nonlinear beam loading theory was developed based on the theory for nonlinear blowout regime [23]. In the ultrarelativistic limit for azimuthally symmetric wakes, the pseudo-potential inside the ion channel is [23]:

$$\psi(r,\xi) \approx \frac{1}{4}(r_b(\xi)^2 - r^2) \tag{1.51}$$

where $r_b(\xi)$ is the boundary of the ion channel, i.e., the blowout radius, which is described by the differential equation [23]:

$$r_b r_b''(\xi) + 2[r_b'(\xi)]^2 + 1 = \frac{4\lambda(\xi)}{r_b(\xi)^2} \tag{1.52}$$

where $\lambda(\xi) = \int_0^\infty r n_b dr$, is the charge per unit length of an electron beam (drive or witness beam) divided by 2π. Here we are only interested in the back half of the bubble because that is where the witness beam is loaded, and we can interpret $\lambda(\xi)$ as the charge per unit length of the trailing beam divided by 2π.

In the beam loading problem, we are interested in the accelerating field, which can be calculated by substituting Eq. (1.51) into Eq. (1.26),

$$E_z = \frac{\partial \psi}{\partial \xi} = \frac{1}{2} r_b r_b'(\xi) \tag{1.53}$$

The goal is to solve for r_b from equation Eq. (1.52), and then to substitute it into Eq. (1.53) to obtain E_z. To accomplish this we change from parameterizing quantities in terms of ξ to r_b in Eq. (1.52), so $r_b''(\xi) = \frac{dr_b'}{d\xi} = \frac{dr_b'}{dr_b}\frac{dr_b}{d\xi} = r_b'\frac{dr_b'}{dr_b}$. Equation (1.52) therefore becomes:

$$r_b r_b' \frac{dr_b'}{dr_b} + 2r_b'^2 + 1 = \frac{4\lambda}{r_b^2} \tag{1.54}$$

The trick to solving this equation is realizing that $r_b' \frac{dr_b'}{dr_b} = \frac{1}{2}\frac{d(r_b'^2)}{dr_b}$, so we can define $u = r_b'^2$ and then rewrite Eq. (1.54) as,

$$\frac{1}{2} r_b \frac{du}{dr_b} + 2u + 1 = \frac{4\lambda}{r_b^2} \tag{1.55}$$

This is a first order differential equation. We can multiply Eq. (1.55) through by $2r_b^3$ leading to

$$\frac{d}{dr_b}(u r_b^4) = 8 r_b \lambda - 2 r_b^3 \tag{1.56}$$

which can be integrated to obtain,

$$r_b'^2 = u = \frac{8\int_{R_b}^{r_b} \lambda(r_b') r_b' dr_b' - \frac{1}{2}(r_b^4 - R_b^4)}{r_b^4} \tag{1.57}$$

where we integrate from $r_{bi} = r_b(\xi = 0) \equiv R_b$ to r_b, thus $\xi = 0$ is defined where the bubble radius is maximum. We denote the location of the head of the witness beam by ξ_s. In the back half of the bubble ($\xi \geq 0$), $r_b' = dr_b/d\xi \leq 0$, and therefore,

$$r_b' = -\sqrt{\frac{8\int_{R_b}^{r_b} \lambda(r_b') r_b' dr_b' - \frac{1}{2}(r_b^4 - R_b^4)}{r_b^4}} \tag{1.58}$$

Finally, we can also solve for the accelerating field,

$$E_z = \frac{1}{2} r_b r_b' = -\frac{r_b}{2\sqrt{2}} \sqrt{\frac{16\int_{R_b}^{r_b} \lambda(r_b') r_b' dr_b'}{r_b^4} - 1 + \frac{R_b^4}{r_b^4}} \tag{1.59}$$

When $0 \leq \xi \leq \xi_s$ (in front of the witness beam), $\lambda = 0$, therefore, the accelerating field is

$$E_z = -\frac{r_b}{2\sqrt{2}} \sqrt{\frac{R_b^4}{r_b^4} - 1} \quad (0 \leq \xi \leq \xi_s) \tag{1.60}$$

When $\xi > \xi_s$, E_z is modified by the λ of the witness beam. We want E_z to be a constant inside the witness beam, so that the energy spread on the witness beam vanishes. We denote this constant by $-E_s$ (so $E_s > 0$), and define $r_b(\xi_s) \equiv r_{bs}$, leading to

$$-E_s = -\frac{r_b}{2\sqrt{2}}\sqrt{\frac{16\int_{r_{bs}}^{r_b}\lambda(r'_b)r'_b dr'_b + R_b^4 - r_b^4}{r_b^4}} \tag{1.61}$$

Using Eq. (1.61) it can be inferred that the longitudinal current profile for the witness beam as a function of r_b that flattens the accelerating field is

$$\lambda(r_b) = E_s^2 + \frac{1}{4}r_b^2 \tag{1.62}$$

where

$$E_s = \frac{r_s}{2\sqrt{2}}\sqrt{\frac{R_b^4}{r_s^4} - 1} \tag{1.63}$$

In order to determine an expression for $r_b(\xi)$ when $\xi \geq \xi_s$, we resort to Eq. (1.53)

$$-E_s = \frac{1}{2}r_b(\xi)r'_b(\xi) = \frac{1}{4}\frac{d(r_b^2)}{d\xi} \tag{1.64}$$

Using the initial condition that $r_b = r_s$ when $\xi = \xi_s$, Eq. (1.64) can be integrated to obtain

$$r_b^2 = r_s^2 - 4E_s(\xi - \xi_s) \tag{1.65}$$

Upon setting $r_b = 0$, we can infer the location of the rear of the loaded bubble, $\xi = \xi_s + \frac{r_s^2}{4E_s}$.

Next, we can substitute Eq. (1.63) and Eq. (1.65) into Eq. (1.62) to determine the expression for the charge density of the witness beam (divided by 2π). To make the expression simpler, we can express r_s^2 in terms of E_s first, using Eq. (1.63),

$$r_s^2 = \sqrt{R_b^4 + 16E_s^4} - 4E_s^2 \tag{1.66}$$

Finally, we arrive at the longitudinal current profile of the witness beam that flattens the accelerating field,

$$\lambda(\xi) = \sqrt{E_s^4 + \frac{R_b^4}{16}} - E_s(\xi - \xi_s) \tag{1.67}$$

This result is very important because it shows the longitudinal current profile that flattens the accelerating field has a linear slope (or a trapezoidal shape).

The total charge in the trailing beam that flattens the wake can then be obtained by integrating over the current profile,

$$Q_s = 2\pi \int_{\xi_s}^{\xi_s + \frac{r_s^2}{4E_s}} \lambda(\xi) d\xi = 2\pi \Big[\sqrt{E_s^4 + \frac{R_b^4}{16}} - \frac{E_s}{2} \frac{r_s^2}{4E_s} \Big] \frac{r_s^2}{4E_s} \tag{1.68}$$

which upon using Eq. (1.66) can be simplified to

$$Q_s E_s = \frac{\pi R_b^4}{16} \tag{1.69}$$

This equations shows that the product of the charge and the accelerating field, i.e., the power being extracted, is $Q_s E_s$, which is fixed. Therefore, there is a trade-off between the strength of the accelerating field and the amount of charge we can accelerate. Recently, Dalichaouch et al. [38] have developed a more accurate beam loading model based on a more accurate description of the sheath. The general results do not change significantly.

1.3 Challenges for a PBA-LC

In this section, we describe some of the major physics obstacles for designing a PBA-LC.

1.3.1 Emittance preservation

One of the biggest challenges for a PBA-LC is to preserve the witness beam's emittance. In Chapter 2 we give precise definitions of a beam's emittance. Here, we define it as the area of a beam in trace space $(x, v_x) \cong \sqrt{\langle x^2 \rangle \langle v_x^2 \rangle}$ where $\langle\rangle$ refers to an average over a beam. Small emittances are required in order to be able to focus the beam to small spot sizes at the interaction point. As we will show in Chapter 2 and Chapter 3, the energy spread of the beam can lead to projected emittance growth. This is because particles with different energies oscillate at different betatron frequencies (wavenumbers)-k_β-, or equivalently, rotate

at different angular frequencies in trace space, (x, v_x) or (y, v_y) space, resulting in a larger projected trace space area (emittance). This is called the 'chromatic effect'. If all particles have the same γ and it is not changing then trace space and phase space (x, p_x) are straightforwardly related.

The solution to this problem is to match the beam into the plasma. A beam with a given energy is matched if its tendency to diverge or diffract due to its emittance is balanced by the attractive force due to ion channel (wakefield) focusing. These opposing effects are balanced, i.e., the beam is matched, when $k_\beta \beta^* = 1$ where $\beta^* \equiv \sigma_0^2/\epsilon$ and σ_0 is the spot size of the beam in vacuum. The resulting matched spot size of a beam slice is given by Eq. (2.72). As we will show in Chapter 2, if a beam is matched, it will not oscillate in size. More importantly, the distribution of the beam will not change as it propagates in a uniform plasma (assuming no longitudinal acceleration). Therefore, the emittance does not change.

However, the ion channel of a PBA operating at densities of interest (typically $10^{16} \sim 10^{17}\text{cm}^{-3}$) will have an extremely large focusing force, corresponding to a very small matched spot size. This is particularly true for parameters in a PBA-LC, where the beam has both a high energy and low emittance. Before we inject the beam into (or after we extract the beam out of) the acceleration stage, the beam is focused by a conventional, external magnetic focusing optic, which provides a much weaker focusing force compared with the focusing forces in the PBA acceleration stage. Therefore, if we inject (extract) a beam with energy spread into (out of) the acceleration stage directly, this huge mismatch in focusing strength (or matched spot size) will lead to catastrophic emittance growth.

Fortunately, there has been recent progress in understanding this issue and developing concepts to mitigate it. These rely on a tailored short plasma ramp or an adiabatic plasma ramp at the entrance and exit of an acceleration stage [39] [40] [41] [42][43] [44] to transition the beam from a large spot size to a small matched spot size in the acceleration stage, while preserving the beam's emittance. However, in a PBA-LC application, there will be ~ 20 or more acceleration stages. It is important to achieve emittance preservation throughout

the entire process, including inside each acceleration stage, transporting the beam in/out of each stage, and between stages.

Another potential issue is if there are longitudinal variations in the betatron frequency (wavelength) along the axial direction. This can occur if there are variations to the focusing force or to the energy along the beam. Axial variations to the betatron frequency could lead to different matched spot sizes along the beam. If the normalized emittance (area in phase space) of each slice is the same, i.e., $\sqrt{< x^2 >< p_x^2 >}$, then the projected emittance will be dominated by the largest $< x^2 >$ and $< p_x^2 >$ for any slice and will thus be larger than the slice emittance. Therefore, preserving the projected emittance is more challenging when we take this into account, and this also shows the importance of obtaining nearly perfect beam loading.

1.3.2 Ion motion

Ion motion induced by the drive particle beam and/or the witness beam is another significant challenge for a PBA-LC if it is operating in the nonlinear blowout regime. In order to build a PBA-LC, the luminosity must be large. This puts constraints on the charge and emittance of the witness beam. For example, in LC designs the emittance is very low ($\sim 0.1\mu m$). For the bunch lengths and charge per bunch needed for a LC [19], the transverse Coulomb field for a matched spot size can pull the ions inward into the beam during the transit time of the beam [45] [46].

For a matched beam (without ion motion) that is nearly Gaussian, $n_b/n_p = 1.4 \times 10^4 (N/10^{10})(\mu\text{m}/\sqrt{\epsilon_{Nx}\epsilon_{Ny}})\sqrt{(\text{Energy}/250\text{GeV})/(k_p\sigma_z)}$ where $n_b = N/[(2\pi)^{3/2}\sigma_r^2\sigma_z]$ and n_p is the plasma density. For large ratios, the ions can move appreciably within a transit time for the short trailing bunch. This can be quantified and understood physically as $\omega_{bi}\sigma_z/c > 1$, i.e., when $n_b/n_p > ZM/m$ where Z is the charge state of the ion, for $k_p\sigma_z \approx 1$. For collider parameters this ratio can approach 10^5 which easily exceeds the mass ratio of Hydrogen and Lithium. This can modify both the focusing (and accelerating fields) such that the trailing

beam may be far from being matched leading to emittance growth. As there are 20 stages, even ten percent growth per stage may not be tolerable. The resulting ion collapse on the axis can also cause a longitudinally slice-dependent, transversely nonlinear focusing force. Therefore, the nice properties of the fields in the blowout regime that we introduced in 1.2.5, which are important for emittance preservation, may no longer exist.

Simulations have shown that matching the beam directly to a uniform plasma (assuming no ion motion) causes ∼80% projected emittance growth for typical LC parameters [47]. This is actually much better than previously thought [46], and the main explanation for the smaller than expected emittance growth is that the ion collapse happens in a narrower region than the initial beam spot size. However, for a PWFA-LC application, $10 \sim 20$ stages will be used, and 80% emittance growth per stage is not desirable. It was also found that if the beam was focused with a spot size smaller than the matched spot there was less emittance growth. This indicates that there may be a modified matching condition where the matched spot size is smaller because of the enhanced focusing force of the ion collapse.

Several ideas have been proposed and studied to mitigate the ion induced emittance growth even further. In Ref.[48] it was proposed to use a plasma matching section with an adiabatically decreasing ion mass. In this concept, the idea is to adiabatically change the amount of ion collapse and thus the effective focusing force. In this work the focus was on the collapse triggered by the drive beam. However, it should also work when the collapse is caused by the witness beam. Although interesting conceptually, it will be difficult to construct a plasma profile that has an adiabatically decreasing ion mass.

In Ref.[49] it was proposed to match the transverse beam phase space distribution to the nonlinear ion motion-perturbed plasma wakefields slice-by-slice. In this concept, the equilibrium profile of the witness beam is first calculated mathematically under some assumptions, then the witness beam is injected into the plasma with this equilibrium profile. Conceptually, this is no different than transporting a witness beam that already had an equilibrium profile in the presence of ion motion into a 'new' plasma section. This idea is also challenging to

implement in practice.

In Ref.[50] it was proposed to start with a witness beam with a low enough energy that its matched spot size does not initially trigger ion motion. As the beam is accelerated, the matched spot size adiabatically decreases, and ion motion is adiabatically triggered. It was shown in simulations that this concept can preserve emittance. However, this idea will only work at the initial stage of PWFA-LC. The problem of transporting the witness beam out of the stage or into and out of later stages where the beam has a higher energy without much emittance growth remains unsolved.

In Chapter 4 of this dissertation, we present a scheme that is able to achieve emittance preservation in the presence of ion motion that is applicable to high energy, high-density electron bunches required in a multi-stage plasma-based LC scenario. We use an adiabatic plasma density upramp to match the witness beam into the uniform density (plateau) acceleration stage, then using an adiabatic plasma density downramp to match the witness beam out from the density plateau. We show this method can almost perfectly preserve the witness beam emittance from start to end, even though there is a significant amount of ion motion triggered in the uniform acceleration stage. We also show that by properly choosing the beam's Courant-Snyder parameters at the plasma entrance the emittance growth can be mitigated even for more general density ramps which are not adiabatic at lower densities. The development of a scheme to preserve emittance throughout an entire stage even in the presence of ion motion is the most important result in this dissertation.

1.3.3 Hosing

Another challenge in PWFA is the hosing instability or even any residual offset between the driver and the witness beam. The hosing instability was first studied using fluid theory [51] [52] and later improved for the nonlinear blowout regime [53]. Hosing occurs if the drive beam and the witness beam are misaligned or if either is tilted. Under these conditions the witness beam centroid will oscillate and couple to the plasma channel, causing an instability.

This results in large emittance growth of the witness beam as well as makes it difficult to collide the electrons and positrons, and is thus detrimental for LC applications. Current linear collider designs are based on using tens of stages. A new driver must be inserted in front of the witness bunch in ease stage. Hosing and misalignment can occur in each stage, and this can be exacerbated by the transverse offsets between the new driver and witness bunch. This will eventually reduce the luminosity of the colliding bunches.

Fortunately, there are various methods to mitigate hosing instability. The first method is using an energy chirp [54]. The variation of energy along the beam will cause the betatron oscillations (resonances) between beam slices to become detuned and damped. The second method is using an asymmetric drive beam to create an asymmetric ion bubble [55]. The focusing force will then be longitudinally dependent and vary along the beam. Similar to the energy chirp idea, this makes the beam particles at different slices oscillate at different betatron frequencies thus mitigating the hosing instability. The third method is taking advantage of the ion motion triggered by the drive beam [55] or witness beam [56]. Although ion motion was initially thought to be detrimental for preserving the emittance of a beam, as we will see later in this dissertation, it induces a head-to-tail variation in the focusing force experienced by the witness beam. Finally, it was shown that tapered plasma profiles can also be used to reduce hosing [54]. The topic of hosing and beam misalignments will be outside the scope of this dissertation.

1.4 Simulation tools

Computer simulation plays an essential role in the study of plasma based acceleration. Simulation is one of the three pillars of the modern scientific methods , along with experiment and theory. It can be used to verify the correctness of theories, provide crucial insights of experimental results, help to design new experiments, and even test new ideas that may lead to the discovery of new physics. In this section, we will introduce several different simulation

tools for modeling PBA, and discuss their advantages and drawbacks.

1.4.1 Particle-in-Cell code

The particle-in-cell (PIC) [57] [58] is the method of choice for simulating plasma physics when fluid descriptions are inappropriate. Although what happens in a plasma can be extremely complicated, at its core is the interaction of particles with the electromagnetic fields that their charges and currents generate. No matter how complicated a system is, each charged particle will move according to the Lorentz force it experiences. The electric and magnetic field in the Lorentz force are given by Maxwell's equations whose source terms are the charge density and current density contributed by the charged particles.

The PIC algorithm simply implements this idea based on discretized equations. Our physical world is intrinsically continuous (time and space), while computer memories are intrinsically discrete. Therefore, to simulate a physical domain, we need to use a grid. In a PIC simulation, the field quantities (electric field, magnetic field, potentials, charge density, current density, etc) are defined on a grid, and simulation particles (macroparticles) can move within the grid. The smallest domain in the grid is the cell. The resolution of the grid used in the simulation has to be high enough to capture the minimum length scales of interest, otherwise, important physics may be lost. Each macroparticle may represent many individual charged particles as long as the charge-to-mass ratio, which determines the dynamics in the force equation, is kept the same. Interestingly, the number of particles within a particle beam are sufficiently small and the memory of today's computers is large enough that it is possible to use one simulation particle for each real beam particle if accurate statistics are needed. As the charge of a particle is distributed to locations within the cell hence the particle has an effective size on the order of the grid. Hence, it is more accurate to call a PIC particle a finite size particle and not a macroparticle.

Next we introduce the PIC algorithm. The basic iteration loop of the PIC algorithm for each time step of the simulation has 4 components:

1. Charge and current deposition: The charge and current densities of each particle species are interpolated or deposited onto the grid.

2. Field solve: Given the charge and current densities on the grid points, we solve a discretized version of Maxwell's equations, and obtain electromagnetic fields on the grid points.

3. Field interpolation: We interpolate the electromagnetic fields from the grid to the locations of the particles, then calculate the Lorentz force on the particle from the interpolated fields.

4. Particle push: The positions and momentum of particles are advanced using a finite difference (leap frog) version of the relativistic equations of motion.

The PIC simulation keeps running in this loop until the desired time step is reached.

The PIC code is suitable for simulating a non-equilibrium and very nonlinear problems, especially when the kinetic effects are important and the fluid models cannot be used. Based on this algorithm, the full PIC code OSIRIS [59] was developed and is being used extensively in plasma simulations. In OSIRIS, the full set of Maxwell's equations are used and the time step must be smaller than a grid size. For problems of interest in this dissertation it is impractical to use OSIRIS.

1.4.2 QuickPIC

As discussed above the PIC code is a great tool for plasma simulations. However, because the PIC algorithm makes few physics approximations, it is also very CPU intensive. Using a full PIC code like OSIRIS to simulate plasma based acceleration problem is extremely computationally expensive. Fortunately, the nature of of plasma based acceleration allows us to make approximations without losing important physics. In plasma based acceleration, the beam particles (or laser) are evolving on a much longer timescale (or length scale)

compared with plasma particles. The beam evolves on the scale of the betatron wavelength: $k_\beta^{-1} \sim \sqrt{2\gamma} k_p^{-1}$, while the plasma evolves on the scale of the plasma skin depth: k_p^{-1}. For a 10 GeV beam, this is a 200 times difference!

To take advantage of this disparity of scales and separate out the evolution of the driver from the plasma wake generation, we apply the quasi-static approximation introduced in 1.2.2 to the PIC algorithm. The first quasi-static based PIC code, WAKE [34], is based on the 2D r-z geometry (technically r-ξ geometry, since it is a quasi-static code). QuickPIC [60][61] was the first 3D PIC code based on this idea and was originally developed at UCLA by Chengkun Huang et al. [60], and maintained as well as improved by Weiming An et al. [61]. QuickPIC is a three-dimensional (3D) quasi-static particle-in-cell (PIC) code for efficiently simulating plasma wakefield acceleration. It is fully parallelized through MPI and OpenMP. It has been an open source code since 2017 [62], with many feature modules actively being developed.

In QuickPIC, instead of using the coordinates $(x, y, z; t)$, we used co-moving coordinates $(x, y, \xi = ct - z, s = z)$. The simulation box (a co-moving window) is moving along with the beams at the speed of light. The beam particles are '3D particles': They are distributed in the simulation box in the 3D (x, y, ξ) space, and are advanced along s. On the contrary, the plasma particles are '2D' particles. They only exist in a 2D 'slice' of the simulation box, described by (x, y), and they are advanced along ξ, with an opposite direction to the direction of the system's propagation. It is assumed that the value for s is the same for every plasma particle.

In each time step of the simulation (3D time step), the beam is frozen in the simulation box. The plasma particles are initialized before the head of the drive bunch, 'sweeping' from head to tail along ξ. They are advanced with a 2D time step $\Delta\xi$, which is the longitudinal resolution of the simulation box. After the 'sweep' is complete, the calculation of the plasma response is finished. We then solve the fields within each ξ slice from the plasma particles, stack them together to construct the 3D fields within the simulation box, and push the beam

particles to the next 3D time step in s. By separating the advance of beam particles, in a Δs, and the advance of plasma particles, in a $\Delta\xi$, several orders of computation is saved, since $\Delta s \gg \Delta\xi$. Meanwhile, the physics is still described very accurately because the beam evolves much more slowly than the plasma, and within the length of a simulation box, the evolution of the beams can be reasonably neglected. Importantly, results from QuickPIC have been extensively compared against those in OSIRIS to verify the algorithm.

1.4.3 QPAD

We have found that QuickPIC is extremely accurate at simulating PWFA problems. However, it is still challenging for QuickPIC to carry out the high resolution simulations needed to resolve the matched spot size of a witness beam and to study ion motion. For example, for a typical PWFA-LC parameters [19][1], the witness beam's matched spot size is very small, while the radius of the ion bubble is three orders of magnitude larger. Including the entire ion channel in the simulation box while resolving the small beam spot size requires many cells. If we use 10^4 cells in the transverse direction, this leads to 10^8 cells transversely, which is extremely computationally expensive and memory consuming.

However, it turns out that for a lot of simulations we are interested in, the problem is nearly axisymmetric. Therefore, instead of using Cartesian geometry, we could use cylindrical geometry that better matches the nature of the problem, and potentially saves a significant amount of computation. This observation led to the development of QPAD [63], which was initially developed by Fei Li and Weiming An et al. at UCLA.

QPAD is a quasi-static particle-in-cell (PIC) code based on the QuickPIC framework. QPAD uses cylindrical geometry (as opposed to Cartesian geometry in QuickPIC) with a PIC description in r-z (technically r-ξ, since QPAD is a quasi-static code) and a gridless description in ϕ. This idea follows that used for full PIC algorithms that is now refereed to as a quasi-3D geometry [64, 65, 66]. The fields, charge and current, defined on an r-ξ grid, are expanded into azimuthal modes in the gridless ϕ direction. The expansion is truncated

at a desired number. Particle data is deposited onto the r-ξ grid for each azimuthal mode based on its ϕ position. The field amplitudes for each azimuthal mode are solved on the same r-ξ grid and they are then added together to get the forces to push the particles. This so-called Quasi-3D description is especially efficient for problems with approximate azimuthal symmetry because we only need to keep a small number of modes. When run with only the m=0 mode it reduces to a 2D quasi-static code such as WAKE [34]; however, it is fully parallelized. Other related reduced model codes such as INF&RNO [67, 68, 69], LCODE, and HiPACE are also used for PBA modeling. QPAD, WAKE, and INF&RNO also have the ability to model laser drivers.

As we will see in Chapter 4, simulating a PWFA-LC stage is very challenging. QPAD permits the use of very fine resolution in r so that the physics of ion motion can be resolved. We note that another option for modeling very fine resolution near the witness beam is the use of mesh refinement. This has been implemented into QuickPIC, HiPACE (another 3D quasi-static PIC code) [70, 71], and INF&RNO [67, 68, 69].

1.4.4 Single particle simulations

We have described how the full PIC algorithm (e.g., OSIRIS) is a powerful tool for plasma simulations. We have also described QuickPIC and QPAD which are more suitable for simulating plasma based acceleration (if self-trapping is not required). All these tools are based on the PIC algorithm. However, under certain circumstances, PIC may not be necessary to understand key physics. A good example can be, if we want to simulate the evolution of a beam slice in the blowout regime, and the focusing and accelerating fields are static. In this case, the beam slice simply feels a linear focusing force provided by the uniform ion background (with some prescribed acceleration). Therefore, it's probably more convenient to track the motion of the beam particles directly under a given focusing force, rather than carrying out a self-consistent simulation. Essentially, a reduced model can be used, and in this model, there is no concept of a plasma any more. All we have is a externally given

focusing force, and a collection of beam particles. The computation is thus much faster and cheaper, which allows us to run many 'small' simulations very quickly. This is very useful for parameter scan, or to just quickly testing new ideas.

Motivated by this, we developed a single particle code written in Python. This code is used in this dissertation to study the evolution of a beam slice under a given focusing force. Essentially, this single particle code numerically integrates the equations of motion in the transverse direction for a collection of non-interacting particles in a prescribed force:

$$\begin{cases} x'(z) = p_x(z)/\gamma \\ p'_x(z) = F_x(x, y, z) \\ y'(z) = p_y(z)/\gamma \\ p'_y(z) = F_y(x, y, z) \end{cases} \tag{1.70}$$

The focusing forces F_x, F_y are predetermined, and their form can be arbitrarily chosen, depending on the problems we are interested in. In Eq. (1.70) we assume there is no longitudinal acceleration. The longitudinal acceleration can also be included by providing a predetermined model for acceleration: $\gamma(z)$.

The numerical integration is done using the solve_ivp function from scipy library in Python. The z steps that are used for solving Eq. (1.70) are internally determined by the numerical solver solve_ivp. We can only select the time steps where we want to evaluate the solution (for dumping the output data). The code is also easily parallelized using mpi4py library, since the particles are completely independent with each other. It is worth noting that the idea behind the single particle code is almost identical to another code [72], which was recently developed at DESY.

1.5 Dissertation outline

This dissertation is aimed at understanding the emittance growth and methods to mitigate it for the witness beam in the electron arm of PBA-LC designs. Issues related to the positron arm are beyond the scope of this dissertation. The results utilize a combination of theory and PIC simulation. The dissertation is outlined as follows. In Chapter 2, we start by reviewing important concepts and previous results, as well as giving some new understanding about the transverse dynamics of a witness beam in the focusing fields of a nonlinear wakefield. In Chapter 3, we derive analytical expressions for the evolution of the beam emittance and the C-S parameters in an arbitrary adiabatic plasma profile based on the WKB solution to a Hill like equation (the acceleration of the beam and ion motion inside the plasma are neglected), and give several important corollaries for these results. We confirm these results with 3D QuicPIC simulation results. In Chapter 4, the method of using adiabatic plasma density ramps to mitigate the emittance growth of the witness beam in the presence of ion motion, energy spread, and acceleration in a PWFA-LC stage is proposed. Simulation results from QPAD show that within a single acceleration stage, this concept can limit the projected emittance growth to only $\sim$2% for a 25 GeV 100 nm and $\sim$20% for a 100 GeV, 100 nm emittance witness beam respectively. The trade-off between the adiabaticity of the plasma density ramp and the initial ion motion at the entrance for a given length of the plasma density ramp is also discussed. In Chapter 5, additional issues for building a plasma based linear collider are investigated using particle-in-cell simulations. Finally, in Chapter 6 we provide a summary and some perspectives.

CHAPTER 2

Single particle dynamics and emittance evolution in a uniform plasma

2.1 Introduction

This dissertation is aimed at understanding and controlling emittance growth within a single plasma based accelerator stage and from a series of stages. In this chapter, we provide the foundation for studying emittance evolution by describing in detail the dynamics of single particles and beam envelope parameters in perfectly linear and radial focusing forces. Such forces arise in the ion channel of an azimuthally symmetric nonlinear wakefield. We then review the ideas of geometrical and normalized emittances, and why both are important for this research.

We start from a single particle or microscopic point of view. The transverse (x, y) equations of motion are derived for a single beam particle moving near the speed of light in the $\hat{z}$ direction in the ion channel. The description includes the situation where the energy is changing (we refer to this as acceleration). We show that it is possible to approximately separate out the effects of the focusing fields from the change in energy from the accelerating fields in a nonlinear wakefield. We then discuss exact and approximate solutions to the transverse motion when there is no accelerating field. Following Courant and Snyder [73], we show that the in the absence of acceleration, the exact solution leads to a parameterized ellipse in trace space (x, x') described by what are now referred to as the Courant-Synder (C-S) parameters whose area is preserved. It is then shown that when there is acceleration

that the area of an ellipse in phase space (x, p_x) is instead conserved. The concept of a transport matrix is then described and examples are given.

We then pivot to a macroscopic view by introducing the beam's geometric emittance and its related Courant-Snyder parameters, which can be used to parameterize the state of the beam. This is followed by a discussion of how the beam Courant-Snyder parameters and the emittance can be used to describe the evolution of the beam in both vacuum and in a uniform plasma. The concept of matching is introduced and it is shown how it is important for preserving the beam's emittance. Last, the normalized emittance is introduced and it is shown that it is the quantity to be preserved when a particle is undergoing acceleration.

2.2 Equation of motion of a beam particle in a uniform plasma

In Chapter 1, we showed that in the blowout regime, the witness beam electrons feel a focusing force that points in the radial direction and that varies linearly in r. The key assumption is that the blowout is azimuthally symmetric so that the focusing force arises purely from the uniform ion column (there is no net force from the sheath electrons). This is shown in Eq. (1.48). Rewriting this equation back in unnormalized units gives,

$$\mathbf{F} = -\frac{1}{2} m \omega_p^2 \mathbf{r} \tag{2.1}$$

Since this focusing force is linear and points in $\hat{r}$ it can be decomposed into Cartesian coordinates as

$$F_x = -\frac{1}{2} m \omega_p^2 r \cos\phi = -\frac{1}{2} m \omega_p^2 x \tag{2.2}$$

and

$$F_y = -\frac{1}{2} m \omega_p^2 r \sin\phi = -\frac{1}{2} m \omega_p^2 y \tag{2.3}$$

where $x = r\cos\phi$ and $y = r\sin\phi$. According to Newton's second law,

$$F_x = \frac{dp_x}{dt} \tag{2.4}$$

$$F_y = \frac{dp_y}{dt} \tag{2.5}$$

from which it follows that

$$\frac{d(\gamma m v_x)}{dt} = -\frac{1}{2} m\omega_p^2 x \tag{2.6}$$

$$\frac{d(\gamma m v_y)}{dt} = -\frac{1}{2} m\omega_p^2 y \tag{2.7}$$

where $p_x = \gamma m v_x$ and $p_y = \gamma m v_y$. We are interested in the situation where an electron is moving in the $\hat{z}$ direction with a speed extremely close to the speed of light, c. As described in Chapter 1, we therefore transform from $(x, y, z; t)$ to $(x, y, \xi; s)$ where $\xi = ct - z$ and $s = z$. Therefore, the convention is to use the variable z (the propagation distance) rather than t (time) to parameterize the motion of the particle (electron). For a particle at a fixed ξ, $dz = cdt$, thus $\frac{d}{dz} = \frac{1}{cdt}$. The equation of motion in the x plane is therefore,

$$\frac{d(\gamma x')}{dz} = -\frac{1}{2}\frac{\omega_p^2}{c^2} x = -\frac{1}{2} k_p^2 x \tag{2.8}$$

where $x' = \frac{dx}{dz}$ ($' \equiv \frac{d}{dz}$) and $k_p = \frac{\omega_p}{c}$ is the plasma wave number.
Thus the differential equation for x can be written as

$$x'' + \frac{\gamma'}{\gamma} x' + k_\beta^2 x = 0 \tag{2.9}$$

where $k_\beta = \frac{k_p}{\sqrt{2\gamma}}$ is the betatron wavenumber. This is a homogeneous second order ordinary differential equation (ODE) with non-constant coefficients of the general form $x'' + p(z)x' + q(z)x = 0$. Similar arguments lead to an equation for y,

$$y'' + \frac{\gamma'}{\gamma} y' + k_\beta^2 y = 0 \tag{2.10}$$

In the ion channel, the acceleration, γ', does not depend on x or y [22, 23] (i.e., the accelerating field is flat in the transverse direction), thus the motion in the two planes are completely decoupled. Therefore, without loss of generality, we henceforth only consider motion in the x direction.

Furthermore, if there is no acceleration ($\gamma' = 0$), then Eq. (2.9) becomes much simpler,

$$x'' + k_\beta^2 x = 0 \tag{2.11}$$

where we note that k_β does depend on γ. This is referred to as the Hill equation [74] if k_β is periodic in z which is true in a circular accelerator. For a linear collider and a PBA stage this is not the case, so equation (2.11) is simply an ordinary homogeneous second order ODE with $p(z) = 0$. We will henceforth refer to it as a Hill like equation.

Typically in PWFA, the energy changes very slowly on the scale of a betatron oscillation. We next show that under this assumption (we will quantify it) the solution to Eq. (2.9) can be straightforwardly obtained from a solution to the Hill like equation, Eq. (2.11), times a scaling factor. We thus focus on exact solutions to Eq. (2.11). We then describe three related approaches for getting approximate solutions to Eq. (2.11), the first is based on approximating the process used to get the exact solution, the second is based on the WKB method, while the third utilizes the concept of the conservation of adiabatic invariants. All three approaches provide the same energy dependence in the solution to Eq. (2.9), which is not surprising since they all rely on the assumption that $k'_\beta/k_\beta^2 \ll 1$.

There is a standard procedure [75] to get rid of the first order (damping like) term in Eq. (2.9). Let's assume

$$x(z) = u(z)v(z) \tag{2.12}$$

Substituting Eq (2.12) into Eq. (2.9) leads to

$$u''v + 2u'v' + uv'' + \frac{\gamma'}{\gamma}(u'v + uv') + k_\beta^2 uv = 0 \tag{2.13}$$

which upon reordering terms can be rewritten as

$$uv'' + (2u' + \frac{\gamma'}{\gamma}u)v' + (u'' + \frac{\gamma'}{\gamma}u' + k_\beta^2 u)v = 0 \tag{2.14}$$

(or regrouped with $u \to v$ and $v \to u$). We choose u such that the coefficient of v' is 0, leading to

$$2u' + \frac{\gamma'}{\gamma}u = 0 \tag{2.15}$$

which can be integrated to obtain $u(z) = \dfrac{C}{\sqrt{\gamma(z)}}$. We can choose C such that

$$u(z) = \sqrt{\frac{\gamma(z_0)}{\gamma(z)}} \tag{2.16}$$

which when substituted back into Eq. (2.14) provides,

$$v'' + \left(\frac{\gamma'^2}{4\gamma^2} - \frac{\gamma''}{2\gamma} + k_\beta^2\right)v = 0 \tag{2.17}$$

Henceforth, when any function of z is evaluated at some initial z_0, we label it with a subscript 0, e.g., $\gamma(z_0) \equiv \gamma_0$. If the normalized acceleration occurs slowly and there is no phase slippage (which is typically the case in PWFA), we can discard the γ' and γ'' terms in the parentheses. This approximation can be quantified as,

$$\gamma'/\gamma \ll k_\beta, \;\; \gamma''/\gamma \ll k_\beta^2 \tag{2.18}$$

For future reference, we note that $\dfrac{\gamma'}{\gamma k_\beta} \simeq \tilde{E}_z\sqrt{\dfrac{2}{\gamma}}$ where $\tilde{E}_z \equiv \dfrac{eE_z}{mc\omega_p}$ is the normalized accelerating field and it is typically of order unity. Thus $\dfrac{\gamma'}{\gamma k_\beta}$ scales as $\gamma^{-\frac{1}{2}}$ which is very small for γ's of interest. Under these assumptions Eq. (2.17) reduces to the Hill like equation,

$$v'' + k_\beta^2 v = 0 \tag{2.19}$$

Thus, the solution to Eq, (2.9) includes the explicit dependence in γ from Eq. (2.16), as well as an implicit dependence embedded in k_β in Eq. (2.19).

2.3 Exact solution to the Hill like equation

We have just shown that a solution to Eq. (2.9) can be obtained by multiplying a solution to

$$x'' + k_\beta^2(z)x = 0 \tag{2.20}$$

by a factor $\sqrt{\gamma_0/\gamma(z)}$. Note that the factor $\sqrt{\gamma_0/\gamma(z)} = 1$ if there is no acceleration. Equation (2.20) has an exact solution for arbitrary expressions for $k_\beta^2(z)$ so long as it is positive (negative), i.e., the force is always focusing (defocusing) in some range of z. To see this, we assume the following expression for $x(z)$

$$x(z) = A\sqrt{\beta}\cos(\phi + \phi_0) \tag{2.21}$$

where β and ϕ are functions of z and A and ϕ_0 are constants. The first and second derivatives with respect to z of x are therefore

$$x' = \frac{A}{2}\frac{\beta'}{\sqrt{\beta}}\cos\psi - A\sqrt{\beta}\phi'\sin\psi \tag{2.22}$$

and

$$x'' = \frac{A}{2}\frac{\beta''}{\sqrt{\beta}}\cos\psi - \frac{1}{4}\frac{\beta'^2}{\beta^{3/2}}\cos\psi - A\frac{\beta'}{\sqrt{\beta}}\phi'\sin\psi - A\sqrt{\beta}\phi''\sin\psi - A\sqrt{\beta}\phi'^2\cos\psi \tag{2.23}$$

where $\psi = \phi + \phi_0$. Substituting these expressions into Eq. (2.20) and grouping the $\cos\psi$ and $\sin\psi$ terms gives

$$\left(\frac{1}{2}\frac{\beta''}{\sqrt{\beta}} - \frac{1}{4}\frac{\beta'^2}{\beta^{3/2}} - \sqrt{\beta}\phi'^2 + k_\beta^2\sqrt{\beta}\right)\cos\psi - \left(\frac{\beta'}{\sqrt{\beta}}\phi' + \sqrt{\beta}\phi''\right)\sin\psi = 0 \tag{2.24}$$

where both terms in the brackets must vanish separately. The $\sin\psi$ term leads to

$$\phi' = \frac{C}{\beta} = \frac{1}{\beta} \tag{2.25}$$

such that

$$\phi = \int_{z_0}^{z}\frac{dz'}{\beta(z')} \tag{2.26}$$

where the constant C can be incorporated into A. Substituting Eq. (2.25) into the coefficient of $\cos\psi$ in Eq. (2.24) gives

$$\frac{1}{2}\beta\beta'' - \frac{1}{4}\beta'^2 + k_\beta^2\beta^2 = 1 \tag{2.27}$$

To make clear the units of x we henceforth write it as

$$x(z) = a\sqrt{\frac{\beta}{\beta_0}}\cos\left(\int_{z_0}^{z}\frac{dz'}{\beta(z')} + \phi_0\right) \tag{2.28}$$

where $a = A\sqrt{\beta_0}$, $\beta_0 \equiv \beta(z_0)$ and $\phi_0 \equiv \psi(z_0)$. Therefore, an exact solution to Eq. (2.20) can be obtained, by first solving Eq. (2.27) to get $\beta(z)$, and then using this result to obtain $\phi(z)$ from Eq. (2.26).

A constant of 'the motion' can be obtained from Eqs. (2.21) and (2.22),

$$\gamma_{cs}x^2 + 2\alpha x x' + \beta x'^2 = a^2/\beta_0 \tag{2.29}$$

where $\alpha \equiv -\dfrac{\beta'}{2}$ and $\gamma_{cs} \equiv \dfrac{1+\alpha^2}{\beta}$. The parameters, $\beta(z), \alpha(z)$, and $\gamma_{cs}(z)$ are referred to as the Courant-Snyder parameters for a single particle. It is unfortunate that γ was chosen for a C-S parameter as it is also used for the relativistic Lorentz factor. We therefore use γ_{cs} for the corresponding C-S parameter. Note that Eq. (2.29) describes a rotated ellipse in trace space (x, x') and the area of the ellipse is $\pi a^2/\beta_0$. We show later that this area is related to the geometric emittance. It is important to note that the points on the ellipse do not correspond to x and x' evolving in z (time), rather they correspond to scaled values as the phase ϕ evolves. The real orbits in trace space do not close on themselves, because β, γ and α also depend on z. In a real orbit, x is maximum when $x' = 0$, however, this relationship does not exist for a rotated ellipse when $\alpha \neq 0$. As can be seen from Eqs. (2.21) and (2.22), x and x' are not $\pi/2$ out of phase because $\beta' \neq 0$. The constant a^2/β_0 is an example of a Poincare invariant [76].

Armed with this solution (Eq. (2.28)) to the Hill like equation Eq. (2.20), we can use Eqs. (2.12) and 2.16 to write a solution to Eq. (2.9) which is valid with the adiabatic acceleration assumption in Eq. (2.18) (which is distinct from any adiabatic assumption regarding

$\beta(z)$),

$$x = a\sqrt{\frac{\beta(z)}{\beta_0}}\sqrt{\frac{\gamma_0}{\gamma(z)}}\cos\left(\int_{z_0}^{z}\frac{dz'}{\beta(z')} + \phi_0\right) \tag{2.30}$$

.

We define $\tilde{\beta} \equiv \beta/\gamma$ where β still satisfies Eq. (2.27), such that

$$x = a\sqrt{\frac{\tilde{\beta}}{\tilde{\beta}_0}}\cos\psi \tag{2.31}$$

where $\psi = \int_{z_0}^{z}\frac{dz'}{\beta(z')} + \phi_0$, so $\psi' = \dfrac{1}{\beta}$, from which it follows that

$$x' = \frac{a}{\gamma\sqrt{\tilde{\beta}_0\tilde{\beta}}}(\frac{\gamma\tilde{\beta}'}{2}\cos\psi - \sin\psi) \tag{2.32}$$

We define $\tilde{\alpha} \equiv -\gamma\tilde{\beta}'/2$ and then combine Eqs. (2.31) and (2.32) to obtain

$$\tilde{\gamma}_{cs}x^2 + 2\gamma\tilde{\alpha}xx' + \gamma^2\tilde{\beta}x'^2 = \frac{a^2}{\tilde{\beta}_0} \tag{2.33}$$

where $\tilde{\gamma}_{cs} \equiv \dfrac{1+\tilde{\alpha}^2}{\tilde{\beta}}$. Notice that the area of this trace space ellipse described by Eq. (2.29) is $\dfrac{\pi a^2}{\gamma\tilde{\beta}_0}$. This scaling of the area with γ^{-1} also follows from general arguments for second order ordinary differential equations (See Appendix B). However, if we introduce (x, p_x) phase space where $p_x = \gamma x'$, then Eq. (2.33) reduces to

$$\tilde{\gamma}_{cs}x^2 + 2\tilde{\alpha}xp_x + \tilde{\beta}p_x^2 = \frac{a^2}{\tilde{\beta}_0} \tag{2.34}$$

and the area of this ellipse remains $\pi\dfrac{a^2}{\tilde{\beta}_0}$ for all z. For this ellipse, we thus have the C-S like parameters

$$\tilde{\beta} = \beta/\gamma, \quad \tilde{\alpha} = -\frac{1}{2}\gamma\tilde{\beta}', \quad \tilde{\gamma}_{cs} = \frac{1+\tilde{\alpha}^2}{\tilde{\beta}} \tag{2.35}$$

We note that if $\gamma' = 0$ then $\tilde{\alpha}$ reduces to α. As we discuss later the area of a single particle's motion on the scaled ellipse of Eq. (2.34) is related to the normalized emittance of a beam.

2.4 Approximate solution to the equation of motion

In 2.3 we found an exact solution to Eq. (2.20) and then used that to get a very accurate ('exact') solution to Eq. (2.9). In this subsection, we describe approximate solutions to Eq. (2.20) which rely on WKB type methods and the related concept of an adiabatic invariant. We will find the same approximate solution from three different approaches where some details can be found in Appendix C.

2.4.1 Approach 1: Adiabatic assumption

In this approach, we find an approximate solution to the Hill like Eq. (2.20) and then multiply it by $1/\sqrt{\gamma}$ based on Eqs. (2.12) - (2.16) to get accurate solutions to Eq. (2.9).

Recall that an exact solution to Eq. (2.11) is of the form

$$\begin{aligned} x &= A\sqrt{\beta}\cos\left(\int_0^z \frac{dz'}{\beta(z')} + \phi_0\right) \\ &= a\sqrt{\frac{\beta}{\beta_0}}\cos\left(\int_0^z \frac{dz'}{\beta(z')} + \phi_0\right) \end{aligned} \tag{2.36}$$

where β satisfies

$$\frac{1}{2}\beta\beta'' - \frac{1}{4}\beta'^2 + k_\beta^2\beta^2 = 1 \tag{2.37}$$

An approximate solution can immediately be obtained if $\beta\beta''$ and $\beta'^2 \ll k_\beta^2\beta^2$ or equivalently if $\dfrac{\beta'}{k_\beta\beta} \ll 1$, which is the adiabatic assumption for β. Under this assumption, Eq. (2.37) gives $\beta = 1/k_\beta$, leading to the solution

$$x = a\sqrt{\frac{k_{\beta 0}}{k_\beta}}\cos\left(\int_0^z dz' k_\beta(z') + \phi_0\right) \tag{2.38}$$

To include acceleration, we simply multiply this by $\sqrt{\frac{\gamma_0}{\gamma}}$ to obtain

$$x = a\sqrt{\frac{\gamma_0 k_{\beta 0}}{\gamma k_\beta}}\cos\left(\int_0^z dz' k_\beta(z') + \phi_0\right) \tag{2.39}$$

This is the form commonly used [77, 78, 79, 80] to describe solutions to Eq. (2.9). Note that the solution of this form has appeared in class notes at UCLA for decades [81], but it was never formally published. Due to the renewed interest in matching sections, it has recently appeared in publications.

2.4.2 Approach 2: WKB

The second approach is to carry out a WKB analysis for Eq. (2.20). A rigorous analysis that can be used to generate an asymptotic expansion to Eq. (2.20) to arbitrary order can be found in Appendix C. Here we show that if only the lowest order terms are kept we get a solution identical to Eq. (2.39). We assume

$$x = Ae^{i(S_0+\epsilon S_1)} \tag{2.40}$$

and that S_0''/S_0' and S_1''/S_1' are $O(\epsilon)$. Upon substituting this into Eq. (2.20) we obtain

$$[-(S_0' + \epsilon S_1')^2 + i(\epsilon S_0'' + \epsilon^2 S_1'') + k_\beta^2]Ae^{i(S_0+\epsilon S_1)} = 0 \tag{2.41}$$

Grouping the ϵ^0 and ϵ^1 terms gives

$$-S_0'^2 + k_\beta^2 = 0 \tag{2.42}$$

and

$$-2S_0'S_1' + iS_0'' = 0 \tag{2.43}$$

leading to

$$S_0 = \int_0^z dz' k_\beta(z') \tag{2.44}$$

and

$$S_1 = \sqrt{\frac{k_{\beta 0}}{k_\beta(z)}} \tag{2.45}$$

such that x is of the same form as Eq. (2.38).

2.4.3 Approach 3: Adiabatic invariant

A third approach to obtain the scaling of the amplitude for x with energy is to use the concept of an adiabatic invariant [76, 82, 83]. This method can also be used to find how the amplitude of the solution depends on a slowly varying plasma density as well. Eq. (2.9) has exactly the same form as the differential equation that describes a simple harmonic oscillator where a mass point m is moving under the restoring force provided by an ideal spring with spring constant k. Imagine the mass m and/or the spring constant k varying slowly. The energy γ in Eq. (2.9) plays the role of m, and the plasma density (contained in k_β^2) plays a role of the spring constant k.

The concept of an adiabatic invariant assumes the motion in x is nearly periodic. During one oscillation we assume k_β does not change. We use the solutions for x and p_x for a constant k_β to calculate $J = \oint p_x dx$ along a closed orbit to get the adiabatic invariant. When γ and the plasma density are both constant (so k_β is also constant), the solution to Eq. (2.9) is simply

$$x = A\sin(k_\beta z + \phi) \tag{2.46}$$

where the amplitude A and phase ϕ are to be determined by initial conditions. We can determine the momentum if k_β and γ are constant,

$$p_x = \gamma x' = \gamma A k_\beta \cos(k_\beta z + \phi) \tag{2.47}$$

The adiabatic invariant is therefore:

$$J = \oint p_x\, dx = \gamma A^2 k_\beta \int_0^{\frac{2\pi}{k_\beta}} \cos^2(k_\beta z + \phi) k_\beta dz = \pi\gamma A^2 k_\beta \tag{2.48}$$

Therefore, we have

$$A \sim \frac{1}{\sqrt{\gamma k_\beta}} \tag{2.49}$$

We should keep in mind that $k_\beta = \frac{\omega_p}{\sqrt{2\gamma}c}$, leading to

$$A \sim \gamma^{-\frac{1}{4}} \omega_p^{-\frac{1}{2}} \tag{2.50}$$

which is identical to the scaling in Eq. (2.39).

2.5 Transport matrices

If the solutions to Eq. (2.9) are known between z_0 and some z, then for a second order ordinary differential equation (ODE), a mapping exists between the initial values $x(z_0) \equiv x_0$ and $x'(z_0) \equiv x'_0$ to the values at any z, $x(z)$ and $x'(z)$. A general description of this procedure is given in Appendix B.1. In this subsection, we show how it leads to what are called transport matrices for tracking particles in the beam line of an accelerator.

2.5.1 Drift space

We start with the simplest case where the beam is propagating in drift space (vacuum). The ODE is $x'' = 0$ for which the coordinates of a single beam particle evolving in trace space are,

$$x(z) = x(0) + x'(0)z,\ x'(z) = x'(0) \tag{2.51}$$

where we use 0 to represent any z_0. This can be rewritten as follows

$$\begin{pmatrix} x(z) \\ x'(z) \end{pmatrix} = \begin{pmatrix} 1 & z \\ 0 & 1 \end{pmatrix} \begin{pmatrix} x(0) \\ x'(0) \end{pmatrix} \tag{2.52}$$

where

$$\begin{pmatrix} 1 & z \\ 0 & 1 \end{pmatrix} \tag{2.53}$$

is the transport matrix. We define the components of the general transport matrix as,

$$\begin{pmatrix} M_{11} & M_{12} \\ M_{21} & M_{22} \end{pmatrix} \tag{2.54}$$

2.5.2 Constant k_β (Uniform plasma, no acceleration)

Another illustrative case is for the motion described by Eq. (2.11) with a constant k_β. This is simply a simple harmonic oscillator. Given the initial conditions $x(0)$, $x'(0)$, the solution is,

$$x(z) = x(0)\cos(k_\beta z) + \frac{x'(0)}{k_\beta}\sin(k_\beta z) \tag{2.55}$$

This gives the transport matrix,

$$\begin{pmatrix} x(z) \\ x'(z) \end{pmatrix} = \begin{pmatrix} \cos(k_\beta z) & \frac{1}{k_\beta}\sin(k_\beta z) \\ -k_\beta \sin(k_\beta z) & \cos(k_\beta z) \end{pmatrix} \begin{pmatrix} x(0) \\ x'(0) \end{pmatrix} \tag{2.56}$$

Note that if k_β varied in z as a step wise function where $k_\beta = k_{\beta i}$ between z_i and $z_i + \Delta z$ that

$$\begin{pmatrix} x(z) \\ x'(z) \end{pmatrix} = \prod_i [k_{\beta i}(\Delta z)] \begin{pmatrix} x(0) \\ x'(0) \end{pmatrix} \tag{2.57}$$

2.5.3 Adiabatic acceleration but arbitrary variation of k_β

We can also obtain a general transport matrix starting from Eq. (2.30). Recall this is an "exact" solution to Eq. (2.9) provided that the acceleration occurs adiabatically $\frac{\gamma'}{\gamma k_\beta^2} \ll 1$.

To get the transport matrix, we start from Eq. (2.31) and Eq. (2.32) and evaluate them at $z = z_0$ to obtain

$$x_0 = a\cos\phi_0 \tag{2.58}$$

$$x_0' = \frac{a}{\gamma_0\tilde{\beta}_0}\left(\frac{\gamma_0\tilde{\beta}_0'}{2}\cos\phi_0 - \sin\phi_0\right) = -\frac{a}{\gamma_0\tilde{\beta}_0}(\tilde{\alpha}_0\cos\phi_0 + \sin\phi_0) \tag{2.59}$$

These can be used to eliminate a and ϕ_0 from Eq. (2.31) to obtain

$$x = \sqrt{\frac{\tilde{\beta}}{\tilde{\beta}_0}}(\cos\phi + \tilde{\alpha}_0 \sin\phi)x_0 + \gamma_0\sqrt{\tilde{\beta}\tilde{\beta}_0}\sin\phi x_0' \tag{2.60}$$

where $\tilde{\alpha}_0 = -\gamma_0\dfrac{\tilde{\beta}_0'}{2}$; and taking a derivative gives,

$$\begin{aligned} x' =& \frac{1}{\gamma\sqrt{\tilde{\beta}_0\tilde{\beta}}}\left[(\tilde{\alpha}_0 - \tilde{\alpha})\cos\phi - (1 + \tilde{\alpha}_0\tilde{\alpha})\sin\phi\right]x_0 \\ &+ \frac{\gamma_0}{\gamma}\sqrt{\frac{\tilde{\beta}_0}{\tilde{\beta}}}(-\tilde{\alpha}\sin\phi + \cos\phi)x_0' \end{aligned} \tag{2.61}$$

Equations (2.60) and (2.61) can then be used to generate the transport matrix,

$$\begin{pmatrix} \sqrt{\dfrac{\tilde{\beta}}{\tilde{\beta}_0}}(\cos\phi + \tilde{\alpha}_0\sin\phi) & \gamma_0\sqrt{\tilde{\beta}\tilde{\beta}_0}\sin\phi \\ \dfrac{1}{\gamma\sqrt{\tilde{\beta}_0\tilde{\beta}}}\left[(\tilde{\alpha}_0 - \tilde{\alpha})\cos\phi - (1 + \tilde{\alpha}_0\tilde{\alpha})\sin\phi\right] & \dfrac{\gamma_0}{\gamma}\sqrt{\dfrac{\tilde{\beta}_0}{\tilde{\beta}}}(-\tilde{\alpha}\sin\phi + \cos\phi) \end{pmatrix} \tag{2.62}$$

If we substitute $\tilde{\beta} = \beta/\gamma$ and $\tilde{\beta}_0 = \beta_0/\gamma_0$ into this transport matrix, then it can be rewritten as

$$\begin{pmatrix} \sqrt{\dfrac{\gamma_0\beta}{\gamma\beta_0}}(\cos\phi + \tilde{\alpha}_0\sin\phi) & \sqrt{\dfrac{\gamma_0}{\gamma}\beta\beta_0}\sin\phi \\ \sqrt{\dfrac{\gamma_0}{\gamma}}\dfrac{(\tilde{\alpha}_0 - \tilde{\alpha})\cos\phi - (1 + \tilde{\alpha}_0\tilde{\alpha})\sin\phi}{\sqrt{\tilde{\beta}_0\tilde{\beta}}} & \sqrt{\dfrac{\gamma_0}{\gamma}\dfrac{\beta_0}{\beta}}(\cos\phi - \tilde{\alpha}\sin\phi) \end{pmatrix} \tag{2.63}$$

where $\phi = \int_0^z \frac{dz'}{\beta(z')}$, β satisfies Eq. (2.27), and $\tilde{\alpha} = -\gamma\tilde{\beta}'/2 = -\dfrac{1}{2}(\beta' - \dfrac{\gamma'}{\gamma}\beta)$. In the WKB or adiabatic approximation, $\beta = 1/k_\beta$, which leads to a transport matrix

$$\begin{pmatrix} \sqrt{\dfrac{\gamma_0 k_{\beta 0}}{\gamma k_\beta}}(\cos\phi + \tilde{\alpha}_0\sin\phi) & \sqrt{\dfrac{\gamma_0}{\gamma k_\beta k_{\beta 0}}}\sin\phi \\ \sqrt{\dfrac{\gamma_0}{\gamma}k_\beta k_{\beta 0}}\left[(\tilde{\alpha}_0 - \tilde{\alpha})\cos\phi - (1 + \tilde{\alpha}_0\tilde{\alpha})\sin\phi\right] & \sqrt{\dfrac{\gamma_0}{\gamma}\dfrac{k_\beta}{k_{\beta 0}}}(\cos\phi - \tilde{\alpha}\sin\phi) \end{pmatrix} \tag{2.64}$$

where $\phi = \int_0^z k_\beta(z')dz'$.

Recently, a similar transport matrix to Eq. (2.64) was presented in Ref.[80] (Note that Eq.(9) in Ref.[80] has a typo in M_{22}: It should be α_m rather than α_{m0}). While there are similarities between the transport matrices derived here and that in Ref.[80], there are several important differences. First, we have obtained an 'exact' solution to Eq. (2.9) which leads to the matrix (2.63). Second, we use a different definition for α which we define as $\tilde{\alpha} = -\frac{1}{2}\gamma\tilde{\beta}' = -\frac{1}{2}\gamma(\frac{\beta}{\gamma})'$, rather than the standard definition used in Ref.[80], $\alpha = -\frac{1}{2}\beta'$. This is an important distinction because if affects the sign of $\tilde{\alpha}$ when the plasma density is constant. As we have seen, the amplitude, which is proportional to $\sqrt{\tilde{\beta}}$, has an energy dependence of $\gamma^{-1/4}$ ($\tilde{\beta} \sim \gamma^{-1/2}$). As the beam accelerates, $\tilde{\beta}$ decreases, i.e., $\tilde{\beta}' < 0$, and thus $\tilde{\alpha} > 0$. On the other hand, $\alpha = -\frac{1}{2}\beta'$, where $\beta = \gamma\tilde{\beta} \sim \sqrt{\gamma}$, has the opposite sign because as the beam accelerates, β increases, so $\beta' > 0$, and thus $\alpha < 0$. It is thus important to use $\tilde{\alpha} = -\frac{1}{2}\gamma\tilde{\beta}' = -\frac{1}{2}\gamma(\frac{\beta}{\gamma})'$ in Eq. (2.63) when near a density plateau.

Conventional accelerator focusing and accelerating elements have their own well known transport matrices. Thus, any beamline constructed from a combination of plasma and conventional elements can be easily analyzed by multiplying out the pertinent transport matrices. As we discuss in this section, transport matrices are also useful for analyzing how ensembles of particles evolve.

2.6 Beam's envelope equation & geometric emittance

In the previous sections of this chapter, we studied the transverse motion of a single beam particle. This is a microscopic view. In the rest of this chapter, we will study a collection of particles (beam) using a macroscopic view. We will also connect this with the single particle point of view. We start by deriving the beam's envelope equation. Our convention is to define our coordinate system in such a way that the beam is propagating in the z direction (the longitudinal direction), and x, y are the two transverse directions. As discussed previously, the motion in the two transverse planes are decoupled in azimuthally symmetric nonlinear

wakes, thus without loss of generality, we only need to study the beam's motion in the x direction, or more precisely, the $x - z$ plane.

We start from the transverse spot size of the beam, which is defined to be the standard deviation of all the beam particles' transverse positions,

$$\sigma \equiv \sqrt{\langle (x - x_c)^2 \rangle} \tag{2.65}$$

where $\langle\rangle$ means taking an ensemble average and $x_c = \langle x \rangle$ is the centroid of the beam. For convenience, we place the transverse centroid of the beam on the z axis, i.e., set $x_c = 0$, in which case,

$$\sigma \equiv \sqrt{\langle x^2 \rangle} \tag{2.66}$$

which is reasonable if x_c did not vary with z. To study how the spot size evolves, we take the first two derivatives of σ with respect to z, leading to,

$$\sigma' = \frac{\langle x x' \rangle}{\sqrt{\langle x^2 \rangle}} \tag{2.67}$$

and

$$\begin{aligned} \sigma'' &= \frac{\left(\langle x'^2 \rangle + \langle x x'' \rangle\right) \langle x^2 \rangle - \langle x x' \rangle^2}{\langle x^2 \rangle^{\frac{3}{2}}} \\ &= \frac{\langle x'^2 \rangle \langle x^2 \rangle - \langle x x' \rangle^2}{\langle x^2 \rangle^{\frac{3}{2}}} + \frac{\langle x x'' \rangle}{\sqrt{\langle x^2 \rangle}} \end{aligned} \tag{2.68}$$

We define the beam's geometric emittance to be

$$\epsilon = \sqrt{\langle x^2 \rangle \langle x'^2 \rangle - \langle x x' \rangle^2} \tag{2.69}$$

In the absence of longitudinal acceleration, we can substitute Eq. (2.11) into $\langle x x' \rangle$ to obtain

$$\sigma'' = \frac{\epsilon^2}{\langle x^2 \rangle^{\frac{3}{2}}} - \frac{\langle k_\beta^2 x^2 \rangle}{\sqrt{\langle x^2 \rangle}} \tag{2.70}$$

Assuming all the particles have the same energy γ (thus they have the same k_β), we find

$$\begin{aligned}\sigma'' &= \frac{\epsilon^2}{\sigma^3} - k_\beta^2 \sigma \\ &= \frac{\epsilon^2}{\sigma^3}(1 - \frac{k_\beta^2 \sigma^4}{\epsilon^2})\end{aligned} \tag{2.71}$$

This is referred to as the beam's envelope equation. It describes the evolution of beam's spot size. When the beam's transverse motion reaches an equilibrium state, the spot size is a constant, so $\sigma'' = 0$ (and $\sigma' = 0$). From Eq. (2.71) we can find this constant spot size

$$\sigma_m = \sqrt{\frac{\epsilon}{k_\beta}} \tag{2.72}$$

which is referred to as the beam's matched spot size, σ_m. When the beam's spot size is equal to σ_m, the beam is matched to the plasma, and it does not oscillate in the plasma. Later, we will show that the normalized emittance growth (geometrical emittance if there is no energy spread) is minimized for matched beams. We will also properly define the normalized emittance $\epsilon_n \cong \bar{\gamma}\epsilon$, where $\bar{\gamma} \equiv \langle\gamma\rangle$ is the average "energy" of the beam.

2.7 Courant-Snyder parameters for a beam

In 1958, E. D. Courant and H. S. Snyder introduced the Courant-Snyder (C-S) parameters in their paper [73] to parametrize the transport matrices in circular accelerators which had determinants equal to unity. The C-S parameters were defined based on the motion of a single particle. However, they are also now commonly used to parametrize the state of a beam,

$$\alpha = -\frac{\langle xx' \rangle}{\epsilon} \ , \ \beta = \frac{\langle x^2 \rangle}{\epsilon} \ , \ \gamma = \frac{\langle x'^2 \rangle}{\epsilon} \tag{2.73}$$

Although defined from two different points of view, the equations that the C-S parameters satisfy for a particle or beam are very similar. In fact, there are numerous connections between these two view points. In the remaining chapters in this dissertation, we use the definitions in Eq. (2.73), and not those for a single particle.

Based on the definition in Eq. (2.73), the C-S parameters for a beam are also related by

$$\beta\gamma = 1 + \alpha^2 \tag{2.74}$$

and

$$\alpha = -\frac{1}{2}\beta' \tag{2.75}$$

if ϵ is constant. From Eq. (2.71), if we assume ϵ is a constant (this is indeed a valid assumption if the beam has no energy spread), we can derive the differential equation for beam's beta function [74],

$$\frac{1}{2}\beta\beta'' - \frac{1}{4}\beta'^2 + k_\beta^2\beta^2 = 1 \tag{2.76}$$

which is identical to the equation for the β function of a single particle.

2.8 Relationship between C-S parameters for single particles and beams

In this section, we investigate the relationship between the C-S parameters for a single particle (introduced in section 2.3) and the C-S parameters for a beam (introduced in section 2.7). Recall in section 2.3 we derived the 'constant of motion'

$$\gamma_{cs}x^2 + 2\alpha x x' + \beta x'^2 \tag{2.77}$$

According to Jeans's theorem [84], any distribution function constructed in terms of constants of the motion satisfies the Vlasov equation,

$$\frac{\partial f}{\partial t} + \mathbf{v}\cdot\nabla f + \frac{\mathbf{F}}{m}\cdot\nabla_v f = 0 \tag{2.78}$$

where f is the distribution function and depends on $(\mathbf{x}, \mathbf{v}, t)$. For a relativistic particle beam, f depends on x, x', z and the Vlasov equation is

$$\frac{\partial f}{\partial z} + \mathbf{x}'\cdot\nabla f + \mathbf{x}''\cdot\nabla_{x'} f = 0 \tag{2.79}$$

where here x'' comes from external forces, $x'' = -k_\beta^2 x$. While Jeans's theorem indicates that any function of the constant Eq. (2.77) is a solution to Eq. (2.79), it is informative to consider a Gaussian function,

$$f(x, x') = \frac{1}{2\pi\epsilon} \exp\left[-\frac{\gamma_{cs}x^2 + 2\alpha x x' + \beta x'^2}{2\epsilon}\right] \tag{2.80}$$

where ϵ is a constant, it satisfies the Vlasov equation, and is therefore a valid distribution function for a beam. For such a beam's distribution, we can calculate the moments for the beam,

$$\begin{aligned}
\langle x^2 \rangle &= \int_{-\infty}^{\infty}\int_{-\infty}^{\infty} x^2 \frac{1}{2\pi\epsilon} \exp\left(-\frac{\gamma_{cs}x^2 + 2\alpha x x' + \beta x'^2}{2\epsilon}\right) dx dx' \\
&= \frac{1}{2\pi\epsilon}\int_{-\infty}^{\infty}\int_{-\infty}^{\infty} x^2 \exp\left[-\beta\frac{(x' + \frac{\alpha}{\beta}x)^2 + (\frac{\gamma_{cs}}{\beta} - \frac{\alpha^2}{\beta^2})x^2}{2\epsilon}\right] dx dx' \\
&= \frac{1}{2\pi\epsilon}\int_{-\infty}^{\infty} x^2 \exp\left(-\frac{x^2}{2\beta\epsilon}\right) dx \int_{-\infty}^{\infty} \exp\left[-\beta\frac{(x' + \frac{\alpha}{\beta}x)^2}{2\epsilon}\right] dx' \\
&= \frac{1}{2\pi\epsilon}(\frac{\sqrt{\pi}}{2}(2\beta\epsilon)^{\frac{3}{2}})(\sqrt{\frac{2\pi\epsilon}{\beta}}) \\
&= \beta\epsilon
\end{aligned} \tag{2.81}$$

Using analogous arguments, we can obtain

$$\langle x'^2 \rangle = \gamma_{cs}\epsilon \tag{2.82}$$

We can also evaluate

$$\begin{aligned}
\langle x x' \rangle &= \int_{-\infty}^{\infty}\int_{-\infty}^{\infty} x x' \frac{1}{2\pi\epsilon} \exp\left(-\frac{\gamma_{cs}x^2 + 2\alpha x x' + \beta x'^2}{2\epsilon}\right) dx dx' \\
&= \frac{1}{2\pi\epsilon}\int_{-\infty}^{\infty} x \exp\left(-\frac{x^2}{2\beta\epsilon}\right) dx \int_{-\infty}^{\infty} x' \exp\left[-\beta\frac{(x' + \frac{\alpha}{\beta}x)^2}{2\epsilon}\right] dx'
\end{aligned} \tag{2.83}$$

which upon substituting $u = x' + \frac{\alpha}{\beta}x$ leads to,

$$\begin{aligned}
\langle xx' \rangle &= \frac{1}{2\pi\epsilon}\int_{-\infty}^{\infty} x \exp\left(-\frac{x^2}{2\beta\epsilon}\right)dx \int_{-\infty}^{\infty}(u - \frac{\alpha}{\beta}x)\exp\left[-\beta\frac{u^2}{2\epsilon}\right]du \\
&= \frac{1}{2\pi\epsilon}\int_{-\infty}^{\infty} x \exp\left(-\frac{x^2}{2\beta\epsilon}\right)dx \int_{-\infty}^{\infty}(-\frac{\alpha}{\beta}x)\exp\left[-\beta\frac{u^2}{2\epsilon}\right]du \\
&= -\frac{\alpha}{\beta}\frac{1}{2\pi\epsilon}\int_{-\infty}^{\infty} x^2 \exp\left(-\frac{x^2}{2\beta\epsilon}\right)dx \int_{-\infty}^{\infty}\exp\left[-\beta\frac{u^2}{2\epsilon}\right]du \\
&= -\frac{\alpha}{\beta}\frac{1}{2\pi\epsilon}(\frac{\sqrt{\pi}}{2}(2\beta\epsilon)^{\frac{3}{2}})(\sqrt{\frac{2\pi\epsilon}{\beta}}) \\
&= -\alpha\epsilon
\end{aligned} \tag{2.84}$$

Recall that γ_{cs} is defined to be $(1+\alpha^2)/\beta$, therefore we can calculate

$$\langle x^2 \rangle \langle x'^2 \rangle - \langle xx' \rangle^2 = (\beta\epsilon)(\gamma_{cs}\epsilon) - \alpha^2\epsilon^2 = \epsilon^2 \tag{2.85}$$

So the constant ϵ in Eq. (2.80) is simply the geometric emittance of the beam, which is defined in Eq. (2.69). From equations (2.81), (2.82) and (2.84), we can see that the C-S parameters of a beam, as defined in Eq. (2.73), are exactly the same as the C-S parameters of a single particle!

In summary, by using Jeans's theorem and assuming the distribution of a beam is Gaussian, Eq. (2.80), we proved that the C-S parameters for a single paricle and C-S parameters for a beam are identical to each other. For other distributions, the relationship between the single particle and beam C-S parameters will be more complex.

2.9 Geometrical interpretation of RMS emittance

The geometric emittance of the beam can be defined in different ways. The most common definition is given by Eq. (2.69). The emittance defined in this way is also called RMS emittance. Other definitions [74] are useful if the beam distribution is far from a Gaussian, e.g., there are tails (halos) at large values of x or x'. In this dissertation, we will use the RMS definition.

Before investigating the evolution of the geometric emittance, let us try to examine the meaning of it and get more intuition. Generally speaking, the geometric emittance is the area occupied in trace space ((x, x') space). But what does this mean exactly?

Consider a particle beam with N particles. According to Eq. (2.69), we have

$$\epsilon^2 = \frac{\sum_{i=1}^{N} x_i^2}{N} \times \frac{\sum_{j=1}^{N} {x'_j}^2}{N} - \frac{\sum_{i=1}^{N} x_i x'_i}{N} \times \frac{\sum_{j=1}^{N} x_j x'_j}{N} \tag{2.86}$$

from which it follows that

$$\begin{aligned} N^2\epsilon^2 &= \frac{1}{2}\left(\sum_{i=1}^{N} x_i^2 \sum_{j=1}^{N} {x'_j}^2 + \sum_{j=1}^{N} x_j^2 \sum_{i=1}^{N} {x'_i}^2 - 2\sum_{i=1}^{N} x_i x'_i \sum_{j=1}^{N} x_j x'_j\right) \\ &= \frac{1}{2}\sum_{i=1}^{N}\sum_{j=1}^{N}(x_i x'_j - x_j x'_i)^2 \\ &= \frac{1}{2}\sum_{i=1}^{N}\sum_{j=1}^{N}\begin{vmatrix} x_i & x'_i \\ x_j & x'_j \end{vmatrix}^2 \\ &= \frac{1}{2}\sum_{i=1}^{N}\sum_{j=1}^{N}|\mathbf{r}_i \times \mathbf{r}_j|^2 \quad (\mathbf{r}_i = (x_i, x'_i)) \\ &= \frac{1}{2}\sum_{i=1}^{N}\sum_{j=1}^{N} S_{ij}^2 \end{aligned} \tag{2.87}$$

Before proceeding, we offer a few explanations for the derivation. The i_{th} particle has a position x_i and velocity x'_i, so it represents a point (x_i, x'_i) in the trace space. We can also think of this point as a vector $\mathbf{r}_i$ pointing from the origin to the point (x_i, x'_i). For a pair of particles i and j, their corresponding $\mathbf{r}_i = (x_i, x'_i)$ and $\mathbf{r}_j = (x_j, x'_j)$ will form a parallelogram, and we denote the area of this parallelogram, calculated by the cross product between $\mathbf{r}_i = (x_i, x'_i)$ and $\mathbf{r}_j = (x_j, x'_j)$, as S_{ij}.

The emittance can thus be defined as

$$\epsilon = \frac{1}{\sqrt{2}} RMS(S_{ij}) \tag{2.88}$$

where

$$RMS(S_{ij}) = \sqrt{\frac{\sum_{i=1}^{N}\sum_{j=1}^{N} S_{ij}^2}{N^2}} \tag{2.89}$$

The geometric emittance is therefore just the RMS value of the area of all the parallelograms formed by each pair of trace space vector $\mathbf{r}_i = (x_i, x_i')$ and $\mathbf{r}_j = (x_j, x_j')$, divided by $\sqrt{2}$. Note: the total number of parallelograms is $N * N = N^2$ (rather than $C_N^2 = N(N-1)/2$) because we include the case when $i = j$ (the area of the parallelogram is 0).

It is straightforward to show that each S_{ij} in Eq. (2.87) is invariant if the elements of the transport matrix M are the same for each particle (no energy spread) and the determinant of M is unity. From Eq. (2.87) we have

$$\begin{aligned}
S_{ij} &= |\begin{vmatrix} x_i & x_i' \\ x_j & x_j' \end{vmatrix}| \\
&= |det(\begin{pmatrix} x_i & x_j \\ x_i' & x_j' \end{pmatrix})| \\
&= |det(M\begin{pmatrix} x_{i0} & x_{j0} \\ x_{i0}' & x_{j0}' \end{pmatrix})| \\
&= |det(M)det(\begin{pmatrix} x_{i0} & x_{j0} \\ x_{i0}' & x_{j0}' \end{pmatrix})| \\
&= |det(\begin{pmatrix} x_{i0} & x_{j0} \\ x_{i0}' & x_{j0}' \end{pmatrix})| \\
&= |\begin{vmatrix} x_{i0} & x_{i0}' \\ x_{j0} & x_{j0}' \end{vmatrix}| \\
&= S_{ij0}
\end{aligned} \tag{2.90}$$

where the subscript 0 denotes the quantities evaluated at the initial position $z = z_0$. As we can see, if the a beam has no energy spread thus the transport matrices are the same for

each particle and the determinant of the transport matrix is unity, then the area of each parallelogram is invariant. Thus under these assumptions the emittance, which is the RMS value of the area of all these parallelograms, is invariant.

2.10 Beam's evolution in vacuum

Earlier, we defined the transport matrix for a beam propagating in vacuum (a drift space). For this case the coordinates of a single beam particle evolve as,

$$x = x_i + x_i' z,\ x' = x_i' \tag{2.91}$$

from which it follows,

$$\begin{aligned}
\epsilon^2 &= \langle x^2 \rangle \langle x'^2 \rangle - \langle x x' \rangle^2 \\
&= \langle (x_i + x_i' z)^2 \rangle \langle x_i'^2 \rangle - \langle (x_i + x_i' z) x_i' \rangle^2 \\
&= \langle x_i^2 + 2 x_i x_i' z + x_i'^2 z^2 \rangle \langle x_i'^2 \rangle - \langle x_i x_i' + x_i'^2 z \rangle^2 \\
&= (\langle x_i^2 \rangle + 2z \langle x_i x_i' \rangle + z^2 \langle x_i'^2 \rangle) \langle x_i'^2 \rangle - (\langle x_i x_i' \rangle + z \langle x_i'^2 \rangle)^2 \\
&= \langle x_i^2 \rangle \langle x_i'^2 \rangle - \langle x_i x_i' \rangle^2 \\
&= \epsilon_i^2
\end{aligned} \tag{2.92}$$

So in vacuum, the beam's geometrical emittance is perfectly conserved, and this is true even if there is energy spread!

As for the evolution of the C-S parameters, we have:

$$\beta = \frac{\langle x^2 \rangle}{\epsilon} = \frac{\langle (x_i + x_i' z)^2 \rangle}{\epsilon_i} = \frac{\langle x_i^2 \rangle + 2z \langle x_i x_i' \rangle + z^2 \langle x_i'^2 \rangle}{\epsilon_i} = \beta_i - 2z\alpha_i + z^2 \gamma_i \tag{2.93}$$

$$\alpha = -\frac{\langle x x' \rangle}{\epsilon} = -\frac{\langle (x_i + x_i' z) x_i' \rangle}{\epsilon_i} = -\frac{\langle x_i x_i' \rangle + z \langle x_i'^2 \rangle}{\epsilon_i} = \alpha_i - z\gamma_i \tag{2.94}$$

$$\gamma = \frac{\langle x'^2 \rangle}{\epsilon} = \frac{\langle x_i'^2 \rangle}{\epsilon_i} = \gamma_i \tag{2.95}$$

If the origin for z is defined where the beam is initially at the vacuum waist, in other words, if

$$\alpha_i = 0, \beta_i = \beta^*, \gamma_i = 1/\beta^* \tag{2.96}$$

at $z = 0$ where the superscript * denotes the quantities at the beam's vacuum focus, then

$$\beta = \beta^* + \frac{z^2}{\beta^*} = \beta^*(1 + \frac{z^2}{{\beta^*}^2}) \tag{2.97}$$

$$\alpha = -\frac{z}{\beta^*} \tag{2.98}$$

$$\gamma = \frac{1}{\beta^*} \tag{2.99}$$

We note that Eq. (2.97) is equivalent to $\sigma = \sigma_0\sqrt{1 + z^2/{\beta^*}^2}$ where $\sigma_0 \equiv \sigma(z = 0)$ which also follows from Eq. (2.71). Sometimes in a computer simulation, we want to initialize a particle beam at a location z_0 that is not at focus ($\alpha \neq 0$). In other words, we want to initialize a beam parametrized by the geometric emittance ϵ and CS parameters β, α. One way to do this is to follow the following steps:

1. Use Eq. (2.74) to calculate γ, then use Eq. (2.99) to calculate the beta function at the vacuum focus β^*.

2. Calculate the beam's spot size σ_x^* and the beam's divergence $\sigma_{x'}^*$ at the vacuum focus: $\sigma_x^* = \sqrt{\beta^*\epsilon}$, $\sigma_{x'}^* = \sqrt{\epsilon/\beta^*}$. Then initialize particles' x and x' with normal distributions: $x^* \sim \mathcal{N}(0, \sigma_x^{*2})$, $x'^* \sim \mathcal{N}(0, \sigma_{x'}^{*2})$

3. Use Eq. (2.98) and Eq. (2.99) to calculate the beam's position relative to the vacuum focus $z = -\frac{\alpha}{\gamma}$. Then translate the particles' position using the mapping $x = x^* + x'^* z = x^* - \frac{\alpha}{\gamma}x'^*$. The particles' velocities x' remain unchanged.

If the beam is initially a Maxwellian, i.e., Gaussian, we can use this procedure to derive the distribution function for the beam away from the focus. We assume that at the vacuum focus, the beam's distribution function in (x, x') space (or trace space) is separable into the product of two Gaussians,

$$f^*(x^*, x'^*) = \frac{1}{2\pi\sigma_x^*\sigma_{x'}^*} \exp\left[-\frac{x^{*2}}{2\sigma_x^{*2}}\right] \exp\left[-\frac{x'^{*2}}{2\sigma_{x'}^{*2}}\right] \tag{2.100}$$

According to the Vlasov equation, the distribution function dos not change if you follow the trajectory of a particle in trace space (assuming γ remains constant), therefore,

$$f(x, x') = f^*(x^*, x'^*) = f^*(x^*(x, x'), x'^*(x, x')) \tag{2.101}$$

which leads to

$$\begin{aligned} f(x, x') &= \frac{1}{2\pi\epsilon} \exp\left[-\frac{(x + \frac{\alpha}{\gamma}x')^2}{2\beta^*\epsilon}\right] \exp\left[-\frac{x'^2}{2\epsilon/\beta^*}\right] \\ &= \frac{1}{2\pi\epsilon} \exp\left[-\frac{\gamma(x + \frac{\alpha}{\gamma}x')^2}{2\epsilon}\right] \exp\left[-\frac{x'^2}{2\gamma\epsilon}\right] \\ &= \frac{1}{2\pi\epsilon} \exp\left[-\frac{\gamma x^2 + 2\alpha x x' + \beta x'^2}{2\epsilon}\right] \end{aligned} \tag{2.102}$$

This is actually a multivariate normal distribution [85]

$$f(\mathbf{x}) = \frac{\exp\left(-\frac{\mathbf{x}^T\Sigma^{-1}\mathbf{x}}{2}\right)}{\sqrt{(2\pi)^2|\Sigma|}} \tag{2.103}$$

where $\mathbf{x} = (x, x')^T$,

$$\Sigma = \epsilon \begin{pmatrix} \beta & -\alpha \\ -\alpha & \gamma \end{pmatrix} \tag{2.104}$$

and

$$\Sigma^{-1} = \frac{1}{\epsilon} \begin{pmatrix} \gamma & \alpha \\ \alpha & \beta \end{pmatrix} \tag{2.105}$$

The distribution function (2.102) could also have been immediately obtained from Jeans's theorem [84] which states that any distribution function constructed in terms of constants of the motion satisfy the Vlasov equation. Therefore a Maxwellian using Eq. (2.29) as its argument describes a particle beam in the absence of acceleration.

2.11 Emittance evolution in a uniform plasma in the blowout regime

In this section, we consider the emittance evolution in a uniform plasma. In the blowout regime, the witness beam feels a linear focusing force. If we assume the witness beam has no longitudinal acceleration, then the transverse motion of a single beam particle is given by the transport matrix in Eq. (2.56). This transport matrix is almost a rotation in trace space. For particles with different energy γ, the k_β in the corresponding transport matrix will be different. Therefore, based on the geometrical interpretation the geometrical emittance will not be preserved if there is any energy spread.

2.11.1 Beam with no energy spread: Emittance is unchanged

We next show that if the beam has no energy spread and there is no acceleration, the beam's geometric emittance will be conserved in the linear focusing force provided by the blowout regime. There are several ways to prove this, but here we will take a more intuitive argument that takes advantage of the geometrical interpretation discussed in the previous section, and save the more mathematical proof for later when we discuss the conservation of normalized emittance.

If the beam has no energy spread, then the k_β in the transport matrix will be the same

for all the particles in the beam. If we normalize x using $\hat{x} = k_\beta x$, then

$$\begin{pmatrix} \hat{x}(z) \\ x'(z) \end{pmatrix} = \begin{pmatrix} \cos(k_\beta z) & \sin(k_\beta z) \\ -\sin(k_\beta z) & \cos(k_\beta z) \end{pmatrix} \begin{pmatrix} \hat{x}(0) \\ x'(0) \end{pmatrix} \tag{2.106}$$

This transport matrix is exactly a rotation in the normalized trace space. Therefore its determinant is unity and its elements are the same for every particle. Therefore, as noted above in section 2.9, these are the conditions for preserving the geometrical emittance. For the specific case of a rotation of $\mathbf{r}_i \equiv (x_i, x_i')$ in trace space, the geometrical interpretation of ϵ in section 2.9 quickly shows that ϵ is preserved. The geometric emittance is just the RMS value of the area of all the parallelograms formed by each pair of trace space vectors, and a rotation in the (normalized) trace space will not change the area of these parallelograms. Therefore, the geometric emittance of a beam with no energy spread is invariant in a linear focusing force, since the transport matrices of all the particles represent the same rotation.

2.11.2 Beam with energy spread. Importance of matching

A real beam usually has some finite energy spread, and in general, this leads to emittance growth. Here we ignore acceleration. We call this phenomenon 'chromatic effects' or 'phase mixing'. From Eq. (2.56) (or Eq. (2.106)) we can see that particles with different energy γ will have different k_β, and that after propagating for the same longitudinal distance z, their phase advance $\phi = k_\beta z$ will be different. This may lead to a larger trace space area, hence the emittance growth.

When the beam has energy spread, we can still preserve the beam's emittance by matching the beam to the plasma [86]. The matching condition is given in Eq. (2.72), also with the requirement $\alpha = 0$. We have already shown that when the beam is matched, its spot size does not oscillate. Here we will prove that when the beam is matched, its geometric emittance is preserved perfectly, even in the presence of energy spread.

Here we offer a simple way to derive an expression for the final emittance after phase

mixing is complete in a uniform plasma. In the next chapter, we will provide a more rigorous and sophisticated approach and derive the emittance evolution as a function of propagation distance z when the plasma density is varying adiabatically, so the uniform plasma is simply a special case of that result.

We start with the transport matrix in Eq. (2.56) (We change the notation slightly for convenience):

$$\begin{pmatrix} x \\ x' \end{pmatrix} = \begin{pmatrix} \cos\phi & \frac{1}{k_\beta}\sin\phi \\ -k_\beta \sin\phi & \cos\phi \end{pmatrix} \begin{pmatrix} x_i \\ x_i' \end{pmatrix} \tag{2.107}$$

where $\phi = k_\beta z$ is the phase advance. We should keep in mind that for particles with different energy γ, k_β and hence ϕ are different. Let's calculate the moments for the beam:

$$\begin{aligned} \langle x^2 \rangle &= \langle (x_i \cos\phi + x_i' \frac{\sin\phi}{k_\beta})^2 \rangle \\ &= \langle x_i^2 \rangle \langle \cos^2\phi \rangle + \langle x_i'^2 \rangle \langle \frac{\sin^2\phi}{k_\beta^2} \rangle + \langle x_i x_i' \rangle \langle \frac{\sin(2\phi)}{k_\beta} \rangle \\ &\approx \langle x_i^2 \rangle \langle \cos^2\phi \rangle + \langle x_i'^2 \rangle \frac{\langle \sin^2\phi \rangle}{\bar{k}_\beta^2} + \langle x_i x_i' \rangle \frac{\langle \sin(2\phi) \rangle}{\bar{k}_\beta} \end{aligned} \tag{2.108}$$

where we assume that a particle's initial position x_i and velocity x_i' are independent of the energy γ in the second step. In the last step we make an approximation by taking the k_β related terms out of the ensemble average and just use the k_β for the particle with an average energy: $\bar{k}_\beta = \frac{\omega_p}{\sqrt{2\bar{\gamma}}c}$. This approximation is reasonable if the energy spread is small. On the other hand we cannot use $\bar{k}_\beta$ in the phase because it grows with z, $\phi = k_\beta z$. Therefore, only the phase terms can deviate substantially between particles with small energy differences.

At equilibrium, the phase mixing is complete, the particles' phase angles are uniformly distributed. More precisely, we introduce the following notation:

$$\phi = 2\pi N + \phi_r \quad (0 \le \phi_r < 2\pi, N = 0, 1, 2...) \tag{2.109}$$

When phase mixing is complete, ϕ_r is uniformly distributed between 0 and 2π. Therefore:

$$\langle \cos^2 \phi \rangle = \langle \cos^2 \phi_r \rangle = \frac{1}{2\pi} \int_0^{2\pi} \cos^2 \phi_r d\phi_r = \frac{1}{2} \tag{2.110}$$

Similarly we can get $\langle \sin^2 \phi \rangle = 1/2$, and $\langle \sin(2\phi) \rangle = 0$, leading to,

$$\langle x^2 \rangle = \frac{1}{2} \left(\langle x_i^2 \rangle + \frac{\langle x_i'^2 \rangle}{\bar{k}_\beta^2} \right) \tag{2.111}$$

Using the same analysis for x', we also have,

$$\langle x'^2 \rangle = \frac{1}{2} \left(\bar{k}_\beta^2 \langle x_i^2 \rangle + \langle x_i'^2 \rangle \right) \tag{2.112}$$

and

$$\langle x x' \rangle = 0 \tag{2.113}$$

Therefore, after phase mixing is complete, we have,

$$\epsilon = \sqrt{\langle x^2 \rangle \langle x'^2 \rangle - \langle x x' \rangle^2} = \frac{1}{2} \left(\bar{k}_\beta \langle x_i^2 \rangle + \frac{\langle x_i'^2 \rangle}{\bar{k}_\beta} \right) \tag{2.114}$$

If we use the inequality of arithmetic and geometric means, we have:

$$\begin{aligned} \epsilon &\geq \sqrt{\langle x_i^2 \rangle \langle x_i'^2 \rangle} \\ &\geq \sqrt{\langle x_i^2 \rangle \langle x_i'^2 \rangle - \langle x_i x_i' \rangle^2} \\ &= \epsilon_i \end{aligned} \tag{2.115}$$

We can see that the final geometric emittance is always greater or equal to the initial emittance. The equal sign is taken when $\bar{k}_\beta \langle x_i^2 \rangle = \frac{\langle x_i'^2 \rangle}{\bar{k}_\beta}$ and $\langle x_i x_i' \rangle = 0$, or equivalently,

$$\sigma_{x_i} = \sqrt{\langle x_i^2 \rangle} = \sqrt{\frac{\epsilon_i}{\bar{k}_\beta}} \ , \ \alpha_i = 0 \tag{2.116}$$

The equations above give the matching condition for a beam, which agrees with what we obtained earlier in Eq. (2.72).

We have derived the matching condition, but what does it mean physically? Is there any physical intuition behind it? To answer these questions, we start with the matching

condition in Eq. (2.116). If the beam is initially matched, then the distribution function is a bi-Gaussian function,

$$f_i(x_i, x_i') = \frac{1}{2\pi\sigma_x\sigma_{x'}} \exp\left[-\frac{x_i^2}{2\sigma_{x_i}^2}\right] \exp\left[-\frac{x_i'^2}{2\sigma_{x_i'}^2}\right] \tag{2.117}$$

The distribution function can be written this way because for a matched beam, $\alpha_i = 0$, and thus x_i and x_i' are decoupled in the distribution function. Furthermore, if $\alpha_i = 0$ then it follows that $\epsilon_i = \sigma_{x_i}\sigma_{x_i'}$, from which it follows that,

$$\frac{\sigma_{x_i'}}{\sigma_{x_i}} = \frac{\epsilon_i}{\sigma_{x_i}^2} = \bar{k}_\beta \tag{2.118}$$

Substituting Eq. (2.118) into Eq. (2.117) permits rewriting the Gaussian distribution function of a matched beam as

$$f_i(x_i, x_i') = \frac{1}{2\pi\sigma_{x_i}\sigma_{x_i'}} \exp\left[-\frac{x_i^2}{2\sigma_{x_i}^2}\right] \exp\left[-\frac{x_i'^2}{2k_\beta^2\sigma_{x_i}^2}\right] \tag{2.119}$$

After the beam propagates for a distance z, the particle that was initially located at (x_i, x_i') will rotate to (x, x'), according to Eq. (2.107). If the initial distribution function is evaluated at the new position (x, x'), it can be seen that it is the same as $f_i(x_i, x_i')$,

$$\begin{aligned} f_i(x, x') &= \frac{1}{2\pi\sigma_{x_i}\sigma_{x_i'}} \exp\left[-\frac{\left(x_i\cos\phi + x_i'\dfrac{\sin\phi}{k_\beta}\right)^2}{2\sigma_{x_i}^2}\right] \exp\left[-\frac{(-x_i k_\beta \sin\phi + x_i'\cos\phi)^2}{2k_\beta^2\sigma_{x_i}^2}\right] \\ &= \frac{1}{2\pi\sigma_{x_i}\sigma_{x_i'}} \exp\left[-\frac{x_i^2}{2\sigma_{x_i}^2}\right] \exp\left[-\frac{x_i'^2}{2k_\beta^2\sigma_{x_i}^2}\right] \\ &= f_i(x_i, x_i') \end{aligned} \tag{2.120}$$

This demonstrates that a particle is rotating along the contour of the distribution function f_i ! This explains why the emittance of a matched beam can be preserved even if the beam has energy spread. Although the particles with different energy are rotating with different angular frequencies in the trace space, they are rotating along the contours of the distribution

function, keeping the distribution function unchanged! To be more rigorous, along a particle trajectory, from the Vlasov equation we have

$$f(x, x') = f_i(x_i, x_i') \tag{2.121}$$

where f is the distribution function of the beam after the beam propagates for a distance z. Combined with Eq. (2.120), we have

$$f(x, x') = f_i(x, x') \tag{2.122}$$

which demonstrates that after the propagation of the beam, the distribution function does not change!

To summarize, if a beam with energy spread is matched to a uniform plasma, as the beam propagates without acceleration, the particles will move along the contours of the distribution function, implying the distribution function does not change, hence the emittance is invariant. From this we can see that matching is essential for preserving the emittance of a beam.

2.12 Normalized emittance

In the previous section, we have shown that assuming there is no longitudinal acceleration, the geometric emittance of a beam with no energy spread is conserved under a linear focusing force. We also showed that if a beam is matched the emittance dos not grow even if there is energy spread. However, when the beam is accelerated, its geometric emittance is no longer conserved. One way to see this, is to note that the determinant of the transport matrix in trace space ((x, x') space) is equal to γ_0/γ (See Appendix B), which is no longer equal to 1. This leads to a smaller trace space area (smaller by a factor of γ_0/γ), hence the geometric emittance decreases if γ is increasing.

However, the determinant of the transport matrix in phase space ((x, p_x) space) is equal to 1! Therefore, in order to describe a property of beam's transverse motion that does not

depend on the kinematic factors, we introduce the normalized emittance, which is defined as

$$\epsilon_n = \frac{1}{m_e c}\sqrt{\langle x^2\rangle \langle p_x^2\rangle - \langle x p_x\rangle^2} \tag{2.123}$$

For a beam with a small energy spread, the normalized emittance and the geometric emittance are related by,

$$\epsilon_n \approx \bar{\gamma}\epsilon \tag{2.124}$$

where $\bar{\gamma}$ is the ensemble average of all the beam particles' γ. In practice, in an accelerator, e.g., a plasma based accelerator, we are more concerned about the preservation of normalized emittance. On the other hand, the geometric emittance is often used together with the Courant-Snyder parameters.

Next, we show an important result. For a beam with no energy spread, the normalized emittance is conserved in a linear focusing force. Let us square Eq. (2.123) and take a derivative with respect to the propagation distance

$$\begin{aligned}
(m_e^2 c^2 \epsilon_n^2)' &= 2[\langle x x'\rangle \langle p_x^2\rangle + \langle x^2\rangle \langle p_x p_x'\rangle - \langle x p_x\rangle (\langle x' p_x\rangle + \langle x p_x'\rangle)] \\
&= 2[\langle x p_x/\gamma\rangle \langle p_x^2\rangle + \langle x^2\rangle \langle p_x p_x'\rangle - \langle x p_x\rangle (\langle p_x^2/\gamma\rangle + \langle x p_x'\rangle)] \\
&= 2[\langle x p_x\rangle \langle p_x^2\rangle /\gamma + \langle x^2\rangle \langle p_x p_x'\rangle - \langle x p_x\rangle \langle p_x^2\rangle /\gamma - \langle x p_x\rangle \langle x p_x'\rangle] \\
&= 2[\langle x^2\rangle \langle p_x p_x'\rangle - \langle x p_x\rangle \langle x p_x'\rangle]
\end{aligned} \tag{2.125}$$

where we used $x' = p_x/\gamma$, and we take γ out of the ensemble average in the third line because the beam has no energy spread so all the particles have the same γ. If the beam is focused by a linear focusing force, $p_x' = -Kx$, then we have

$$\begin{aligned}
(m_e^2 c^2 \epsilon_n^2)' &= 2[-\langle x^2\rangle \langle p_x K x\rangle + \langle x p_x\rangle \langle x K x\rangle] \\
&= 2[-K\langle x^2\rangle \langle p_x x\rangle + K\langle x p_x\rangle \langle x^2\rangle] \\
&= 0
\end{aligned} \tag{2.126}$$

This means ϵ_n is conserved. Therefore, we showed that if a beam has no energy spread, the normalized emittance is unchanged under a linear focusing force.

Another way to show this is to use the geometrical interpretation of RMS emittance discussed in section 2.9. Although in section 2.9 we gave the geometrical interpretation of geometric emittance in trace space (x, x'), the exact same idea applies to the geometrical interpretation of normalized emittance in phase space (x, p_x) as well. In appendix B we have already shown that when the beam has acceleration, the determinant of the transport matrix in phase space (not trace space) is unity. Therefore, according to the conclusion we found in section 2.9, the normalized emittance is invariant if the beam has no energy spread (thus all the particles have the same transport matrices).

We provide a concrete example to show the determinant of the transport matrix is unity in phase space. We substitute $x' = p_x/\gamma$ and $x'_0 = p_{x0}/\gamma_0$ into the 'exact' transport matrix in trace space in Eq. (2.62) and get the transport matrix in phase space,

$$\begin{pmatrix} \sqrt{\frac{\tilde{\beta}}{\tilde{\beta}_0}}(\cos\phi + \tilde{\alpha}_0 \sin\phi) & \sqrt{\tilde{\beta}\tilde{\beta}_0}\sin\phi \\ \frac{1}{\sqrt{\tilde{\beta}_0\tilde{\beta}}}[(\tilde{\alpha}_0 - \tilde{\alpha})\cos\phi - (1 + \tilde{\alpha}_0\tilde{\alpha})\sin\phi] & \sqrt{\frac{\tilde{\beta}_0}{\tilde{\beta}}}(-\tilde{\alpha}\sin\phi + \cos\phi) \end{pmatrix} \tag{2.127}$$

It can be easily verified that the determinant of this matrix is unity.

However, a real beam always has some finite energy spread. Usually this leads to normalized emittance growth. In the absence of acceleration, the evolution of the normalized emittance for a beam with energy spread in a longitudinally uniform plasma will be [78] [41] [44]

$$\frac{\epsilon_n}{\epsilon_{n0}} = \frac{\gamma_{cs0}\beta_m + \beta_0/\beta_m}{2}\sqrt{1 - \frac{(\gamma_{cs0}\beta_m + \beta_0/\beta_m)^2 - 4}{(\gamma_{cs0}\beta_m + \beta_0/\beta_m)^2}\exp\left[-(\frac{\sigma_\gamma}{\bar{\gamma}}\bar{\phi})^2\right]} \tag{2.128}$$

where $\beta_0, \gamma_{cs0} \equiv (1 + \alpha_0^2)/\beta_0$ are the beam's initial C-S parameters, $\beta_m \equiv \sqrt{2\bar{\gamma}}c/\omega_p$, $\bar{\gamma}$ is the average relativistic Lorentz factors of the beam, $\sigma_r/\bar{\gamma}$ is the energy spread, and $\bar{\phi} = \int_0^z dz'/\beta_m(z')$ is the phase advance. This is just a special case of what we will see in Chapter 3, so we will not show the derivation here. From Eq. (2.128), it is straightforward to see that

if and only if the beam is matched, i.e., if

$$\beta_0 = \beta_m, \alpha_0 = 0 \tag{2.129}$$

then $\epsilon_n = \epsilon_{n0}$, which means the normalized emittance is preserved. Otherwise, the normalized emittance will grow first and eventually saturate at $\frac{\gamma_{cs0}\beta_m + \beta_0/\beta_m}{2}\epsilon_{n0}$. Therefore, it is clear that matching is important to preserve the normalized emittance.

In the presence of acceleration, as pointed out in Ref. [78] it is hard to write the emittance evolution in as a useful form as Eq. (2.128). But as we will see from the simulation results in next Chapter, if the beam starts as matched, as the beam gets accelerated adiabatically, the beam will stay matched, with essentially no emittance growth in the entire process. Therefore, matching is essential to preserve the beam's normalized emittance.

2.13 Summary

In this chapter, we started by solving the transverse equation of motion of a single beam particle in a linear focusing force as exists in the nonlinear blowout regime of PWFA. Assuming the acceleration happens adiabatically, we can factor out the explicit dependence of energy and get an exact solution to the Hill like equation. In this process, we introduced the C-S parameters for a single particle. We found constants of the motion which describe an ellipse in trace and phase space. We then used three different methods (adiabatic assumption, WKB, adiabatic invariant) to get an approximate solution if the plasma density also changes adiabatically. Using the solution to the motion of a single particle, we defined and constructed the transport matrices, which are useful to study the beam's evolution as an ensemble of particles.

In the second part of this chapter, we switched to a macroscopic view to study a beam. We introduced the geometric emittance and C-S parameters for a beam, and showed the connection between the C-S parameters for a single particle and the C-S parameters for a beam. We also gave a geometrical interpretation of the emittance. We then studied the

evolution of a beam in vacuum, and showed how to initialize a beam using C-S parameters in a simulation when the beam is not at the vacuum focus. Finally, we studied the evolution of the geometric & normalized emittance of a beam in a uniform plasma. We then discussed the importance of matching for emittance preservation.

CHAPTER 3

Emittance preservation through density ramp matching sections in a plasma wakefield accelerator

3.1 Introduction

This chapter describes results that were published in Ref.[44]. In order that the Chapter be self-contained the introduction repeats points described in Chapter 1 and 2. In Plasma Wakefield Acceleration (PWFA), an ultra-relativistic electron beam (the drive beam) is used to form a plasma wake that accelerates a second electron beam (the witness beam) that is properly loaded inside the wake. In the so-called blowout regime, the drive beam density is much higher than the plasma density. The electric field of the drive beam will expel all the plasma electrons away and leave an ion channel (i.e. a bubble) behind it. As shown in Fig. 3.1 and discussed in Sec. 1.2.6, when the witness beam is located at a proper position inside the wake, the accelerating field can be flattened in order to preserve the energy spread. At the back of the bubble, where the witness beam is located, not only is there a longitudinal electric field that provides a high acceleration gradient, but there is also a transverse focusing force. In addition, when there is azimuthal symmetry, in these nonlinear wakes the longitudinal electric field (the accelerating field) does not depend on r and the transverse focusing force is linear (proportional to r), points radially inward, and does not depend on $\xi = ct - z$ inside the bubble [23]. The fact that the accelerating field does not depend on r ensures that the beam particles will not gain additional slice energy spread when undergoing acceleration and betatron oscillations inside the bubble. Furthermore, the fact that the transverse linear

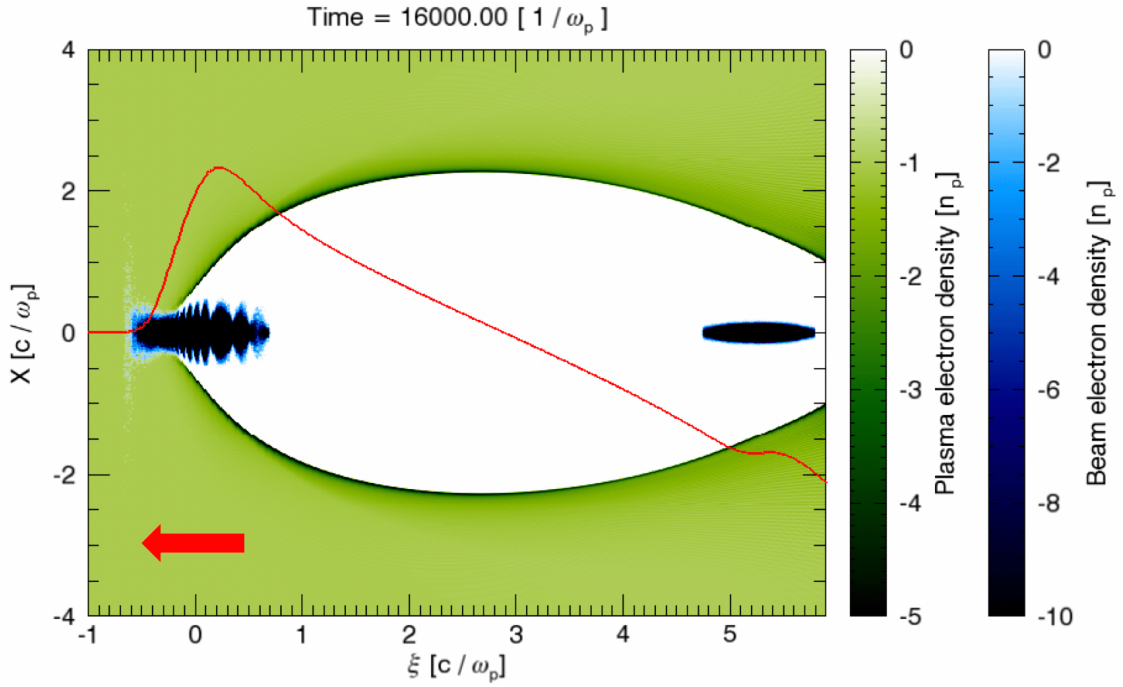

Figure 3.1: A snapshot of the drive and witness beam of a sample simulation of a two bunch PWFA. A data is in the $x - \xi$ plane at $y = 0$. Both beams (blue) are propagating to the left. The green area shows the unperturbed plasma electron density, the white area is the uniform plasma ions (ion channel/bubble). The red curve is the lineout of the accelerating field E_z on the axis (in arbitrary units).

focusing force does not depend on ξ ensures that the beam particles at different longitudinal positions will oscillate at the same betatron frequency, if they have the same energy. If one of these properties is satisfied then the Panofsky Wenzel theorem [32, 33] guarantees that the other is as well.

When the beam has no energy spread, its emittance is conserved under a linear focusing force inside the symmetric bubble. When the beam has an energy spread, and/or there is acceleration with imperfect beam loading (particles at different longitudinal positions in the beam feel a different accelerating field, E_z), the beam's emittance may increase during its propagation in the plasma. The topic of emittance growth and preservation is very important and is being actively studied [86, 40, 87, 88, 41, 78, 39, 42, 89].

Recently, expressions for emittance evolution in uniform plasma, both for cases when the beam does [41] or does not have [78] longitudinal acceleration have been published. It has also been shown that several plasma density profiles provide exact solutions to single particle motion [41, 39], therefore the evolution of the beam's C-S parameters can be calculated and used to match the beam into a plasma. In this chapter, we investigate how the emittance grows when a beam is not matched in an adiabatic plasma ramp. In complementary work, R. Ariniello et al. [42] recently showed that if a beam is matched to an adiabatic plasma profile, the emittance will oscillate around its initial value with a small amplitude (10^{-4} times the initial emittance) for a 2% energy spread (and the amplitude of oscillations scales as σ_γ^2).

In typical experiments (e.g. the FACET II experiments at SLAC [90]), the plasma density profile is usually fixed with density ramps at the entrance and the exit. Therefore the beam parameters need to be optimized to match the beam to the plasma. It has been shown that if the witness beam is initially matched to the plasma, its emittance can be well preserved [90]. However, if the witness beam parameters are fixed, it usually cannot be perfectly matched to an arbitrary plasma density ramp. In this chapter, we investigate the witness beam's emittance evolution in this situation. We first derive an analytical expression for the

beam's emittance evolution in an arbitrary adiabatic plasma profile, assuming the beam has no longitudinal acceleration. This analytical expression can be used to predict the emittance growth when the beam has an energy spread and is not initially matched. This analysis is complementary to that in [42] where it was assumed that the beam was nearly matched and the emittance growth was small. We also discuss how to choose the relative focal plane by either moving the plasma or the focal position of the beam to minimize the emittance growth for an unmatched beam with fixed parameters. It is found that the beam emittance growth can be minimized when choosing the focal plane to be the vacuum focus for a beam that was matched. Another issue that may cause emittance growth in a proposed experiment to double the energy of the witness beam at FACET II [14] is the ionization of helium buffer gas when using a Lithium plasma source. Additional self-ionization [91] by the beam can modify the focusing fields in the buffer region. In the last section, we show that under that situation the emittance growth is due to the nonlinear focusing force felt by the beam, which is caused by the nonuniform helium ion density in the plasma. The helium ionization can be minimized by using a 20 μm initial emittance witness bunch. Therefore such a bunch can be propagated while gaining energy without measurable emittance growth.

3.2 Theoretical analysis of emittance evolution in arbitrary adiabatic plasma density profile

In the blowout regime of PWFA with the assumption of azimuthal symmetry (we will henceforth use this assumption), as shown in Chapter 1 and 2 the focusing force felt by an electron in the witness beam is $\mathbf{F}_\perp = -m_e\omega_p^2\mathbf{r}/2$ (where m_e is the electron mass, $\omega_p = \sqrt{\frac{n_p e^2}{\epsilon_0 m_e}}$ is the plasma frequency, n_p is the plasma density, ϵ_0 is the vacuum permittivity, e is the elementary charge), which is proportional to the radial distance r and independent of $\xi = ct - z$. Therefore the motions of the beam particle in x and y directions are decoupled, and we will only study the beam particle motion in the x direction. If we assume a beam particle's energy is

a constant, the equation of motion for this particle is the Hill like equation,

$$x''(z) + k_\beta(z)^2 x(z) = 0 \tag{3.1}$$

where z is the coordinate along the direction of propagation, $k_\beta(z) = \frac{\omega_p(z)}{\sqrt{2\gamma}c}$, $\omega_p(z)$ is the plasma frequency at position z, γ is the relativistic factor of the beam particle, c is the speed of light. In a uniform plasma, $\omega_p(z)$ is a constant, so the solution to equation (3.1) is simple harmonic oscillation. With a given initial phase space distribution for the beam, we can obtain an analytical expression for the emittance evolution[41, 78]. As shown in Sec. 2.3, for a nonuniform plasma, there is a general analytical solution to equation (3.1). For such a solution it is not possible to construct transport matrices amenable to theoretical analysis. However, as long as the plasma density is changing adiabatically, i.e.,

$$\frac{|k'_\beta(z)|\frac{2\pi}{k_\beta(z)}}{k_\beta(z)} \ll 1 \tag{3.2}$$

or

$$\frac{\pi}{k_\beta(z) n_p(z)} \left| \frac{dn_p(z)}{dz} \right| \ll 1 \tag{3.3}$$

we can use WKB method [92] to get an approximate solution to equation (3.1). This solution can be incorporated into transport matrices which can be used to calculate the emittance evolution with the WKB solution.

The WKB solution to equation (3.1) is (details of the derivation are shown in Sec. 2.3 and Appendix C):

$$\begin{aligned} x(z) = {} & x(0)\frac{\sqrt{\beta_m(z)}}{\sqrt{\beta_m(0)}}\cos[\phi(z)] \\ & + \sqrt{\beta_m(z)\beta_m(0)}\Big[x'(0) + \frac{\alpha_m(0)}{\beta_m(0)}x(0)\Big]\sin[\phi(z)] \end{aligned} \tag{3.4}$$

where

$$\beta_m(z) = 1/k_\beta(z),\ \alpha_m(z) = -\frac{1}{2}\frac{d\beta_m(z)}{dz} \tag{3.5}$$

are the C-S parameters for a single particle in an adiabatically changing profile, and $\phi(z) = \int_0^z k_\beta(s)ds$ is the phase advance. $x(0)$ and $x'(0)$ are the initial values for the beam particle. Note that this solution can also be obtained from Eq. (2.38) after imposing the appropriate initial conditions. The adiabatic condition (3.2) can be simplified to [42]

$$|\alpha_m(z)| \ll 1 \tag{3.6}$$

We note that if the plasma density profile is $n_p(z) = \frac{n_{p0}}{(1+z/l)^4}$ (where l is a constant), then equation (3.1) has an exact solution [39], which is the same as its WKB solution described in equation (3.4), i.e., $\frac{1}{2}\beta\beta'' - \frac{1}{4}\beta'^2 = 0$ when $\beta = 1/k_\beta$.

For brevity, we henceforth denote $x(z)$ by x, $x(0)$ by x_i, $\beta_m(z)$ by β_m, $\beta_m(0)$ by β_{mi}, $\alpha_m(z)$ by α_m, $\alpha_m(0)$ by α_{mi}, and $\phi(z)$ by ϕ. From (3.4) and its derivative, we can obtain

$$\begin{pmatrix} x \\ x' \end{pmatrix} = M \begin{pmatrix} x_i \\ x_i' \end{pmatrix} = \begin{pmatrix} M_{11} & M_{12} \\ M_{21} & M_{22} \end{pmatrix} \begin{pmatrix} x_i \\ x_i' \end{pmatrix} \tag{3.7}$$

where M is the transport matrix and

$$\begin{aligned} M_{11} &= \sqrt{\frac{\beta_m}{\beta_{mi}}}(\cos\phi + \alpha_{mi}\sin\phi) \\ M_{12} &= \sqrt{\beta_m\beta_{mi}}\sin\phi \\ M_{21} &= \frac{(\alpha_{mi} - \alpha_m)\cos\phi - (1 + \alpha_{mi}\alpha_m)\sin\phi}{\sqrt{\beta_m\beta_{mi}}} \\ M_{22} &= \sqrt{\frac{\beta_{mi}}{\beta_m}}(\cos\phi - \alpha_m\sin\phi) \end{aligned} \tag{3.8}$$

The geometric emittance is defined as

$$\epsilon = \sqrt{\langle x^2\rangle \langle x'^2\rangle - \langle xx'\rangle^2} \tag{3.9}$$

where $\langle\rangle$ is the ensemble average. It then follows that (see Appendix D.1 for details)

$$\begin{aligned} \langle x^2\rangle &= \langle (M_{11}x_i + M_{12}x_i')^2\rangle \\ &= \epsilon_i\beta_m(A + B_1C + B_2S), \end{aligned} \tag{3.10}$$

where:

$$
\begin{aligned}
A &= \frac{\beta_i\gamma_{mi} + \gamma_i\beta_{mi} - 2\alpha_i\alpha_{mi}}{2}, \\
B_1 &= \frac{\beta_i}{\beta_{mi}} - A = \frac{\beta_i}{\beta_{mi}} - \frac{\beta_i\gamma_{mi} + \gamma_i\beta_{mi} - 2\alpha_i\alpha_{mi}}{2}, \\
B_2 &= \frac{\beta_i}{\beta_{mi}}\alpha_{mi} - \alpha_i, \\
C &= \int d\phi f_\phi(\phi)\cos 2\phi, \\
S &= \int d\phi f_\phi(\phi)\sin 2\phi,
\end{aligned}
\tag{3.11}
$$

and $\epsilon_i = \sqrt{\langle x_i^2\rangle \langle x_i'^2\rangle - \langle x_i x_i'\rangle^2}$, $\beta_i = \langle x_i{}^2\rangle / \epsilon_i$, $\gamma_i = \langle x_i'^2\rangle / \epsilon_i$, $\alpha_i = -\langle x_i x_i'\rangle / \epsilon_i$ are the beam's initial geometric emittance and C-S parameters, $\gamma_m = (1+\alpha_m^2)/\beta_m$, and $f_\phi(\phi)$ is the distribution function for the beam particles' phase advance. For a beam with no energy spread, $f_\phi(\phi) = \delta(\phi - \phi_0)$ where $\phi_0 = \int_0^z k_\beta(s)ds = \int_0^z \frac{\omega_p(s)}{\sqrt{2}\gamma_c}ds$.

We can also obtain

$$
\begin{aligned}
\langle x'^2\rangle = \epsilon_i\Big[&A\gamma_m + \frac{-B_1 - 2B_2\alpha_m + B_1\alpha_m^2}{\beta_m}C \\
&+ \frac{-B_2 + 2B_1\alpha_m + B_2\alpha_m^2}{\beta_m}S\Big]
\end{aligned}
\tag{3.12}
$$

and

$$
\langle xx'\rangle = -\epsilon_i[A\alpha_m + (B_1\alpha_m - B_2)C + (B_2\alpha_m + B_1)S] \tag{3.13}
$$

Using equations (3.10)-(3.13), and noting that A, B_1 and B_2 satisfy $B_1^2 + B_2^2 = A^2 - 1$, we can obtain an analytical expression of emittance growth for arbitrary $f_\phi(\phi)$ with small energy spread

$$
\begin{aligned}
\epsilon &= \sqrt{\langle x^2\rangle \langle x'^2\rangle - \langle xx'\rangle^2} \\
&= \epsilon_i\sqrt{A^2 - (A^2-1)(C^2+S^2)}
\end{aligned}
\tag{3.14}
$$

We denote the average relativistic factor of the beam as $\bar{\gamma}$. When the relative energy spread of the beam is very small (i.e. for every particle $|\Delta\gamma| = |\gamma - \bar{\gamma}| \ll \bar{\gamma}$), the particle's phase advance in the plasma ϕ will become $\phi(\gamma) = \bar{\phi} - \frac{\bar{\phi}}{2\bar{\gamma}}\Delta\gamma$, where $\bar{\phi} = \phi(\bar{\gamma})$ (See Appendix D.3 for details). Assuming a Gaussian energy distribution, for the beam particles we have:

$$f_\gamma(\gamma) = \frac{1}{\sqrt{2\pi}\sigma_\gamma} \exp\left[-\frac{(\gamma - \bar{\gamma})^2}{2\sigma_\gamma^2}\right] \tag{3.15}$$

As a result, ϕ will also have a Gaussian distribution

$$f_\phi(\phi) = \frac{1}{\sqrt{2\pi}\sigma_\phi} \exp\left[-\frac{(\phi - \bar{\phi})^2}{2\sigma_\phi^2}\right] \tag{3.16}$$

where

$$\sigma_\phi = \frac{\bar{\phi}}{2}\frac{\sigma_\gamma}{\bar{\gamma}} \tag{3.17}$$

$\frac{\sigma_\gamma}{\bar{\gamma}}$ is the relative energy spread of the beam. With this Gaussian distribution of ϕ, we can obtain:

$$C = \exp\left(-2\sigma_\phi^2\right)\cos\left(2\bar{\phi}\right), \quad S = \exp\left(-2\sigma_\phi^2\right)\sin\left(2\bar{\phi}\right) \tag{3.18}$$

Inserting (3.18) into (3.14) and using (3.17), we get an analytical expression of emittance growth for a beam that has a Gaussian energy distribution with a small energy spread:

$$\frac{\epsilon}{\epsilon_i} = A\sqrt{1 - \frac{A^2 - 1}{A^2}\exp\left[-(\frac{\sigma_\gamma}{\bar{\gamma}}\bar{\phi})^2\right]} \tag{3.19}$$

where $\frac{\sigma_\gamma}{\bar{\gamma}}$ is the normalized energy spread, and $\bar{\phi} = \frac{1}{\sqrt{2\bar{\gamma}}c}\int_0^z \omega_p(s)ds$ is the phase change of an electron with energy $\bar{\gamma}$ after it propagates for a longitudinal distance of z inside the plasma. Note that for large $\bar{\phi}$, $\epsilon/\epsilon_i \to A$. Under the assumption that the beam's energy, $\bar{\gamma}$, does not change, it follows that

$$\frac{\epsilon}{\epsilon_i} = \frac{\bar{\gamma}\epsilon}{\bar{\gamma}\epsilon_i} \approx \frac{\epsilon_n}{\epsilon_{ni}} \tag{3.20}$$

where $\epsilon_n = \frac{1}{m_e c}\sqrt{\langle x^2\rangle \langle p_x^2\rangle - \langle x p_x\rangle^2}$ is the normalized emittance and p_x is the transverse momentum of the particle. This means the normalized emittance growth is approximately the same as the geometric emittance growth. Note that in order to keep the analysis tractable we have only kept the effects of the energy spread in the betatron phase advance and not on the amplitude of the betatron oscillation in the elements of the transport matrix. The amplitudes are functions of the local values of the C-S parameters while the phase is an integral in z over $1/\beta_m$. Therefore, only the phase terms can deviate substantially between particles with small energy differences. Thus, the small amplitude oscillation of the emittance seen in Ref. [42] when a matched beam has finite energy spread is absent here.

In Fig. 3.2, we compare the theoretical results from (3.19) with QuickPIC [60, 61] simulation results. We choose a plasma density profile $n_p(z) = \frac{n_{p0}}{(1+z/l)^2}$, for which the adiabatic condition is independent of z. In the simulation, we turn off the longitudinal acceleration for the beam particles (i.e. the energy of the beam particle essentially does not change), and choose appropriate beam parameters to make the simulation in the blowout regime. Figure 3.2(a) shows that when the beam is initially matched, the beam's emittance is a constant during its propagation inside the plasma. As shown in Fig. 3.2(b)(c)(d), if the beam is not initially matched, the theoretical results based on the WKB solution agree with the simulation result very well.

Note that in Eq. (3.19), $A \geqslant 1$ is always true (see the Appendix D.2); therefore $\epsilon/\epsilon_i \leqslant A$. When the beam propagates in the plasma for a very long distance, $\bar{\phi}$ will become very large, and the beam will evolve to a saturated emittance:

$$\frac{\epsilon_{sat}}{\epsilon_i} = A = \frac{\beta_i\gamma_{mi} + \gamma_i\beta_{mi} - 2\alpha_i\alpha_{mi}}{2} \tag{3.21}$$

For the special case when the plasma is uniform along z, we have $\alpha_m = \alpha_{mi} = 0$, so $\gamma_m = \gamma_{mi} = 1/\beta_{mi}$, from which it follows,

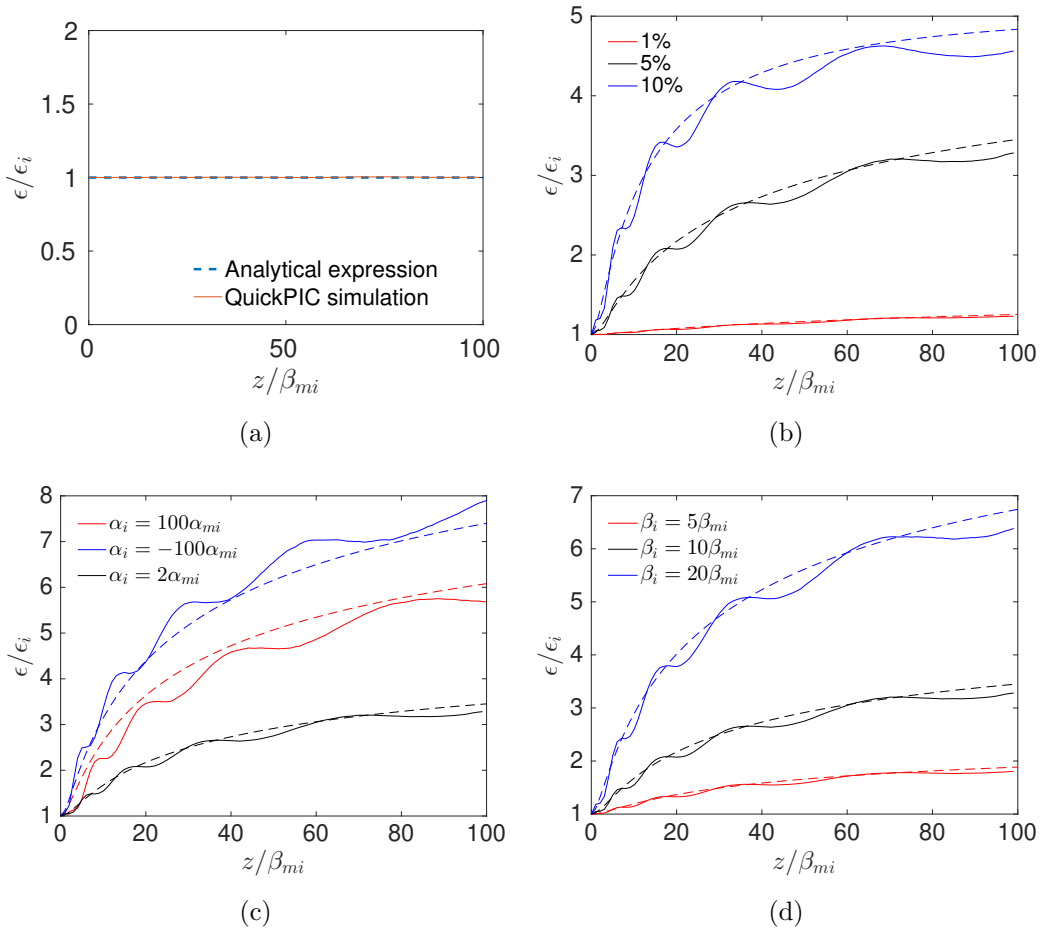

Figure 3.2: Emittance evolution in plasma ramp: $n_p(z) = \frac{n_{p0}}{(1+z/l)^2}$ ($l = 5$, l and z are normalized to β_{mi}). For (a) the beam is initially matched: $\beta_i = \beta_{mi}$, $\alpha_i = \alpha_{mi} = -\frac{1}{2l} = -0.1$, and the beam has a 5% energy spread. For (b) the beam is initially unmatched: $\beta_i = 10\beta_{mi}$, $\alpha_i = 2\alpha_{mi}$, and the beam has 1%, 5%, 10% initial energy spreads respectively. For (c) the beam is initially unmatched: $\beta_i = 10\beta_{mi}$, $\alpha_i = 2\alpha_{mi}, 100\alpha_{mi}, -100\alpha_{mi}$ respectively, and the beam has a 5% energy spread. For (d) the beam is initially unmatched: $\alpha_i = 2\alpha_{mi}$, $\beta_i = 5\beta_{mi}, 10\beta_{mi}, 20\beta_{mi}$ respectively, and the beam has a 5% energy spread. In (b)(c)(d), the solid lines are from QuickPIC simulations, and the dashed lines are from the analytical expression (3.19). In these three plots, the solid black lines correspond to the same simulation result, and the dashed black lines correspond to the same analytical expression.

$$A = \frac{\gamma_i \beta_{mi} + \beta_i / \beta_{mi}}{2} \tag{3.22}$$

Therefore, the emittance growth in a longitudinally uniform plasma will be

$$\frac{\epsilon}{\epsilon_i} = \frac{\gamma_i \beta_{mi} + \beta_i / \beta_{mi}}{2} \times \sqrt{1 - \frac{(\gamma_i \beta_{mi} + \beta_i / \beta_{mi})^2 - 4}{(\gamma_i \beta_{mi} + \beta_i / \beta_{mi})^2} \exp\left[-(\frac{\sigma_\gamma}{\bar{\gamma}} \bar{\phi})^2 \right]} \tag{3.23}$$

which is mathematically equivalent to equation (7) in [78], and similar to equation (1) in [41] (difference is due to the different assumptions for $f_\phi(\phi)$).

We define the beam to be initially matched when

$$\alpha_i = \alpha_{mi},\ \beta_i = \beta_{mi},\ \gamma_i = \gamma_{mi} \tag{3.24}$$

for which $A = 1, B_1 = 0, B_2 = 0$. Therefore, from equations (3.10) - (3.13) and (3.19), we have $\langle x^2 \rangle / \epsilon_i = \beta_m$, $\langle x'^2 \rangle / \epsilon_i = \gamma_m$, $- \langle x x' \rangle / \epsilon_i = \alpha_m$ and $\epsilon = \epsilon_i$. Therefore, $\beta = \langle x^2 \rangle / \epsilon = \beta_m$, $\gamma = \langle x'^2 \rangle / \epsilon = \gamma_{mi}$, and $\alpha = - \langle x x' \rangle / \epsilon = \alpha_m$. Therefore, with an adiabatic plasma density profile, when neglecting the beam's energy change, if the beam is initially matched, the beam's C-S parameters along z will be $\beta_m, \gamma_m, \alpha_m$, and the beam's geometric emittance will not change. We can therefore interpret β_m, α_m defined in (3.5) and γ_m as the matched C-S parameters.

If the beam's initial C-S parameters deviate from the matched ones, i.e.,

$$\alpha_i = \alpha_{mi} + \Delta\alpha,\ \beta_i = \beta_{mi} + \Delta\beta \tag{3.25}$$

where $|\Delta\alpha| \ll 1$ and $|\Delta\beta|/\beta_{mi} \ll 1$, then it follows that,

$$A \approx 1 + \frac{1}{2}\Delta\alpha^2 + \frac{\gamma_{mi}}{2\beta_{mi}}\Delta\beta^2 - \frac{\alpha_{mi}}{\beta_{mi}}\Delta\alpha\Delta\beta \tag{3.26}$$

Inserting this into (3.19) gives

$$\frac{\epsilon}{\epsilon_i} \approx 1 + (\frac{1}{2}\Delta\alpha^2 + \frac{\gamma_{mi}}{2\beta_{mi}}\Delta\beta^2 - \frac{\alpha_{mi}}{\beta_{mi}}\Delta\alpha\Delta\beta)[1 - e^{-(\frac{\sigma_\gamma}{\bar{\gamma}}\bar{\phi})^2}] \tag{3.27}$$

We can also get the expression for β from the above equations. Inserting (3.18) into (3.10) and using (3.17) leads to

$$\langle x^2 \rangle = \epsilon_i \beta_m \left\{ A + \left[B_1 \cos\left(2\bar{\phi}\right) + B_2 \sin\left(2\bar{\phi}\right) \right] e^{-\frac{1}{2}(\frac{\sigma_\gamma}{\bar{\gamma}}\bar{\phi})^2} \right\} \tag{3.28}$$

Dividing both sides by ϵ and using (3.19) gives

$$\beta = \beta_m \frac{A + \left[B_1 \cos\left(2\bar{\phi}\right) + B_2 \sin\left(2\bar{\phi}\right) \right] \exp\left[-\frac{1}{2}(\frac{\sigma_\gamma}{\bar{\gamma}}\bar{\phi})^2 \right]}{A\sqrt{1 - \frac{A^2-1}{A^2}\exp\left[-(\frac{\sigma_\gamma}{\bar{\gamma}}\bar{\phi})^2 \right]}} \tag{3.29}$$

If there is no energy spread ($\sigma_\gamma = 0$), this equation can be simplified to

$$\beta = \beta_m \left[A + B_1 \cos(2\phi) + B_2 \sin(2\phi) \right] \tag{3.30}$$

which is similar in form to Eq. (11) in [42] but with different coefficients.

3.3 On minimizing the emittance growth for a fixed beam

In the previous section, it was shown that the beam emittance will be preserved as long as the beam satisfies the matching condition (equation (3.24)). In this case $\beta^* = 1/\gamma_{mi}$ (β^* is β when $\alpha = 0$) which we define as the matched β^*, i.e., β^*_m. It was also shown how the emittance grows if the beam is slightly mismatched as might be the case if there are shot to shot variations of the beam and/or plasma conditions. In addition, in a controlled experiment that might for example be conducted at FACET II [90], the beam emittance and optics are relatively fixed so that β^* can be assume to be fixed. However, for a given plasma profile the plasma conditions at the plasma entrance are such that it will not be possible to match a beam with a given β^* (i.e. $\beta^* \neq \beta^*_m$). It is therefore useful to determine the best location to focus such a beam. This is defined to be the focal position in vacuum ($z = s$)

that minimizes the emittance growth for a given beam and plasma profile, assuming the plasma entrance is at $z = 0$. Therefore,

$$\alpha(s) = 0,\ \beta(s) = \beta^* \tag{3.31}$$

where β^* is β at the focal plane in vacuum. According to the evolution of C-S parameters in a drift space [74], the beam's initial C-S parameters at the plasma entrance ($z = 0$) are

$$\alpha_i = \alpha(0) = \frac{s}{\beta^*},\ \beta_i = \beta(0) = \beta^* + \frac{s^2}{\beta^*},\ \gamma_i = \gamma(0) = \frac{1}{\beta^*} \tag{3.32}$$

Using equation (3.19), we can calculate the emittance growth using the above initial condition, and find the optimal s defined to be when $d\epsilon/ds = 0$. For a fixed plasma density profile, $d\epsilon/ds = 0$ reduces to $dA/ds = 0$, which gives us the optimal s,

$$s_o = \frac{\alpha_{mi}}{\gamma_{mi}} \tag{3.33}$$

This optimal $s = s_o$ is actually the focal position in vacuum for the matched beam (whose initial C-S parameters at the plasma entrance are α_{mi}, β_{mi} and γ_{mi}). In other words, by putting the unmatched beam's focal plane at the same position as the matched beam's focal plane in vacuum, the unmatched beam will have minimal emittance growth in the plasma. We can calculate this minimal emittance growth by evaluating A using the initial C-S parameters from (3.32) and (3.33), giving $A = A_o \equiv \frac{1}{2}(\beta^*\gamma_{mi} + \frac{1}{\beta^*\gamma_{mi}})$. We then insert this into (3.19) to get the minimal emittance growth, which approaches A for large $\bar{\phi}$.

If the witness beam's focal plane in vacuum deviates from the the optimal position (3.33): $s = s_o + \Delta s$, from (3.32) and (3.33) we can obtain:

$$A = A_o + \frac{\gamma_{mi}}{2\beta^*}\Delta s^2 \tag{3.34}$$

We can see that for $s = s_o + \Delta s$ and $s = s_o - \Delta s$, the corresponding A are the same, so according to (3.19), the emittance growth are the same as well. In other words, the emittance growth as a function of s is symmetric about $s = s_o$.

If we assume Δs is a small quantity, then for a fixed z we get,

$$\frac{\epsilon}{\epsilon_i} \approx \frac{\epsilon_o}{\epsilon_i} + \left\{1 - \exp\left[-(\frac{\sigma_\gamma}{\bar{\gamma}}\bar{\phi})^2\right]\right\} \frac{A_o}{\epsilon_o/\epsilon_i} \frac{\gamma_{mi}}{2\beta^*} \Delta s^2 \tag{3.35}$$

where $\epsilon_o \equiv \epsilon(A_o)$ is the emittance when $\Delta s = 0$ (or $s = s_o$).

This analysis also permits examining how the shot to shot variance of the plasma density at the entrance of the profile affects the emittance growth (essentially A), assuming the beam profile and the position of the plasma entrance (β^* and s) are fixed. From equation (3.21) and the relation $\gamma_{mi} = (1 + \alpha_{mi}^2)/\beta_{mi}$, we have

$$A = \frac{\beta_i(1 + \alpha_{mi}^2)/\beta_{mi} + \gamma_i\beta_{mi} - 2\alpha_i\alpha_{mi}}{2} \tag{3.36}$$

Since we assume the beam profile and the position of the plasma entrance are fixed, from equation (3.32) we know α_i, β_i, γ_i are fixed. The shot to shot changes to the plasma profile lead to the variances of α_{mi} and β_{mi}, which leads to the first order variance of A:

$$\begin{aligned} \delta A_1 &= \frac{\partial A}{\partial \alpha_{mi}}\delta\alpha_{mi} + \frac{\partial A}{\partial \beta_{mi}}\delta\beta_{mi} \\ &= (\frac{\beta_i}{\beta_{mi}}\alpha_{mi} - \alpha_i)\delta\alpha_{mi} + \frac{1}{2}(\gamma_i - \gamma_{mi}\frac{\beta_i}{\beta_{mi}})\delta\beta_{mi} \end{aligned} \tag{3.37}$$

Importantly, we can see that at the matching point, the variance of α_{mi} and β_{mi} will not cause the variance of A to the first order. The second order variation of A is

$$\delta A_2 = \frac{1}{2}\delta\alpha_{mi}^2 + \frac{\gamma_{mi}}{2\beta_{mi}}\delta\beta_{mi}^2 - \frac{\alpha_{mi}}{\beta_{mi}}\delta\alpha_{mi}\delta\beta_{mi} \tag{3.38}$$

which is consistent with equation (3.26). Essentially, variations can arise from either the plasma profile or beam profile at the plasma entrance.

Next we carry out some QuickPIC simulations using plasma and beam parameters that are close to the ones in the proposed FACET II experiment, while satisfying all the theoretical assumptions (adiabatic plasma profile, azimuthal symmetry in plasma wake, etc). More details for the parameters are given in the next section. We turn off the longitudinal push in the simulation so that the beam has no longitudinal acceleration. The plasma density profile

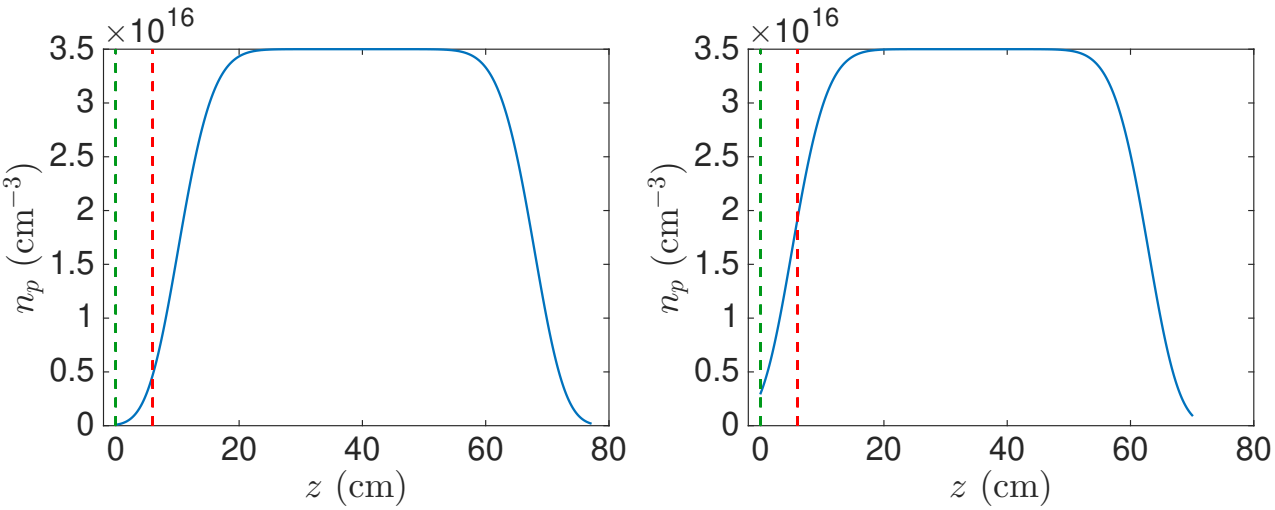

(a) (b)

Figure 3.3: Plasma density profile. The green dashed line is the entrance of the plasma, and the red dashed line is the position of the witness beam's focal plane in vacuum. The beams propagate to the right in the plot. (a) The FACET II plasma density profile. (b) The profile used for the simulation results in Fig. 3.4. Only the region between 5 cm and 75 cm of the profile in (a) is used. In this region the adiabatic condition is always satisfied.

we use is shown in Fig. 3.3(b). This profile is the region between 5 cm (entrance) and 75 cm (exit) of the full profile (Fig. 3.3(a)) which has a ramp, a plateau with $n_0 = 3.5 \times 10^{16}\text{cm}^{-3}$ and a downramp. The adiabatic condition ($|\alpha_m| < 1$) is now satisfied throughout the entire profile. At the entrance and exit $|\alpha_m| = 0.24$ and 0.56 respectively. In addition, $\alpha_{mi} = 0.24$, $\beta_{mi} = 0.0194$ m for the simulation. The theory could be easily modified to include a matching section [41] or a perturbative section as in [42] in front of 5 cm and after 75 cm. We use a non-evolving symmetric drive beam to create a well formed ion bubble, and the witness beam is the same as the one in FACET II (See Table I and II). Fig. 3.4 shows the simulation results and the good agreement between the simulations and the theory. It also shows that the expression for emittance growth in a uniform plasma (Eq. (3.23)) cannot describe the emittance growth in an adiabatic plasma precisely.

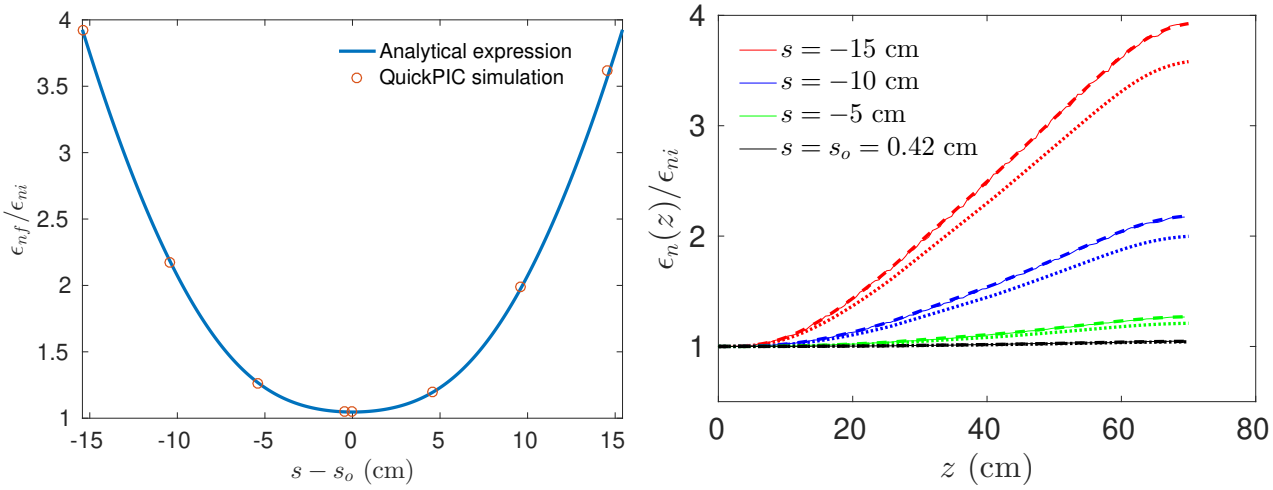

(a) (b)

Figure 3.4: Witness beam's emittance growth for different focal planes, s, in the adiabatic plasma in Fig. 3.3(b). (a) The ratio of final emittance (at the plasma exit) to the initial emittance (at the plasma entrance) for different cases. (b) The evolution of ϵ_n inside the plasma for 4 different cases, corresponding to the 4 orange spots for $s - s_o \leq 0$ in (a). The solid lines are from QuickPIC simulations, the dashed lines are from expression (3.19), and the dotted lines are from expression (3.23).

3.4 Emittance evolution in preformed plasma using FACET II parameters

In this section we examine the emittance evolution in the full profile shown in Fig. 3.3(a). We use a shows a possible set of beams parameters for the two-bunch FACET II experiments described in Table 3.1 and 3.2.

	Energy(GeV)	Q(nC)	$\sigma_z(\mu m)$	$\epsilon_{n_x}(\mu m)$	$\epsilon_{n_y}(\mu m)$
Drive	10	1.6	6.4	3.4	3.0
Witness	10	0.5	5.0	3.15	3.15

Table 3.1: Possible beam parameters for two-bunch PWFA experiment at FACET II

	α_x	α_y	$\beta_x(m)$	$\beta_y(m)$
Drive Beam	59	12	127	27
Witness Beam	40	40	80	80

Table 3.2: The C-S parameters of both beams at the exit of the final focusing magnet.

Both beams are tri-Gaussian with $n_b = \frac{N}{(2\pi)^{\frac{3}{2}}} e^{-\frac{x^2}{2\sigma_x^2}} e^{-\frac{y^2}{2\sigma_y^2}} e^{-\frac{z^2}{2\sigma_z^2}}$. The σ_z is the rms pulse length for the beam, and ϵ_{n_x} and ϵ_{n_y} are the normalized emittance in x, y directions respectively. The distance between the centers of the drive and witness beam is 150 μm. The initial relative rms energy spread for both beams is 0.25%. Table 3.2 shows the C-S parameters for both beams at the exit of the final focusing magnet. Note that in this setup the drive beam is asymmetric and the witness beam is symmetric, so the wake felt by the witness beam is not azimuthally symmetric and thus the two planes are coupled.

The plasma density profile in the simulation is shown in the Fig. 3.3(a), which is close to the plasma density profile of the lithium source used in the FACET II experiment. This density profile comes from experimental data, given by two long arrays (z and $n_p(z)$). It is not

exactly symmetric, although it appears to be. The peak plasma density is $3.5 \times 10^{16}\text{cm}^{-3}$, which is chosen to ensure that the witness beam is located inside the bubble wake at a position that flattens the accelerating field (as shown in Fig. 3.1).

With such a plasma density profile, the initial matched C-S parameters for the witness beam at the plasma entrance are:

$$\alpha_{mi} = 0.916,\ \beta_{mi} = 0.068\text{m} \tag{3.39}$$

These parameters are not calculated directly from Eq. (3.5) at $z = 0$ because the plasma near the entrance does not satisfy the adiabatic condition Eq. (3.6). Instead, they are obtained by neglecting any energy spread, and integrating the following equation (See appendix D.4 for derivation) for β,

$$\frac{1}{2}\beta(z)\beta''(z) - \frac{1}{4}\beta'(z)^2 + \beta(z)^2 k_\beta(z)^2 = 1\ , \alpha(z) = -\frac{1}{2}\beta'(z) \tag{3.40}$$

from the flat-topped region (plateau) of the plasma back to the entrance of the plasma with initial C-S parameters $\beta = \sqrt{2\bar{\gamma}}\frac{c}{\omega_p}$, $\alpha = 0$ (where ω_p is the plasma frequency for the flat-topped plasma) [90]. According to the matched parameters given in Eq. (3.39), the optimal s for the plasma density profile can be calculated from Eq. (3.33), $s = s_o = 3.39$ cm. Figure 3.5 shows the evolution of β for the real witness beam when its focal plane in vacuum is located at a different $s = s_o + \Delta s$. The solid red line is the case if the witness beam was initially matched to the plasma profile. We can see that for a matched beam β evolves smoothly and stays constant in the uniform plasma region while for an unmatched beam the beam's β will oscillate. We note that Eq. (3.40) could also be integrated to obtain the matching conditions even if the density goes to 0 at the entrance (and exit) of the density profile.

Next, we run QuickPIC simulations in which we vary s but with the same beams as described in Table 3.1 and 3.2. This time we turn on the longitudinal push in the simulation so the witness beam is gaining energy. Figure 3.6(a) shows the normalized emittance growth

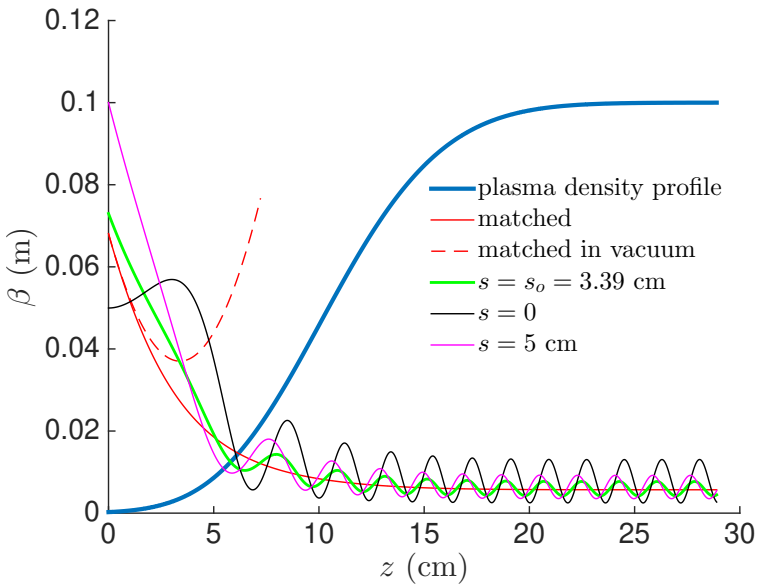

Figure 3.5: The evolution of β for the witness beam for different s from numerical calculation. The plasma density profile is in arbitrary units.

at the exit of the plasma when the witness beam's focal plane in vacuum is located at s = -10, -5, 0, 3.39, 5, 10, 15, 20 cm (note that negative s means the focal plane of the witness beam is outside the plasma). We can clearly see that the optimal s for minimizing the emittance growth is at $s = 3.39$ cm. This illustrates that experiments can be performed at FACET II that provide easily measurable differences in the emittance growth as the focal point is changed.

We note that the different emittance growth in x and y directions is caused by the asymmetry of the drive beam, which excites asymmetric wakefields that have different linear focusing forces in x and y directions [55]. We note that even though the plasma and the beam parameters used in these simulations do not satisfy the assumptions we made in the previous sections (the drive beam is asymmetric and the plasma near the entrance and the exit is not adiabatic), Eq. (3.33) still appears to predict the optimal focal position of the witness beam very well, although the initial matched C-S parameters α_{mi}, β_{mi} are calculated in a different manner. Figure 3.6(b) shows the evolution of witness beam's ϵ_{n_x} along z. We

can see that when $s = 3.39$ cm, ϵ_{n_x} is almost preserved although the beam is not initially matched.

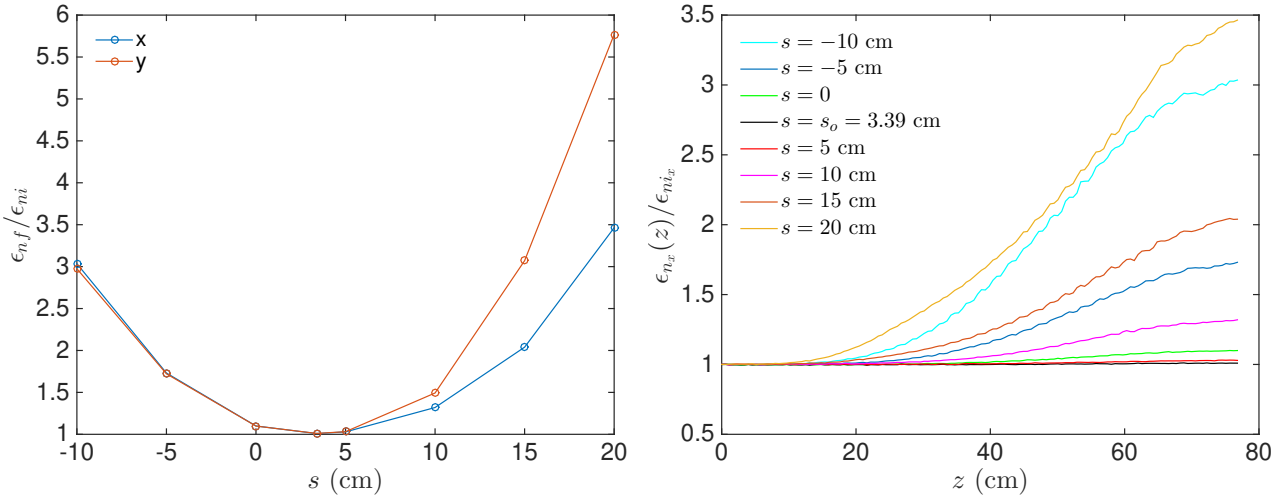

(a) (b)

Figure 3.6: The normalized emittance growth of the witness beam for different s. (a) The ratio of final emittance (at the plasma exit) to the initial emittance (at the plasma entrance) for different cases. (b) The evolution of ϵ_{n_x} inside the plasma for different cases, corresponding to the blue line in (a).

3.5 Emittance evolution in lithium plasma with helium buffer gas

In FACET II experiments, lithium will be one of the choices for the plasma source. The hot lithium vapor will be confined and cooled at each end by the helium buffer gas [14, 15]. The plasma is generated by the intense electric field of the drive/witness beams when they pass through and ionize the lithium vapor. In the previous section, we simulated the beams evolving in a preformed and radially uniform plasma. In this section, we use QuickPIC to simulate the emittance evolution when the plasma is self-formed by field ionization of a neutral gas from the intense electric field of the drive and witness beams. Fig. 3.7 shows the profile for the lithium gas and the helium buffer gas in our simulation.

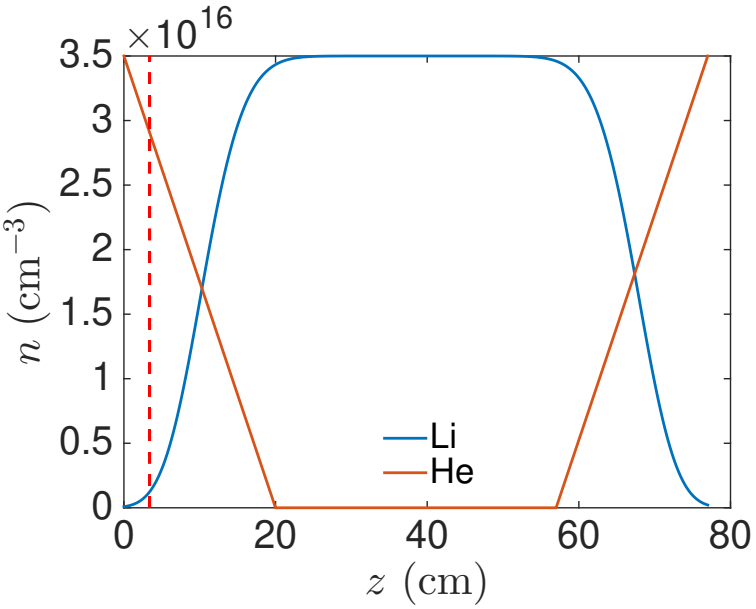

Figure 3.7: Helium and lithium gas density profile. The red dashed line is the position of the witness beam's focal plane: $z = 3.39$ cm

The blue line in Fig. 3.7 is the lithium gas density, which is the same as the profile shown in Fig. 3.3(a) in the previous section. There are two linear helium ramps (orange line in Fig. 3.7) at the entrance and exit of the lithium gas. The beam parameters are the same as described in the previous section, and we choose the optimal value $s = 3.39$ cm for the witness beam's focal position in vacuum. Fig. 3.8(a) shows the witness beam's emittance evolution inside the plasma. We can see that in the beginning and the end of the simulation, emittance growth occurs. In the middle of the lithium region where there is no helium, the emittance essentially stays the same.

The reason for the large emittance growth is that the beams can ionize the helium buffer gas which results in a nonlinear focusing force inside the bubble. Fig. 3.9(a) shows the helium ion density snapshot when the beams propagate for 1 cm in the plasma. The drive beam's center is located at $\xi = -5.27$, and the witness beam's center is located at $\xi = 0$. Both beams are propagating from right to left. The drive beam enters the plasma with a larger spot size than the witness beam, so it can only ionize a part of the neutral helium

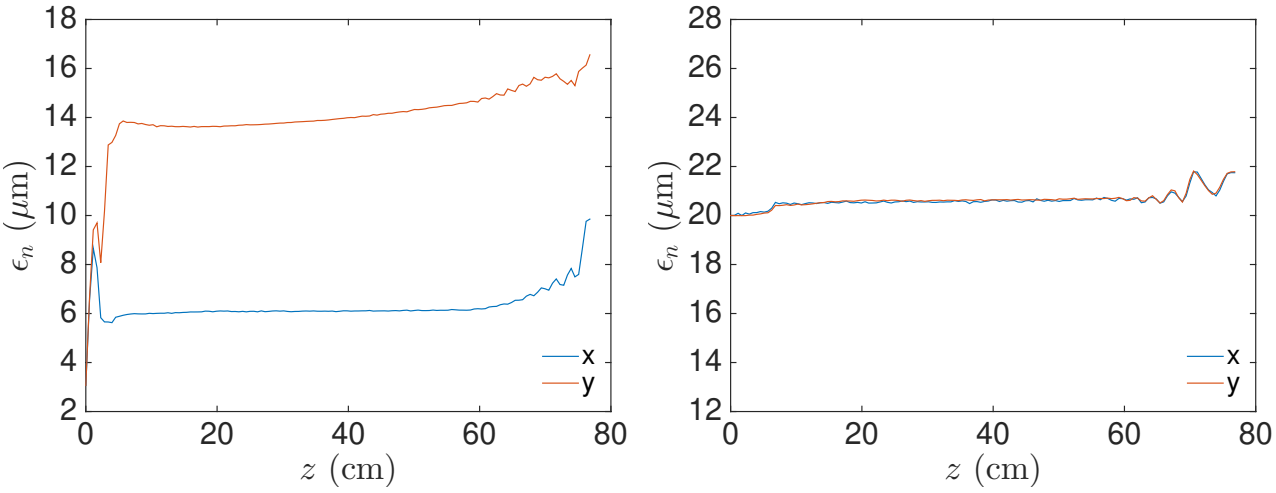

(a) (b)

Figure 3.8: The evolution of normalized emittance of the witness beam: (a) We use the same parameters as we used in the preformed plasma simulation in the previous section: Drive beam: $\epsilon_{n_x} = 3.4$ μm, $\epsilon_{n_y} = 3.0$ μm, witness beam: $\epsilon_{n_x} = \epsilon_{n_y} = 3.15$ μm. (b) We increase the initial emittance for both beams to 20 μm (in both x and y directions).

while the witness beam can ionize most of the neutral helium around it. Fig. 3.9(b) shows the focusing fields felt by the witness beam at different ξ at the same propagation distance as Fig. 3.9(a). The focusing fields felt by the witness beam is no longer linear when helium is ionized by itself. Therefore, the witness beam has a large emittance growth in the region where the helium gas is ionized. In the region where there is only lithium, the witness beam will still feel a linear focusing force and its emittance only grows because the witness beam is no longer matched in the uniform region of lithium plasma, which causes a much smaller growth than that from the region where helium gas exists.

In order to avoid the emittance growth in the lithium plasma source, we can increase the initial emittances for both the drive beam and witness beam. In Fig. 3.8(b), we show the QuickPIC simulation results when using an initial beam emittance of 20 μm while keeping the other parameters the same as the simulation shown in Fig. 3.8(a). When the initial beam emittance becomes larger, the initial spot sizes of both beams will increase, and the Coulomb

field around the beam will become smaller. Therefore, when the beams pass through the helium buffer gas, the neutral helium is weakly ionized. However, the lithium can still be ionized and form the plasma wake because lithium has a lower ionization energy than helium. When there is no helium ionization, the focusing force felt by the witness beam is linear, and its emittance barely grows, as shown in Fig. 3.8(b). The small emittance growth at the exit of the plasma in Fig. 3.8(b) is still caused by the helium ionization because the witness beam enters into the exit ramp of helium with a smaller spot size compared to its initial spot size at the entrance of the plasma.

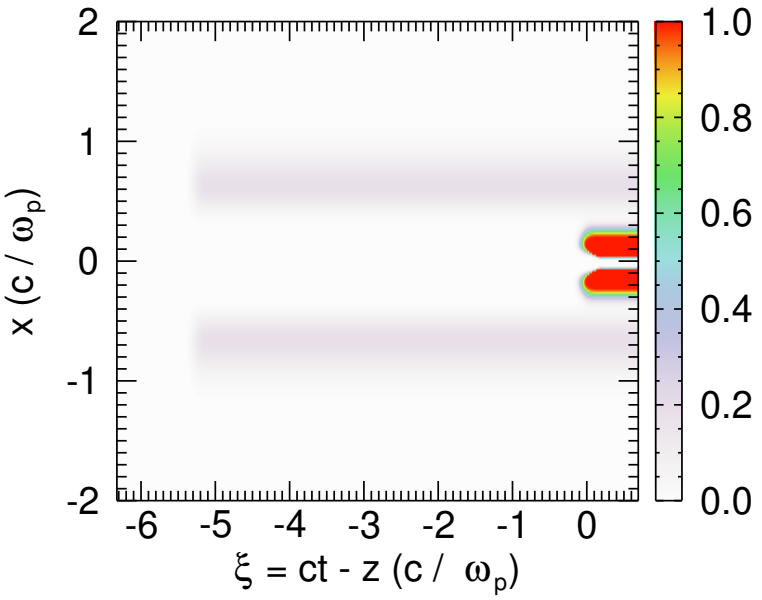

(a)

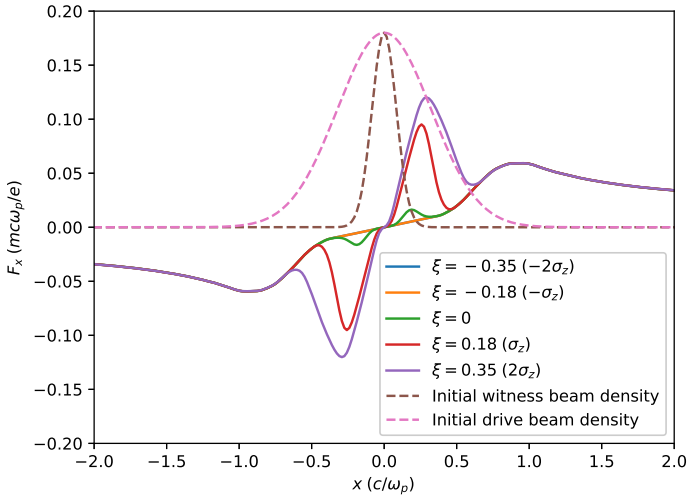

(b)

Figure 3.9: (a) Helium ion charge density. The grey area is the helium ions produced by the drive beam, and the red area is the helium ions produced by the witness beam. (b) The F_x transverse lineouts at different longitudinal positions, ξ, and the initial beam density profiles (in arbitrary units).

3.6 Conclusion

We have used theory and QuickPIC simulations to examine the evolution of the emittance and the C-S parameters of particle beams in plasmas whose density is changing adiabatically. We use the WKB solution for each particle and assume the energy of each particle in the beam does not change to obtain an analytical expression for the beam's emittance evolution in an arbitrary adiabatic plasma density profile in a nonlinear PWFA. When the beam has no initial energy spread, its emittance will remain nearly constant in the azimuthally symmetric blowout regime. When there is an initial energy spread, the beam's emittance can be preserved as long as its initial C-S parameters are matched to the density profile of the plasma ramp. We also use this expression to analyze the emittance growth when the position of the witness beam's focal plane in vacuum is changed while keeping the beam parameters and the plasma density profile fixed. When the beam cannot be matched, the emittance growth can be minimized by focusing the unmatched beam to the same vacuum focal plane position as the matched beam. We used QuickPIC simulations for possible FACET II beam parameters to show that the emittance can indeed be preserved very well when we choose the focal plane position to be the same as for a matched beam, even when the assumptions of symmetric blowout and adiabatic density evolution for the entire plasma region are not satisfied. For other focal plane positions, the witness beam's emittance is larger at the exit of the plasma.

In addition, we also examined through simulations the effect of additional self-ionization of the buffer gas by the drive beam. At FACET II a lithium gas is confined by a helium buffer gas. When the drive and/or witness beam emittance is small (around 3 μm), they can be focused to small enough spot sizes so that they can ionize the helium buffer gas. This will lead to the focusing fields felt by the witness beam to be strongly nonlinear. We find that this can potentially lead to the witness beam's emittance growing by a factor of 3 and 5 in the x and y planes respectively for sample FACET II parameters. The different growth

in x and y directions is caused by the asymmetry of the drive beam forming an asymmetric plasma wake. By using an initial emittance of 20 μm, the helium buffer gas is weakly ionized and the witness beam's emittance can be preserved very well.

CHAPTER 4

Emittance preservation in the presence of ion motion in a single stage of a plasma based acceleration linear collider

4.1 Introduction

As for Chapter 3, we offer an introduction for Chapter 4 that is repetitive but that makes the chapter fully self-contained. In plasma based acceleration (PBA) an intense drive particle or laser beam is used to form a plasma wake that accelerates a second electron/positron beam (the witness beam) that is properly loaded inside the wake. When a particle beam or laser beam creates the wake the process is referred to as plasma wakefield acceleration (PWFA) or laser wakefield acceleration (LWFA) respectively. In the blowout regime of PWFA [22] [23], where the drive beam is made of electrons, an azimuthally symmetric wakefield provides an ideal focusing force that is linear in transverse position r and independent of the longitudinal position $\xi = ct - z$, while the accelerating field is independent of r. For such conditions, a trailing beam with even a slice dependent energy spread can be matched to the focusing force thereby almost perfectly preserving the beam's slice and projected emittance [86]. The motion of a single particle in azimuthally symmetric ion column is given by the Hill like equation (see sections 2.2 and 2.3),

$$x'' + k_\beta^2 x = 0 \tag{4.1}$$

where $x' \equiv dx/dz$, $k_\beta \equiv k_p/\sqrt{2\gamma}$ is the betatron wave number, $k_p \equiv \omega_p/c$, ω_p is the plasma frequency, and c is the speed of light. The rms spot size of the beam, $\sigma \equiv \sqrt{\langle x^2 \rangle}$ evolves as (see section 2.6),

$$\sigma'' = \frac{\epsilon^2}{\sigma^3}(1 - k_\beta^2 \sigma^4/\epsilon^2) \tag{4.2}$$

where $\epsilon \equiv \sqrt{\langle x^2 \rangle \langle x'^2 \rangle - \langle x x' \rangle^2}$ is the beam's geometrical emittance. Thus, the beam's matched spot size in a linear focusing force is [90]

$$\sigma_m = \sqrt{\frac{\epsilon}{k_\beta}} = \sqrt{\sqrt{\frac{2}{\gamma}} \epsilon_n \frac{c}{\omega_p}} \tag{4.3}$$

where γ is the relativistic Lorentz factor of the beam and $\epsilon_n = \gamma\epsilon$ is beam's normalized emittance (which we hereafter refer to as emittance unless otherwise noted).

However, the beam's σ_m in the acceleration stage is typically much smaller than the conventional focusing optics can provide. Such a mismatch can lead to large emittance growth when there is any energy spread. To overcome this, it has been proposed to use a tailored short plasma ramp or an adiabatic plasma ramp [39, 40, 41, 42, 43, 89, 44] (also see Chapter 3) to transition the beam from a large spot size to a small matched spot size in the acceleration stage, while preserving the beam's emittance.

In order to build a TeV class linear collider, the luminosity $L = fN^2/4\pi\sigma_x\sigma_y$ must be as large as $\sim 10^{34}\,\mathrm{cm}^{-2}\mathrm{s}^{-1}$ (N is the number of particles in each colliding bunch, f is the repetition rate of collisions, and $\sigma_{x,y}$ is the spot size of the bunch at the interaction point). In order to achieve such a luminosity, a beam with ~ 1 nC charge and ~ 100 nm emittance is proposed [19]. For such a beam, the transverse Coulomb field for a matched spot size can pull the ions inward during the transit time of the beam [45] [46]. The resulting ion collapse on the axis can cause a longitudinally slice-dependent, transversely nonlinear focusing force, that can potentially result in large emittance growth. Simulations have shown that matching the beam directly to a uniform plasma causes $\sim$80% projected emittance growth for typical LC parameters [47].

Several ideas have been proposed and studied to mitigate the emittance growth even

further in the presence of ion motion. Ref.[48] proposed to use a plasma matching section with an adiabatically decreasing ion mass. Ref.[49] proposed slice-by-slice matching the transverse beam phase space distribution to the nonlinear ion motion-perturbed plasma wakefields. But these ideas may be difficult to realize experimentally. Ref.[50] proposed an adiabatic matching procedure where the beam is injected with a low enough energy that ion motion effects are initially small. However, this idea will only work at the initial stage.

In this chapter, we present a scheme that is able to achieve emittance preservation in the presence of ion motion that is applicable to high energy, high-density electron bunches required in a multi-stage plasma-based LC scenario. We use an adiabatic plasma density upramp to match the witness beam into the uniform density (plateau) acceleration stage, then using an adiabatic plasma density downramp to match the witness beam out from the density plateau. We show this method can almost perfectly preserve the witness beam emittance from start to end, even though there is a significant amount of ion motion triggered in the uniform acceleration stage. We also show that by properly choosing the beam's Courant-Snyder parameters at the plasma entrance, the emittance growth can be mitigated even for more general density ramps which are not adiabatic at lower densities.

4.2 Ion motion parameter

For a plasma based linear collider, the witness beam typically has a very low emittance and spot size, corresponding to a high density. The large space-charge field will induce the motion of background ions significantly during the time the witness beam passes by. In order to quantify how severe the ion motion is, we can introduce an ion motion parameter, which is defined to be the phase advance of a single ion. To lowest order, we can estimate the phase advance of an ion using a simple harmonic oscillation model [45] [46] . We assume near the axis, the witness beam is simply a uniform density cylinder with density n_{b0}. Since $n_{b0} \gg n_0$ (n_0 is the background plasma density) in the ion motion regime, we neglect the

self-consistent repelling fields between the ions and only consider the electric field of the witness beam. From Gauss's law the equation of motion for a single plasma ion initially located inside the beam is

$$r''(z) + k_i^2 r(z) = 0 \tag{4.4}$$

where

$$k_i = \sqrt{Z\frac{n_{b0}e^2}{2\epsilon_0 Mc^2}} = \sqrt{Z\frac{n_{b0}/n_0}{2M/m}}k_{p0} \tag{4.5}$$

$z = ct$ is the coordinate along the propagation direction, Z is the ion charge state, n_{b0} is the witness beam's peak density, ϵ_0 is the permittivity of free space, M is the mass of a single ion, $k_{p0} = \omega_{p0}/c$ is the plasma wavenumber, $\omega_{p0} = \sqrt{\frac{n_0 e^2}{\epsilon_0 m}}$ is the plasma frequency, n_0 is the plasma density, ϵ_0 is the vacuum permittivity, and e is the electron charge.

In this work we always use a wide drive bunch with a low peak density to avoid perturbing the background ions. Therefore, we only consider ion motion triggered by the witness beam. For the slice of the witness beam at the very front, there is no ion motion and thus the focusing force is linear. However, the space charge forces at the front will begin to pull the ions in, which will affect the later part of the beam. Thus, as we move from head to tail in the witness beam, the ion motion collapse is stronger. We can quantify the degree of ion motion through the phase advance parameter Φ for a given slice of the witness beam:

$$\Phi(\xi) = k_i \xi \tag{4.6}$$

where ξ is the longitudinal distance between the beam slice and the beam head. We choose $\xi = 0$ to be at the head of the beam). We can also define the ion motion parameter for the entire witness beam to be the ion motion parameter at the tail of the witness beam:

$$\Phi_b = \Phi(L_b) = k_i L_b \tag{4.7}$$

where L_b is the length of the witness beam. Qualitatively, ion motion is important when $\Phi_b \gtrsim 1$.

It is worth noting that for a beam with a longitudinal Gaussian density profile, the length of the beam L_b is not well defined. However, we can use the effective bunch length $L_b = \sqrt{2\pi}\sigma_z$ in the equation above to estimate the degree of ion motion.

It turns out Eq. (4.4) is fairly accurate when the phase advance of the ion is less than $\pi/2$ (before the first ion collapses), and it can therefore be used to accurately predict the location of the first ion density peak on the axis ($\frac{\pi}{2k_i}$).

4.3 Gaussian phenomenological model

For linear collider parameters, $k_i L_b \gg 1$, and the first ion density peak resides within the bunch. Therefore, the exact transverse profile of ion density is complicated and longitudinally slice-dependent. In order to study how a beam slice evolves in the nonlinear focusing force from the ion collapse, we model the ion collapse as a Gaussian function [47] (other functions can be used as well):

$$n_{ion}(r)/n_0 = 1 + A_0 \exp\left(-r^2/2\sigma_{ion}^2\right) \tag{4.8}$$

We note that this profile does not conserve charge, however, it is reasonable for radii within the beam. This model is parametrized by A_0 and σ_{ion}. The corresponding focusing force is:

$$F_r(r) = \left[-\frac{r}{2} - A_0\sigma_{ion}^2 \frac{1-\exp\left(-\frac{r^2}{2\sigma_{ion}^2}\right)}{r}\right] m_e\omega_{p0}^2 \tag{4.9}$$

In a later part of the paper, we will use this phenomenological model to gain insights for the evolution of a beam slice in a given nonlinear focusing force.

4.4 Emittance evolution in a uniform plasma

We begin by investigating how the emittance evolves for an unmatched beam focused to a density plateau.

4.4.1 Immobile ions

To set the stage for matching sections including ion motion, we review the concept of matching in a uniform plasma in the absence of ion motion (linear focusing force). From the beam's envelope equation (longitudinal acceleration is neglected):

$$\sigma_x'' = \frac{\epsilon^2}{\sigma_x^3}(1 - \bar{k}_\beta^2 \frac{\sigma_x^4}{\epsilon^2}) \tag{4.10}$$

where $\epsilon = \sqrt{\langle x^2 \rangle \langle x'^2 \rangle - \langle x x' \rangle^2}$ is the beam's geometric emittance ($\langle\rangle$ means the ensemble average).

By setting $\sigma_x'' = 0$, we can get the matched beam spot size:

$$\sigma_m = \sqrt{\frac{\epsilon}{\bar{k}_\beta}} \tag{4.11}$$

where $\bar{k}_\beta = \dfrac{k_p}{\sqrt{2\bar{\gamma}}}$, and $\bar{\gamma}$ is the average relativistic factor among all the beam particles. Henceforth we will refer to Eq. (4.11) as the linearly matched spot size, and matching the beam's spot size to this value is called 'linearly matched'.

To explicitly see the dependence on density and energy, Eq. (4.11) can also be written as:

$$\sigma_m = (\frac{2}{\bar{\gamma}} \frac{\epsilon_n^2}{k_{p0}^2} \frac{n_0}{n})^{\frac{1}{4}} \tag{4.12}$$

where $\epsilon_n = \frac{1}{m_e c}\sqrt{\langle x^2 \rangle \langle p_x^2 \rangle - \langle x p_x \rangle^2}$ is the beam's normalized emittance. For a beam with small energy spread, we have $\epsilon_n \approx \bar{\gamma}\epsilon$, and k_{p0}^{-1} is the plasma skin depth corresponding to the reference density n_0, and n is the local plasma density. We define a local plasma density, n, to set the stage for considering density ramps. We can see that for small n, σ_m is large. This means a matched beam's peak density will be low, so the ion motion effects are small. This motivates us to use a plasma density ramp with a low density at the entrance so that the matched beam would trigger negligible ion motion, as we will see in Sec. 4.5.2.

We use the Courant–Snyder (C-S) parameters β and α to parametrize the beam, which

are defined as:

$$\beta = \frac{\langle x^2 \rangle}{\epsilon} \ , \ \alpha = -\frac{\langle x x' \rangle}{\epsilon} \tag{4.13}$$

and $\alpha = -\frac{1}{2}\beta'$. The matching condition in a uniform plasma in terms of CS parameters is:

$$\beta = \beta_m, \ \alpha = 0 \tag{4.14}$$

where

$$\beta_m = \frac{\sigma_m^2}{\epsilon} = \frac{1}{\bar{k}_\beta} \tag{4.15}$$

is the matched beta function.

For an unmatched beam with energy spread, its emittance will grow due to a chromatic effect, particles with different energies rotate at different angular frequencies in the phase space, thus taking a larger phase space area (Fig. 4.1 (a)). If the beam is matched, the normalized phase space looks like a circle (Fig. 4.1 (b)). The phase space area remains the same even if there is phase mixing due to the energy spread, so the emittance is well preserved. This was discussed in section 2.11.2.

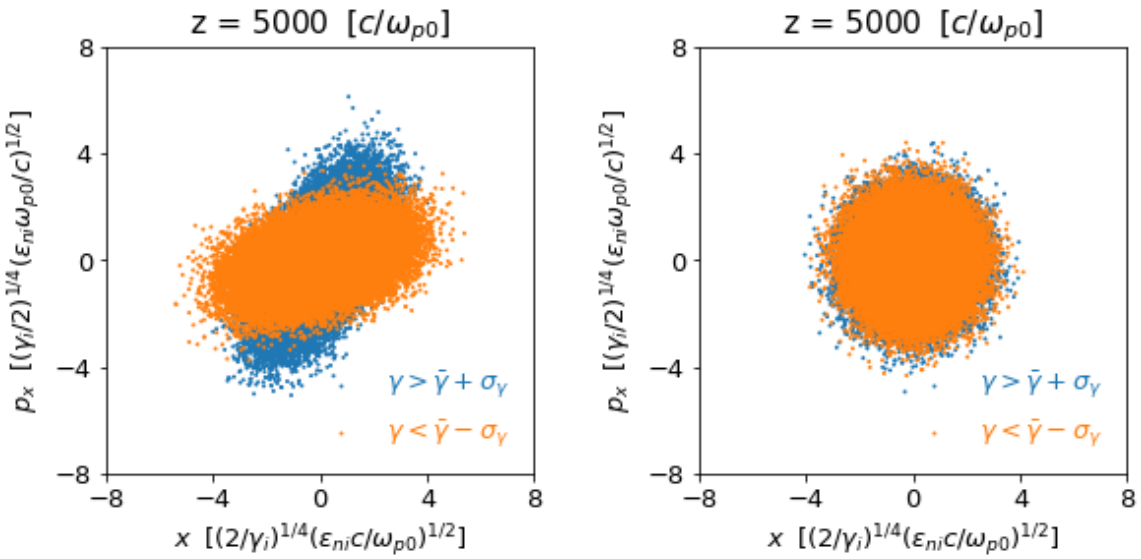

(a) (b)

Figure 4.1: (a) Unmatched ($\beta = 2\beta_m, \alpha = 0$) 10 GeV beam with 2% energy spread, emittance grows due to phase mixing from the energy spread: particles with high energy (blue) and low energy (orange) rotate at different angular frequencies in the phase space. (b) Matched ($\beta = \beta_m, \alpha = 0$) 10 GeV beam with 2% energy spread. Normalized phase space is a circle.

4.4.2 Mobile ions

To study the witness beam's emittance evolution in the presence of ion motion, we run self-consistent QPAD simulations. We start with parameters not as severe as would be for a LC design to illustrate some physics. These parameters also overlap somewhat with what might be available at FACET II. The background plasma is pre-ionized hydrogen with a uniform density n_0 which we assume to be 10^{17}cm^{-3} when switching to absolute units.

The drive beam's density profile is tri-Gaussian, $n_b = n_{b0} \exp\left(-\frac{x^2}{2\sigma_x^2}\right) \exp\left(-\frac{y^2}{2\sigma_y^2}\right) \exp\left(-\frac{z^2}{2\sigma_z^2}\right)$, with a symmetric transverse spot size $\sigma_x = \sigma_y = 0.8k_{p0}^{-1}$, longitudinal bunch length $\sigma_z = \sqrt{2}k_{p0}^{-1}$, and a peak density of $n_{b0}/n_0 = 4$. We assume the drive beam is moving at speed of light and is non-evolving. We use a drive beam with a low ion motion parameter Φ_b so that

the ion motion triggered by the drive beam is negligible.

The witness beam's density profile is transversely bi-Gaussian and longitudinally trapezoidal, with $I_{head} = 27.2$ kA at the head and $I_{tail} = 17.6$ kA at the tail (this longitudinal current profile is taken from Ref. [50] for convenience), so the accelerating field E_z is nearly flattened across the witness beam ($E_z \sim -0.56mc\omega_{p0}/e$) [36][38]. The length of the witness beam is $L = 2k_{p0}^{-1}$, and its head is located $5k_{p0}^{-1}$ behind the center of the drive beam. The witness beam has an initial energy of 10GeV, and an initial normalized emittance of $\epsilon_{ni} = 1\mu\text{m} = 0.06k_{p0}^{-1}$ for $n_0 = 10^{17}\text{cm}^{-3}$.

The simulation is performed in 2D axisymmetric geometry, where we used a (r, ξ) simulation box ($\xi = ct - z$) with 7340 cells in r and 2640 cells in ξ. The resolution is $\Delta r = 1.36 \times 10^{-3}k_{p0}^{-1}$ and $\Delta\xi = 5 \times 10^{-3}k_{p0}^{-1}$. The drive beam is non-evolving. The witness beam is sampled with a million numerical particles. The witness beam particles are pushed every 3D time step $\Delta t = 10\omega_{p0}^{-1}$. Both plasma electrons and plasma ions are initialized with 4 particles per cell. For every particle location in an r-ξ grid we initialize 16 particles in the azimuthal direction. We only keep the lowest $m = 0$ azimuthal mode unless noted.

First, we consider cases where the witness beam is linearly matched (Eq. (4.11)) with 0 and 2% initial energy spread respectively. (We stress that conventional optics cannot be used to provide such a small spot size or β function.) This means the witness beam is unmatched to the nonlinear focusing force triggered by the ion motion, which leads to emittance growth. This is shown in Fig. 4.2. We can see that only after a few betatron oscillations, the emittance basically saturates, and the spot size stabilizes to a smaller value. The slow emittance increase and spot size decrease that occurs after the rapid emittance growth are due to the acceleration. The initial emittance growth is dominated by ion motion. If the beam is linearly matched, having an initial energy spread does not lead to emittance growth, as we can see from Fig. 4.2 (a).

A possible way to mitigate emittance growth is to focus the beam to a smaller spot size than the linearly matched spot size[47], so that it is closer to some nonlinear equilibrium value

after ion motion is triggered. We ran another QPAD simulation with the witness beam's initial spot size to be 85% the linearly matched spot size and no initial energy spread. In Fig. 4.2 we see a smaller emittance growth, but now the emittance and spot size are oscillating with a larger amplitude. This is because the slices closer to the head of the witness beam experience less ion motion (See Eq. (4.6)), so the focusing force is just slightly perturbed from the linear focusing force corresponds to a fixed ion background. Since initially these slices are not linearly matched and there is no energy spread, the corresponding phase space ellipses will rotate for a long time before they reach equilibrium states, leading to an oscillatory projected phase space area and the beam spot size. In particular, the very first slice of the witness beam feels a completely linear focusing force (no ion motion at all). Since it is initially unmatched and has no energy spread, the phase space ellipse will rotate forever and never reach a steady state, contributing to an oscillatory projected emittance and spot size (the green lines in Fig. 4.2).

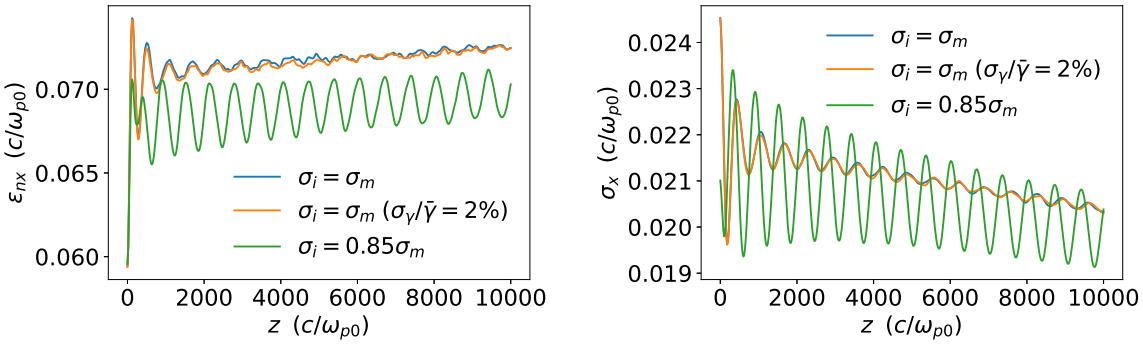

(a) (b)

Figure 4.2: The emittance (a) and spot size (b) evolution for beams with different initial parameters for QPAD simulations.

We also consider a case where the witness beam has LC parameters used in [47], except here we simulate the entire transverse region of the wake. This is possible from the advent of QPAD. The physical and simulation parameters are as follows: The pre-ionized hydrogen plasma density is 10^{17}cm^{-3}, the drive beam has 3×10^{10} electrons, normalized emittance

1 mm and bunch length $\sigma_z = 30\,\mu$m. The drive beam is still set to be moving at speed of light and nonevolving, and its spot size is set to be linearly matched, so it has a peak density of $n_{b0}/n_0 \sim 6$, which triggers negligible ion motion. The witness beam has 10^{10} electrons, an initial energy of 25GeV, an initial energy spread of 2%, and an initial projected emittance of $\epsilon_{ni} = 0.1\mu m$ $(0.006k_{p0}^{-1})$. It has a tri-Gaussian density profile with bunch length $\sigma_z = 10\mu m$ $(0.6k_{p0}^{-1})$. The distance between the centers of the two beams is $115\mu m$ $(6.8k_{p0}^{-1})$.

The (r, ξ) simulation box has 32768 by 1024 cells with a resolution of $3.6 \times 10^{-4}k_{p0}^{-1}$ by $1.8 \times 10^{-2}k_{p0}^{-1}$. There are 16 particles initialized in the azimuthal direction for each particle location in the r-ξ grid for both plasma and beam particles. Both plasma electrons and plasma ions are initialized with 4 particle locations per r-ξ cell. The witness beam is initialized with 8 particle locations per r-ξ cell. The beam particles are pushed every 3D time step $\Delta t = 10\omega_{p0}^{-1}$. We only keep the lowest $m = 0$ azimuthal mode.

In Fig. 4.3(a) we observe an $\sim 80\%$ projected emittance growth from linearly matching the beam to the uniform plasma for these LC relevant parameters. Overfocusing the initial witness beam's spot size to 1/2 of the linearly matched spot size reduces the emittance growth but causes an oscillation in the projected emittance. These results agree with the results in [47] perfectly.

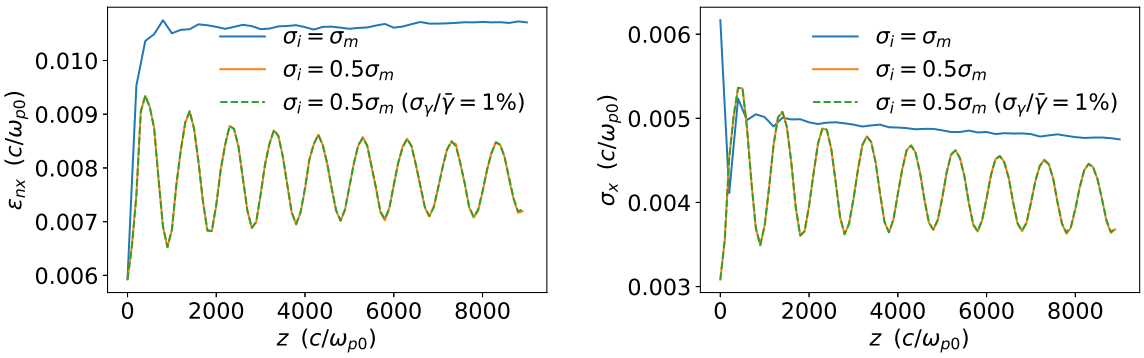

(a) (b)

Figure 4.3: The emittance (a) and spot size (b) evolution for beams with different initial parameters for QPAD simulations. The witness beam has LC parameters.

4.4.3 Phenomenological description for the ion collapse using a single particle code

In general, the ion collapse near the axis and the corresponding focusing force is slice-dependent and complicated. In this section, we will study the evolution of a beam slice by modeling the ion collapse using Eq.(4.8). We choose $A_0 = 100$ and $\sigma_{ion} = 0.005k_{p0}^{-1}$ to model a Gaussian ion collapse. We will use single particle simulations (See Sec. 1.4.4) to study the evolution of a beam slice. The beam slice has 10 GeV energy with $\epsilon_n = 0.0594k_{p0}^{-1}(1\mu m)$, and no initial energy spread. The beam has no longitudinal acceleration in the simulation. We use 10^5 numerical particles in the beam slice. For simplicity we assume the particles' transverse motion is 1D, where they move under a 1D version of the focusing force in Eq. (4.9). We simply replace r with x in Eq. (4.9) which is not strictly valid for a nonlinear focusing force except if $y = 0$.

If we match the beam with spot size equal to Eq. (4.11) (the matched spot size for $A_0 = 0$), we can see that both the emittance and the spot size saturate very quickly within a few betatron oscillations (solid curves in Fig. 4.4 (a)), which is qualitatively similar to what we observed in Fig. 4.2. The rapid emittance growth at the beginning is due to the nonlinear phase mixing, and Fig. 4.4 (b) shows the spiral phase space at an early time of the simulation.

We also tried to nonlinearly match the beam's spot size to the steady state spot size of the Gaussian ion model. Appendix E.3 shows how to estimate the steady state spot size. We can see that if the beam's initial spot size is closer to the steady state spot size in the nonlinear focusing force, emittance growth can be mitigated significantly.

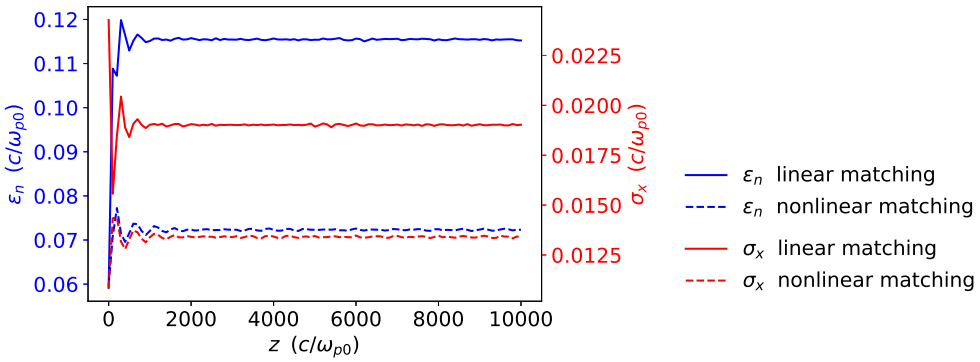

(a)

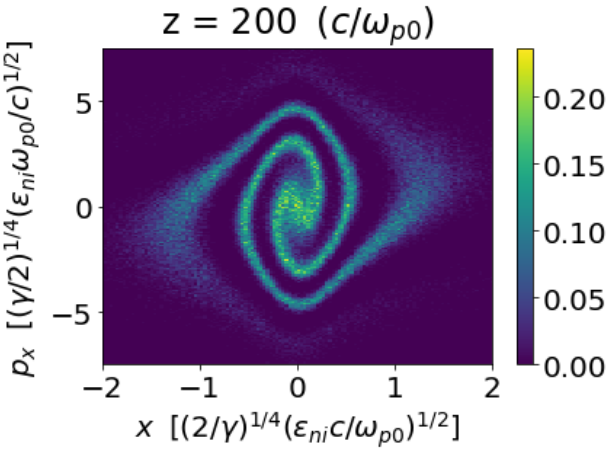

(b)

Figure 4.4: (a) Emittance and spot size evolution using a Gaussian phenomenological model (b) Spiral phase space due to nonlinear phase mixing

To make connections to the self-consistent QPAD simulations, we take the simulation result from Sec. 4.4.2 where the witness beam has LC parameters (blue curves in Fig.4.3). We plot the steady-state transverse ion density lineout at the longitudinal centroid of the witness beam (blue curve in Fig. 4.5 (a)) and the emittance growth of the beam slice at the longitudinal centroid (blue curve in Fig. 4.5 (b)). To make comparisons, we run two 2D single particle simulations (the motion in x and y are coupled) with two different ion collapse models. Both of them have the same on-axis ion density $(1 + A_0)$ as the QPAD simulation, but their σ_{ion} are different. The orange curve in Fig. (4.5)(a) has a small

$\sigma_{ion} = 4 \times 10^{-4} k_{p0}^{-1}$. While it captures the central part of the ion density lineout from from the self-consistent QPAD simulation well, it fails to capture the long tails on both sides, therefore underestimating the slice emittance growth (see orange curve in Fig. (4.5)(b)). If we choose a wider $\sigma_{ion} = 10^{-3} k_{p0}^{-1}$ (green curve in Fig. (4.5)(a)), our model is wider than the self-consistent result, so the slice emittance growth is overestimated a little (see green curve in Fig. (4.5)(b)).

Note that it is shown in [47] (although in 1D) that a larger A_0 or a larger σ_{ion} in the Gaussian ion collapse model will lead to a larger slice emittance growth. Due to the complicated nature of ion collapse, it is not accurately represented by a Gaussian function, especially the "long tail" parts that are further away from the axis. However, we can still gain enough qualitative insights from this model.

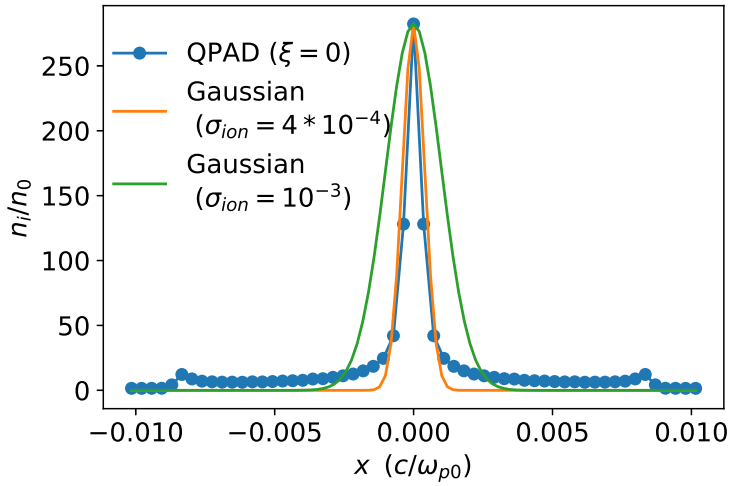

(a)

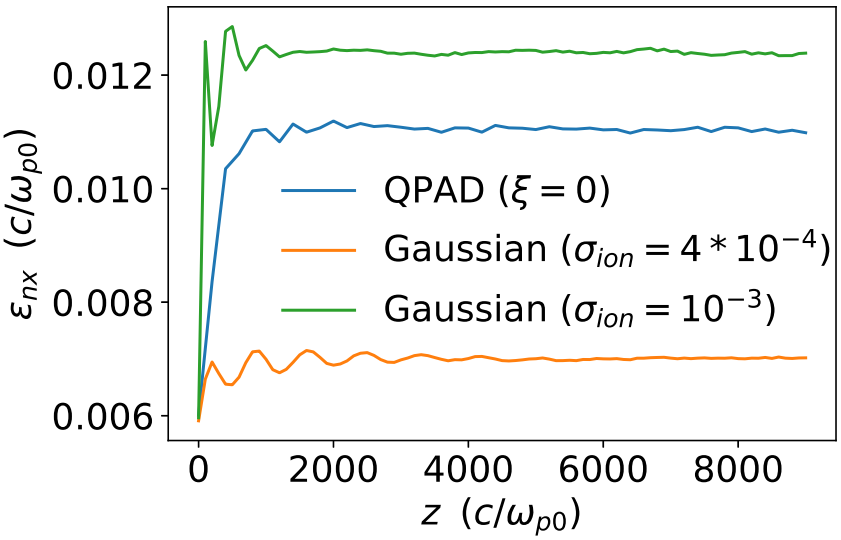

(b)

Figure 4.5: Comparison of QPAD simulation and 2D single particle simulations with a Gaussian ion collapse model. (a) Blue: The transverse ion density lineout at the centroid of the witness beam ($\xi = 0$) from QPAD simulation. The dots correspond to the grid points in the simulation. Orange and green: Gaussian ion collapse models with the same on-axis density and different σ_{ion}. (b) Blue: Emittance evolution of witness beam's centroid slice from QPAD simulation. Orange and green: Emittance of a beam evolving in a fixed focusing force corresponding to the Gaussian ion collapse models shown in (a).

4.5 Matching using an adiabatic density ramp

In this section, we investigate if emittance growth can be mitigated through the use of an adiabatic density upramp and downramp, placed on each side of a density plateau.

4.5.1 Without ion motion

In a non-uniform plasma, the matching condition is modified from Eq. (4.14) and becomes:

$$\beta = \beta_m,\ \alpha = \alpha_m \tag{4.16}$$

where β_m, α_m are the matched Courant-Snyder (C-S) parameters [42][44][93], defined as

$$\beta_m(z) = \sqrt{2\gamma}c/\omega_p(z) \tag{4.17}$$

and

$$\alpha_m(z) = -\frac{1}{2}\beta_m'(z) \tag{4.18}$$

where z is the propagation distance. Eq. (4.18) is analogous to the relationship between α and β. An adiabaticity parameter can be defined as $\mathcal{A} = |\alpha_m|$ [42] [93], which describes how adiabatic the plasma density is changing from the beam's point of view. The adiabatic condition is given by

$$\mathcal{A} \ll 1 \tag{4.19}$$

If the adiabatic condition is satisfied, it means the betatron frequency k_β changes very little within one betatron wavelength. Loosely speaking, the beam feels the plasma density is changing very slowly.

For an adiabatic plasma ramp, it has been shown that if we match the beam to the plasma entrance, the beam will stay matched as it propagates in the plasma, and the emittance can be preserved perfectly even if the beam has a finite energy spread [39] [44] [80], and see Chapter 3.

Here we show results from a self-consistent QPAD simulation that illustrate this including upramp and downramp matching sections. The beam parameters are identical to the ones in Sec. 4.4.2. The plasma density profile is shown in Fig. 4.6(a): When discussing absolute units, we assume the background plasma is pre-ionized hydrogen plasma with density $n_0 = 10^{17}\,\mathrm{cm}^{-3}$ at the density plateau. The plasma ions are kept fixed. The length of the plateau is $40000k_{p0}^{-1}$ ($k_{p0}^{-1} = c/\omega_{p0}$ is the plasma wavelength at the density plateau n_0). Before the density plateau, we use an adiabatic density upramp designed as follows: At the entrance of the plasma upramp, the density is $n_{entrance} = 0.01n_0$. In the density upramp, α_m (defined in Eq. (4.18)) starts from $\alpha_{mi} = 0.1$ at the entrance and decreases linearly to 0 at the end of the upramp. An upramp that satisfies this condition is shown in Fig. 4.6(a). The analytical expression for this density profile is:

$$\frac{n(z)}{n_0} = \frac{1}{\left(1 + \dfrac{\alpha_{mi}(z-L)^2}{\beta_{m0}L}\right)^2} \tag{4.20}$$

where $\alpha_{mi} = 0.1, \beta_{m0} = \sqrt{2/\gamma}k_{p0}^{-1} = 200k_{p0}^{-1}$ for a 10 GeV beam, and $L = 18000k_{p0}^{-1}$ is the length of the upramp. We design the density profile this way so that the adiabatic condition (Eq. (4.19)) is satisfied everywhere in the upramp, and $\mathcal{A}$ is continuous at the end of the upramp. More details about the ramp design can be found in Appendix E.1. We use a plasma density profile for the downramp which is completely symmetric to the upramp. The entire plasma density profile is shown in Fig. 4.6(a). It is worth noting that after being accelerated in the density plateau, the beam's energy is higher in the downramp than in the upramp, so it may be beneficial to carefully design a different downramp that accounts for this energy gain. Here we just choose a symmetric downramp for simplicity. Also, when designing the ramp, we assume there is no longitudinal acceleration and ion motion. In the presence of ion motion(discussed later), the adiabatic condition is not well defined and may not strictly hold due to the enhanced betatron frequency. But in principle, we can always elongate the ramp to make it more adiabatic.

As for the simulation parameters, we used 4000 by 1200 cells in a (r, ξ) simulation box.

The resolution is $2.5 \times 10^{-3} k_{p0}^{-1}$ by $10^{-2} k_{p0}^{-1}$. The drive beam is non-evolving. The witness beam is sampled with a million numerical particles. The beam particles are pushed every 3D time step $\Delta t = 10\omega_{p0}^{-1}$. There are 16 particles distributed uniformly for each designated location in the r-ξ cell. Both plasma electrons and plasma ions are initialized with 4 designated locations for particles in each r-ξ cell. We only keep the lowest 3 azimuthal modes: $m = 0, 1, 2$. We did this to verify the azimuthal symmetry – lack of hosing growth. We found that all the quantities for $m = 1, 2$ are indeed essentially vanish, verifying that our simulation remains axisymmetric.

We match a witness beam with a 2% initial energy spread to the plasma entrance (Eq. 4.16). In Fig. 4.6 (b) we can see that as the witness beam propagates, its spot size evolution strictly follows the locally matched spot size (Eq. 4.12), so the beam always stays matched, and its emittance is preserved perfectly.

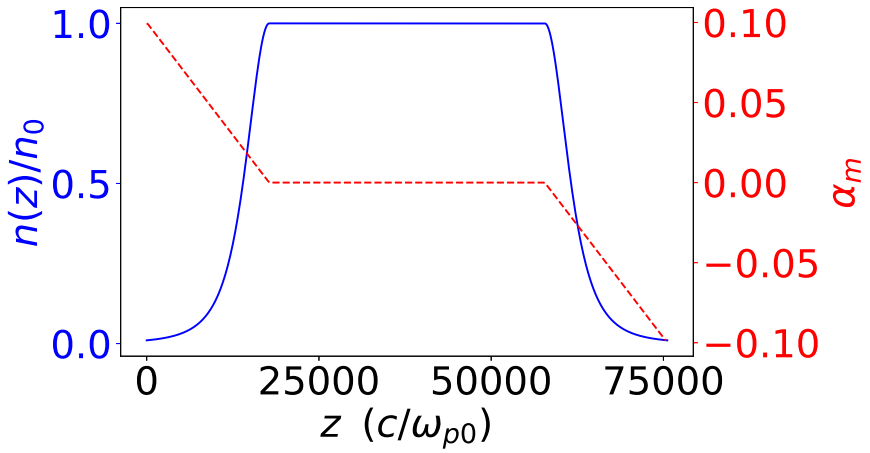

(a)

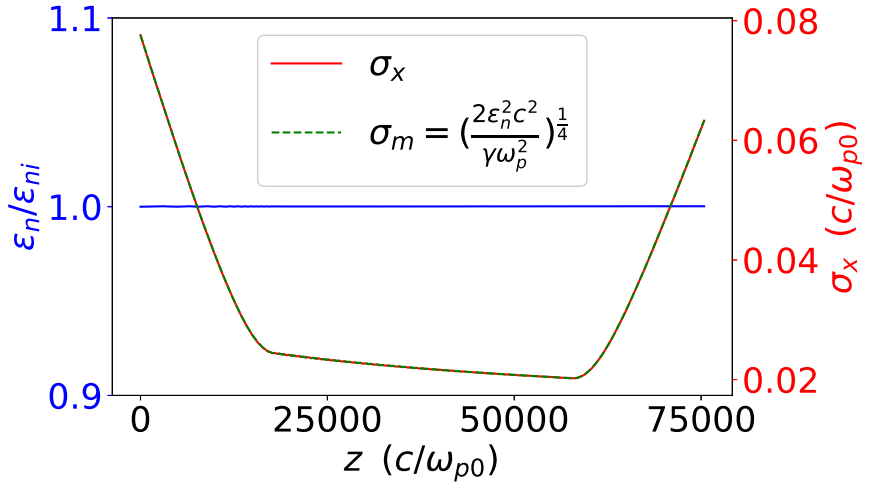

(b)

Figure 4.6: (a) Plasma density ramp (blue) with α_m (red). (b) Emittance (blue) and spot size (red) evolution for a matched beam in the absence of ion motion.

4.5.2 With ion motion

In the previous section, we saw that in the absence of ion motion, the witness beam emittance can be perfectly preserved using adiabatic plasma density ramps. In this section, we will show that by using the same method, even in the presence of ion motion, the beam emittance can still be almost perfectly preserved. We consider a simulation with identical parameters

to the ones in Sec. 4.5.1, except that we allow the plasma ions to move this time. Fig. 4.8 (a) shows the evolution of the projected emittance and the slice emittance at 3 different longitudinal positions. The witness beam (with a trapezoidal current profile) is located within the range $0 \leq \xi \leq 2k_{p0}^{-1}$, where $\xi = 0$ is at the beam head and $\xi = 2k_{p0}^{-1}$ is at the beam tail. We can see that the projected emittance (red dashed line) grows first, but then decreases in the downramp, with only $\sim 1\%$ emittance growth at the exit of the plasma downramp.

For the beam slice at the head of the beam (blue, $\xi = 0.05k_{p0}^{-1}$), the slice emittance remains constant, and the slice spot size is just the linearly matched spot size. They are the same as in Fig. 4.6(b), because the beam slice at the head experiences no ion motion.

For slices in the middle (orange, $\xi = 1k_{p0}^{-1}$) and tail (green, $\xi = 1.95k_{p0}^{-1}$) of the beam, the emittance grows in the upramp due to the nonlinear focusing force from the ion motion. But in the density downramp, the slice emittances decrease with there only being a 1% net growth. In Fig. 4.7 we can see that the slice spot sizes are also smaller than the linearly matched spot size due to ion motion.

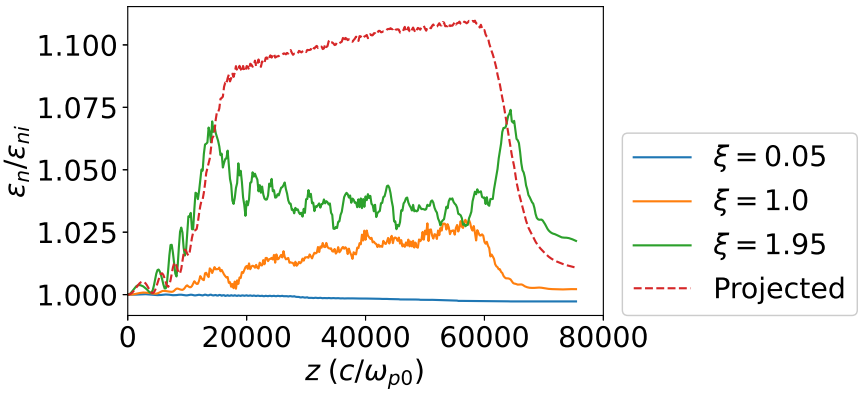

(a)

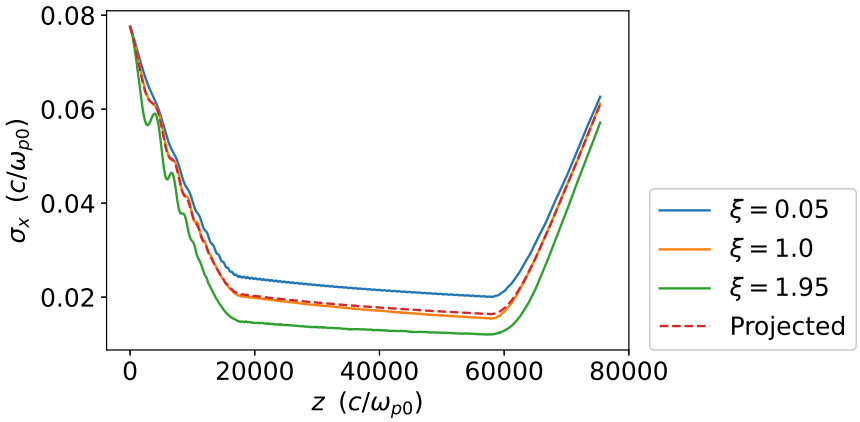

(b)

Figure 4.7: (a) Evolution of projected emittance (red dashed) and slice emittance (b) Evolution of projected spot size (red dashed) and slice spot sizes

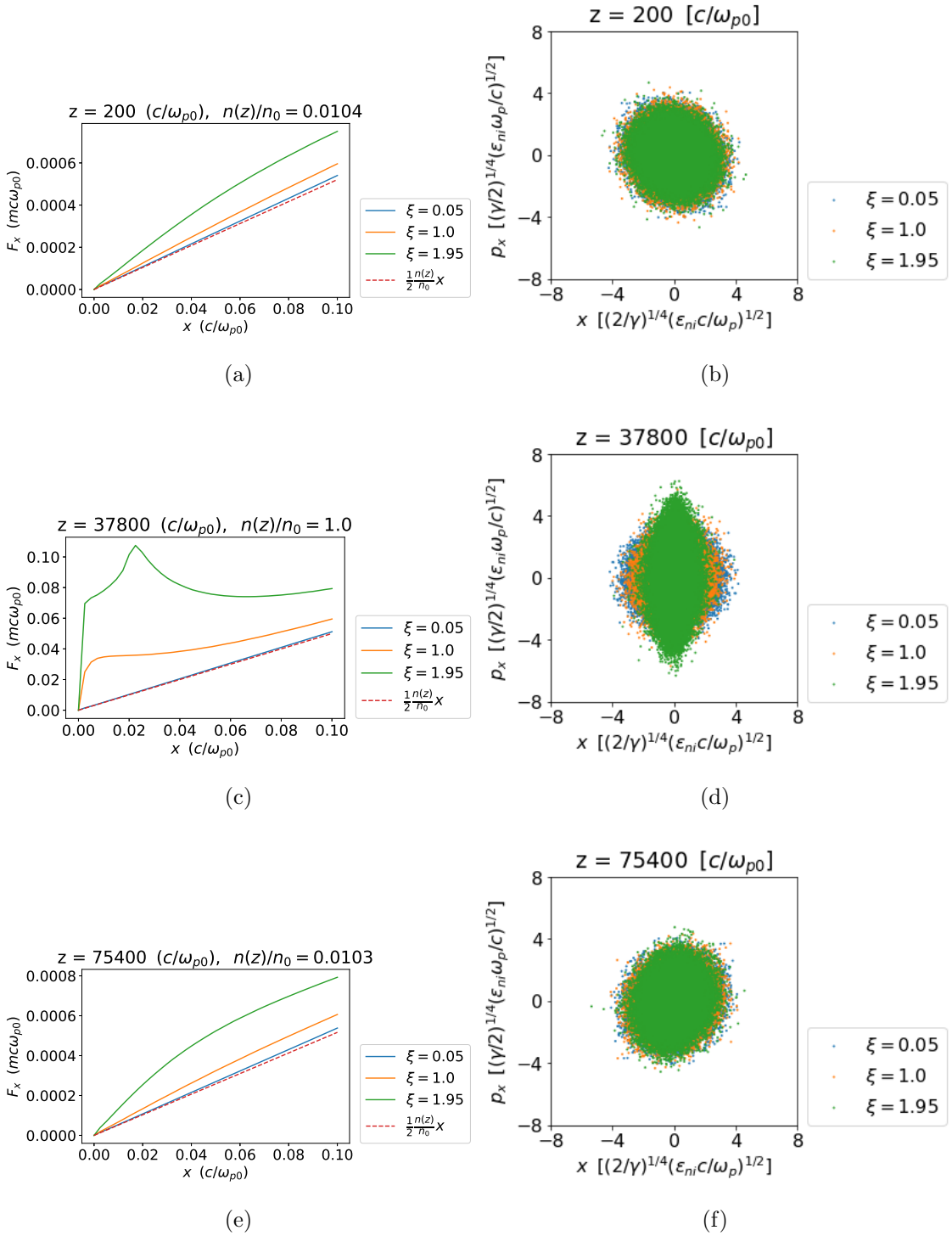

Figure 4.8: (a)(c)(e) focusing force at different longitudinal positions (b)(d)(f) phase space ellipses correspond to different longitudinal slices

After having provided a high level description that the net emittance growth is limited to $\sim 1\%$, we now give a detailed analysis of the whole process. At the entrance, we linearly matched the witness beam. Since the plasma density is low, according to Eq.(4.12), the matched spot size is large, leading to a low peak density. Hence the ion parameter is relatively small, $\Phi_b \sim 0.69$ (estimated using equation (E.7)),so the ion motion effect is relatively small, thus the focusing force is essentially linear (Fig. 4.8 (a)). At the entrance the normalized phase space ellipses are shown in Fig.4.8(b)). The three phase space ellipses correspond to $\xi = 0.05$ (head), $\xi = 1.0$ (middle), $\xi = 1.95$ (tail) overlap with each other. They are slightly tilted to the left because the beam has an initial $\alpha_i = 0.1$ in order to be linearly matched at the entrance. Note that x and p_x values are normalized to their matched values at a given z in the absence of ion motion.

As the beam propagates in the density upramp, its spot size is adiabatically compressed, so the peak density gets higher, and the ion motion is gradually triggered. The beam's distribution will slowly and continuously evolve to match the local nonlinear focusing force. At the density plateau, the ion parameter has increased to $\Phi_b \sim 2.2$, so ion motion is important. Due to the nonlinear focusing force induced by the ion motion, the distribution of a beam slice is no longer Gaussian, and this deformation of the distribution leads to a larger value in the emittance, as shown in Fig.4.8(a)). However, in contrast to the emittance growth due to phase mixing, this emittance increase is reversible. We will analyze the slice emittance evolution in greater detail later in Sec. 4.5.3 using the phenomenological model described in Sec. 4.3. The projected emittance also grows in this process. This arises mainly because the focusing force at different longitudinal slices are different (See Fig.4.8(c)), so the phase space ellipses for different slices evolve differently and have different shapes, thus they no longer overlap with each other (Fig.4.8(d)), leading to a larger projected phase space area.

In the density plateau, each slice of the beam finds its own equilibrium state. The slow increase in the projected emittance and the slow decrease in the spot size are due to beam's

acceleration. In the density downramp, the beam's spot size slowly expands, so the peak density becomes lower, and ion motion gets weaker, the focusing force gradually evolves back to being linear, as shown in Fig. 4.8(e). The distributions of different beam slices evolve back to the same Gaussian distributions, and the phase space ellipses for the selected slices overlap with each other again, leading to a small projected phase space area (Fig. 4.8(f)). The final projected emittance decreases to nearly its original value.

4.5.3 Single particle simulation using Gaussian phenomenological model

In Sec. 4.5.2, we explained that the projected emittance first increases and then decreases back to near its original value due to the independent evolution of each beam slice. However, the evolution of the slice emittance is more subtle. In this section, we study the evolution of a beam slice in a predetermined focusing force. To take into account the longitudinal plasma density variation, we modify our model for the ion collapse in Eq. (4.8) and assume the following for the ion density,

$$n_{ion}(r,z)/n_0 = n(z)/n_0 + A(z)\exp\left(-r^2/2\sigma_{ion}^2\right) \tag{4.21}$$

where $A(z) = A_0\frac{n(z)-n(0)}{n_0-n(0)}$, so that the nonlinear part of the ion density is exactly 0 at the entrance, and has a peak density of A_0 at the plasma density plateau.

The corresponding focusing force is

$$F_r(r,z) = \left[-\frac{r}{2}\frac{n(z)}{n_0} - A(z)\sigma_{ion}^2\frac{1-\exp\left(-\frac{r^2}{2\sigma_{ion}^2}\right)}{r}\right] m_e\omega_{p0}^2 \tag{4.22}$$

We choose $A_0 = 100$, $\sigma_{ion} = 0.005k_{p0}^{-1}$, $n(z)/n_0$ to be same as in Fig. 4.6 (a). This predetermined focusing force is used in Eq. (3.1) to solve for the phase space trajectories of a group of particles. The beam slice still has 10 GeV energy with $\epsilon_n = 0.0594k_{p0}^{-1}(1\mu m)$, no initial energy spread, and is initially linearly matched at the plasma entrance. The beam has no longitudinal acceleration in the simulation. We use 10^5 particles in the beam.

In Fig. 4.9 (a) we show the evolution of the emittance and spot size of the beam slice, which are similar to the results from the self-consistent QPAD simulation. The emittance grows in the upramp, remains relatively constant in the plateau, and decreases to near the original value at the plasma exit. To understand this emittance evolution, we need to analyze the beam's dynamics in more detail.

At the entrance of the plasma upramp, the beam's distributions in x and p_x are both Gaussian, which remain matched distributions in a linear focusing force. As the beam propagates in the density upramp, the nonlinear part of the focusing force adiabatically increases. The beam will keep adjusting its profile to match to the local nonlinear focusing force, resulting in non-Gaussian profiles in both x and p_x, (Fig. 4.10 (e)(f)), and a corresponding non-elliptical phase space (Fig. 4.10 (b)), which looks like a rhombus. Particles at the 'tips' make a larger contribution to the 'spread' in x and p_x, leading to a larger value of the RMS emittance as compared to a 90% or 95% value. In other words, this RMS measurement of emittance is no longer an accurate reflection of the phase space area when the distribution is not Gaussian. This 'emittance increase' is because the beam profile deviates from a Gaussian profile, or the phase space deviates from an ellipse. It is purely a geometrical effect and is reversible. This is different from the emittance growth caused by phase mixing within a slice (Fig. 4.4(b)), which is difficult to reverse.

As the beam propagates in the density downramp, the nonlinear part of the focusing force adiabatically decreases, and becomes zero at the exit. The evolution of the beam's profile in the downramp is essentially reversed from that in the upramp. Eventually at the exit, the focusing force is back to linear, and the beam's distribution is back to Gaussian (Fig. 4.10(g)(h)), so the RMS emittance remains unchanged from its original value.

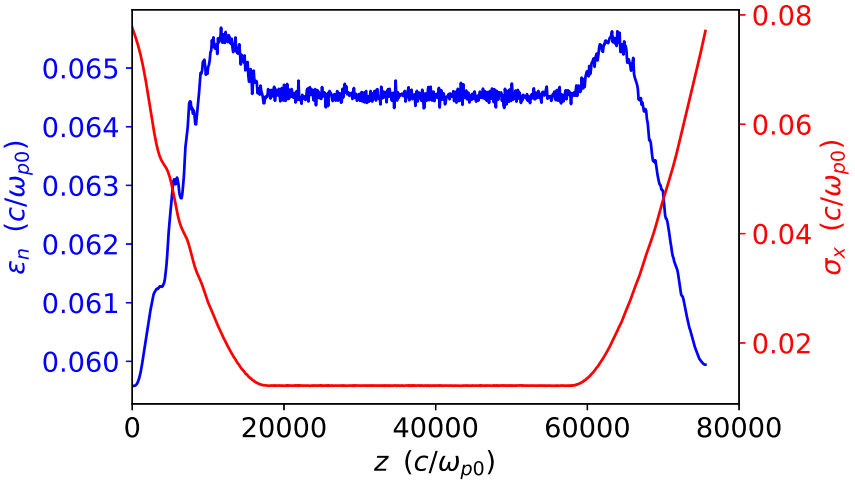

(a)

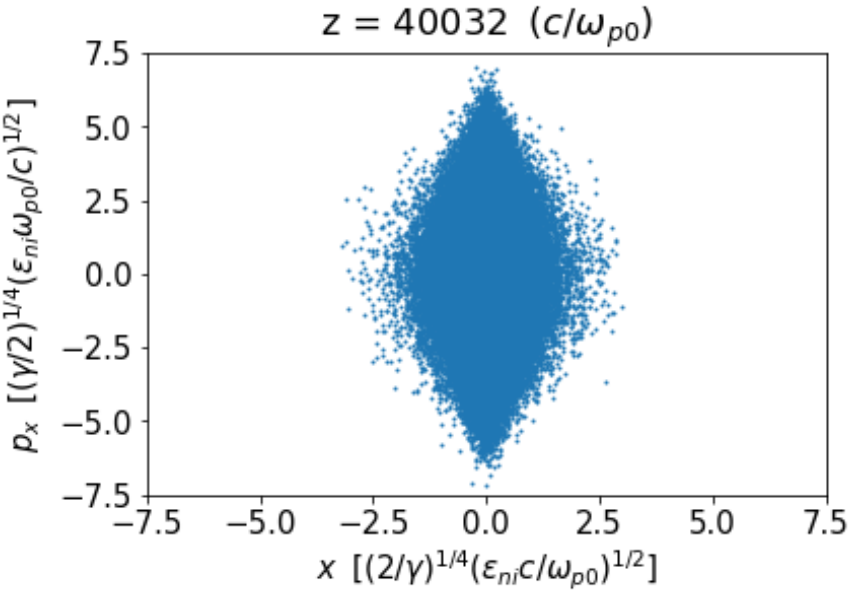

(b)

Figure 4.9: (a) Emittance and spot size evolution using a Gaussian phenomenological model (b) Normalized phase space at the density plateau.

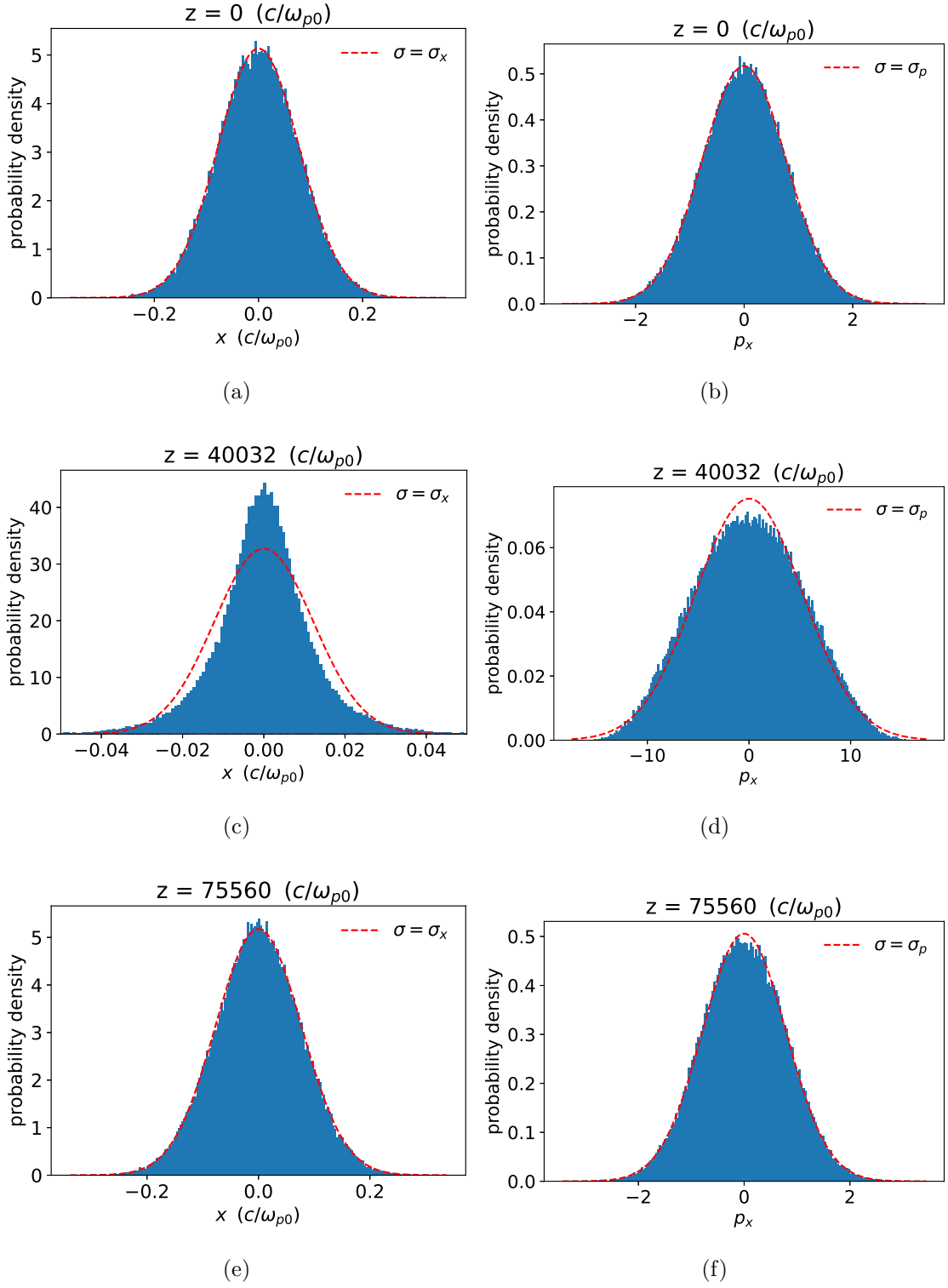

Figure 4.10: (a) $\sim$ (f) The distribution of beam particles' x and p_x at the beginning, middle, and end of the simulation

4.6 LC parameters

In this section we consider the utility of adiabatic matching sections for LC design parameters in the presence of ion motion.

4.6.1 Adiabatic ramps

For linear collider (LC) relevant witness beam parameters, adiabatic density ramps are still beneficial for preserving emittance. To demonstrate this, we undertake a QPAD simulation: With a preformed hydrogen plasma of density $n_0 = 10^{17}\text{cm}^{-3}$ for the uniform acceleration section. It is $4 \times 10^4\, k_{p0}^{-1}$ (67.3 cm) long. The drive beam has an initial energy of 25 GeV, 3.0×10^{10} electrons (4.8 nC), a normalized emittance $\epsilon_n = 1\,\text{mm}$, and a tri-Gaussian density profile with $\sigma_r = 10.4\,\mu\text{m}$, $\sigma_z = 30\,\mu\text{m}$. It is thus matched to the uniform acceleration section. The drive beam's peak density $n_{b0} = 5.89\, n_0$ is high enough to produce a fully blown-out wake but not trigger any ion motion. The drive beam is set to be non-evolving (it is represented by a specified current profile) in the simulation to isolate the physics. The witness beam also has an initial energy of 25 GeV, but with a normalized emittance, $\epsilon_n = 100\,\text{nm}$, and a trapezoidal longitudinal current profile ranging from $I_{b,head} = 25.26\,\text{kA}$ at the head to $I_{b,tail} = 6.42\,\text{kA}$ at the tail. Its length is $1.8\, k_{p0}^{-1}$ ($30.3\,\mu\text{m}$), so the total charge is 1.0×10^{10} electrons (1.6 nC). The head of the witness beam is located at a distance of $6.25\, k_{p0}^{-1}$ ($105.2\,\mu\text{m}$) behind the center of the drive beam such that the blowout wake is optimally loaded [36] [38], as shown in Fig. 4.11. The nearly constant accelerating field along the witness beam is around $E_z = -1.2\, mc\omega_{p0}/e$ for all beam slices. The witness beam is initialized with no energy spread to isolate physics.

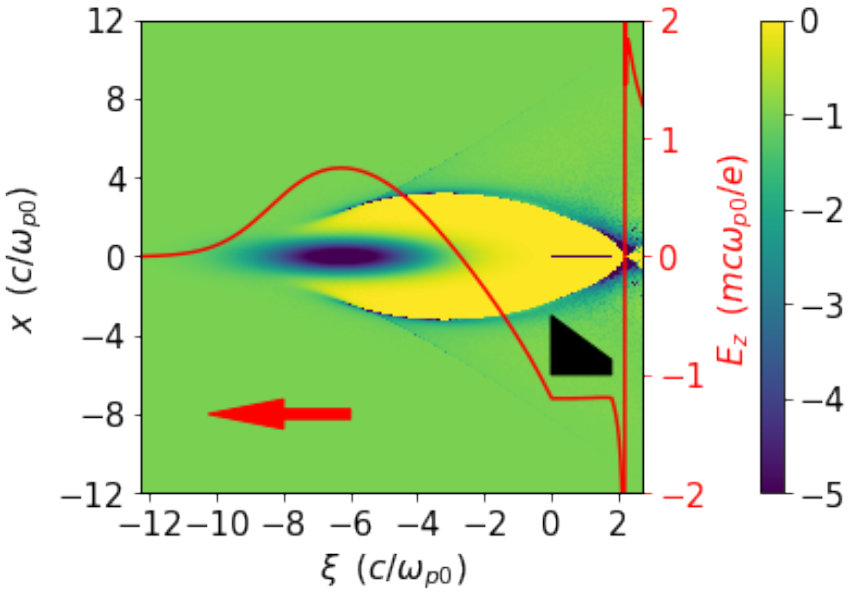

Figure 4.11: A snapshot of the wake and beams in the density plateau. The color bar shows the charge density for the plasma electron, and drive and witness beams. The witness beam has a trapezoidal longitudinal current profile (black) in order to flatten the accelerating field E_z (on-axis lineout in red).

To smoothly match the witness beam into the uniform acceleration section (henceforth referred as density plateau), we use a $L = 3 \times 10^4\, k_{p0}^{-1}$ (50.5 cm) long adiabatic plasma density upramp before the density plateau and a symmetric downramp after the density plateau. The entire longitudinal plasma density profile is shown by the black solid curve in Fig. 4.12(a).

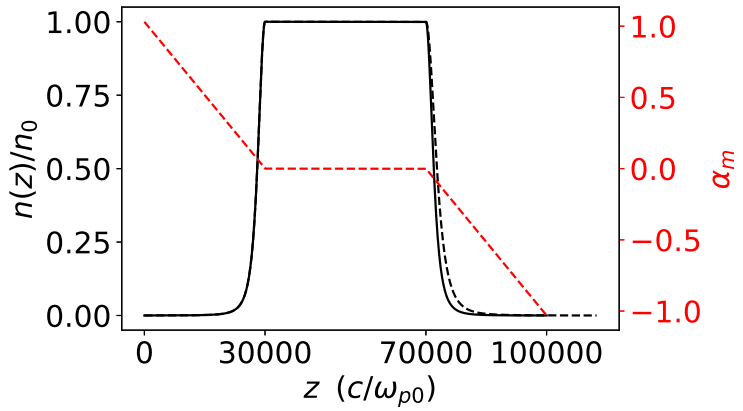

(a)

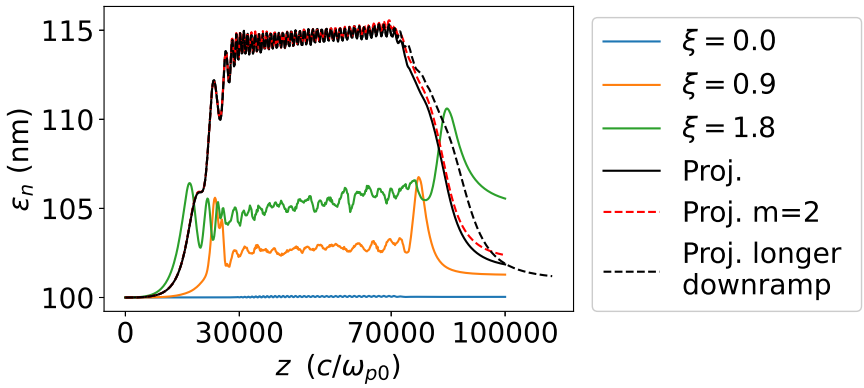

(b)

Figure 4.12: (a) The resulting adiabatic plasma density profile (solid black) based on a linear ramp for α_m. The profile assumes the witness beam energy remains constant, so the downramp is symmetric to the upramp. The black dashed downramp takes into account the energy doubling of the witness beam, thus it is $\sqrt{2}$ times as long as the solid black downramp. (b) Evolution of the projected emittance (solid black) and selected slice emittances. The witness beam's head and tail are located at $\xi = 0, 1.8k_{p0}^{-1}$ respectively. The red dashed curve shows the evolution of the projected emittance when three azimuthal modes, $m = 0, 1, 2$, are kept in a QPAD simulation. The black dashed curve shows the evolution of the projected emittance for the case where the black dashed downramp in (a) is used.

In a density upramp (downramp) α_m is positive (negative). Therefore, we design an

adiabatic plasma density upramp with α_m linearly decreasing to 0 (at the plateau), so that the transition from the upramp to the plateau is smooth. Based on this assumed linear dependence of α_m, we can integrate to solve for the density dependence of the upramp (See Appendix E.1),

$$\frac{n(z)}{n_0} = \frac{1}{\left(1 + \frac{\alpha_{mi}(z-L)^2}{\beta_{m0}L}\right)^2} \tag{4.23}$$

where $\beta_{m0} = \sqrt{2\gamma}c/\omega_{p0}$ is β_m evaluated at the density plateau, and the adiabaticity parameter at the entrance, α_{mi}, is related to the choice of the plasma density at the entrance by Eq. (4.23). We choose a small density at the entrance of the upramp $n_i = n(0) = 10^{-4}n_0$, such that the corresponding $\alpha_{mi} \approx 1$. We match the witness beam to the plasma entrance with $\sigma = \sigma_{mi}$ and $\alpha = \alpha_{mi}$ where σ_{mi} is Eq. (4.12) evaluated using the density n_i.

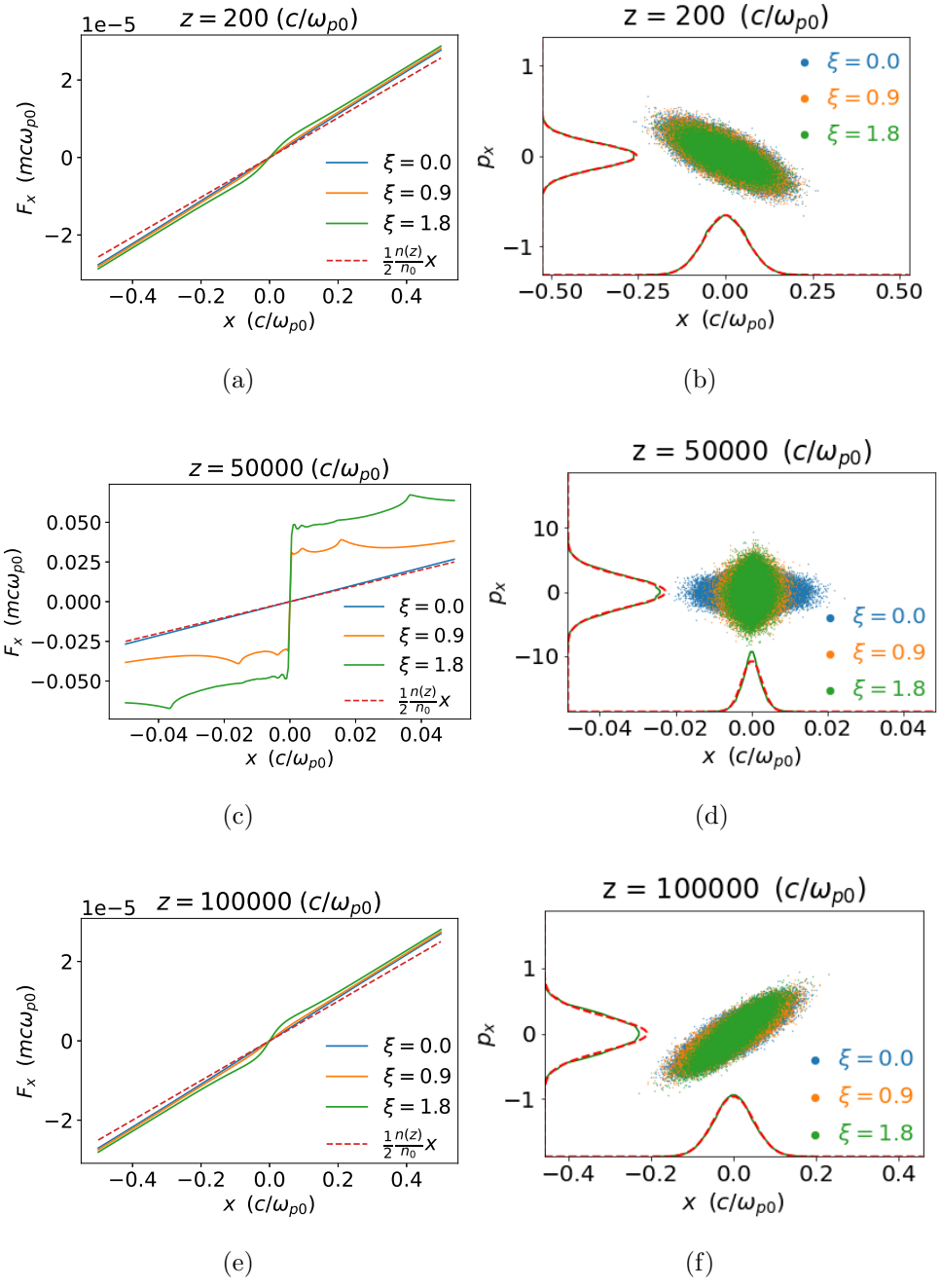

Figure 4.13: (a)(c)(e): Focusing force in $\hat{x}$ at different longitudinal ξ positions for different z propagation distances. (b)(d)(f): Phase space ellipses corresponding to different longitudinal slices. The colors of each particle correspond to colors of the ξ for the focusing force. The distribution for p_x and x are shown for the $\xi = 1.8$ slice (green curve) and a Gaussian fits that match the standard deviations of the distributions are shown as red dashed lines.

In the QPAD simulation, we use a (r, ξ) simulation box with dimensions $12k_{p0}^{-1} \times 15k_{p0}^{-1}$ (See Fig. 4.11), and cell size $5 \times 10^{-4}k_{p0}^{-1} \times 10^{-2}k_{p0}^{-1}$. The witness beam consists of 10^7 numerical particles . The beam particles are pushed every 3D time step $\Delta t = 10\omega_{p0}^{-1}$. Both plasma electrons and ions are initialized with 4 locations for particles per r, ξ cell with 16 particles distributed in the azimuthal direction at each cell location when initializing plasma particles. Unless otherwise noted, we only keep the lowest $m = 0$ azimuthal mode because we assume axisymmetric beam and plasmas distributions.

In Fig. 4.12(b) we show the evolution of the projected emittance (black solid) and the slice emittance at the head (blue), middle (orange) and tail (green) of the witness beam. The thickness of the slices is chosen to be $\Delta\xi = 0.1k_{p0}^{-1}$. The projected emittance steadily grows in the density upramp, then grows very slowly in the density plateau[50], but eventually decreases in the density downramp, with only a $\sim 2\%$ net emittance growth at the exit of the plasma downramp!

To understand why the projected emittance evolves this way, we need to once again investigate how the phase space evolves within individual slices. At the entrance of the plasma upramp, the density is low. According to Eq. (4.12), σ_m is large. This means the beam's peak density (and self-electric field) is low. As a result, the ion motion effects are initially small, and the beam is essentially matched to the unperturbed linear focusing force. In Fig. 4.13 we present the the focusing force at the head ($\xi = 0$), middle ($\xi = 0.9k_{p0}^{-1}$), and tail ($\xi = 1.8k_{p0}^{-1}$) of the witness beam for three propagation distances that correspond to the entrance of upramp, middle of plateau, and exit of downramp. We also show the phase space for slices centered at the same ξ locations (represented by different colored dots). In the upramp region before there is any ion motion, it can be seen in Fig. 4.13 (a) that the focusing force at each slice are all nearly the same as from the ion column. In Fig. 4.13 (b) the phase space distributions for each slice all overlap as well.

As the beam propagates into the ramp the plasma density slowly increases, causing the the beam to be adiabatically compressed. This leads to a higher peak density (thus

a stronger self-electric field), so ion motion is adiabatically triggered. In this process, the beam's distribution will slowly and continuously evolve to match the local nonlinear focusing force. Each slice of the beam experiences a different transverse focusing force and therefore evolves differently. At the density plateau, we can see the focusing forces at different ξ are different (Fig. 4.13 (c)), leading to different evolution for each phase space ellipse (Fig. 4.13 (d)).

Due to the nonlinear focusing force there is some emittance growth within each slice. However, in contrast to the emittance growth due to the phase mixing that occurs for initially unmatched beams, this growth here is reversible in the downramp [94]. Due to the nonlinear focusing force, the distributions of the beam particles are no longer Gaussian. We can see the green curves deviate from the red dashed curves in Fig. 4.13 (d). This non-Gaussian profile, which is just a geometric effect, leads to a larger value in the slice emittance in the density plateau, as shown in Fig. 4.12(b). In addition, slices at head, middle and tail of the beam feel different focusing forces, so their corresponding phase space ellipses no longer overlap with each other, resulting in a larger projected area. Thus the projected emittance growth is much larger than for any given slice.

The evolution of the witness beam in the density downramp is essentially the reverse of the process in the density upramp. The beam's spot size slowly expands, so the peak density becomes lower, the ion motion retreats, the focusing force eventually becomes roughly linear and longitudinally independent again, see Fig. 4.13 (e). Therefore, the geometrical effect that led to a slight increase in the emittance of each slice is reversed and the different phase space ellipses that correspond to different longitudinal slices gradually overlap with each other again at the exit (Fig. 4.13 (f)). After the entire acceleration stage, the witness beam gained 25 GeV while maintaining a very small energy spread ($\sigma_\gamma/\bar{\gamma} \sim 0.1\%$ at the exit), and with only a 2% projected emittance growth.

The simulation above only includes $m = 0$ mode in azimuthal direction. We also ran another simulation that includes $m = 0, 1, 2$ modes. The projected emittance is shown in red

dashed curve in 4.12(b), which is similar to the $m = 0$ mode only result (solid black curve). This indicates that there is no hosing growth from noise during the entire stage.

The downramp we used is symmetric to the upramp for simplicity. However, the witness beam's energy doubled after being accelerated in the density plateau, so β_{m0} becomes $\sqrt{\gamma_f/\gamma_i} = \sqrt{2}$ times, where γ_i and γ_f denote the witness beam's energy at the entrance and the exit of the density plateau, respectively. From Eq. (4.23) we can see that in order to keep the same amount of adiabaticity, the length of the downramp should be $\sqrt{2}$ times that of the upramp, shown by the black dashed curve in Fig. 4.12(a). Using this downramp instead, the evolution of the projected emittance in the downramp is shown in Fig. 4.12(b). We can see that the projected emittance growth at the exit of the downramp is even smaller. In general, a longer ramp is more adiabatic, therefore is better at preserving the beam emittance. It is also worth noting that the total length of the upramp, plateau, and downramp is 2.5 times the plateau along. Thus, the effective gradient of the full stage is 15 GeV/m and not 37 GeV/m.

4.6.2 Realistic ramps

A fully adiabatic ramp is challenging to construct, therefore, we consider more general ramp profiles. Specifically, we use the following fifth order polynomial

$$n(z) = n_0 \left[6(\frac{z}{L})^5 - 15(\frac{z}{L})^4 + 10(\frac{z}{L})^3\right] \ (0 \le z \le L) \tag{4.24}$$

. This profile has the following properties: $n(0) = n'(0) = 0$, $n(L) = n_0, n'(L) = 0$, $n(L/2) = n_0/2$, $n'(z)$ is maximum at $z = L/2$. We choose the length of the ramp to be the same as before, $L = 3 \times 10^4 k_{p0}^{-1}$. The density upramp is shown as the blue curve in Fig. 4.14. The density downramp is still chosen to be symmetric to that of the upramp. Unlike the fully adiabatic ramp given by Eq. (4.23), the density of the the ramp given by Eq. (4.24) vanishes at the entrance. As a result, both the matched spot size defined in Eq. (4.12), i.e., β_m and the adiabaticity parameter α_m diverge towards infinity as the density approaches 0.

Despite the divergence of the adiabaticity at the beginning of the ramp, we find it is still possible to roughly match the beam. In the absence of ion motion and any longitudinal acceleration, the C-S parameters evolve according to [74]:

$$\frac{1}{2}\beta\beta'' - \frac{1}{4}\beta'^2 + \beta^2 k_\beta^2 = 1 \ , \ \alpha = -\frac{1}{2}\beta' \tag{4.25}$$

Starting from the matched C-S parameters at the density plateau: $\beta_m = \sqrt{2\gamma}k_{p0}^{-1}, \alpha_m = 0$ as the initial conditions for β and α, we numerically integrate Eq. (4.25) backwards along the upramp [90] (see dashed curves in Fig. 4.14), and get β_i, α_i at the plasma entrance. This procedure was used in section 3.4 of chapter 3. It is worth noting that for an adiabatic ramp (where the density does not vanish at the entrance), the C-S parameters calculated using this numerical backward-propagation agree with the matched C-S parameters defined in Eq. (4.17). We then initialize the witness beam's C-S parameters using β_i, α_i in QPAD. Besides that, the drive and witness beam parameters are the same as that used in section 4.6.1, so the initial emittance of the witness beam is still 100 nm.

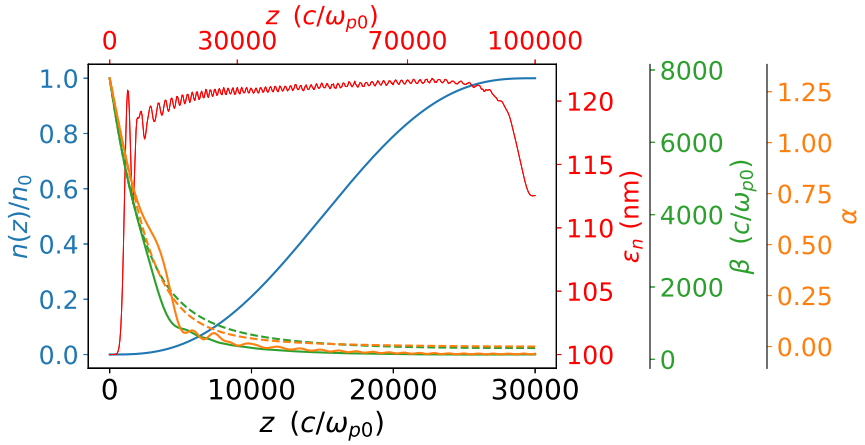

Figure 4.14: The density profile for the fifth order polynomial upramp (blue) and the evolution of the C-S parameters. The solid green and orange curves are the β and α of the witness beam from the QPAD simulation; and the dashed curves are from numerical backward-propagation. The red curve shows the projected emittance evolution in the entire plasma density (upramp, plateau, and downramp) profile shown as the blue curve in Fig. 4.16 (a)

The solid green and orange curves in Fig. 4.14 show the actual evolution of the C-S parameters. Initially they follow the backward-propagated β, α because the density is low near the entrance such that the matched beam spot size is large. Therefore, ion motion effects are small and Eq. (4.25) is valid. Ion motion starts to play a role when the solid curves and the dashed curves deviate from each other where the beam has already entered the adiabatic region. The solid red curve in Fig. 4.14 shows the emittance evolution from a QPAD simulation for the entire plasma density profile shown (upramp, plateau, downramp) in the blue curve in Fig. 4.16(a). As before, the emittance evolution reverses in the downramp, and the overall emittance growth is around 13%.

In order to further justify that using numerical backward-propagation can indeed match the beam into the plasma well, we performed a parameter scan with similar a setup, but a shorter plasma profile to save computation. Here, we choose $L = 2 \times 10^4 k_{p0}^{-1}$ (33.7cm). The density plateau has a length of $10^4 k_{p0}^{-1}$, followed by a density downramp which is symmetric to the upramp. The plasma is still preformed hydrogen plasma. The overall plasma density profile is shown in Fig. 4.15(a). The beam parameters are the same as Sec. 4.4.2, but now the witness beam has a transverse normalized emittance $\epsilon_n = 0.1\mu m$, and an initial energy of 25 GeV with no initial energy spread. The witness beam with the trapezoidal current profile (see Sec. 4.4.2) has a perfect beam loading at the density plateau [36][38], so its energy spread will be nearly 0 as it propagates. Therefore we can isolate the emittance growth due to ion motion. The (r, ξ) simulation box has 10000 by 1000 cells with a resolution of $1 \times 10^{-3} k_{p0}^{-1}$ by $1.2 \times 10^{-2} k_{p0}^{-1}$. The witness beam is sampled with a million numerical particles. The beam particles are pushed every 3D time step $\Delta t = 10\omega_{p0}^{-1}$. There are 16 particles distributed uniformly in the azimuthal direction for each (r-ξ) location where particles are initialized. Both plasma electrons and plasma ions are initialized with 4 particles per (r-ξ) cell. We only keep the lowest $m = 0$ azimuthal mode.

To match the beam into the plasma through this non-adiabatic ramp, we numerically integrate Eq. (4.25) backwards along the upramp, and get $\beta_i = 6087 k_{p0}^{-1}, \alpha_i = 1.3$ at the

plasma entrance. This corresponds to $\sigma^* = 2.7\sigma_{m0}$, $s = 2940k_{p0}^{-1}$, where σ^* is the beam's spot size at the vacuum waist, σ_{m0} is the linearly matched spot size at the density plateau n_0, and s is the vacuum focal position inside the plasma entrance. The emittance grows by only 18% in this case (green dot in Fig. 4.15).

We also performed a parameter scan to compare with the result above. This parameter scan is similar to the one in section 3.4. We tried two different beam vacuum profiles with $\sigma^* = \sqrt{10}\sigma_{m0}$ and $\sigma^* = (10)^{\frac{1}{4}}\sigma_{m0}$ respectively. These two spot sizes are linearly matched to the density $n = 0.01n_0$ (at $z = 2120k_{p0}^{-1}$) and $n = 0.1n_0$ (at $z = 4940k_{p0}^{-1}$) respectively. For each σ^*, we scanned the vacuum focal position s [44]. The result is shown in Fig 4.15 (b). All the parameter combinations for (σ^*, s) we have explored show a larger emittance growth. This implies that the witness beam parameters suggested by numerically integrating Eq. (4.25) gives a reasonably good estimate for obtaining the best results, even though it ignores ion motion. A possible explanation is that this method ensures that in the absence of ion motion, the beam transitions smoothly from the entrance to the density plateau, with minimal oscillations in CS parameters (or spot size). So for the slice at the head of the witness beam, it can go through this smooth transition because it hardly experiences any ion motion.

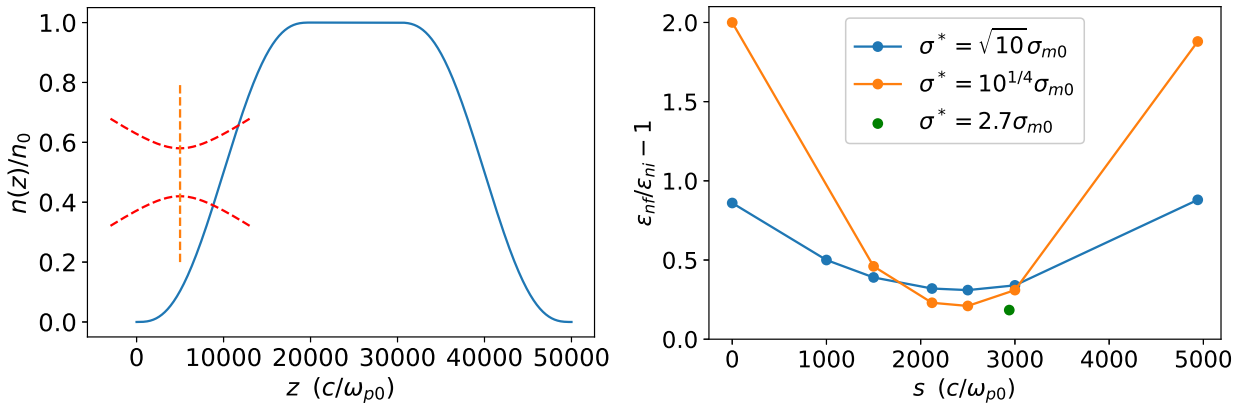

(a) (b)

Figure 4.15: (a) Realistic plasma density profile (blue) with envelope of the witness beam in vacuum (red) and the corresponding vacuum focus (orange). (b) Emittance growth for different vacuum focusing. The green dot corresponds to numerically integrate Eq. (4.25)

4.7 100GeV witness beam simulation

In order to preserve the emittance well, there are 2 important factors. First, at the plasma entrance, ideally the matched witness beam should trigger negligible ion motion, which requires the density at the entrance n_i to be low. Second, ideally the plasma density ramp is adiabatic (a small α_{mi}). However, for a given length of the ramp, improving one aspect will deteriorate the other. This trade-off can be seen by substituting $z = 0$ in Eq. (4.23):

$$\frac{n_i}{n_0} = \frac{1}{\left(1 + \frac{\alpha_{mi} L}{\beta_{m0}}\right)^2} \tag{4.26}$$

From Eq. (4.26) we can see that for a given ramp length L, n_i and α_{mi} change in different directions. If we want to have less initial ion motion by decreasing n_i, we need to sacrifice the adiabaticity of the plasma ramp, and vice versa. Another observation is that for a higher energy beam (e.g. in later acceleration stages), β_{m0} is larger. The constraint from Eq. (4.26)

tells us we have to either increase α_{mi} (so the ramp becomes less adiabatic), or increase n_i (so initially more ion motion is triggered). This makes the emittance preservation for progressively higher energy beams more challenging.

A PBA-LC will require limiting emittance growth over 20+ stages during which the witness beam energy will be higher for the later stages. As can be seen from Eq. (3) the matched spot size scales as $\gamma^{-1/4}$. Therefore, ion motion and emittance growth will be more severe in the later stages. To examine this scaling we carried out simulations with a 100 GeV witness beam. The longitudinal current profile of the witness beam is the same as that used in 4.6.1 such that the beam loading is still optimized at the density plateau. We still used preformed hydrogen plasma. We used the three different plasma density ramps shown in Fig. 4.16(a). The blue upramp is for the same profile used in Fig. 4.14. We match the witness beam through the numerical backward-propagation of Eq. (4.25). The black profile is the same as the solid black curve in Fig. (4.12), with the expression of the upramp given by Eq. (4.23). However, in this case $\alpha_{mi} \sim 2$ since the witness beam's energy is 100 GeV. Furthermore, since the beam's energy is higher, σ_{mi} is smaller, leading to more initial ion motion. The orange upramp is also described by Eq. (4.23), but with $n_i/n_0 = 2.5 \times 10^{-5}$, ensuring the same initial matched spot size, σ_{mi}, as the 25 GeV case. However, the use of a lower density leads to a larger $\alpha_{mi} \sim 4$, such that the adiabatic condition is severely violated. For the black and orange profiles, we match the witness beam directly to the entrance rather than back propagate Eq. (4.25). Fig. 4.16(b) shows the projected emittance evolution corresponding to the profiles in Fig. 4.16(a). We can see that the emittance growth of a 100 GeV witness beam can be limited within 20% if we appropriately choose the plasma density ramp and match the beam.

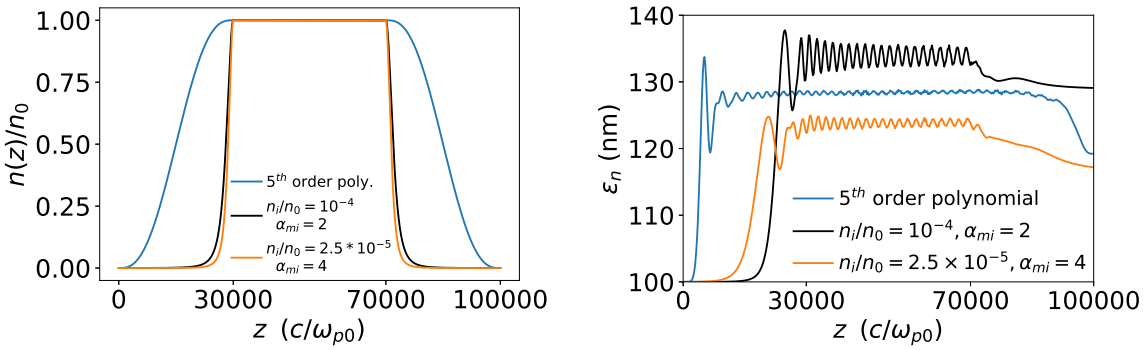

(a) (b)

Figure 4.16: (a) Various plasma density profiles used for a 100 GeV witness beam. The downramps are symmetric to the corresponding upramps. The upramp in blue is the same as the upramp in Fig. 4.14. The density profile in black is that same as in Fig. 4.12(a). The α_{mi} is now 2 rather than 1 because the initial energy of the witness beam becomes 4 times higher (100 GeV compared to 25 GeV). The orange profile has an even lower density at the entrance to such that the witness beam has the same initial σ_m as for the case in Fig. 4.12, but at the expense of a worse adiabatic condition ($\alpha_{mi} = 4$). (b) Projected emittance evolution for a 100 GeV witness beam when matching to the corresponding ramps in (a)

4.8 Summary

In this chapter, we examined emittance growth in a PBA-LC that is induced by the ion collapse caused by the intense space charge forces of matched witness beams. We first introduced and reviewed the ion motion parameter that is used to quantify the degree of ion motion caused by the witness beam. This parameter measures the phase advance of an ion oscillation caused by the space charge of the beam. We also introduced a Gaussian phenomenological model for the ion density profile, which is used in the single particle simulation to gain insight on the evolution of a beam slice in a predetermined nonlinear focusing force.

Next, we studied the ion motion induced emittance growth in a uniform plasma including ion collapse. Self-consistent QPAD simulation results showed that directly matching the witness beam to a uniform plasma will cause $\sim$ 20% emittance growth for a beam with what we refer to as FACET II like parameters ($\epsilon_n \sim 1\mu m$ and 10 GeV) and $\sim$ 80% emittance growth for a beam with what we refer to as LC like parameters ($\epsilon_n \sim 0.1\mu m$ and 25 GeV). We also showed that the emittance growth can be mitigated by focusing the beam to a smaller spot size than the linearly matched spot size such that it is closer to 'some' equilibrium state after ion motion is triggered. This agrees with the results we found from single particle simulations, where we showed that nonlinearly matching the beam's spot size to the estimated steady state spot size of the Gaussian ion model can mitigate the emittance growth significantly.

It is quite challenging to focus a beam to the matched spot size using conventional optics. We proposed to use adiabatic plasma density ramps as matching sections where ion collapse is negligible at the entrance of the ramp but significant at the plateau. These matching sections further reduce the emittance growth. We used an adiabatic plasma density upramp to match the witness beam into the uniform density (plateau) acceleration stage, and an adiabatic plasma density downramp to match the witness beam out from the density plateau. For witness beam parameters that are either close to FACET II like parameters or to LC like parameters, we showed this method can almost perfectly preserve the witness beam emittance from start to end, even though there is a significant amount of ion motion triggered in the uniform acceleration stage. We also showed that by properly choosing the beam's Courant-Snyder parameters at the plasma entrance, the emittance growth can be mitigated for general density ramps which are not adiabatic at lower densities. We closed with a discussion on the trade-off between the adiabaticity of the plasma density ramp and the initial ion motion at the entrance when designing plasma density ramps with a given length.

CHAPTER 5

Additional issues for a plasma based linear collider

5.1 Introduction

In the previous chapters, we investigated the emittance evolution of a trailing electron beam in the blowout regime including the effects of ion motion triggered by matched witness beams, and proposed ways to mitigate this emittance growth. These results provide hope that maintaining high quality electron beams during the acceleration process is possible. Ultimately, we want to build a plasma based linear collider, and there are numerous additional issues to be considered. In this chapter we discuss some of these and how the results in this dissertation impact them. In some cases preliminary simulations results are presented. The results in this chapter are far from definitive but illustrate areas for future work.

In a linear collider, an electron beam will be colliding with a positron beam. Positron acceleration and the matching of positron beams are beyond the scope of this dissertation. It is easy to see that the approaches of matching used in the previous chapters no longer work for the positron beam case. When we use an electron driver (or laser) to drive a nonlinear wake, the ion channel provides an ideal focusing for a trailing electron beam. However, a positron is defocused in the ion channel. The region after the first ion bubble (before the second ion bubble) is where the blown out electrons come back to the axis and form a high electron density. Although this region does provide a focusing for a positron, the size of this region is very small, thus introducing great challenges to load a positron beam. Furthermore, in a ramp the location of the high density region moves relative to the positron bunch, this

makes using density ramps as matching sections not straightforward. Several ideas have been proposed to overcome the challenges of positron acceleration [26, 27, 28], and it is an active research area in the recent years. However, addressing how to match positron beams has not received any attention. In the remainder of this chapter, we will only address additional issues related to matching sections for the electron arm of a PBA-LC. Also note that in the entire chapter, the plasma we used in the simulations is pre-ionized hydrogen plasma.

5.2 Staging

In the previous chapter, we showed that energy doubling of a 25GeV witness beam can be achieved within a single PWFA stage, which is about $\sim$ 1m long. The energy gain in a single wakefield-based accelerator stage is ultimately limited by the energy stored in the driver (either particle beam or laser). In order to build a TeV level linear collider, we need to combine the energy of several individual drivers, by distributing these drivers across many separately driven stages chained together – a concept known as staging [95]. A design for a PBA-LC based on staging is shown [1, 19, 96]. For example, in the design of Ref.[19], 20 PWFA cells are used, where each cell provides 25 GeV of energy to the witness beam in about a meter of plasma, so in the end, the witness beam acquires an energy of 500 GeV.

We start by summarizing the result for the first stage presented in the previous chapter. In Fig. 5.1 the density profile of the ramp, evolution of ϵ_n, spot size,σ, α, γ and σ_γ/γ of the witness beam are presented. We note that due to longitudinal acceleration, the spot size and α of the witness beam are not symmetric between the upramp and downramp, while we have used an upramp and downramp that are completely symmetric. Therefore, compared with the beam parameters at the entrance, the beam at the exit has a smaller spot size because the matched spot size scales as $\gamma^{-1/4}$ which is smaller for a higher energy beam. Furthermore, the matched $\beta = \sqrt{2\gamma}c/\omega_p$ scales as $\sqrt{\gamma}$ which is higher for a higher energy beam. As $\beta \propto \sqrt{\gamma/n}$, the magnitude of α at the exit also scales with $\sqrt{\gamma}$ and is thus larger

than α at the entrance, since $\alpha = -\beta'/2$.

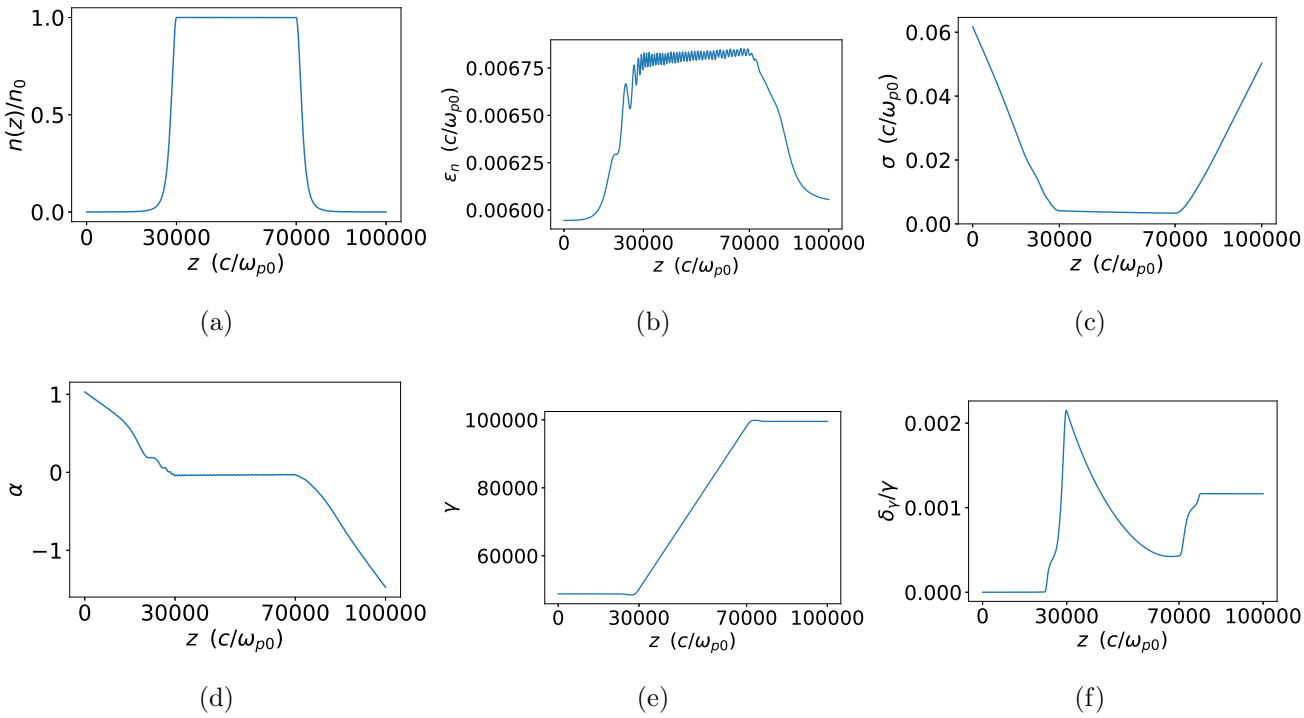

Figure 5.1: Evolution of the witness beam in the first acceleration stage. (a) The plasma density profile. (b) $\sim$ (d) The witness beam's normalized emittance, spot size and α in x direction. (e) and (f): The witness beam's energy and energy spread.

After the witness beam exits the first acceleration stage, it has a negative α. This means the beam is diverging. Before the beam enters the second acceleration stage, the beam needs to be focused again. We assume that through a combination of conventional focusing optics between the first stage and the second stage, the beam's state can be changed from diverging to converging, while having the same spot size, emittance and $|\alpha|$. Essentially, we assume that when the beam enters the second acceleration stage, it has the same spot size as when it exits the first stage, while the α flips sign. In the simulation, we initialize the beam at the entrance of the second stage by taking the raw beam particle data from the last time step of the simulation for stage 1, keeping all the particle positions to be the same while flipping the sign of all the particles' transverse momentum. In other words, for each

particle with coordinate (x, p_x, y, p_y, z, p_z), at the end of the simulation for the first stage, we initialize a corresponding particle with $(x, -p_x, y, -p_y, z, p_z)$ at the entrance of the second stage. Ideally, we should probably use a different plasma density profile for the second stage, since the beam has a higher energy and a larger α after being accelerated in the first stage. However, for simplicity, we use the identical plasma density profile as we used for the first stage.

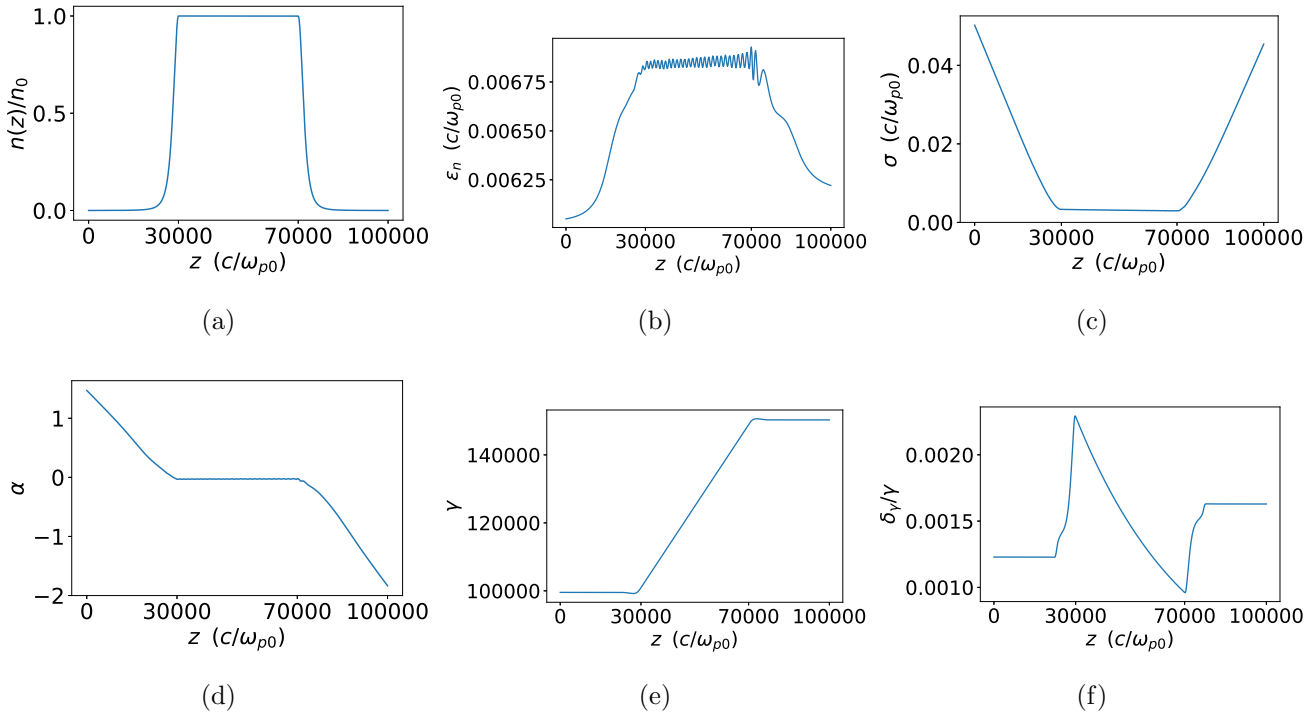

Figure 5.2: Evolution of the witness beam in the second acceleration stage. (a) The plasma density profile. (b) $\sim$ (d) The witness beam's normalized emittance, spot size and α in x direction. (e) and (f): The witness beam's energy and energy spread.

As seen in Fig. 5.2 the emittance is still well preserved. We can see that the beam's emittance growth in stage 2 is slightly larger than in stage 1, but still within 3%. The beam gained another 25GeV, reaching $\sim$ 75 GeV. The energy spread is still very small at the end of the second stage (less than 0.2%). These results taken together with the results shown in Chapter 4 for a 25 GeV witness beam show that if we can somehow successfully construct the

conventional focusing optics between stages as desired, building a PWFA-LC with cascaded stages while preserving the witness beam's emittance is possible for round beams with no offsets. These results are very promising.

5.3 Shaped witness beams

In a PWFA-LC, a high quality witness beam requires not only a low emittance, but also a low energy spread. In order to maintain a low energy spread, ideally all the particles in the beam should be accelerated at the same rate. In other words, they should experience the same accelerating field E_z. It turns out that ion motion does not affect the accelerating field E_z much, since ion motion hardly affects the boundary of the ion bubble, which is the dominant contribution for E_z [23]. Therefore, we do not need to worry about ion motion when analyzing the accelerating field E_z.

It is well known that in the blowout regime, inside the ion channel, E_z is independent of the transverse position [22, 23]. This guarantees the beam will not acquire additional slice energy spread. We also desire that E_z to be a constant along the longitudinal position to ensure the beam will not acquire any energy chirp during acceleration. In 2008, M. Tzoufras et al pointed out that using a trapezoidal longitudinal current profile can flatten the longitudinal accelerating field E_z [36]. (This was reviewed in Chapter 2). Recently, Dalichaouch et al. have refined this theory [38]. In the simulation results shown previously, a trapezoidal current profile has been used, and the energy spread is indeed preserved very well.

In reality, it may be hard to generate a beam with such a trapezoidal current profile. Therefore, we also carried out a simulation using a witness beam that has a tri-Gaussian charge density profile but with the same amount of total charge. We compare the simulation results between a tri-Gaussian beam and a shaped (trapezoidal) beam in the Fig. 5.3 to bracket the possibilities.

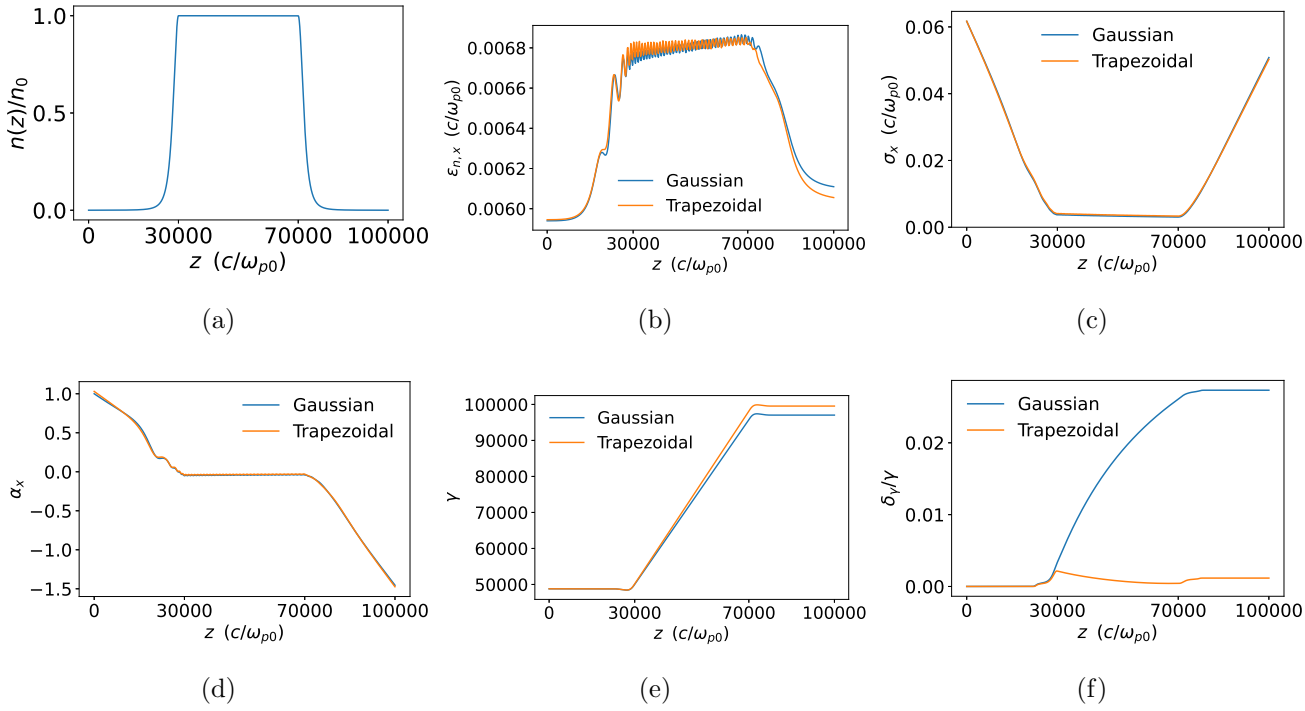

Figure 5.3: Comparison of the tri-Gaussian beam and the trapezoidal beam

We can see from this preliminary simulation that even though the beam has a different current profile, the beam emittance, spot size, α, and energy evolve in a very similar way. We can also see that although the energy spread of the tri-Gaussian beam grows significantly more than the energy spread of the shaped beam, due to the imperfect beam loading, however, it is still less than 3% for the unshaped case.

5.4 Witness beam with an initial offset

So far we have assumed the centroid of the witness beam is on the axis defined by the centroid of the driver and the propagation direction, i.e., there is perfect alignment. In reality, the witness beam's centroid may have a small offset relative to the axis and/or the drive beam might have a head-tail tilt. This could lead to emittance growth and the hosing instability. In this section, we discuss now a misalignment could lead to emittance growth. We consider

cases where there is negligible ion motion, where only the witness beam causes ion motion, and where the both the drive and witness beam cause ion motion.

5.4.1 Insight from no ion motion case

We start with calculating the saturated slice emittance for a witness beam with an initial offset without ion motion using a simple model: We assume the beam slice feels a linear and axisymmetric focusing force from the uniform ion background in the blowout regime. We neglect the asymmetry of the focusing force caused by the perturbation to the plasma electron sheath.

We start from the transport matrix derived from the WKB solution of Hill's equation (Eq.(2.64) or (3.8)). To calculate the beam's emittance, we need to calculate some beam moments $\langle x^2\rangle$, $\langle x'^2\rangle$ and $\langle xx'\rangle$.

Let us first calculate $\langle x^2\rangle$,

$$\begin{aligned}
\langle x^2\rangle &= \langle \left(\sqrt{\frac{\beta_m}{\beta_{mi}}}(\cos\phi + \alpha_{mi}\sin\phi)\, x_i + \sqrt{\beta_m\beta_{mi}}\sin\phi\, x_i'\right)^2 \rangle \\
&= \langle \frac{\beta_m}{\beta_{mi}}(\cos\phi + \alpha_{mi}\sin\phi)^2\, x_i^2\rangle + \langle \beta_m\beta_{mi}\sin^2\phi\, x_i'^2\rangle + \langle 2\beta_m(\cos\phi + \alpha_{mi}\sin\phi)\sin\phi\, x_i x_i'\rangle \\
&\approx \frac{\beta_m}{\beta_{mi}}\langle(\cos\phi + \alpha_{mi}\sin\phi)^2\rangle\langle x_i^2\rangle + \beta_m\beta_{mi}\langle\sin^2\phi\rangle\langle x_i'^2\rangle + 2\beta_m\langle(\cos\phi + \alpha_{mi}\sin\phi)\sin\phi\rangle\langle x_i x_i'\rangle
\end{aligned} \tag{5.1}$$

In the last step, when β_m, β_{mi} are removed from the averaging procedure, we change their definition slightly: They are now evaluated at $\bar{\gamma}$ (while previously they depended on the γ of a specific particle).

When the beam reaches a steady state, the phase mixing is complete and ϕ is evenly distributed. This differs from Chapter 3 where we derived expressions for how the emittance evolves. At the final equilibrium, we have $\langle\cos^2\phi\rangle = \langle\sin^2\phi\rangle = \frac{1}{2}$, $\langle\cos\phi\sin\phi\rangle = 0$, leading to,

$$\begin{aligned}\langle x^2\rangle &= \frac{\beta_m}{2\beta_{mi}}(1+\alpha_{mi}^2)\langle x_i^2\rangle + \frac{1}{2}\beta_m\beta_{mi}\langle x_i'^2\rangle + \beta_m\alpha_{mi}\langle x_i x_i'\rangle \\ &= \frac{\beta_m}{2}(\gamma_{mi}\langle x_i^2\rangle + \beta_{mi}\langle x_i'^2\rangle + 2\alpha_{mi}\langle x_i x_i'\rangle)\end{aligned} \tag{5.2}$$

Similarly, we can evaluate the other moments,

$$\langle x'^2\rangle = \frac{\gamma_m}{2}(\gamma_{mi}\langle x_i^2\rangle + \beta_{mi}\langle x_i'^2\rangle + 2\alpha_{mi}\langle x_i x_i'\rangle) \tag{5.3}$$

and

$$\langle xx'\rangle = -\frac{\alpha_m}{2}(\gamma_{mi}\langle x_i^2\rangle + \beta_{mi}\langle x_i'^2\rangle + 2\alpha_{mi}\langle x_i x_i'\rangle) \tag{5.4}$$

Finally, the three moments can be used to calculate the emittance,

$$\begin{aligned}\epsilon &= \sqrt{\langle x^2\rangle\langle x'^2\rangle - \langle xx'\rangle^2} \\ &= \frac{1}{2}(\gamma_{mi}\langle x_i^2\rangle + \beta_{mi}\langle x_i'^2\rangle + 2\alpha_{mi}\langle x_i x_i'\rangle)\end{aligned} \tag{5.5}$$

Note, this is the same result as in Eq. (3.21). If the beam has an initial offset Δx in position and initial offset $\Delta x'$ in velocity, then

$$x_i = \Delta x + \tilde{x}_i \tag{5.6}$$

$$x_i' = \Delta x' + \tilde{x}_i' \tag{5.7}$$

where $\langle\tilde{x}_i\rangle = \langle\tilde{x}_i'\rangle = 0$ and $\tilde{x}_i$ and $\tilde{x}_i'$ have normal distributions,

$$\tilde{x}_i \sim \mathcal{N}(0,\sigma_i), \quad \tilde{x}_i' \sim \mathcal{N}(0,\sigma_i') \tag{5.8}$$

Therefore, the moments become

$$\langle x_i^2\rangle = \langle(\Delta x + \tilde{x}_i)^2\rangle = \Delta x^2 + \sigma_i^2 \tag{5.9}$$

$$\langle x_i'^2\rangle = \langle(\Delta x' + \tilde{x}_i')^2\rangle = \Delta x'^2 + \sigma_i'^2 \tag{5.10}$$

$$\langle x_i x_i'\rangle = \Delta x\Delta x' + \langle\tilde{x}_i\tilde{x}_i'\rangle \tag{5.11}$$

and upon substitution into Eq. (5.5) we obtain,

$$\epsilon = \frac{1}{2}\left(\gamma_{mi}(\Delta x^2 + \sigma_i^2) + \beta_{mi}(\Delta x'^2 + \sigma_i'^2) + 2\alpha_{mi}(\Delta x \Delta x' + \langle \tilde{x}_i \tilde{x}_i' \rangle)\right) \tag{5.12}$$

which upon substituting $\sigma_i^2 = \epsilon_i \beta_i, \sigma_i'^2 = \epsilon_i = \gamma_i$ and $\langle \tilde{x}_i, \tilde{x}_i' \rangle = -\epsilon_i \alpha_i$

$$\frac{\epsilon}{\epsilon_i} = \frac{1}{2}(\gamma_{mi}\beta_i + \beta_{mi}\gamma_i - 2\alpha_{mi}\alpha_i) + \frac{1}{2\epsilon_i}\left(\gamma_{mi}\Delta x^2 + \beta_{mi}\Delta x'^2 + 2\alpha_{mi}\Delta x \Delta x'\right) \tag{5.13}$$

The first term represents emittance growth due to the initial mismatch (same as Eq. (3.21)), and the second term is emittance growth due to the initial offset (in Δx and $\Delta x'$). This expression is similar to Eq. (20) derived in [80]. Note that in this final state the offsets, $\langle x \rangle$ and $\langle x' \rangle$ vanish.

For the special case when $\alpha_{mi} = 0$ (This can be achieved either by using a uniform plasma or a carefully designed density ramp such that the density gradient vanishes at the entrance), we have $\beta_{mi}\gamma_{mi} = 1$, and the above expression simplifies to,

$$\epsilon = \frac{\epsilon_i}{2}\left(\frac{\beta_i}{\beta_{mi}} + \beta_{mi}\gamma_i\right) + \frac{1}{2}\left(\frac{\Delta x^2}{\beta_{mi}} + \beta_{mi}\Delta x'^2\right) \tag{5.14}$$

If we go one step further and assume the beam is initially matched, then

$$\epsilon = \epsilon_i + \frac{1}{2}\left(\frac{\Delta x^2}{\beta_{mi}} + \beta_{mi}\Delta x'^2\right) \tag{5.15}$$

The second term on the right hand side is the same as Eq. (2) in the proceeding [97]; however no derivation was offered. If we then assume $\Delta x' = 0$, then the emittance growth only due to the initial offset is

$$\frac{\epsilon}{\epsilon_i} = 1 + \frac{1}{2}\frac{\Delta x^2}{\sigma_{mi}^2} \tag{5.16}$$

We can see that the saturated emittance only depends on the beam's initial offset relative to the matched spot size: $\Delta x/\sigma_{mi}$. This makes intuitive sense because for the case where the offset is large compared to the spot size then after phase mixing the spot size will be $\sim \Delta x$, while if Δx is small compared to the spot size, there will only be a small correction.

One piece of insight we can get from Eq. (5.16) is that for the same amount of transverse offset Δx, in order to decrease the saturated emittance, we could increase the beam's initial

matched spot size σ_{mi}. This can be achieved using an adiabatic plasma upramp, so that the plasma has a smaller density at the entrance. In this way, we make the offset Δx "less severe" by matching the beam with a larger initial spot size. Although all the derivation and analysis above is done in the context of linear focusing force (no ion motion), the same idea may be applied to the ion motion case as well.

5.4.2 Uniform plasma

We next offer a brief discussion and some preliminary simulation results on how ion motion effects a beam with an initial offset. To simplify the problem we only consider the case of a density plateau and separate the discussion into the case where the drive beam does or does not trigger ion motion.

5.4.2.1 Drive beam does not trigger ion motion

A witness beam with an initial offset may experience the hosing instability [51, 52, 53]. Fortunately, it was discovered that ion motion triggered by the witness beam itself can suppress the hosing growth [55, 56]. Based on the simulation we carried out in Fig. 4.2 (we use the same simulation parameters here, and the witness beam has no initial energy spread), we shift the initial centroid of the witness beam in the x direction by one matched spot size, $\Delta x = \sigma_m$, while the centroid in y is still on the axis. Although the witness beam starts off-axis in the x direction, we can see in Fig.5.4 (a) that the centroid in x, x_c, is essentially doing a simple harmonic motion, and the amplitude of the oscillation is not amplified like what we see in hosing. This confirms that the ion motion induced by the witness beam alone can mitigate the hosing instability.

In Fig. 5.4 (b), we can see that in the simulation where $\Delta x = \sigma_m$, the emittance evolution in x (blue) and y (orange) are similar, and they are also similar to the emittance evolution when the beam has no initial offset (dashed green). Note that the green dashed curves in

Fig. (5.4) are exactly the same as the blue curves in Fig. (4.2) since they come from the same simulation. We can also see that the orange curve is closer to the dashed green curve than the blue curve, and this makes sense because the beam's initial offset is in the x direction rather than in the y direction. In these simulations there was no energy spread, if there was energy spread the saturated emittance would saturate at Eq. (5.16) and the centroid would vanish.

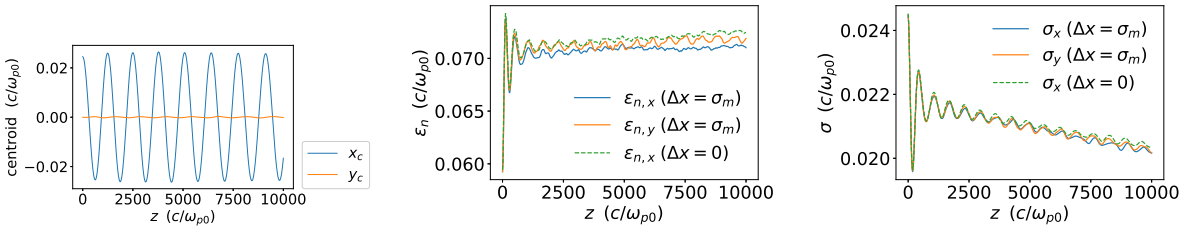

(a) (b) (c)

Figure 5.4: Results from a simulation with a witness beam initially offset from a driver where only the witness beam induces ion motion. (a) The beam centroid evolution. It essentially performs simple harmonic motion in x and essentially remains 0 in y. (b)(c) The emittance and spot size evolution of the beam with an initial offset $\Delta x = \sigma_m$ in two transverse planes. Emittance and spot size evolution are similar to the no offset case.

5.4.2.2 Drive beam triggers ion motion

We just observed that taking advantage of the ion motion triggered by the witness beam can mitigate the hosing instability [56]. The initial offset of the witness beam, instead of oscillating with an increasing amplitude, just oscillates with a nearly constant amplitude, i.e., it does not grow.

However, a witness beam with an oscillating amplitude may not be a great idea because this may lead to appreciable radiation and it could make the final collision at the interaction point more challenging if there is not predictive knowledge of the precise transverse location of the beam.

Fortunately, it was discovered that the ion motion triggered by the drive beam can eliminate this witness beam oscillation [55]. In the simulation used for Fig. 5.4 the drive beam's density is too low to trigger any ion motion ($n_{b0}/n_0 = 4$), and therefore all the ion motion is triggered by the witness beam itself. The basic idea is that if the drive beam's density is high enough to trigger ion motion, ions will collapse on the axis defined by the centroid of the driver. The witness beam will also effect the ions so the axis for the 'effective' ion collapse is between that of the driver and the witness bunch. Thus, the beam gets pulled towards an 'axis' defined where the focusing force vanishes that is off axis the drive beam. It thus overshoots the original axis by a smaller amount. This gradually decreases the offset. The physics is actually quite complicated as it depends on how much ion collapse has been triggered by the drive beam before the location of the witness beam, so simulations are essential.

We demonstrate this process using QPAD [98]. We use FACET II like parameters where there is a uniform preformed hydrogen plasma with density $n_0 = 4 \times 10^{16}\text{cm}^{-3}$ that is $10^4\, k_{p0}^{-1}$ (26.6 cm) long. The drive beam has an initial energy of 10 GeV, a normalized emittance of $\epsilon_n = 1\,\mu$m, and a tri-Gaussian density profile with $\sigma_r = 0.52\,\mu$m, $\sigma_z = 12.8\,\mu$m. It is thus matched to the uniform plasma. The drive beam's peak density $n_{b0} = 4651.4\, n_0$ is high enough to trigger ion motion at the location of the witness beam. The total charge of the drive beam is 1.6 nC. The witness beam has the same initial energy, ϵ_n, σ_r as the drive beam, but with a $\sigma_z = 6.4\,\mu$m. It has a total charge of 0.48 nC. The axial center of the witness beam is located at a distance of $147.7\,\mu$m behind the center of the drive beam, and is offset by $\Delta x = 1\,\mu\text{m} \approx 2\sigma_r$ from the axis. Both beams are initialized with no energy spread, and we also turn off the longitudinal acceleration for both beams to isolate the transverse dynamics. The simulation keeps $m = 0, 1, ..., 5$ azimuthal modes to resolve the asymmetry of the problem (we did the convergence test by running another simulation using $m = 0, 1, ..., 6$ modes and found the results are identical).

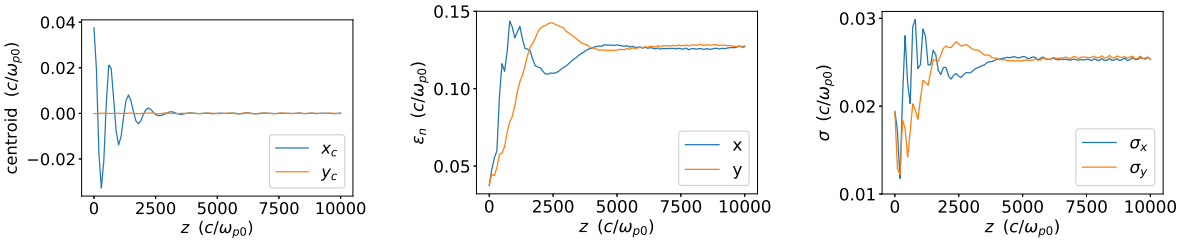

(a) (b) (c)

Figure 5.5: The beam centroid, emittance, transverse spot size evolution for a simulation where the witness beam is offset from the drive beam and both the drive beam and witness beam induce ion motion.

The simulation results are shown in Fig. (5.5). In (a) we can see the centroid of the witness beam quickly damps to zero only after a few betatron oscillations, due to the ion motion triggered by the drive beam. However, this is at the expense of a larger emittance growth, as we can see in (b). The final saturated emittance is 3.4 times the initial emittance, which corresponds to 240% growth. This is significantly larger than the case in Fig.5.4, where the emittance growth is only $\sim 20\%$. The percentage increase in the saturated emittance should scale as $\dfrac{\Delta x^2}{\sigma_{mi}^2}$ (see Eq. (5.16)).

5.4.3 Using adiabatic plasma density ramps to reduce emittance growth

In the previous section, we found in a preliminary simulation that the ion motion from the witness beam can mitigate the hosing instability. If the drive beam does not trigger ion motion, the centroid of the witness beam will oscillate like a simple harmonic oscillator, and the emittance growth is similar to the case when there is no offset. If we use a higher density drive beam, such that the driver also triggers ion motion, the centroid of the witness beam will quickly damp to zero, but at the expense of a much larger emittance growth.

Recall the conclusion from Eq. (5.16) is that for the same initial offset Δx, increasing the initial matched spot size σ_{mi} will reduce the emittance growth. Although this equation is

derived assuming an axisymmetric linear focusing force (no ion motion), this idea may still work in the presence of ion motion (a nonlinear focusing force), since the intuition is the same: When using a larger initial spot size, the offset looks relatively small (compared with the spot size), and this may lead to a better result.

In chapter 4 we used a large σ_{mi} to match the beam into a plasma with small initial ion motion. Here, we use a larger σ_{mi} to make Δx look relatively small. Although the motivation is different, the philosophy is the same. We can achieve the desired goal by using a plasma density ramp, because at the plasma entrance the density is low, the corresponding σ_{mi} is large.

We carried out the following simulation with a similar setup as was used in 5.4.2.2. This time, we include a $1.5\times10^4\, k_{p0}^{-1}$ (39.9 cm) long plasma density upramp before the $10^4\, k_{p0}^{-1}$ (26.6 cm) long density plateau. The density at the entrance of the upramp is 1% of the density at the plateau. We also add a symmetric density downramp after the density plateau. The entire plasma density profile is $4 \times 10^4\, k_{p0}^{-1}$ (106.4 cm) long, shown in Fig. (5.6)(a). The α_m is plotted as the red dashed curve. It forms half of a sinusoidal oscillation inside the upramp (downramp), with $\mathcal{A} = |\alpha_m|$ bounded by 0.1, so the adiabatic condition holds for the entire plasma. We used this type of density upramp so that the witness beam can be matched to the entrance of the plasma with $\alpha = 0$. Note that because the witness beam parameters we used here are FACET II like, which have $\mathcal{A} < 0.1 \ll 1$ (the adiabatic condition strictly holds), the emittance growth is insensitive to the exact form of the ramp. However, if the witness beam parameters are LC like, for ramps with a reasonable length, $\mathcal{A} \sim 1$, like what we showed in section 4.6.1. In that case, the upramp corresponding to an α_m with a constant slope (see Fig. 4.12(a)) works better in terms of emittance preservation. One hypothesis is that for the type of ramp in Fig. 4.12(a), the matched C-S parameters at the entrance agree with the C-S parameters at the entrance calculated from numerical backward-propagation using Eq. (4.25) (see section 4.6.2). But more investigations are needed.

The drive beam is initialized with the same total charge, spot size σ_r, and bunch length

σ_z at the plasma entrance as for the case in 5.4.2.2. However, in order that the matched spot size be the same, the emittance of the drive beam is 10 times smaller ($\epsilon_n = 0.1\,\mu$m) to compensate for the lower density at the entrance. The witness beam still has the same total charge and emittance, and has no initial energy spread. However, the matched spot size of the witness beam is now $1.63\,\mu$m. Everything else remains the same (the initial transverse offset of the witness beam Δx, the azimuthal mode number m, etc.).

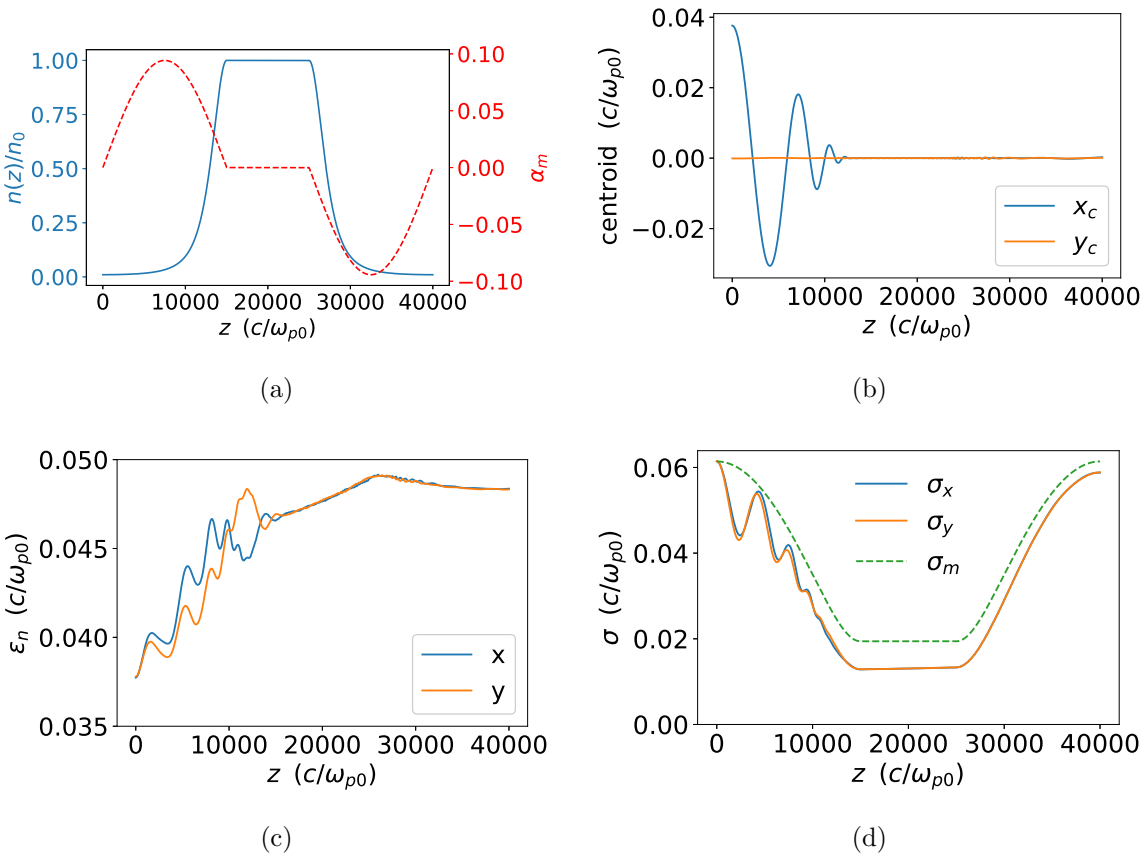

Figure 5.6: (a) Plasma density profile (b)(c)(d) Evolution of the centroid, emittance, and transverse spot sizes of the witness beam with an initial offset $\Delta x = 1\,\mu$m.

The simulation results are shown in Fig. 5.6. In (b) we can see the offset of the witness beam damps very quickly within a few betatron oscillations, and becomes essentially zero before even entering the density plateau. Again, this is due to the ion motion induced by

the drive beam. In Fig. 5.6(c) we found that the emittance growth is only around 30%. Compared with Fig. 5.5(b), we can see that using adiabatic plasma density ramps reduces the emittance growth by almost an order of magnitude!

5.5 Asymmetric beams

In LC designs, asymmetric emittances are used to minimize the beamstrahlung that occurs during disruption at the final focus. In such a case, the ion collapse also becomes asymmetric, and emittance growth becomes more complicated. Preliminary results in Ref. [47] showed that the growth of $\sqrt{\epsilon_{Nx}\epsilon_{Ny}}$ is even smaller than the symmetric case, assuming we still linearly match the beam to the plasma.

In this section, we try to use QPAD to self-consistently simulate an asymmetric witness beam, which Ref. [47] was not able to do. However, the asymmetric witness beam used in Ref. [47] has a large ratio of $\epsilon_{Nx}/\epsilon_{Ny}$ ($\epsilon_{Nx}/\epsilon_{Ny} = 2\,\mu\text{m}/0.005\,\mu\text{m} = 400$), which is very challenging for QPAD because we would need to use numerous azimuthal modes to simulate such a highly asymmetric beam. Therefore, we used a slightly asymmetric witness beam with $\epsilon_{Nx} = 2\mu\text{m}, \epsilon_{Nx} = 0.5\mu\text{m}$ instead for our preliminary study.

We are interested in how the adiabatic plasma density ramps affect the emittance evolution for this asymmetric witness beam. To investigate this, we use the simulation parameters from section 4.6.1. We still use the plasma density profile described by the black curve in Fig. 4.12(a). The driver is still the same as the one described in section 4.6.1. Most of the witness beam parameters are also the same, but with the following differences: 1. The initial normalized emittance in x, y are $\epsilon_{Nx} = 2\mu\text{m}, \epsilon_{Nx} = 0.5\mu\text{m}$ respectively corresponding to initially matched spot sizes of $\sigma_x = 1.468\mu\text{m}$ and $\sigma_y = 0.734\mu\text{m}$ respectively, 2. The longitudinal resolution is $\Delta\xi = 5 \times 10^3 k_{p0}^{-1}$, and 3. We used $m = 0, 1, 2$ azimuthal modes.

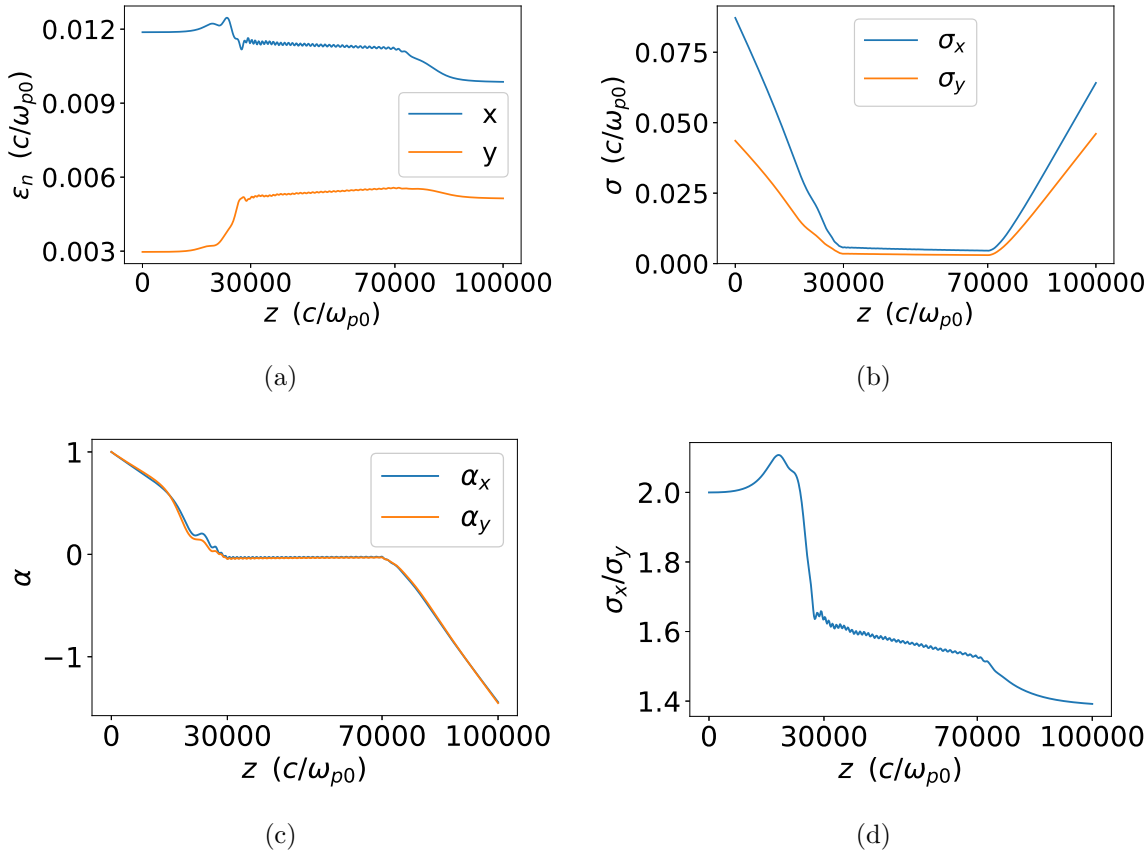

Figure 5.7: Normalized emittance, spot size, α, and aspect ratio, σ_x/σ_y evolution for an asymmetric witness beam.

The evolution of the witness beam is shown in Fig. (5.7). Surprisingly, the emittance in x, which starts with a larger value, decreases throughout the entire process! It turns out that ϵ_{Nx} decreases by 17%, and ϵ_{Ny} increases by 73%. If we calculate their geometric mean, we find that $\sqrt{\epsilon_{Nx}\epsilon_{Ny}}$ has only a 20% growth. The spot sizes in the two transverse planes are shown in Fig. 5.7(b). From the spot size evolution we can see that the degree of asymmetry of the beam seems to decrease as the beam propagates. This is shown explicitly in Fig. 5.7(d), where the aspect ratio, σ_x/σ_y, decreases from 2 to 1.4, suggesting that the beam becomes more "round" when it exits the plasma ramp. The α in two planes evolve in a similar way, as shown in Fig. 5.7(c).

Note that this study is very preliminary. For more asymmetric beams the use of a full quasi-static code with mesh refinement, such as QuickPIC will be more appropriate.

5.6 Afterburner concept

The afterburner concept is the idea of placing a short plasma section at the end of an existing collider to double the center of mass energy at the collision point [2]. Electrons and positrons are accelerated to the collider's nominal operating energy, overcompressed to form two microbunches each, then the trailing half-bunches are doubled in energy over a few meters in the plasma afterburner. An afterburner could be also be placed at the end of either a LWFA or PWFA linear collider.

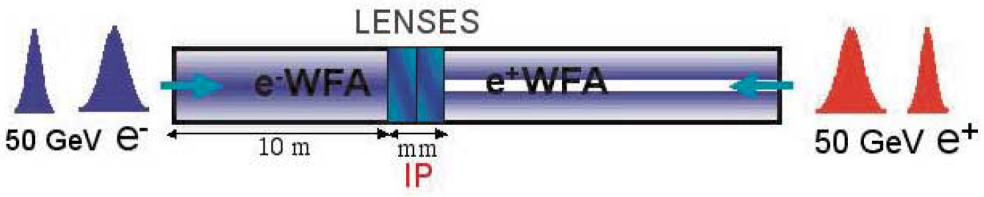

Figure 5.8: Schematic of the plasma afterburner concept [2]. Plasma wake field acceleration (WFA) sections are placed at the interaction point (IP); short plasma lens sections of higher density further focus the beams before collision. Note that the WFAs are not symmetric; the positron section may be longer to reach the same energy and may have a channel to enhance the wake.

Simulating an afterburner stage at the 500 GeV energy level is computationally challenging, since doubling the energy of a beam at this very high energy requires tens of meters acceleration distance and very small matched spot sizes. This requires running very long simulations with many cells. However, typically nothing really interesting happens in the uniform acceleration section because the beam has stabilized. The emittance does not really grow because it has already saturated, and the spot size gradually decreases due to

the acceleration (adiabatic damping). Therefore, we can simulate a much shorter uniform acceleration section for the plasma afterburner, while gaining most of the physics insight.

We carry out simulations with the drive and witness beams having 500 GeV while the emittances and current profiles are the same as for the cases in section 4.6.1. For those higher energy beams the matched spot sizes are $20^{1/4}$ times smaller, which would require much smaller cell sizes to resolve. However, we have found that even for under resolved simulations, $\Delta r \sim \sigma_m$, that the emittance growth is similar to the properly resolved cases. Thus, in this preliminary simulation we used the same Δr as was used in section 4.6.1. There are only 3.5 Δr across the minimal spot size of the witness beam in the simulation. We match the witness beam directly into the uniform plasma with density $n_0 = 10^{17}\text{cm}^{-3}$. We can see that due to ion motion, the emittance quickly doubles and then saturates, similarly to what happens to a 25 GeV beam shown in [47] and in chapter 4.

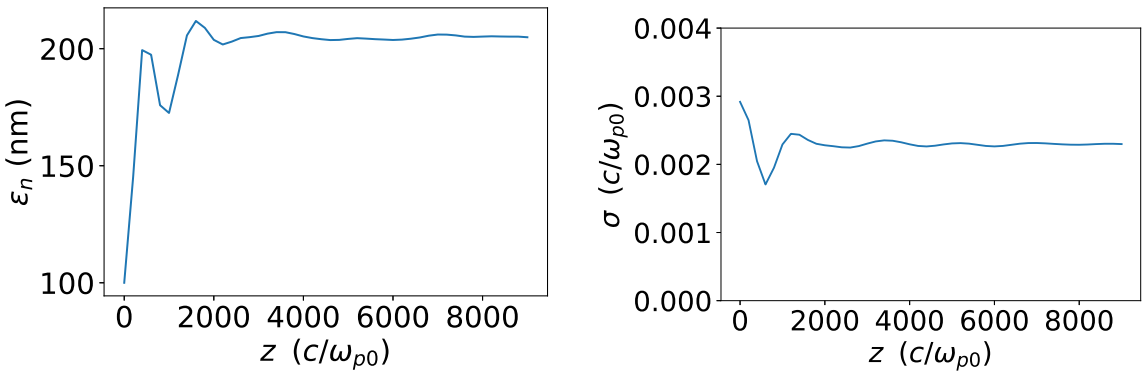

(a) (b)

Figure 5.9: Emittance and spot size evolution of a witness beam with initial energy of 500 GeV, initial emittance of 100 nm when directly matching to a uniform plasma with density $n_0 = 10^{17}\text{cm}^{-3}$

Next, we investigate the effect of plasma density ramps on the witness beam. We still use a uniform plasma with density $n_0 = 10^{17}\text{cm}^{-3}$, but add realistic plasma density ramps at both the entrance and the exit of the density plateau. The entire plasma density profile

is the same as the blue curve in Fig. 4.16(a).

To study how the emittance evolution depends on the initial emittance of the witness beam, we ran three simulations, where the initial emittance of the witness beam is 100 nm, 200 nm, and 400 nm respectively. For each case, we match the witness beam into the plasma using the numerically-backpropagation method described in section 4.6.2. The simulation results are shown in Fig. 5.10. Note that there are 3.5, 5, 8 Δr in the minimal spot size of the witness beam in the simulation for cases where the initial emittances are 100 nm, 200 nm, 400 nm respectively.

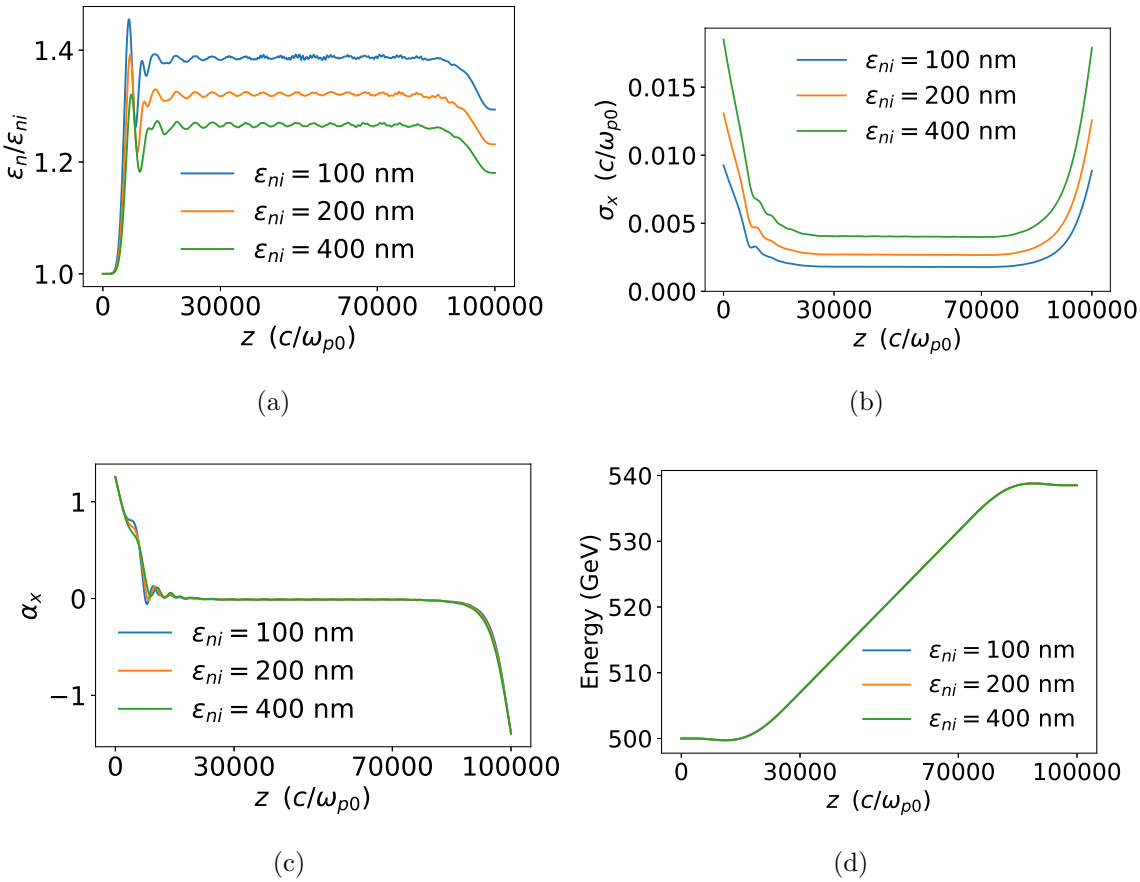

Figure 5.10: Evolution of 500 GeV witness beams with initial emittance of 100 nm, 200 nm, 400 nm respectively. The plasma density profile used in the simulation is the blue curve in Fig. 4.16(a)

We can see in Fig. 5.10(a) that the beam with a smaller initial emittance has a larger percentage emittance growth. This is intuitive since smaller emittance corresponds to smaller spot size (as we can see in Fig. 5.10(b)), which leads to more ion motion. We also note that $20\% \sim 40\%$ emittance growth for a witness beam with a few hundred nanometers emittance may be satisfactory for the afterburner. In Fig. 5.10(c) and (d) we can see that the α and energy of the beams evolve in a very similar way, despite the difference in their initial emittance.

5.7 Summary

In this chapter, we described some preliminary investigations of several additional issues for a plasma-based linear collider through QPAD simulations. The first one is staging. In order to build a TeV class linear collider, multiple acceleration stages must be cascaded together. Preliminary QPAD simulation results showed that after the beam exits from the previous acceleration stage, the beam's emittance growth in the next stage will be similar to that in the previous stage. In this simulation we refocused the beam to the same spot size but opposite α at the entrance of the next acceleration stage. This requires an accurate beam delivery / focusing system between two adjacent stages. We also showed that a shaped witness beam which provides better beam loading can provide improved energy spread of the witness beam. It was found that the emittance growth induced by ion motion is still limited when using a matching section. The third issue is the offset of the witness beam. Although it has been shown that ion motion triggered by the witness beam can mitigate the hosing instability, resulting in the witness beam oscillating around the axis, this is still not desirable for a collider as it can also lead to significant betatron radiation as well as make it difficult to collide the beams. We showed that ion motion induced by the drive beam can 'drag' the centroid of the witness beam back on the axis, but at an expense of a large emittance growth. Inspired by the analytical expression of the saturated emittance in the absence of ion motion,

increasing the initial matched spot size of the beam can mitigate the emittance growth for a given initial offset. This can be achieved by using a plasma density ramp. Preliminary results showed that the combination of a carefully chosen drive beam that triggers ion motion and an adiabatic plasma ramp can eliminate the beam's initial offset and reduce the emittance growth by an order of magnitude. We also explored the evolution of an asymmetric witness beam in a plasma with adiabatic density ramps. Preliminary result showed that in the two transverse planes, the emittance with a larger initial value can decrease during the entire process. Last, we carried out simulations with 500 GeV witness beams with different initial emittance to get insight for an afterburner. The parameter scan showed that the beam with a smaller initial emittance has a larger emittance growth in percentage. The results in this chapter are not meant to be definitive, but rather to be an impetus for future work.

CHAPTER 6

Summary and final thoughts

Experiments on plasma-based acceleration have demonstrated ultra-high acceleration gradients, acceleration over meter and pump depletion distances, high energy transfer efficiency from a drive beam to a witness beam, positron acceleration, and staging. Therefore, there are now serious conversations regarding the development of roadmaps for true designs of a plasma-based linear collider. For example, while each of the aforementioned milestones relate to essential components of a collider, they have not been demonstrated for a true prototype of a single or multiple stage of a PBA-LC. Thus many challenges remain. Emittance preservation is believed to be one of the biggest challenges. In this dissertation, the evolution and growth of emittance, and the mitigation of emittance growth are investigated for the nonlinear blowout regime of PBA. Different scenarios were considered, including a plasma plateau, a plateau with density up and downramp matching sections, cases with and without acceleration, and cases with and without ion motion. Parameters close to FACET II (10 GeV and $\epsilon_n = 1\mu m$) and (parameters those relevant to a PBA-LC (25 GeV and $\epsilon_n = 0.1\mu m$) were studied.

In chapter 2, important concepts and results are reviewed and new results are given to set the stage for the later chapters. Details on the motion of a single witness beam particle were given. The "exact" solution to the transverse equation of motion of a single beam particle was derived under the weak assumption that acceleration happens adiabatically. Approximate solutions were obtained under the additional assumption that the plasma density changes adiabatically, which is just the WKB assumption. These solutions were used to introduce

the C-S parameters for a single particle and it was shown how they are related to the C-S parameters for an ensemble or particles, i.e., a beam. The transport matrix for various cases were given as well as the concepts of the geometric and normalized emittance of a beam. It was shown that the emittance of a matched beam is conserved even if there is energy spread so long as there is no acceleration; and it was shown that the normalized emittance is conserved where there is no energy spread but there is acceleration. While the results presented in Chapter 2 are mostly review it does contain some new perspectives and results. Furthermore, it provides a comprehensive description on emittance preservation from both the single particle and beam points of view. These results will be used in Chapter 3 to study the beam evolution in plasma density ramps.

In Chapter 3, analytical expressions for the evolution of the beam emittance and the C-S parameters in an arbitrary adiabatic plasma profile are derived base on the WKB solution to the Hill like equation (the acceleration of the beam and ion motion inside the plasma are neglected). Several important corollaries of the expressions were given: 1. The beam emittance can be preserved in an adiabatic plasma ramp under the matching condition assumption, even when the beam has an initial energy spread and 2. The emittance growth for an unmatched beam is minimized when it is focused to the same vacuum plane as for a matched beam. These corollaries were confirmed with 3D QuickPIC simulation results.

Simulations with parameters that are consistent with FACET II capabilities showed that even when some assumptions used in deriving the analytical expressions are not satisfied, the emittance growth can still be minimized by choosing the optimal focal plane. QuickPIC simulations for FACET II experiments where the lithium plasma source is sandwiched by a helium buffer gas showed how the emittance evolution was affected by the nonlinear focusing force triggered by the field ionization of the helium gas.

However, the parameters available at FACET II cannot meet the requirement of the luminosity of a linear collider. In some plasma-based LC designs the extreme accelerating beam parameters are expected to trigger background ion motion. This means the important

assumption about "fixed ion background" we made in chapter 3 is no longer valid. Ion motion could be deleterious as it can lead to longitudinally varying nonlinear focusing forces and thus result in emittance growth of the beam. In Chapter 4, a mitigation method that uses an adiabatic plasma density ramp as a matching section was proposed. This concept requires matching the witness beam to the low density plasma entrance, where the beam initially has a large matched spot size so the ion motion effects are relatively small. As the beam propagates in the plasma density upramp (downramp), it is adiabatically focused (defocused) and its distribution evolves slowly towards an equilibrium distribution including the effects of the adiabatically changing ion motion. Simulation results from QPAD show that within a single acceleration stage, this concept can limit the projected emittance growth to only $\sim$2% for a 25 GeV 100 nm and $\sim$20% for a 100 GeV, 100 nm emittance witness beam respectively. The trade-off between the adiabaticity of the plasma density ramp and the initial ion motion at the entrance for a given length of the plasma density ramp is also discussed.

In Chapter 5, additional issues for building a plasma based linear collider are investigated using particle-in-cell simulations. Preliminary simulation results showed that: 1. Even in the presence of ion motion, the beam's emittance growth in a later stage can be similar to that in the previous stage, assuming the beam can be properly delivered and refocused between stages. 2. A shaped witness beam can improve beam loading, i.e., reduce the variation of the accelerating field, and thus reduce the induced energy spread during acceleration. The emittance evolution is therefore still dominated by ion motion, given that the beam is matched properly. 3. Ion motion from the drive beam and plasma density ramps together can eliminate an offset of the witness beam with respect to the drive beam while reducing the emittance growth by a significant amount. 4. When an asymmetric witness beam evolves in a plasma with density ramps, the emittance in the direction with the larger initial value can decrease over the entire process. 5. In an afterburner, the emittance growth of a 500 GeV witness beam with a few hundred nanometers emittance is estimated to be 20% $\sim$ 40%, and the emittance growth in percentage appears to be smaller if the initial emittance is larger.

The results of this dissertation show that emittance preservation for the electron arm of a PBA-LC may be possible. The results point toward the need of for carefully designed experiments on the use of matching sections. The results also indicate areas for future theoretical and simulation work. These include emittance preservation and matching in positron acceleration and alignment and emittance preservation of asymmetric beams.

APPENDIX A

Conserved quantity for a plasma particle in a wakefield

For completeness, in this appendix we will derive a conservation law for a plasma electron moving in a plasma wave wakefield that is valid within the QSA,

$$\gamma - p_z = 1 + \psi \tag{A.1}$$

where p_z and ψ are in normalized units.

We start from the equation of momentum in the axial directions,

$$\frac{dp_z}{dt} = -e(\mathbf{E} + \mathbf{v} \times \mathbf{B}) \cdot \hat{z} = -E_z - (\mathbf{v} \times \mathbf{B}) \cdot \hat{z} \tag{A.2}$$

and the equation of conservation of energy,

$$\frac{d(\gamma mc^2)}{dt} = -e\mathbf{v} \cdot \mathbf{E} = -\mathbf{v} \cdot \mathbf{E} \tag{A.3}$$

where we henceforth use normalized units, so $e = 1$, $m = 1$, and $c = 1$. Substituting Eq. (1.4) (which has the same form in normalized units) into Eqs. (A.2) and (A.3) gives,

$$\begin{aligned} \frac{dp_z}{dt} &= \frac{\partial \phi}{\partial z} + \frac{\partial A_z}{\partial t} - (\mathbf{v} \times (\nabla \times \mathbf{A})) \cdot \hat{z} \\ &= \frac{\partial \phi}{\partial z} + \frac{\partial A_z}{\partial t} - (\nabla \mathbf{A} \cdot \mathbf{v} - \mathbf{v} \cdot \nabla \mathbf{A}) \cdot \hat{z} \\ &= \frac{\partial \phi}{\partial z} + \frac{\partial A_z}{\partial t} - (\frac{\partial \mathbf{A}}{\partial z} \cdot \mathbf{v} - (\mathbf{v} \cdot \nabla) A_z) \end{aligned} \tag{A.4}$$

and

$$\frac{d\gamma}{dt} = \mathbf{v} \cdot \nabla \phi + \mathbf{v} \cdot \frac{\partial \mathbf{A}}{\partial t} \tag{A.5}$$

Subtracting Eq. (A.4) from Eq. (A.5) gives,

$$\begin{aligned}\frac{d}{dt}(\gamma - p_z) &= (\mathbf{v}\cdot\nabla)(\phi - A_z) + \mathbf{v}\cdot(\frac{\partial}{\partial t} + \frac{\partial}{\partial z})\mathbf{A} - \frac{\partial\phi}{\partial z} - \frac{\partial A_z}{\partial t} \\ &= (\mathbf{v}\cdot\nabla + \frac{\partial}{\partial t})(\phi - A_z) + \mathbf{v}\cdot(\frac{\partial}{\partial t} + \frac{\partial}{\partial z})\mathbf{A} - (\frac{\partial}{\partial t} + \frac{\partial}{\partial z})\phi \\ &= \frac{d}{dt}\psi + \mathbf{v}\cdot(\frac{\partial}{\partial t} + \frac{\partial}{\partial z})\mathbf{A} - (\frac{\partial}{\partial t} + \frac{\partial}{\partial z})\phi\end{aligned} \tag{A.6}$$

where we used Eq. (1.24) and $\frac{d}{dt} \equiv \frac{\partial}{\partial t} + \mathbf{v}\cdot\nabla$ for field quantities in the last step. We recognize that $\frac{\partial}{\partial t} + \frac{\partial}{\partial z} = \frac{\partial}{\partial s}$ (see Eqs.(1.6) and (1.7)), which can be neglected within the QSA to obtain

$$\frac{d}{dt}(\gamma - p_z - \psi) = 0 \tag{A.7}$$

from which it follows that $\gamma - p_z - \psi$ is a constant. If we assume that the plasma is at rest in front of the beam, where $\psi = p_z = 0$, then,

$$\gamma - p_z - \psi = (\gamma - p_z - \psi)|_{t=-\infty} = 1 \tag{A.8}$$

which is just Eq. (A.1).

APPENDIX B

General analysis of a second order ordinary differential equation

In this appendix we analyze properties for solutions to general second order homogeneous differential equations of the following form,

$$x''(z) + p(z)x'(z) + q(z)x(z) = 0 \tag{B.1}$$

which is the general form of the transverse equation of motion of a particle in a wakefield. If we define $p(z) = \gamma'(z)/\gamma(z)$ and $q(z) = k_\beta(z)^2$ then Eq. (B.1) reduces to Eq. (2.9). Without longitudinal acceleration, $p(z) = 0$, and Eq. (B.1) reduces to Eq. (2.11).

We denote the two independent solutions of Eq. (B.1) as $x_1(z)$ and $x_2(z)$. From the theory of differential equations, the Wronskian, defined as,

$$W(z) = \begin{vmatrix} x_1(z) & x_2(z) \\ x_1'(z) & x_2'(z) \end{vmatrix} \tag{B.2}$$

is non-zero everywhere.

Using Eq. (B.1), it is easy to show $W'(z) = -p(z)W(z)$ which can be integrated to get

$$W(z) = W(z_0)e^{-\int_{z_0}^{z} p(z)dz} \tag{B.3}$$

which implies that if $W(z_0)$ does not vanish then $W(z)$ never vanishes. We note that if W does not vanish then the matrix constructed for the linearly independent solutions, x_1 and x_2,

$$\begin{pmatrix} x_1(z) & x_2(z) \\ x_1'(z) & x_2'(z) \end{pmatrix} \tag{B.4}$$

is invertible.

Therefore, the general solutions for x and x' are

$$x(z) = C_1 x_1(z) + C_2 x_2(z) \tag{B.5}$$

and

$$x'(z) = C_1 x_1'(z) + C_2 x_2'(z) \tag{B.6}$$

These can be combined as

$$\begin{pmatrix} x(z) \\ x'(z) \end{pmatrix} = \begin{pmatrix} x_1(z) & x_2(z) \\ x_1'(z) & x_2'(z) \end{pmatrix} \begin{pmatrix} C_1 \\ C_2 \end{pmatrix} \tag{B.7}$$

where the two constants can be obtained from the initial conditions: $x(0)$ and $x'(0)$ as follows. We evaluate Eq. (B.7) at $z = 0$

$$\begin{pmatrix} x(0) \\ x'(0) \end{pmatrix} = \begin{pmatrix} x_1(0) & x_2(0) \\ x_1'(0) & x_2'(0) \end{pmatrix} \begin{pmatrix} C_1 \\ C_2 \end{pmatrix} \tag{B.8}$$

and then recall that since $W \neq 0$ this can be inverted to obtain

$$\begin{pmatrix} C_1 \\ C_2 \end{pmatrix} = \begin{pmatrix} x_1(0) & x_2(0) \\ x_1'(0) & x_2'(0) \end{pmatrix}^{-1} \begin{pmatrix} x(0) \\ x'(0) \end{pmatrix} \tag{B.9}$$

This can then be substituted back into Eq. (B.8) to obtain

$$\begin{pmatrix} x(z) \\ x'(z) \end{pmatrix} = \begin{pmatrix} x_1(z) & x_2(z) \\ x_1'(z) & x_2'(z) \end{pmatrix} \begin{pmatrix} x_1(0) & x_2(0) \\ x_1'(0) & x_2'(0) \end{pmatrix}^{-1} \begin{pmatrix} x(0) \\ x'(0) \end{pmatrix} \tag{B.10}$$

We can now define a transformation matrix in trace space as

$$M_{trace} = \begin{pmatrix} x_1(z) & x_2(z) \\ x_1'(z) & x_2'(z) \end{pmatrix} \begin{pmatrix} x_1(0) & x_2(0) \\ x_1'(0) & x_2'(0) \end{pmatrix}^{-1} \tag{B.11}$$

The determinant of M_{trace} can be calculated,

$$\begin{aligned} det(M_{trace}) &= det\begin{pmatrix} x_1(z) & x_2(z) \\ x_1'(z) & x_2'(z) \end{pmatrix} det(\begin{pmatrix} x_1(0) & x_2(0) \\ x_1'(0) & x_2'(0) \end{pmatrix}^{-1}) \\ &= \frac{det\begin{pmatrix} x_1(z) & x_2(z) \\ x_1'(z) & x_2'(z) \end{pmatrix}}{det\begin{pmatrix} x_1(0) & x_2(0) \\ x_1'(0) & x_2'(0) \end{pmatrix}} \\ &= \frac{W(z)}{W(0)} \\ &= e^{-\int_0^z p(z)dz} \end{aligned} \tag{B.12}$$

from which it follows that the $det(M_{trace}) = 1$ only when $p(z) = 0$. Therefore, in general, the determinant of the transformation matrix (Jacobian) in trace space is not unity, and the area in trace space is not conserved (unless $p(z) = 0$).

However, as we show next the determinant of the transformation matrix in phase space is unity, and thus the phase space area is conserved. To see this, we apply the result from our general theory to the specific case, described by Eq. (2.9) which we rewrite here

$$x'' + \frac{\gamma'}{\gamma}x' + k_\beta^2 x = 0 \tag{B.13}$$

where $\frac{\gamma'}{\gamma} = p(z)$ and $k_\beta^2 = q(z)$ for the general case. Therefore, for this case,

$$\begin{aligned} det(M_{trace}) &= e^{-\int_0^z \frac{\gamma'}{\gamma}dz'} \\ &= \frac{\gamma_0}{\gamma} \end{aligned} \tag{B.14}$$

This result indicates that $\gamma\, det(M_{trace})$ is constant and thus phase space, (x, p_x), and not trace space area is conserved. This can also be proven straightforwardly by following the same procedure from above. We first rewrite x, p_x in terms of x_1, x_2, x_1', x_2' and γ

$$\begin{pmatrix} x(z) \\ p_x(z) \end{pmatrix} = \begin{pmatrix} x(z) \\ \gamma x'(z) \end{pmatrix} = \begin{pmatrix} x_1(z) & x_2(z) \\ \gamma x_1'(z) & \gamma x_2'(z) \end{pmatrix} \begin{pmatrix} C_1 \\ C_2 \end{pmatrix} \tag{B.15}$$

The constants C_1 and C_2 can be evaluated by evaluating Eq. (B.15) at $z = 0$

$$\begin{pmatrix} x(0) \\ p_x(0) \end{pmatrix} = \begin{pmatrix} x(0) \\ \gamma_0 x'(0) \end{pmatrix} = \begin{pmatrix} x_1(0) & x_2(0) \\ \gamma_0 x_1'(0) & \gamma_0 x_2'(0) \end{pmatrix} \begin{pmatrix} C_1 \\ C_2 \end{pmatrix} \tag{B.16}$$

and then inverting Eq. (B.16) to obtain

$$\begin{pmatrix} x(z) \\ p_x(z) \end{pmatrix} = \begin{pmatrix} x_1(z) & x_2(z) \\ \gamma x_1'(z) & \gamma x_2'(z) \end{pmatrix} \begin{pmatrix} x_1(0) & x_2(0) \\ \gamma_0 x_1'(0) & \gamma_0 x_2'(0) \end{pmatrix}^{-1} \begin{pmatrix} x(0) \\ p_x'(0) \end{pmatrix} \tag{B.17}$$

The phase space transformation matrix is therefore,

$$M_{phase} = \begin{pmatrix} x_1(z) & x_2(z) \\ \gamma x_1'(z) & \gamma x_2'(z) \end{pmatrix} \begin{pmatrix} x_1(0) & x_2(0) \\ \gamma_0 x_1'(0) & \gamma_0 x_2'(0) \end{pmatrix}^{-1} \tag{B.18}$$

The determinant for M_{phase} is therefore

$$\begin{aligned} det(M_{phase}) &= det \begin{pmatrix} x_1(z) & x_2(z) \\ \gamma x_1'(z) & \gamma x_2'(z) \end{pmatrix} det(\begin{pmatrix} x_1(0) & x_2(0) \\ \gamma_0 x_1'(0) & \gamma_0 x_2'(0) \end{pmatrix}^{-1}) \\ &= \frac{\gamma}{\gamma_0} det \begin{pmatrix} x_1(z) & x_2(z) \\ x_1'(z) & x_2'(z) \end{pmatrix} det(\begin{pmatrix} x_1(0) & x_2(0) \\ x_1'(0) & x_2'(0) \end{pmatrix}^{-1}) \\ &= \frac{\gamma}{\gamma_0} det(M_{trace}) \\ &= \frac{\gamma}{\gamma_0} \frac{\gamma_0}{\gamma} \\ &= 1 \end{aligned} \tag{B.19}$$

The determinant of the transformation matrix (Jacobian) in phase space is unity, and the phase space area is conserved.

APPENDIX C

WKB analysis of the Hill like equation

The WKB theory has numerous subtleties and requires insight. We first introduce a small parameter ϵ into the equation,

$$\epsilon^2 x''(z) + k_\beta(z)^2 x(z) = 0 \tag{C.1}$$

We then assume an ansatz for $x(z)$, which is called the WKB series,

$$x(z) \sim \exp\left[\frac{1}{\epsilon}\sum_{n=0}^{\infty} S_n(z)\epsilon^n\right] \tag{C.2}$$

Substituting this into Eq. (C.1), leads to

$$\left(\sum_{n=0}^{\infty} S_n'(z)\epsilon^n\right)^2 + \epsilon\sum_{n=0}^{\infty} S_n''(z)\epsilon^n + k_\beta(z)^2 = 0 \tag{C.3}$$

which can be rewritten as,

$$\sum_{n=0}^{\infty}\epsilon^n\sum_{i=0}^{n} S_i'(z)S_{n-i}'(z) + \sum_{n=1}^{\infty} S_{n-1}''(z)\epsilon^n + k_\beta(z)^2 = 0 \tag{C.4}$$

An expansion is obtained if it is assumed that terms grouped for each power of ϵ^n vanish separately,

$$S_0'(z)^2 + k_\beta(z)^2 = 0 \tag{C.5}$$

$$\sum_{i=0}^{n} S_i'(z)S_{n-i}'(z) + S_{n-1}''(z) = 0 \quad (n \geq 0) \tag{C.6}$$

The zero order term (Eq. (C.5)) can be solved easily,

$$S_0(z) = \pm i\int k_\beta(z)dz \tag{C.7}$$

The first order equation ($n = 1$ in Eq. (C.6)) is:

$$2S_0'(z)S_1'(z) + S_0''(z) = 0 \tag{C.8}$$

leading to

$$S_1(z) = -\int \frac{S_0''(z)}{2S_0'(z)}dz = -\frac{1}{2}\int \frac{k_\beta'(z)}{k_\beta(z)}dz = -\frac{1}{2}\ln k_\beta(z) \tag{C.9}$$

We can continue this iterative process to solve for $S_2(z)$, $S_3(z)$, ... using Eq. (C.6). In practice this is not usually done, and we usually only keep the first 2 terms. But here we give the expression for S_2 as well:

$$S_2 = \pm i\frac{3k_\beta'^2 - 2k_\beta'' k_\beta}{8k_\beta^3} \tag{C.10}$$

If we only keep the first two terms and set $\epsilon = 1$, we are left with:

$$x(z) \sim \exp(S_0(z) + S_1(z)) = \frac{1}{\sqrt{k_\beta(z)}}\exp\left[\pm i\int k_\beta(z)dz\right] \tag{C.11}$$

which is the same result of Eq. (2.38) in chapter 2. We can take the linear combination of these two solutions and get the real representation, and after imposing initial conditions, our final WKB solution is,

$$x(z) = x(0)\sqrt{\frac{k_\beta(0)}{k_\beta(z)}}\cos\left(\int_0^z k_\beta(s)ds\right) + \frac{x'(0) + x(0)\frac{k_\beta'(0)}{2k_\beta(0)}}{\sqrt{k_\beta(0)k_\beta(z)}}\sin\left(\int_0^z k_\beta(s)ds\right) \tag{C.12}$$

APPENDIX D

Derivations of relationships used in Chapter 3

D.1 Calculation of the evolution of the beam spot size: $\sqrt{\langle x^2 \rangle}$

In this appendix we provide details on calculating the second moment of the beam, i.e., the square of the spot size,

$$\begin{aligned} \langle x^2 \rangle &= \int x^2 f(x, x') dx dx' \\ &= \int x^2 f_i(x_i, x_i') dx_i dx_i' \\ &= \int (M_{11} x_i + M_{12} x_i')^2 f_i(x_i, x_i') dx_i dx_i' \end{aligned} \tag{D.1}$$

where $f(x, x')$ is the distribution function at z and f_i is the initial distribution function. From the Vlasov equation we have $f(x, x') = f_i(x_i, x_i')$, and $dxdx' = dx_i dx_i'$ because det(M) = 1.

The last step above is correct only if all the particles have the same energy. However, since different particles have different energy γ, their corresponding transport matrices M are different. In order to calculate the above integral with an energy spread in the beam, we assume the main difference in M is the phase advance ϕ. Even though the β_m, α_m in M are different (because of different γ), we assume them to be the same for all the particles and use $\gamma = \bar{\gamma}$ ($\bar{\gamma}$ is the mean energy among all the particles), while claiming the main difference in the motion of particles is the variation in ϕ due to their different energy γ. After the beam propagates for a distance z, we denote the distribution of the phase advance ϕ as $f_\phi(\phi)$ (with the normalization $\int f_\phi(\phi) d\phi = 1$), leading to,

$$
\begin{aligned}
\langle x^2 \rangle &= \iiint (M_{11}x_i + M_{12}x_i')^2 f_i(x_i, x_i') f_\phi(\phi) dx_i dx_i' d\phi \\
&= \langle x_i^2 \rangle \int d\phi f_\phi(\phi) M_{11}^2 + \langle x_i'^2 \rangle \int d\phi f_\phi(\phi) M_{12}^2 \\
&\quad + \langle x_i x_i' \rangle \int d\phi f_\phi(\phi) 2M_{11}M_{12} \\
&= \epsilon_i \Big[\beta_i \int d\phi f_\phi(\phi) M_{11}^2 + \gamma_i \int d\phi f_\phi(\phi) M_{12}^2 \\
&\quad - \alpha_i \int d\phi f_\phi(\phi) 2M_{11}M_{12} \Big]
\end{aligned}
\tag{D.2}
$$

where

$$
\begin{aligned}
&\int d\phi f_\phi(\phi) M_{11}^2 \\
&= \frac{\beta_m}{\beta_{mi}} \int d\phi f_\phi(\phi) (\cos\phi + \alpha_{mi} \sin\phi)^2 \\
&= \frac{1}{2} \frac{\beta_m}{\beta_{mi}} [(1 + C) + \alpha_{mi}^2 (1 - C) + 2\alpha_{mi} S] \\
&= \frac{1}{2} \frac{\beta_m}{\beta_{mi}} [\beta_{mi}\gamma_{mi} + (1 - \alpha_{mi}^2) C + 2\alpha_{mi} S]
\end{aligned}
$$

$$
\begin{aligned}
&\int d\phi f_\phi(\phi) M_{12}^2 \\
&= \beta_m \beta_{mi} \int d\phi f_\phi(\phi) \sin^2\phi \\
&= \frac{1}{2} \beta_m \beta_{mi} (1 - C)
\end{aligned}
\tag{D.3}
$$

$$
\begin{aligned}
&\int d\phi f_\phi(\phi) 2M_{11}M_{12} \\
&= \beta_m \int d\phi f_\phi(\phi) (2\cos\phi \sin\phi + 2\alpha_{mi} \sin^2\phi) \\
&= \beta_m [S + \alpha_{mi}(1 - C)]
\end{aligned}
$$

and where

$$
C = \int d\phi f_\phi(\phi) \cos 2\phi, \quad S = \int d\phi f_\phi(\phi) \sin 2\phi \tag{D.4}
$$

Finally, we obtain:

$$\begin{aligned}\langle x^2\rangle = \epsilon_i\beta_m\Big[&\frac{\beta_i\gamma_{mi}+\gamma_i\beta_{mi}-2\alpha_i\alpha_{mi}}{2}\\&+(\frac{\beta_i}{\beta_{mi}}-\frac{\beta_i\gamma_{mi}+\gamma_i\beta_{mi}+2\alpha_i\alpha_{mi}}{2})C\\&+(\frac{\beta_i}{\beta_{mi}}\alpha_{mi}-\alpha_i)S\Big]\end{aligned} \tag{D.5}$$

We can define:

$$\begin{aligned}A &= \frac{\beta_i\gamma_{mi}+\gamma_i\beta_{mi}-2\alpha_i\alpha_{mi}}{2}\\B_1 &= \frac{\beta_i}{\beta_{mi}}-A=\frac{\beta_i}{\beta_{mi}}-\frac{\beta_i\gamma_{mi}+\gamma_i\beta_{mi}-2\alpha_i\alpha_{mi}}{2}\\B_2 &= \frac{\beta_i}{\beta_{mi}}\alpha_{mi}-\alpha_i\end{aligned} \tag{D.6}$$

Leading to:

$$\langle x^2\rangle = \epsilon_i\beta_m(A+B_1C+B_2S) \tag{D.7}$$

D.2 Proof of $A \geqslant 1$

$$\begin{aligned}A &= \frac{\beta_i\gamma_{mi}+\gamma_i\beta_{mi}-2\alpha_i\alpha_{mi}}{2}\\&\geqslant \frac{2\sqrt{\beta_i\gamma_{mi}\gamma_i\beta_{mi}}-2\alpha_i\alpha_{mi}}{2}\\&= \sqrt{(1+\alpha_i^2)(1+\alpha_{mi}^2)}-\alpha_i\alpha_{mi}\\&= \sqrt{1+\alpha_i^2+\alpha_{mi}^2+\alpha_i^2\alpha_{mi}^2}-\alpha_i\alpha_{mi}\\&\geqslant \sqrt{1+2\alpha_i\alpha_{mi}+\alpha_i^2\alpha_{mi}^2}-\alpha_i\alpha_{mi}\\&= |1+\alpha_i\alpha_{mi}|-\alpha_i\alpha_{mi}\\&\geqslant 1\end{aligned} \tag{D.8}$$

D.3

In this appendix we derive the first order correction to the phase advance due to variations of the energy of the particle. We begin with the definition for the phase

$$\phi = \int_0^z \frac{\omega_p(s)}{\sqrt{2\gamma}c} ds \tag{D.9}$$

Due to the variation of γ, the variation of ϕ is

$$\begin{aligned}
\Delta\phi &= \Delta \int_0^z \frac{\omega_p(s)}{\sqrt{2\gamma}c} ds \\
&= \int_0^z \Delta(\frac{\omega_p(s)}{\sqrt{2\gamma}c}) ds \\
&= \int_0^z -\frac{1}{2}(\frac{\omega_p(s)}{\sqrt{2}\gamma^{\frac{3}{2}}c})\Delta\gamma ds \\
&= -\frac{\Delta\gamma}{2\gamma}\int_0^z \frac{\omega_p(s)}{\sqrt{2\gamma}c} ds \\
&= -\frac{\phi}{2\gamma}\Delta\gamma
\end{aligned} \tag{D.10}$$

So the difference between the phase advance of a particle with energy γ and the phase advance of a particle with the average energy $\bar{\gamma}$ is

$$\phi(\gamma) - \phi(\bar{\gamma}) = -\frac{\phi(\bar{\gamma})}{2\bar{\gamma}}\Delta\gamma \tag{D.11}$$

and

$$\phi(\gamma) = \bar{\phi} - \frac{\bar{\phi}}{2\bar{\gamma}}\Delta\gamma \tag{D.12}$$

D.4 Differential equation for β

In this appendix, we offer a derivation of equation (3.40) in chapter 3. We start from the definition of the beam's spot size:

$$\sigma_x = \sqrt{\langle x^2 \rangle} \tag{D.13}$$

Taking derivatives with respect to z provide:

$$\sigma_x' = \frac{\langle xx' \rangle}{\sigma_x} \tag{D.14}$$

$$\sigma_x'' = \frac{\langle x^2 \rangle \langle x'^2 \rangle - \langle xx' \rangle^2}{\sigma_x^3} + \frac{\langle xx'' \rangle}{\sigma_x} \tag{D.15}$$

Using the definition of geometric emittance (3.9) and the equation of motion (3.1), leads to:

$$\sigma_x'' = \frac{\epsilon^2}{\sigma_x^3} - k_\beta^2 \sigma_x \tag{D.16}$$

If we assume the beam has no energy spread, then under a linear focusing force, the beam's normalized emittance ϵ_n is a constant, so $\epsilon = \epsilon_n/\gamma$ is also a constant. Finally, if we use the definition of β: $\beta = \frac{\sigma_x^2}{\epsilon}$, we obtain

$$\frac{1}{2}\beta\beta'' - \frac{1}{4}\beta'^2 + \beta^2 k_\beta^2 = 1 \tag{D.17}$$

APPENDIX E

Derivations of expressions used in Chapter 4

E.1 Adiabatic ramp design

In this Appendix, we show how to design the plasma density upramp such that the α_m linearly decreases from α_{mi} to 0. Assume the plasma density upramp is in the range of $-L \leq z \leq 0$, where L is the length of the upramp, then we have:

$$\alpha_m(z) = -\alpha_{mi}\frac{z}{L} \tag{E.1}$$

From $\alpha_m(z) = -\frac{1}{2}\frac{d\beta_m(z)}{dz}$, we can get:

$$\beta_m(z) = \beta_{m0} + \alpha_{mi}\frac{z^2}{L} \tag{E.2}$$

We also assume that the beam's energy is a constant when propagating in the density ramp (This prior assumption can be verified in the simulation). From $\beta_m(z) = \sqrt{2\bar{\gamma}}\frac{c}{\omega_p(z)}$, we get:

$$\frac{n(z)}{n_0} = \frac{\omega_p(z)^2}{\omega_{p0}^2} = \frac{\beta_{m0}^2}{\beta_m(z)^2} = \frac{1}{\left(1 + \frac{\alpha_{mi}z^2}{\beta_{m0}L}\right)^2} \tag{E.3}$$

The density at the entrance, n_i, is related to α_{mi} and L by the constraint:

$$\frac{n_i}{n_0} = \frac{n(-L)}{n_0} = \frac{1}{\left(1 + \frac{\alpha_{mi}}{\beta_{m0}}L\right)^2} \tag{E.4}$$

So among n_i, α_{mi}, L, we can choose two parameters, and the third one is determined by the constraint above. Note that if we want the degree of ion motion to be small at the entrance

(small n_i), and also an adiabatic plasma ramp (small α_{mi}), then we have to use a longer upramp (large L). So there is a trade off among the (1) degree of ion motion at the entrance (2) adiabaticity of the ramp, and (3) length of the ramp. This trade off is something we need to consider when designing the ramp.

E.2 Ion motion parameter for a linearly matched beam

In this Appendix, we calculate the ion motion parameter Φ_b when the beam is linearly matched to the plasma. This follows arguments in Ref. [45] and Ref. [46].

Assume the density profile of the witness beam is transversely bi-Gaussian and longitudinally a flat-top, with a bunch length L_b, then the peak density is given by:

$$n_{b0} = \frac{N}{2\pi\sigma_r^2 L_b} \tag{E.5}$$

If the beam is linearly matched to the plasma, then we substitute σ_r with equation (4.12) and get:

$$n_{b0} = \sqrt{\frac{\bar{\gamma}}{2}}\frac{N\omega_p}{2\pi L_b \epsilon_n c} \tag{E.6}$$

Substituting the expression above into equation(4.7) leads to,

$$\begin{aligned}\Phi_b &= k_i L_b \\ &= \left(Z\frac{n_{b0}/n_0}{2M/m}k_{p0}^2 L_b^2\right)^{\frac{1}{2}} \\ &= \left(Z\frac{1}{2\pi}\frac{1}{2M/m}\sqrt{\frac{\bar{\gamma}}{2}}N\frac{k_{p0}^3}{n_0}\frac{L_b}{\epsilon_n}\sqrt{\frac{n}{n_0}}\right)^{\frac{1}{2}}\end{aligned} \tag{E.7}$$

where n_0 is the initial electron density and $Zn_{i0} = n_0$. If the beam is Gaussian along z with a bunch length σ_z, similarly we can get,

$$n_{b0} = \frac{N}{(2\pi)^{\frac{3}{2}}\sigma_r^2\sigma_z} \tag{E.8}$$

$$\begin{aligned}\Phi_b &= k_i(\sqrt{2\pi}\sigma_z) \\ &= \left(Z\frac{n_{b0}/n_0}{2M/m}k_{p0}^2(\sqrt{2\pi}\sigma_z)^2\right)^{\frac{1}{2}} \\ &= \left(Z\frac{1}{\sqrt{2\pi}}\frac{1}{2M/m}\sqrt{\frac{\bar{\gamma}}{2}}N\frac{k_{p0}^3}{n_0}\frac{\sigma_z}{\epsilon_n}\sqrt{\frac{n}{n_0}}\right)^{\frac{1}{2}}\end{aligned} \tag{E.9}$$

E.3 Nonlinear matching the spot size in a uniform plasma

In this appendix, we numerically find the approximated steady state spot size of the beam in a given nonlinear focusing force described by the 1D Gaussian phenomenological model. Details of the derivation will appear in a future publication by Hildebrand et al. We start from the definition of the beam spot size,

$$\sigma_x = \sqrt{< x^2 >} \tag{E.10}$$

and then take the first and second derivatives with respect to z to get

$$\sigma_x' = \frac{< xx' >}{\sigma_x} \tag{E.11}$$

and

$$\begin{aligned}\sigma_x'' &= \frac{< x'^2 >< x^2 > - < xx' >^2}{\sigma_x^3} + \frac{< xx'' >}{\sigma_x} \\ &= \frac{\epsilon_x^2}{\sigma_x^3} + \frac{< xF_x >}{\gamma\sigma_x}\end{aligned} \tag{E.12}$$

where we have assumed the beam has no energy spread. At steady state, $\sigma_x'' = 0$. If F_x is linear in x, $F_x = -k_\beta x$, then we obtain Eq. (2.71) in chapter 2. However, even if F_x is nonlinear, useful expressions can still be obtained. For example, consider the 1D phenomenological model for F_x including ion motion,

$$n_{ion}(x)/n_0 = 1 + A_0\exp\left(-x^2/2\sigma_{ion}^2\right) \tag{E.13}$$

$$F_x(x) = -\frac{x}{2} - A_0\sigma_{ion}^2\frac{1-\exp\left(\frac{-x^2}{2\sigma_{ion}^2}\right)}{x} \tag{E.14}$$

We cannot determine $< xF_x >$ as a function of σ because we do not know the beam distribution function in x. We therefore assume the beam's steady state distribution can be approximated by a Gaussian distribution:

$$f(x) = \frac{1}{\sqrt{2\pi}\sigma_x} \exp\left(-\frac{x^2}{2\sigma_x^2}\right) \tag{E.15}$$

Under this assumption

$$\begin{aligned} < xF_x > &= \int_{-\infty}^{+\infty} xF_x f(x)\, dx \\ &= -\frac{\sigma_x^2}{2} - A_0\sigma_{ion}^2 \left(1 - \frac{\sigma_{ion}}{\sqrt{\sigma_x^2 + \sigma_{ion}^2}}\right) \end{aligned} \tag{E.16}$$

which leads to the following steady state or nonlinear matching condition,

$$0 = \frac{\epsilon_x^2}{\sigma_x^3} - \frac{1}{\gamma}\left(\frac{\sigma_x}{2} + \frac{A_0\sigma_{ion}^2}{\sigma_x}\left(1 - \frac{\sigma_{ion}}{\sqrt{\sigma_x^2 + \sigma_{ion}^2}}\right)\right) \tag{E.17}$$

For given ion collapse model parameters (A_0 and σ_{ion}) and given beam parameters (ϵ_x and γ), we can find a numerical solution to σ_x for the above equation, which is a reasonable estimate of beam's steady state spot size.

REFERENCES

[1] Jean-Pierre Delahaye, Erik Adli, Spencer Gessner, Mark Hogan, Tor Raubenheimer, Weiming An, Chan Joshi, and Warren Mori. A Beam Driven Plasma-wakefield Linear Collider from Higgs Factory to Multi-TeV. In *5th International Particle Accelerator Conference*, pages 3791–3793, 7 2014.

[2] S. Lee, T. Katsouleas, P. Muggli, W. B. Mori, C. Joshi, R. Hemker, E. S. Dodd, C. E. Clayton, K. A. Marsh, B. Blue, S. Wang, R. Assmann, F. J. Decker, M. Hogan, R. Iverson, and D. Walz. Energy doubler for a linear collider. *Phys. Rev. ST Accel. Beams*, 5:011001, Jan 2002.

[3] John M. Dawson. Nonlinear electron oscillations in a cold plasma. *Phys. Rev.*, 113:383–387, Jan 1959.

[4] Alexander I. Akhiezer and R. V. Polovin. Theory of wave motion of an electron plasma. 1956.

[5] T. Tajima and J. M. Dawson. Laser electron accelerator. *Phys. Rev. Lett.*, 43:267–270, Jul 1979.

[6] E. Esarey, P. Sprangle, J. Krall, and A. Ting. Overview of plasma-based accelerator concepts. *IEEE Transactions on Plasma Science*, 24(2):252–288, 1996.

[7] Pisin Chen, J. M. Dawson, Robert W. Huff, and T. Katsouleas. Acceleration of electrons by the interaction of a bunched electron beam with a plasma. *Phys. Rev. Lett.*, 54:693–696, Feb 1985.

[8] C. Joshi, S. Corde, and W. B. Mori. Perspectives on the generation of electron beams from plasma-based accelerators and their near and long term applications. *Physics of Plasmas*, 27(7):070602, 2020.

[9] P. Muggli, B. E. Blue, C. E. Clayton, S. Deng, F.-J. Decker, M. J. Hogan, C. Huang, R. Iverson, C. Joshi, T. C. Katsouleas, S. Lee, W. Lu, K. A. Marsh, W. B. Mori, C. L. O'Connell, P. Raimondi, R. Siemann, and D. Walz. Meter-scale plasma-wakefield accelerator driven by a matched electron beam. *Phys. Rev. Lett.*, 93:014802, Jun 2004.

[10] M. J. Hogan, C. D. Barnes, C. E. Clayton, F. J. Decker, S. Deng, P. Emma, C. Huang, R. H. Iverson, D. K. Johnson, C. Joshi, T. Katsouleas, P. Krejcik, W. Lu, K. A. Marsh, W. B. Mori, P. Muggli, C. L. O'Connell, E. Oz, R. H. Siemann, and D. Walz. Multi-gev energy gain in a plasma-wakefield accelerator. *Phys. Rev. Lett.*, 95:054802, Jul 2005.

[11] S. P. D. Mangles, C. D. Murphy, Z. Najmudin, A. G. R. Thomas, J. L. Collier, A. E. Dangor, E. J. Divall, P. S. Foster, J. G. Gallacher, C. J. Hooker, D. A. Jaroszynski, A. J. Langley, W. B. Mori, P. A. Norreys, F. S. Tsung, R. Viskup, B. R. Walton, and

K. Krushelnick. Monoenergetic beams of relativistic electrons from intense laser–plasma interactions. *Nature*, 431(7008):535–538, 2004.

[12] J. Faure, Y. Glinec, A. Pukhov, S. Kiselev, S. Gordienko, E. Lefebvre, J. P. Rousseau, F. Burgy, and V. Malka. A laser–plasma accelerator producing monoenergetic electron beams. *Nature*, 431(7008):541–544, 2004.

[13] C. Geddes, Csaba Toth, J. Tilborg, E. Esarey, C. Schroeder, David Bruhwiler, Chet Nieter, John Cary, and Wim Leemans. High quality electron beams from a plasma channel guided laser wakefield accelerator. *Nature*, 431, 07 2004.

[14] Ian Blumenfeld, Christopher Clayton, Franz-Josef Decker, Mark Hogan, C.-K Huang, Rasmus Ischebeck, Richard Iverson, Chandrashekhar Joshi, Thomas Katsouleas, Neil Kirby, Wei Lu, Kenneth Marsh, W. Mori, P. Muggli, Erdem Oz, Robert Siemann, Dieter Walz, and Miaomiao Zhou. Energy doubling of 42 gev electrons in a metre-scale plasma wakefield accelerator. *Nature*, 445:741–4, 03 2007.

[15] Michael Litos, E Adli, Weiming An, C Clarke, Christopher Clayton, Sébastien Corde, Delahaye jean pierre, R. England, Alan Fisher, Joel Frederico, S Gessner, S Green, M Hogan, Chandrashekhar Joshi, W Lu, K Marsh, W. Mori, P. Muggli, N. Vafaei-Najafabadi, and Gerald Yocky. High-efficiency acceleration of an electron beam in a plasma wakefield accelerator. *Nature*, 515:92–5, 11 2014.

[16] S. Corde, E. Adli, J. M. Allen, W. An, C. I. Clarke, C. E. Clayton, J. P. Delahaye, J. Frederico, S. Gessner, S. Z. Green, M. J. Hogan, C. Joshi, N. Lipkowitz, M. Litos, W. Lu, K. A. Marsh, W. B. Mori, M. Schmeltz, N. Vafaei-Najafabadi, D. Walz, V. Yakimenko, and G. Yocky. Multi-gigaelectronvolt acceleration of positrons in a self-loaded plasma wakefield. *Nature*, 524(7566):442–445, 2015.

[17] W. P. Leemans, A. J. Gonsalves, H.-S. Mao, K. Nakamura, C. Benedetti, C. B. Schroeder, Cs. Tóth, J. Daniels, D. E. Mittelberger, S. S. Bulanov, J.-L. Vay, C. G. R. Geddes, and E. Esarey. Multi-gev electron beams from capillary-discharge-guided subpetawatt laser pulses in the self-trapping regime. *Phys. Rev. Lett.*, 113:245002, Dec 2014.

[18] S Steinke, J van Tilborg, C Benedetti, C G R Geddes, C B Schroeder, J Daniels, K K Swanson, A J Gonsalves, K Nakamura, N H Matlis, B H Shaw, E Esarey, and W P Leemans. Multistage coupling of independent laser-plasma accelerators. *Nature*, 530(7589):190–193, Feb 2016.

[19] Andrei Seryi, Mark Hogan, Shilun Pei, Tor Raubenheimer, Peter Tenenbaum, Tom Katsouleas, Chengkun Huang, Chan Joshi, Warren Mori, and Patric Muggli. A Concept of Plasma Wake Field Acceleration Linear Collider (PWFA-LC). In *Particle Accelerator Conference (PAC 09)*, page WE6PFP081, 2010.

[20] Carlo Benedetti, S. Bulanov, E. Esarey, C. Geddes, Anthony Gonsalves, A. Huebl, R. Lehe, Kei Nakamura, C. Schroeder, Davide Terzani, J. Tilborg, M. Turner, Jean-Luc Vay, T. Zhou, Fert Albert, J. Bromage, Mike Campbell, Dustin Froula, John Palastro, and N. Vafaei-Najafabadi. Linear collider based on laser-plasma accelerators, 03 2022.

[21] http://www.linearcollider.org/.

[22] J. B. Rosenzweig, B. Breizman, T. Katsouleas, and J. J. Su. Acceleration and focusing of electrons in two-dimensional nonlinear plasma wake fields. *Phys. Rev. A*, 44:R6189–R6192, Nov 1991.

[23] W. Lu, C. Huang, M. Zhou, W. B. Mori, and T. Katsouleas. Nonlinear theory for relativistic plasma wakefields in the blowout regime. *Phys. Rev. Lett.*, 96:165002, Apr 2006.

[24] W. Lu, M. Tzoufras, C. Joshi, F. S. Tsung, W. B. Mori, J. Vieira, R. A. Fonseca, and L. O. Silva. Generating multi-gev electron bunches using single stage laser wakefield acceleration in a 3d nonlinear regime. *Phys. Rev. ST Accel. Beams*, 10:061301, Jun 2007.

[25] Alexander Pukhov and Jürgen Meyer ter Vehn. Laser wake field acceleration: the highly non-linear broken-wave regime. *Applied Physics B*, 74:355–361, 2002.

[26] S. Diederichs, T. J. Mehrling, C. Benedetti, C. B. Schroeder, A. Knetsch, E. Esarey, and J. Osterhoff. Positron transport and acceleration in beam-driven plasma wakefield accelerators using plasma columns. *Phys. Rev. Accel. Beams*, 22:081301, Aug 2019.

[27] Shiyu Zhou, Jianfei Hua, Weiming An, Warren B. Mori, Chan Joshi, Jie Gao, and Wei Lu. High efficiency uniform wakefield acceleration of a positron beam using stable asymmetric mode in a hollow channel plasma. *Phys. Rev. Lett.*, 127:174801, Oct 2021.

[28] Shiyu Zhou, Weiming An, Siqin Ding, Jianfei Hua, Warren B. Mori, Chan Joshi, and Wei Lu. Positron beam loading and acceleration in the blowout regime of plasma wakefield accelerator. 11 2022.

[29] P. Sprangle, E. Esarey, and A. Ting. Nonlinear interaction of intense laser pulses in plasmas. *Phys. Rev. A*, 41:4463–4469, 1990.

[30] W. B. Mori, C. D. Decker, D. E. Hinkel, and T. Katsouleas. Raman forward scattering of short-pulse high-intensity lasers. *Phys. Rev. Lett.*, 72:1482–1485, Mar 1994.

[31] G. Shvets and J. S. Wurtele. Instabilities of short-pulse laser propagation through plasma channels. *Phys. Rev. Lett.*, 73:3540–3543, Dec 1994.

[32] W. K. H. Panofsky and W. A. Wenzel. Some considerations concerning the transverse deflection of charged particles in radio-frequency fields. *Review of Scientific Instruments*, 27(11):967–967, 1956.

[33] P. B. Wilson. Introduction to wakefields and wake potentials. *AIP Conference Proceedings*, 184(1):525–564, 1989.

[34] Patrick Mora and Thomas M. Antonsen, Jr. Kinetic modeling of intense, short laser pulses propagating in tenuous plasmas. *Physics of Plasmas*, 4(1):217–229, 1997.

[35] Warren B. Mori. class notes, 2019.

[36] M. Tzoufras, W. Lu, F. S. Tsung, C. Huang, W. B. Mori, T. Katsouleas, J. Vieira, R. A. Fonseca, and L. O. Silva. Beam loading in the nonlinear regime of plasma-based acceleration. *Phys. Rev. Lett.*, 101:145002, Sep 2008.

[37] Thomas C. Katsouleas, S. Wilks, P. Chen, J. M. Dawson, and J. J. Su. Beam Loading in Plasma Accelerators. *Part. Accel.*, 22:81–99, 1987.

[38] T. N. Dalichaouch, X. L. Xu, A. Tableman, F. Li, F. S. Tsung, and W. B. Mori. A multi-sheath model for highly nonlinear plasma wakefields. *Physics of Plasmas*, 28(6):063103, 2021.

[39] Klaus Floettmann. Adiabatic matching section for plasma accelerated beams. *Phys. Rev. ST Accel. Beams*, 17:054402, May 2014.

[40] I. Dornmair, K. Floettmann, and A. R. Maier. Emittance conservation by tailored focusing profiles in a plasma accelerator. *Phys. Rev. ST Accel. Beams*, 18:041302, Apr 2015.

[41] X. L. Xu, J. F. Hua, Y. P. Wu, C. J. Zhang, F. Li, Y. Wan, C.-H. Pai, W. Lu, W. An, P. Yu, M. J. Hogan, C. Joshi, and W. B. Mori. Physics of phase space matching for staging plasma and traditional accelerator components using longitudinally tailored plasma profiles. *Phys. Rev. Lett.*, 116:124801, Mar 2016.

[42] R Ariniello, C.E. Doss, K Hunt-Stone, J.R. Cary, and M.D. Litos. Transverse beam dynamics in a plasma density ramp. *Physical Review Accelerators and Beams*, 22, 04 2019.

[43] M. D. Litos, R. Ariniello, C. E. Doss, K. Hunt-Stone, and J. R. Cary. Beam emittance preservation using gaussian density ramps in a beam-driven plasma wakefield accelerator. *Philosophical Transactions of the Royal Society A: Mathematical, Physical and Engineering Sciences*, 377(2151):20180181, 2019.

[44] Yujian Zhao, Weiming An, Xinlu Xu, Fei Li, Lance Hildebrand, Mark Hogan, Vitaly Yakimenko, Chandrashekhar Joshi, and Warren Mori. Emittance preservation through density ramp matching sections in a plasma wakefield accelerator. *Physical Review Accelerators and Beams*, 23, 01 2020.

[45] S. Lee and T. Katsouleas. Wakefield accelerators in the blowout regime with mobile ions. *AIP Conference Proceedings*, 472(1):524–533, 1999.

[46] J. B. Rosenzweig, A. M. Cook, A. Scott, M. C. Thompson, and R. B. Yoder. Effects of ion motion in intense beam-driven plasma wakefield accelerators. *Phys. Rev. Lett.*, 95:195002, Oct 2005.

[47] Weiming An, Wei Lu, Chengkun Huang, Xinlu Xu, Mark J. Hogan, Chan Joshi, and Warren B. Mori. Ion motion induced emittance growth of matched electron beams in plasma wakefields. *Phys. Rev. Lett.*, 118:244801, Jun 2017.

[48] Reza Gholizadeh, Thomas C. Katsouleas, Patric Muggli, C. K. Huang, and Warren B. Mori. Preservation of beam emittance in the presence of ion motion in future high-energy plasma-wakefield-based colliders. *Physical review letters*, 104 15:155001, 2010.

[49] C. Benedetti, C. B. Schroeder, E. Esarey, and W. P. Leemans. Emittance preservation in plasma-based accelerators with ion motion. *Phys. Rev. Accel. Beams*, 20:111301, Nov 2017.

[50] C. Benedetti, T. J. Mehrling, C. B. Schroeder, C. G. R. Geddes, and E. Esarey. Adiabatic matching of particle bunches in a plasma-based accelerator in the presence of ion motion. *Physics of Plasmas*, 28(5):053102, 2021.

[51] David H. Whittum, William M. Sharp, Simon S. Yu, Martin Lampe, and Glenn Joyce. Electron-hose instability in the ion-focused regime. *Phys. Rev. Lett.*, 67:991–994, Aug 1991.

[52] Andrew A. Geraci and David H. Whittum. Transverse dynamics of a relativistic electron beam in an underdense plasma channel. *Physics of Plasmas*, 7(8):3431–3440, 2000.

[53] C. Huang, W. Lu, M. Zhou, C. E. Clayton, C. Joshi, W. B. Mori, P. Muggli, S. Deng, E. Oz, T. Katsouleas, M. J. Hogan, I. Blumenfeld, F. J. Decker, R. Ischebeck, R. H. Iverson, N. A. Kirby, and D. Walz. Hosing instability in the blow-out regime for plasma-wakefield acceleration. *Phys. Rev. Lett.*, 99:255001, Dec 2007.

[54] T. J. Mehrling, R. A. Fonseca, A. Martinez de la Ossa, and J. Vieira. Mitigation of the hose instability in plasma-wakefield accelerators. *Phys. Rev. Lett.*, 118:174801, Apr 2017.

[55] L Hildebrand, Weiming An, Xinlu Xu, Fang Li, Y Zhao, M J. Hogan, Vitaly Yakimenko, S S. Nagaitsev, E Adli, Chandrashekhar Joshi, and W Mori. Mitigation techniques for witness beam hosing in plasma - based acceleration. *2018 IEEE Advanced Accelerator Concepts Workshop (AAC)*, 00:1–5, 08 2018.

[56] T. J. Mehrling, C. Benedetti, C. B. Schroeder, E. Esarey, and W. P. Leemans. Suppression of beam hosing in plasma accelerators with ion motion. *Phys. Rev. Lett.*, 121:264802, Dec 2018.

[57] Charles K. Birdsall and A. Bruce Langdon. *Plasma physics via computer simulation*. Taylor and Francis, New York, 2005.

[58] John M. Dawson. Particle simulation of plasmas. *Rev. Mod. Phys.*, 55:403–447, Apr 1983.

[59] Ricardo Fonseca, Luís Silva, Frank Tsung, Viktor Decyk, Wei Lu, Chuang Ren, W. Mori, Shaogui Deng, Shiyoun Lee, T. Katsouleas, and J. Adam. Osiris: A three-dimensional, fully relativistic particle in cell code for modeling plasma based accelerators. pages 342–351, 04 2002.

[60] C. Huang, V.K. Decyk, C. Ren, M. Zhou, W. Lu, W.B. Mori, J.H. Cooley, T.M. Antonsen, and T. Katsouleas. Quickpic: A highly efficient particle-in-cell code for modeling wakefield acceleration in plasmas. *Journal of Computational Physics*, 217(2):658 – 679, 2006.

[61] Weiming An, Viktor K. Decyk, Warren B. Mori, and Thomas M. Antonsen. An improved iteration loop for the three dimensional quasi-static particle-in-cell algorithm: Quickpic. *Journal of Computational Physics*, 250:165 – 177, 2013.

[62] https://github.com/ucla-plasma-simulation-group/quickpic-opensource.

[63] Fei Li, Weiming An, Viktor K. Decyk, Xinlu Xu, Mark J. Hogan, and Warren B. Mori. A quasi-static particle-in-cell algorithm based on an azimuthal fourier decomposition for highly efficient simulations of plasma-based acceleration: Qpad. *Computer Physics Communications*, 261:107784, 2021.

[64] A.F. Lifschitz, X. Davoine, E. Lefebvre, J. Faure, C. Rechatin, and V. Malka. Particle-in-cell modelling of laser–plasma interaction using fourier decomposition. *Journal of Computational Physics*, 228(5):1803–1814, 2009.

[65] A. Davidson, A. Tableman, W. An, F.S. Tsung, W. Lu, J. Vieira, R.A. Fonseca, L.O. Silva, and W.B. Mori. Implementation of a hybrid particle code with a pic description in r–z and a gridless description in into osiris. *Journal of Computational Physics*, 281:1063–1077, 2015.

[66] Rémi Lehe, Manuel Kirchen, Igor A. Andriyash, Brendan B. Godfrey, and Jean-Luc Vay. A spectral, quasi-cylindrical and dispersion-free particle-in-cell algorithm. *Computer Physics Communications*, 203:66–82, 2016.

[67] C. Benedetti, C. B. Schroeder, E. Esarey, C. G. R. Geddes, and W. P. Leemans. Efficient modeling of laser-plasma accelerators with inf&rno. *AIP Conference Proceedings*, 1299(1):250–255, 2010.

[68] C. Benedetti, C. B. Schroeder, C. G. R. Geddes, E. Esarey, and W. P. Leemans. Efficient modeling of laser-plasma accelerator staging experiments using inf&rno. *AIP Conference Proceedings*, 1812(1):050005, 2017.

[69] C Benedetti, C B Schroeder, C G R Geddes, E Esarey, and W P Leemans. An accurate and efficient laser-envelope solver for the modeling of laser-plasma accelerators. *Plasma Physics and Controlled Fusion*, 60(1):014002, oct 2017.

[70] T Mehrling, C Benedetti, C B Schroeder, and J Osterhoff. Hipace: a quasi-static particle-in-cell code. *Plasma Physics and Controlled Fusion*, 56(8):084012, jul 2014.

[71] S. Diederichs, C. Benedetti, A. Huebl, R. Lehe, A. Myers, A. Sinn, J.-L. Vay, W. Zhang, and M. Thévenet. Hipace++: A portable, 3d quasi-static particle-in-cell code. *Computer Physics Communications*, 278:108421, 2022.

[72] Ángel Ferran Pousa, Ralph Assmann, and Alberto Martinez de la Ossa. Wake-t: a fast particle tracking code for plasma-based accelerators. *Journal of Physics: Conference Series*, 1350:012056, 11 2019.

[73] E.D Courant and H.S Snyder. Theory of the alternating-gradient synchrotron. *Annals of Physics*, 3(1):1–48, 1958.

[74] S. Y. Lee. *Accelerator Physics*. World Scientific Publishing Co. Pte. Ltd, 2 edition, 2004.

[75] Carl Bender. Mathematical physics - lecture 2, nov 2011. PIRSA:11110041 see, `https://pirsa.org`.

[76] Manuel Vogel. Plasma physics: an introduction, by richard fitzpatrick: Scope: textbook. level: advanced undergraduate, postgraduate. *Contemporary Physics*, 57:1–1, 08 2016.

[77] X. L. Xu, J. F. Hua, F. Li, C. J. Zhang, L. X. Yan, Y. C. Du, W. H. Huang, H. B. Chen, C. X. Tang, W. Lu, P. Yu, W. An, C. Joshi, and W. B. Mori. Phase-space dynamics of ionization injection in plasma-based accelerators. *Phys. Rev. Lett.*, 112:035003, Jan 2014.

[78] Alexander Aschikhin, Timon Johannes Mehrling, Alberto Martinez de la Ossa, and Jens Osterhoff. Analytical model for the uncorrelated emittance evolution of externally injected beams in plasma-based accelerators. *Nuclear Instruments and Methods in Physics Research Section A: Accelerators, Spectrometers, Detectors and Associated Equipment*, 909:414 – 418, 2018. 3rd European Advanced Accelerator Concepts workshop (EAAC2017).

[79] Navid Vafaei-Najafabadi Warren B. Mori. Class notes of uspas, 2020.

[80] R. Ariniello, C. E. Doss, V. Lee, C. Hansel, J. R. Cary, and M. D. Litos. Chromatic transverse dynamics in a nonlinear plasma accelerator. *Phys. Rev. Res.*, 4:043120, Nov 2022.

[81] Warren B. Mori. Master thesis, 1984.

[82] L.D. Landau and E.M. Lifshitz. *Mechanics: Volume 1.* Number v. 1. Elsevier Science, 1982.

[83] H. Goldstein. *Classical Mechanics.* Pearson India, 2011.

[84] Luca Ciotti. *The Collisionless Boltzmann Equation and the Jeans Theorem*, pages 151–171. Cambridge University Press, 2021.

[85] Marco Taboga. *Multivariate normal distribution.* Kindle Direct Publishing, 2021.

[86] T. Mehrling, J. Grebenyuk, F. S. Tsung, K. Floettmann, and J. Osterhoff. Transverse emittance growth in staged laser-wakefield acceleration. *Phys. Rev. ST Accel. Beams*, 15:111303, Nov 2012.

[87] P. Antici, A. Bacci, C. Benedetti, E. Chiadroni, M. Ferrario, A. R. Rossi, L. Lancia, M. Migliorati, A. Mostacci, L. Palumbo, and L. Serafini. Laser-driven electron beamlines generated by coupling laser-plasma sources with conventional transport systems. *Journal of Applied Physics*, 112(4):044902, 2012.

[88] M. Migliorati, A. Bacci, C. Benedetti, E. Chiadroni, M. Ferrario, A. Mostacci, L. Palumbo, A. R. Rossi, L. Serafini, and P. Antici. Intrinsic normalized emittance growth in laser-driven electron accelerators. *Phys. Rev. ST Accel. Beams*, 16:011302, Jan 2013.

[89] Xiangkun Li, Antoine Chancé, and Phu Anh Phi Nghiem. Preserving emittance by matching out and matching in plasma wakefield acceleration stage. *Phys. Rev. Accel. Beams*, 22(2):021304, 2019.

[90] C Joshi, E Adli, W An, C E Clayton, S Corde, S Gessner, M J Hogan, M Litos, W Lu, K A Marsh, W B Mori, N Vafaei-Najafabadi, B O'shea, Xinlu Xu, G White, and V Yakimenko. Plasma wakefield acceleration experiments at facet ii. *Plasma Physics and Controlled Fusion*, 60(3):034001, 2018.

[91] David L. Bruhwiler, D. A. Dimitrov, John R. Cary, Eric Esarey, Wim Leemans, and Rodolfo E. Giacone. Particle-in-cell simulations of tunneling ionization effects in plasma-based accelerators. *Physics of Plasmas*, 10(5):2022–2030, 2003.

[92] David J. Griffiths. *Introduction to Quantum Mechanics.*

[93] R. L. Williams and T. Katsouleas. Numerical studies on the ramped density plasma lens. *AIP Conference Proceedings*, 279(1):565–578, 1992.

[94] Patrick G. O'Shea. Reversible and irreversible emittance growth. *Phys. Rev. E*, 57:1081–1087, Jan 1998.

[95] Carl A. Lindstrøm. Staging of plasma-wakefield accelerators. *Phys. Rev. Accel. Beams*, 24:014801, Jan 2021.

[96] Wim Leemans and Eric Esarey. Esarey, e.: Laser-driven plasma-wave electron accelerators. phys. today 62(3), 44. *Physics Today - PHYS TODAY*, 62, 03 2009.

[97] Carl Lindstrøm, E Adli, Juergen Pfingstner, Eduardo Marin, and Daniel Schulte. Transverse tolerances of a multi-stage plasma wakefield accelerator. 06 2016.

[98] Lance Hildebrand. Private communication.